博士論文


Heat Transfer Effects in Small Wave Rotors

（小型ウェーブロータにおける熱伝達の影響）


鄧　実

Heat Transfer Effects

in

Small Wave Rotors

（小型ウェーブロータにおける熱伝達の影響）

A Dissertation

Submitted to the Faculty of Graduate School of Frontier Sciences of

the University of Tokyo

in Partial Fulfillment of the Requirements for the degree of

Doctor of Philosophy

in

Advanced Energy

by

Shi Deng

（鄧 実）

THE UNIVERSITY OF TOKYO

December 2014

# ACKNOWLEDGEMENTS

# ABSTRACT

Although the wave rotor is expected to enhance the performance of micro and ultra-micro gas turbines, the device itself may be affected by downsizing. Apart from the immediate effect of viscosity on flow dynamics when size reduces, the effects of heat transfer on flow field rise in such small sizes.

Heat transfer and its effects of wave rotor, including but not limited to the small ones, are analyzed and presented in this work. Only limited prior work has been conducted to explain the effects of heat transfer since the influence of heat transfer on wave rotors of conventional sizes seems to be inconspicuous, although no evidence suggests whether heat transfer is influential or not in conventional sizes. Therefore, as a first step, the present work aims to settle the heat transfer problem of wave rotor cell, in which compression and expansion take place.

The current investigation focuses on heat transfer between internal flow passage and its surrounding wall of 3-D single cell of through-flow wave rotor. Conjugate heat transfer boundary treatment that simulates unsteady heat transfer across fluid-solid interface is employed to analyze heat transfer. To simulate typical internal flow dynamics and heat transfer in wave rotor cell, conjugate heat transfer module is integrated into the existing in-house code that was developed to analyze internal flow dynamics of wave rotor cell. Verifications of the code are conducted for unsteady conduction problem, shock tube convective heat transfer problem, and internal flow dynamics and heat transfer associated with wave-rotor-like flow field that is designed to reflect essential characteristics of flow field in wave rotor cell and realized by experimental test run.

The situation that the whole cell is thermally insulated from outside is the major concern in this work. With the light shed by delving into heat flux distribution and by comparing adiabatic case and heat transfer case in conventional size and small size, this work presents investigations of causes of intense heat flux, as well as effects of heat transfer on internal flow field, charging processes and discharging processes for various sizes. High-speed inflows of hot gas and cold air, compressed gas and air, and shock waves are found to create noticeable heat flux at all sizes investigated. In small size, heat fluxes caused by primary shock wave propagating in air, expansion waves and compression wave becomes noticeable. When heat transfer is taken into account, states of fluid in cell before compression process are affected, shock waves in compression process are weaker, and corresponding changes in the charging and discharging processes are observed as common phenomena at all sizes investigated. A unique phenomenon that arrival of reflected shock wave delayed owing to considerable heat transfer effects is discovered at the smallest size investigated. This delay demonstrates a necessity of port degree modification in wave rotor design. Besides, by conducting comparison across sizes, heat transfer effects on charging and discharging are found to grow rapidly when reducing size from 1X size. Moreover, it is indicated that with an appropriate temperature assigned to the lateral boundary as uniform wall temperature, isothermal boundary condition that costs less computation resource may be as acceptable for investigation of heat transfer problem related to through-flow wave rotor.

In addition, the elementary situation that the cell subjects to constant convective heat transfer at the external surface of shroud and hub walls is considered with external flow temperature of average temperature of ports. Since external flow temperature is close to wall temperature, heat transfer effects are similar to those in the situation when external surfaces of wall are adiabatic.

# TABLE OF CONTENTS

# LIST OF ILLUSTRATIONS

# LIST OF TABLES

# NOMENCLATURE

| | |
|---|---|
| $a$ | Coefficient in discretization equation |
| $a_{nb}$ | Neighbor coefficient in discretization equation |
| Bi | Biot number |
| $c_p$ | Specific heat at constant pressure |
| $c_v$ | Specific heat at constant volume |
| $D$ | Midspan diameter of wave rotor |
| $D_H$ | Hydraulic diameter of flow passage of wave rotor cell |
| $e$ | Base of the natural logarithm |
| Fo | Fourier number |
| $H$ | Height; Radial internal height of wave rotor cell |
| $h$ | Heat transfer coefficient |
| $I$ | Input |
| $k$ | Thermal conductivity |
| $L$ | Axial length of wave rotor cell |
| $Ma_2$ | Mach number behind shock wave in zone "2" in shock tube test |
| $Ma_s$ | Mach number of shock wave in shock tube test |
| Nu | Nusselt number |
| $nb$ | Code number of neighbor node |
| $nbr$ | Code number of face |
| $P$ | Pressure |
| $p_1$ | Pressure in zone "1" in shock tube test |
| $p_2$ | Pressure in zone "2" in shock tube test |
| $p_4$ | Pressure in zone "4" in shock tube test |
| Pr | Prandtl number |
| $q$ | Heat flux |
| $q"$ | Heat flux related to shock tube test |
| $q_m$ | Mass flow rate |
| $R$ | Response |
| $r$ | Radial coordinate; Radius |
| Re | Renolds number |
| $S$ | Entropy |
| $T$ | Temperature |
| $T_2$ | Temperature in zone "2" in shock tube test |
| $t$ | time |
| $u$ | Axial velocity; Velocity component along $x$ direction |
| $u_2$ | Flow speed in zone "2" in shock tube test |

| | |
|---|---|
| $W$ | Circumferential internal width of wave rotor cell; Width |
| $W_s$ | Shock wave speed in shock tube test |
| $x$ | Axial coordinate; Axial location; depth coordinate in analytical solution for unsteady conduction; $x$ direction |
| $y$ | $y$ direction |
| $z$ | $z$ direction |

*Greek Letters*

| | |
|---|---|
| $\gamma$ | Heat capacity ratio |
| $\delta$ | Plate thickness; Wall thickness of wall rotor cell |
| $\delta_{BL}$ | Boundary layer thickness |
| $\Theta$ | Dimensionless temperature in analytical solution for unsteady conduction |
| $\theta$ | Angular coordinate; Degree; Degree of internal passage of wave rotor cell |
| $\mu$ | Dynamic viscosity |
| $\mu_n$ | Parameter in analytical solution for unsteady conduction [1] |
| $\rho$ | Density |
| $\tau$ | Time constant |
| $\omega$ | Angular velocity |

*Subscripts*

| | |
|---|---|
| 0 | Total parameter |
| AL | AL port |
| avg | Average |
| ext | External fluid; External surface |
| f | Fluid |
| fin | Final |
| GH | GH port |
| HFM | Measured by heat flux sensor HFM |
| intf | Conjugate interface; Interface |
| $L$ | Charicteristic length |
| o | Outer |
| port | State parameter related to port |
| $r$ | Rotational |
| s | Solid |
| tot | Total parameter |
| w | Wall |
| $x$ | $x$ direction; $x$ coordinate |

*Superscripts*

| | |
|---|---|
| 0 | Old state |

# CHAPTER 1: INTRODUCTION

## 1.1    General Issues of Small Wave Rotor

### 1.1.1    Issues of Micro Energy System

Small power systems like micro and ultra-micro turbomachinery have been attractive to researchers over the last decades [2–12]. However, since the experiences and solutions developed for turbomachinery at conventional scale do not necessarily work in the same way at such small scales, efforts should be made to realize feasible turbomachinery at micro and ultra-micro scales. Although many challenging problems have been solved, the development of micro and ultra-micro turbomachinery is still deterred by the poor efficiency of each component and some other deficiencies. For example, the low compressor efficiency (40~50%) and the low efficiency (1~10%) of micro-fabricated Brayton and Rankine cycle devices has been obtained by Müller et al. [13], whereas a total efficiency of about 5% is addressed in the performance study of ONERA's research program DecaWatt [3].

### 1.1.2    Benefits of Utilizing Wave Rotor for Micro and Ultra-Micro Gas Turbine

Wave rotor, a proposed solution for dealing with low efficiency at the small scales, is a promising device that can enhance gas turbine efficiency at micro and ultra-micro scales by elevating the overall pressure ratio.

In contrast with using vanes and blades in turbomachinery, the wave rotor performs inter-fluid energy exchange by taking advantage of the travelling pressure waves. Initially proposed as pressure exchanger combined with gas turbine of locomotive to obtain higher compression pressure in a more economical way than sole turbomachinery [14], though, the wave rotor is firstly commercialized as a supercharging device for diesel engine instead of supercharger and turbocharger [15], [16].

Since 1990s, research efforts have been focused on improving the performance of gas turbine and jet engine by implementing wave rotor as topping unit at NASA and MSU [17–26], as well as at ONERA and the University of Tokyo [27–31]. Basically, a wave rotor consists of a series of tubes (cells) arranged around the rotation axis and several ports charging and discharging fluid. A schematic arrangement of wave rotor components is shown in Fig. 1-1, and the photographs for the rotating part, including the shaft and the circumferential array of cells, are exhibited in Fig. 1-2. Shock, compression and expansion waves are generated at the ends of cells and propagate axially in the cells due to different pressures (or different energy density) in the ports, and thus pressure exchange between different fluids is realized by propagation of those pressure waves.

Pressure exchange resulting in compression and expansion is based on direct energy exchange between high-pressure hot gas and low-pressure cold air. At small scales when heat management becomes critical, the cell does not have to tolerate the peak temperature, and this feature undoubtedly facilitates the heat management.
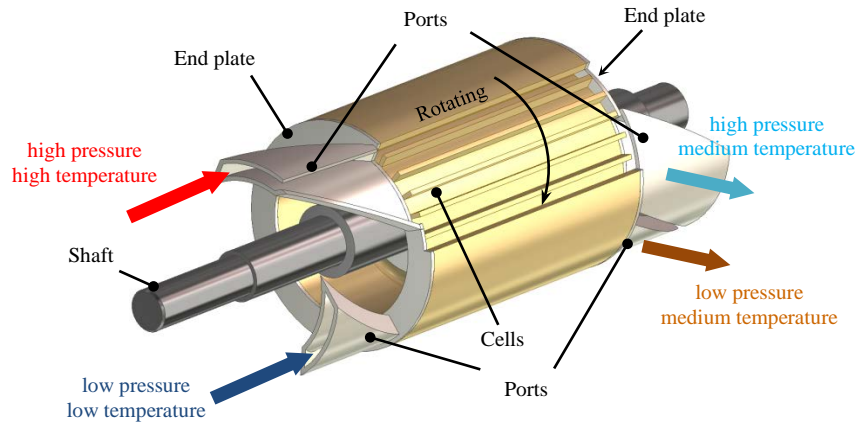
Fig. 1-1 Schematic of wave rotor components and arrangements
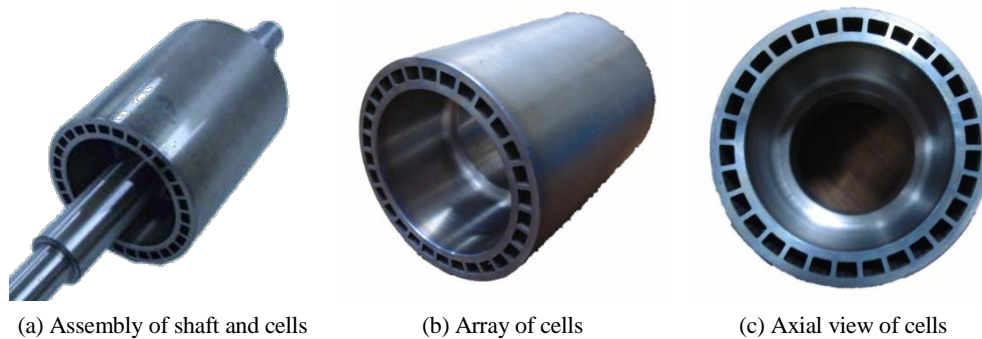


(a) Assembly of shaft and cells      (b) Array of cells      (c) Axial view of cells

Fig. 1-2 Photographs of rotating components of wave rotor

Furthermore, wave rotor is supposed to suffer much less compression efficiency drop as size reduces [32]. And thereby, at small scale, when compression and expansion are more efficient than in turbomachinery, integration of wave rotor is expected to be useful, and higher optimum pressure ratio is attainable. As is known, the performance of gas turbine is primarily determined by the cycle pressure ratio and the turbine inlet temperature. For micro compressor, not only the efficiency is low but also the optimum pressure ratio is as low as 2 [13]. With wave rotor topped, optimum cycle pressure ratio can be elevated and the inlet pressure of turbine can be lifted without changing the turbine inlet temperature that is restricted by materials technology and costs. The schematic thermodynamic cycles of gas turbines with and without wave rotor topping are depicted in Fig. 1-3, using which the benefits of wave-rotor-topping cycle can be explained. The well-known Brayton cycle in baseline gas turbine consists of compression process in compressor (state 0 ~ state 1), constant-pressure combustion in combustor (state 1 ~ state 4'), and expansion process in turbine (state 4' ~ state 5), corresponding to the arrangement of gas turbine components described in Fig. 1-4. When wave rotor is incorporated (Fig. 1-5), it is located downstream the compressor, upstream the turbine, and parallel with the combustor. Thereupon, the cycle with wave rotor topped in the T-S diagram (Fig. 1-3) consists of two more processes: one for compression (state 1 ~ state 2) and the other for expansion (state 3 ~ state 4). Since the air is further compressed, given the same initial states at point 0 and the same compression process in compressor (state 0 ~ state 1), the combustion is executed at a greater pressure (state 2 ~ state 3) than in baseline, and the cycle peak temperature $T_3$ at state 3 is also higher than $T_{4'}$ at state 4' in baseline. Admittedly, the change in inlet pressure of turbine requires certain modification of the design of baseline turbine; but, positively and more importantly, the greater inlet pressure helps improve the efficiency of turbine. As a result of the topping cycle, the optimum cycle pressure ratio and the cycle peak temperature can be raised by wave rotor topping.

Meanwhile, pressure gain of $P_{4, \text{topped}} - P_{4', \text{baseline}}$ can be achieved with identical turbine inlet temperature $T_4 = T_{4'}$.

Moreover, the cell in which the pressure exchange comes about can be manufactured easily as straight duct as long as the cell does not contribute to compression or expansion like a vane or blade but just provides with a room for compression and expansion, and this feature is also fit for small scale.

In the wake of the potential capability of elevating optimum cycle pressure ratio and cycle peak temperature for gas turbines at micro and ultra-micro scales, the research group of the University of Tokyo has conducted extensive investigations on micro wave rotor, which is envisioned to be incorporated to a micro or ultra-micro gas turbine, by means of both numerical simulations and experimental tests [33–39].
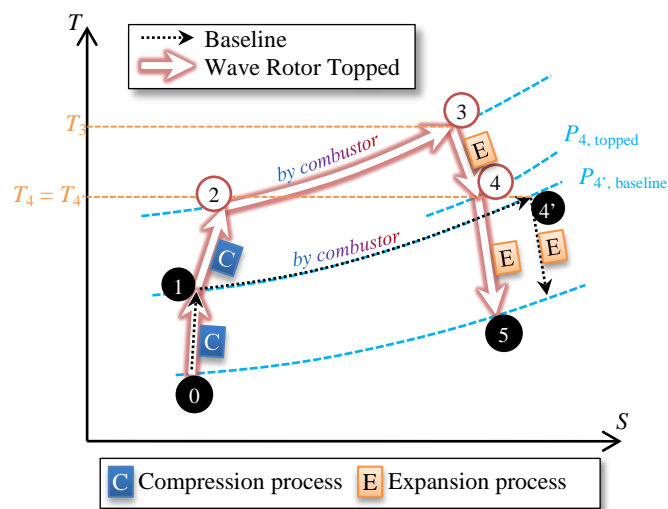
Fig. 1-3 T-S diagram of thermodynamic cycle for both baseline gas turbine
and wave rotor topped gas turbine
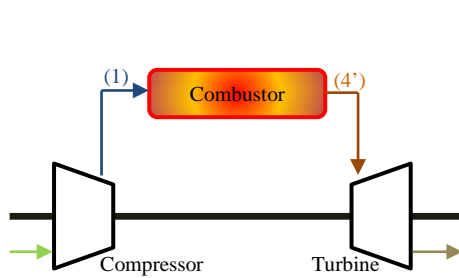
Fig. 1-4 Flow diagram of baseline gas turbine
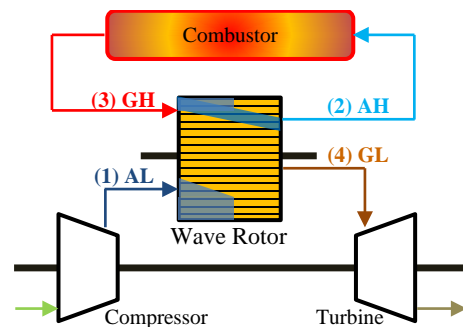
Fig. 1-5 Flow diagram of four-port through-flow wave rotor topping gas turbine

## 1.2    Operating Principles

Many kinds of wave rotor cycle can be conceived and designed by varying the conditions for pressure wave generation, and a variety of wave rotor configurations have been designed, investigated and developed for diverse purposes. For example, the port number could be three [40–42] or four, the flow type could be through-flow or reverse-flow [16], [24], [43], the flow direction could be axial or radial [44]. The applications include diesel engine [16], refrigeration [45], [46], jet engine [18], [25], ultra-micro gas turbine [2], [8–11] and so forth [47].

As far as wave rotor topping gas turbine is concerned, most frequently investigated is four-port axial wave rotor of through-flow configuration. A typical four-port through-flow axial wave rotor for micro gas turbine is introduced into the thermodynamic cycle as illustrated in Fig. 1-3 and the location of wave rotor among gas turbine components and the flow paths can be seen in Fig. 1-5. In a through-flow configuration, most of the fluid flows through full length of cell (Fig. 1-6 (a)), whereas most of the fluid in reverse-flow configuration enters and leaves cell through the same end (Fig. 1-6 (b)).

The schematic configuration of such through-flow wave rotor is shown in Fig. 1-7. Cells rotate between end plates with the shaft driven by an electrical motor or turbine's power, and ports mounted on the stationary end plates are responsible for charging and discharging of fluid at fixed and relatively steady states. In cell, a variety of pressure waves propagate, and the flow field is highly unsteady. In the port, however, the flow is relatively uniform and steady. The role of rotation is to provide cell with timed opening to ports and shutting. Cold and low pressure air from compressor enters wave rotor cell through Air Low pressure port (AL), and after being compressed it departs from Air High pressure port (AH) for combustor. Hot and high pressure gas is exhausted from combustor and enters wave rotor cell through Gas High pressure port (GH), and part of it exits to the turbine through Gas Low pressure port (GL). By periodically exposing cells to ports of different pressures, pressure waves are generated and propagate in cells.

### 1.2.1    Compression Process

Wave rotor is designed to open and close at definite timings to ensure the flow field in cells proceeds as expected. To detail the relationship between the wave propagation and the events of opening and shutting of cell ends, Fig. 1-8 schematically illustrates the unwrapped view of flow field in the compression process. This graph translates a degree (or time) series of flow states in cells from cylindrical into planar, looking from radially outer side. While in Fig. 1-7 it rotates clockwise about the axis, cell in Fig. 1-8 moves downwards, opens to ports, and shuts.

The cell prior to compression process is initially filled with low pressure fluid in quiescence (state 0). The cell moves on and the left end opens to GH port (state 1). The difference in pressure between high pressure gas in the GH port and low pressure fluid in the cell causes a primary shock wave (incident shock wave) that travels rightwards (red solid line), compressing the fluid in the cell. Right behind the primary shock wave (to the left side of shock wave) is the compressed fluid flowing rightwards at a speed lower than the primary shock wave; therefore, the contact front between the hot gas from the GH port and the compressed fluid moves rightwards slower than the primary shock wave (dark blue dotted line). The primary shock wave arrives at the right end of the cell, and then it is reflected by the end wall (between states 2 and 3). The right end of the cell starts exposing to the AH port at this degree. The reflected shock wave travels left, encounters the contact front, and moves on until arrival at the left end (states 3~5). Behind the reflected shock wave (to the right side of shock wave), opening of the right end of the cell to the AH port drives the compressed fluid moving right (states 3~6). The contact front proceeds traveling

right (states 4~6) and arrives at the right end at shutting (between states 6 and 7), and thus the compressed fluid is fully expelled to the AH port heading for combustor. The left end of the cell shuts when the reflected shock wave arrives (between states 5 and 6). An expansion fan (or a series of expansion waves) is generated by the shut, propagates rightwards (state 6), and arrives at the other end at shutting (between states 6 and 7). The compression process finishes.

### 1.2.2　Expansion Process

Sequentially, the cell moves on and undergoes expansion process, which is shown in Fig. 1-9. The right end of the cell opens to the GL port of low pressure, and thereby expansion waves are generated at the right end, propagate leftwards, and reducing the pressure of the compressed gas in the cell. Part of the expanded gas is expelled to turbine through the GL port. After the pressure in the cell declines to a certain level, the left end opens to the AL port and fresh air is admitted. Since both the gas and the air flow rightwards, the contact front between the fresh air and the expanded gas moves right, too. Then, the right end shuts and a compression wave is generated. The compression wave travels left and reduces the flow speed in the cell. It arrives at the left end at shutting, and the expansion process is halted. Together with the fresh air, part of the gas remains in the cell waiting for the compression process in the next wave rotor cycle.

(a) Through-flow configuration　　　　　　　　(b) Reverse-flow configuration
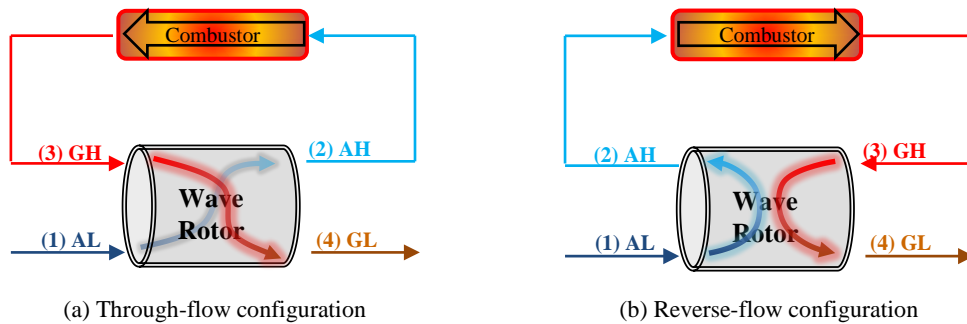
Fig. 1-6 Schematic of flow configuration types for four-port axial wave rotor [48]
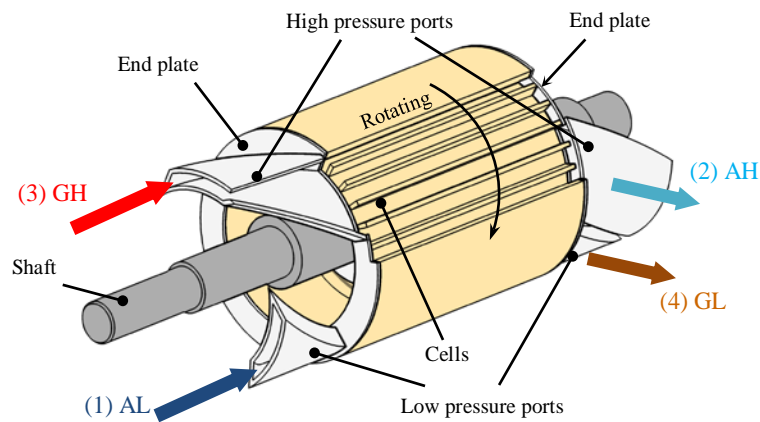
Fig. 1-7 Configuration of a four-port through-flow wave rotor
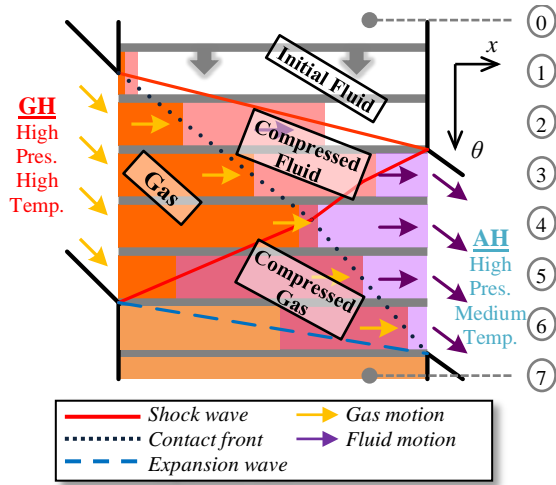
Fig. 1-8 Schematic of flow regions and major characteristic lines in compression process
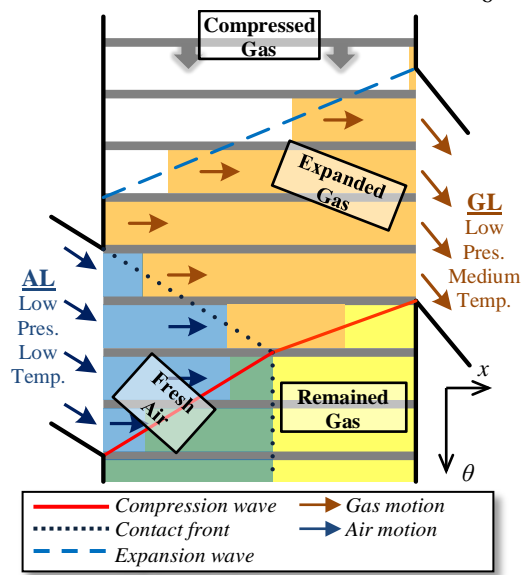


Fig. 1-9 Schematic of flow regions and major characteristic lines in expansion process
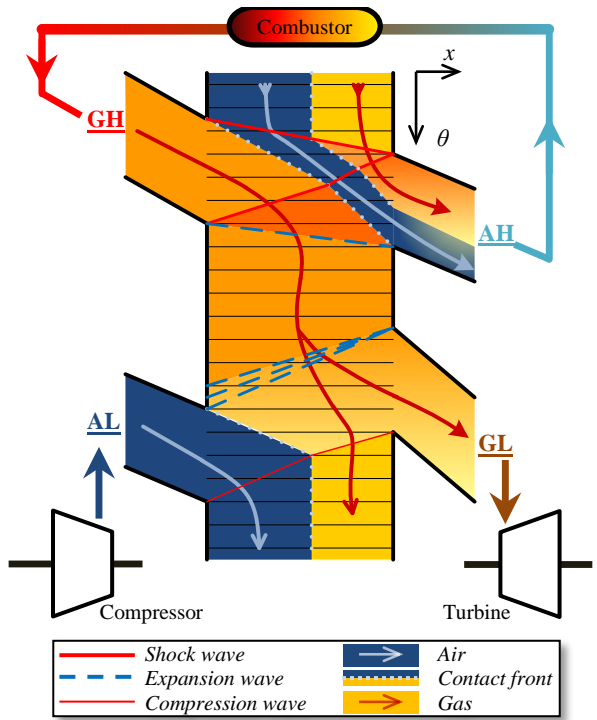


Fig. 1-10 Schematic wave diagram with flow paths and connections with other components in gas turbine

### 1.2.3    Overview of a Wave Rotor Cycle

A full wave rotor cycle consists of both the compression process and the expansion process (Fig. 1-10), accomplishes what compressor and turbine do within a sole device. It compresses the air from compressor, discharges the compressed air to combustor. The burnt gas returns to wave rotor, functions as

the driver power of shock wave in compression process. The burnt gas is expanded to a pressure level higher than the fresh air's, and it is directed to turbine. In through-flow wave rotor for gas turbine, the burnt gas remains in the cell after expansion process will be discharged to combustor again in the next wave rotor cycle. The portion of such recirculation of once-burnt gas could be 30~50% [49].

Actions of opening and shutting of cell ends correspond to the generations and arrivals of pressure waves and contact fronts. Hence, the degrees of open and shut should be design in accordance with the characteristic lines, which are generally determined by rotations speed of the cells and the propagation speeds of pressures waves and contact fronts.

## 1.3    Motivation: Heat Transfer Concerns

Working fluid in cell inevitably exchanges energy with lateral wall through the interface between fluid and solid (Fig. 1-11), whose temperature is determined by heat transfer across the interface between internal fluid and solid wall of cell. That is, in practice, after start up, wall temperature varies owing to unremitting influence of flow field, and eventually reaches limited and cyclic oscillation under cyclic flow field (Fig. 1-12). Compared with oscillation of flow temperature, oscillation amplitude of wall temperature in limit cycle is absolutely small and can be regarded as stable because the duration of a wave rotor cycle is so short (see Appendix C). Meanwhile, under such definite wall temperature, flow field receives or releases heat energy through the interface between fluid and solid. The exact heat transfer potentially affects propagation speed and resultant arrival timing of pressure wave. Flow field in cells subjects to deviate from planned pattern when heat transfer effect is substantial, and compression and expansion may become less effective as a result.

In the past researches, heat transfer and its effects were not examined in detail. The lateral boundaries of fluid passage were usually treated as adiabatic or in a steady-flow manner even though the internal flow dynamics of a wave rotor is highly unsteady [36], [50–53] (further interpretation to be presented in Subsection 1.4.2); and these treatments were developed and studied for conventional sizes. When referring to conventional sizes, Table 1-1 gives a general survey of the geometry sizes of the wave rotor cells used by NASA & Allison, Kentfield, GE and Comprex® as example. Regarding the enumerated cells at conventional scale, the length varies from 90 mm to 300 mm and the hydraulic diameter from 9 mm to 60 mm.

Besides, it is imaginable that in smaller cell, the effect of heat transfer on internal flow field tends to be greater because the surface-area-to-volume ratio gets larger. An example of small size is described also in Table 1-1. The length and the hydraulic diameter of the cell of the small wave rotor designed and tested in the University of Tokyo are 69 mm and 3.4 mm, respectively. Comparing with the small size, the conventional sizes are obviously larger. As size reduces, the influence on the internal flow field is enhanced, and an estimation of such influence is presented in Appendix B. Since port design is timed with rotation speed and propagation of pressure waves and contact fronts, given a fixed rotation speed and fixed port configurations, change in the internal flow field may vary the characteristic lines in wave diagram, i.e. the propagation of pressure wave and contact front, and the flow variables (like pressure, temperature and mass flow rate) during charging and discharging are also subject to change.

For both reasons, at small scales the effects of heat transfer on internal flow field, and on charging and discharging, is potentially significant but still unbeknown. Therefore, it is necessary to treat the heat transfer carefully in numerical analysis for wave rotor smaller than conventional size.
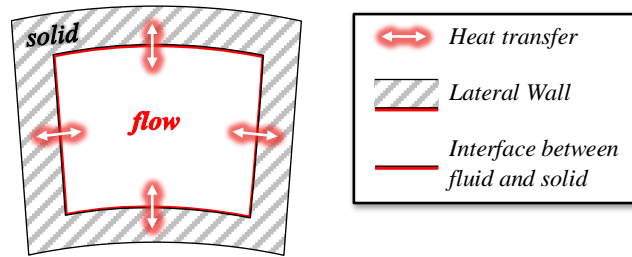
Fig. 1-11 Axial view of a wave rotor cell
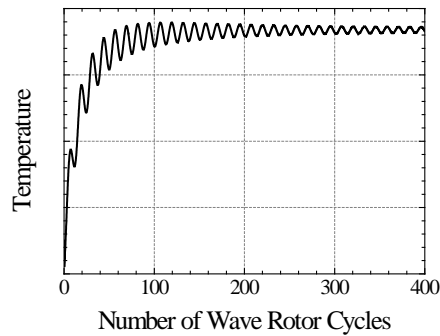


Fig. 1-12 Example for evolution of wall temperature in wave rotor cell

Table 1-1 Dimensions of cell of various wave rotors [10], [37]

| Cell dimensions (in mm) | | Conventional Size | | | | Small Size |
|---|---|---|---|---|---|---|
| | | NASA & Allison | Kentfield | GE | Comprex® | U. Tokyo |
| Axial Length | $L$ | 152 | 280 | 300 | 93.2 | 69.0 |
| Nominal Hydraulic Diameter | $D_H$ [*)] | 12.5 | 25.8 | 14.0 | 9.47 | 3.40 |
| Nominal Width | $W$ | 8.75 | 16.8 | 10.0 | 9.00 | 3.92 |
| Radial Height | $H$ | 22.0 | 55.9 | 23.1 | 10.0 | 3.00 |

*) $D_H = 2 \times W \times H \div (W+H)$

## 1.4 Literature Review

### 1.4.1 Wave Rotor Losses

A mathematical model based on macroscopic balances of mass and energy, one-dimensional gas dynamics, and entropy production for wave rotor was developed by Welch, in which the following loss mechanisms were considered [54]:

1. Non-uniform mixing loss in port, which concerns diffusion of momentum driven by non-uniform velocity profile in port.

2. Viscous losses in boundary layer inside port and cell.

3. Blockage. As can be seen in Fig. 1-2, cells are divided by walls. When fluid flows axially from port to cell, the finite blade thickness provides blockage that produces total pressure loss and reduces mass flow rate because of less flow area.

4. Gradual opening and closing, referred as partial opening on occasion. The schematic in Fig. 1-13 illustrates the statuses of cell ends in partial opening or full opening to port. As the cells rotates, a cell end experiences close – partial open – full open – partial open – close, and thereby the cell end gradually opens to port or closes. Gradual opening and closing causes oblique shock wave during partial opening (time = 0.031 in Fig. 1-14), which is reflected on the opposite side, and thus the density profile (as well as the pressure profile) behind the primary shock wave may be non-uniform (time = 0.5 in Fig. 1-14). Besides, the contact front between gas and air is distorted (also time = 0.5 in Fig. 1-14).

5. Incidence loss caused by non-uniform velocity profile of inflow from port, which is illustrated in Fig. 1-15.

And some other effects adversely impacting wave rotor performance were commented as influential factors though neglected. They are

6. Viscous losses in rotor wake, separated flow, and rotor windage.

7. Mixing and redistribution of hot gas and cold air caused by three-dimensional flow effects, which are associated with coupled phenomena caused by both gradual opening and rotation [55].

8. Heat transfer. As a thermo-fluid device, heat transfer between fluid and solid occurs everywhere.

9. Leakage. As cells rotate between stationary end plates, clearance gap cannot be avoided (Fig. 1-16 (a)). The existence of such gap allows fluidic connection between cell and surroundings (Fig. 1-16 (b)), and fluid movement from one cell to another as well.

These loss mechanisms included in Welch's model, along with three-dimensional effects, heat transfer and leakage, have been studied and incorporated into numerical models in manifold researches [15], [19], [20], [36], [37], [39], [42], [50], [53], [55–59].



(a) Shaft, rotating cells and end plates     (b) Axial view
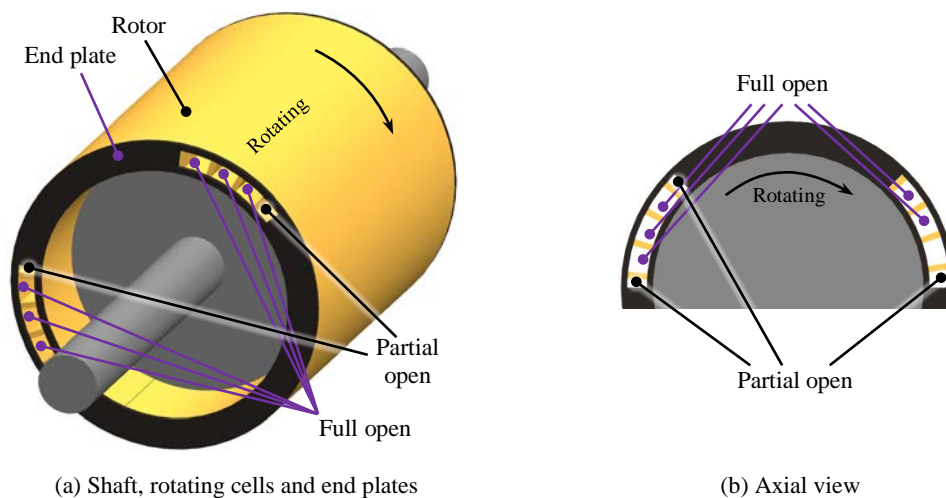
Fig. 1-13 Schematic of gradual opening and closing (partial open and full open)
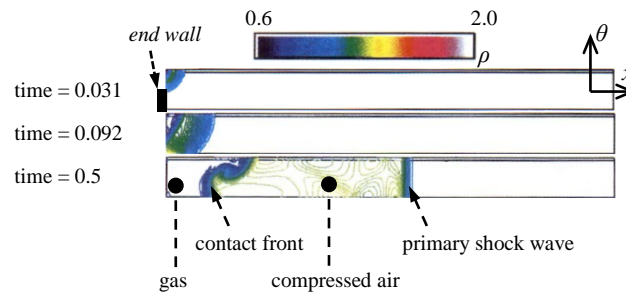
Fig. 1-14 Example for evolution of density on midspan surface from half open to full open [55]
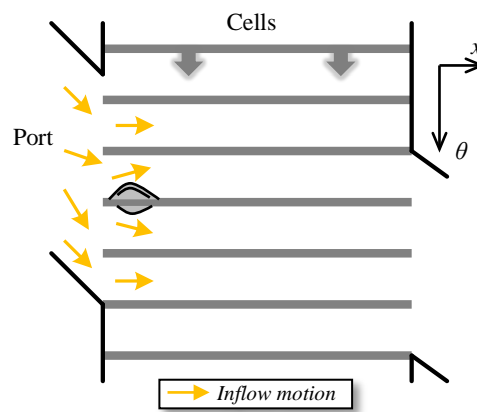


Fig. 1-15 Schematic of non-uniform port velocity and resultant incidence flow



(a) Gap between end plate and rotor

(b) Leakage flow through gap between cell and end wall
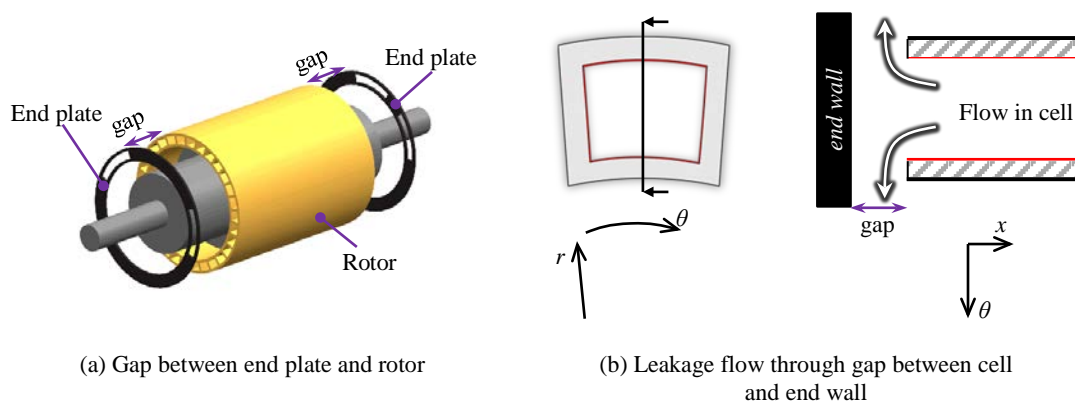
Fig. 1-16 Schematic of clearance gap and leakage

*1.4.2    Heat Transfer of Wave Rotor*

In 1992, a one-dimensional numerical model was developed to describe the dynamic performance of the wave rotor [21]. It was later improved by introducing losses related to finite passage opening time, heat transfer, friction, and so forth, and the numerical predictions were compared with experimental results to examine whether the losses were modeled properly [19], [20], [51], [57]. However, the comparisons with measurements were conducted to examine the code's capability of predicting global performance: charging and discharging variables (pressure, temperature and mass flow rate) were compared at various rotation speeds. The effects of heat transfer, as well as leakage and other loss mechanisms, were not discussed independently. Furthermore, in this solution, to evaluate local skin friction coefficient ($C_f = \alpha Re_\delta^{-j}$), empirical parameters ($\alpha$ & $j$) whose values were determined by experimental data was used, which required reassessment for each operating point. The Reynolds number $Re_\delta$ based on the thickness of boundary layer $\delta$ was estimated using the analogy of Stokes first problem, and the heat transfer coefficient was derived from steady flow over a flat plate.

Alternatively, Elloye et al. [50] employed Woschni's correlation equation [60] to calculate the instantaneous heat transfer coefficient, and Woschni's equation is based on steady assumption and is an average estimation of the whole channel. The boundary temperatures were fixed at three different values virtually varies from the lowest flow temperature to the highest. The influence of the three isothermal wall temperatures on the operation of Comprex® was presented, and the heat transfer from the compressed air to wall was concluded to be meaningfully influential.

Respecting local heat transfer, transient thermal response to the movement of contact front between hot gas and cold air was analyzed numerically, and the transient local heat transfer rate was found to differ greatly from that of the quasi-steady solution [61]. Further association with internal flow field was not studied.

*1.4.3    Heat Transfer of Shock Tube and Microchannel*

Although it is complex and affected by many factors, flow field in wave rotor cell is intrinsically akin to that in shock tube. Researches on heat transfer in shock tube furnish underlying knowledge. The heat transfer of steady hot gas flow compressed by primary shock wave in shock tube was experimentally studied by Zal'Tsman et al.[62] On the other hand, numerically, a heat conduction model was developed to estimate the gas temperature behind the reflected wave in shock tube test for relatively long-term heat transfer ($\geq$ 15 ms), and a conjugate heat transfer solution for a reflected shock test of one typical condition (initial argon gas of 800 K and 1 atm) was presented [63]. And the conclusions were obtained that as long as the shock tube inner diameter is large (> 80 mm), heat loss to wall in test time up to 20 ms or higher does not significantly reduce the average temperature behind the reflected shock wave, and that small diameters no greater than 30 mm may lead to considerable temperature loss near the reflected shock region. As regards the propagation of shock waves in small diameter shock tubes, viscosity and heat losses were found to be main causes of attenuation of shock speed and shock intensity in relatively long time [64]. In addition, the scaling effects in microchannel flows were explored by Yao et al. [65] In the detailed study of the heat transfer characteristics, the dependency of Nusselt number on Reynolds number and length is scrutinized, and it was summarized that when the channel is smaller than certain size (height of 0.3 mm in the 2D problem involved) the heat transfer effect may be significantly enhanced.

## 1.5    Objectives, Overview and Features of This Work

The present investigation is an effort to study the effects of heat transfer across the interface between internal fluid and solid wall of cell on internal flow field, as well as on charging and discharging processes, for small wave rotors, and to clarify the effects of heat transfer as size reduces.

Because of the essential necessity of numerically simulating the internal flow field and the heat transfer, the computational fluid dynamics (CFD) model is established and the conjugate heat transfer methodology (CHT) is employed to describe the heat transfer. The numerical scheme with conjugate heat transfer boundary treatment is described in Chapter 2, accompanied with fundamental verifications for heat conduction in solid wall and convective heat transfer in shock tube test. Further verification in Chapter 3 is implemented for conjugate problem in relation to complex flow field, characteristics of which are analogous to those in wave rotor cell flow. The results and discussions of heat transfer based on the numerical simulations for single wave rotor cell are presented in Chapter 4. To analyze the effects, the characteristics of heat flux are studied by delving into the causes of intense heat flux. Then, heat transfer effects on internal flow field, charging and discharging in conventional size and small size are addressed, and the trend across sizes is analyzed.

Major obstacles in studying the heat transfer across internal surface of wave rotor cell are due to the lack of substantial understanding in the behavior of heat transfer in wave rotor cell, and the scarcity of experience on heat transfer modeling for wave rotor cell. As is indicated in Section 1.3 and 1.4, heat transfer was modeled with steady state assumptions although the flow is known to be highly unsteady; the loss mechanisms were accounted in performance analyses as a whole; but the characteristics of heat transfer were not examined. To deal with these limitations and to cover the areas not discussed, this investigation employs numerical CFD-CHT solution for 3-D cell flow, and the causes of intense heat flux, along with heat transfer effects on flow, are revealed for the first time. This work is also the first attempt to discuss the outstanding effects in small wave rotor, and the variation of heat transfer effects as size reduces. Admittedly, scientific researches in analyzing conjugate problems relating to flow in pipe / microchannel, in shock tube, over flat plate or in turbomachinery have been developed, and these researches do provide indispensable guidance on heat transfer issues.

# CHAPTER 2: NUMERICAL SCHEME

This chapter discusses the computational methods adopted for fluid domain and solid domain, and the approximate solution of conjugate interface temperature between both domains for a single cell. Through decades of accumulation, the numerical methodology has been developed and tested by several researchers [5], [66–69], and is refined by the author as well. Fundamental verifications for heat conduction in solid wall and convection heat transfer induced by propagation of shock wave have been implemented, which are also presented.

## 2.1    Computational Model for Fluid Domain

### 2.1.1    Governing Equations

According to the nature of the problem in rotational cell fluid domain, three-dimensional Navier-Stokes equations for unsteady compressible flow are employed for the flow solver. The equations of conservation of mass, momentum and energy are:

$$\frac{\partial \hat{Q}}{\partial t} + \sum_{i=1}^{3} \frac{\partial \hat{E}_i}{\partial \xi_i} = \mathrm{Re}^{-1} \sum_{i=1}^{3} \frac{\partial \hat{S}_i}{\partial \xi_i} \tag{2.1}$$

$$\hat{Q} = J^{-1} \begin{bmatrix} \rho \\ \rho u \\ \rho v \\ \rho w \\ e \end{bmatrix} \tag{2.2}$$

$$\hat{E}_i = J^{-1} \begin{bmatrix} \rho U_i \\ \rho u U_i + \left(\xi_i\right)_x p \\ \rho v U_i + \left(\xi_i\right)_y p \\ \rho w U_i + \left(\xi_i\right)_z p \\ \left(e + p\right) U_i \end{bmatrix} \tag{2.3}$$

$$\hat{S}_i = J^{-1} \begin{bmatrix} 0 \\ \mu m_1 u_{\xi_i} + \frac{\mu}{3} m_2 \left(\xi_i\right)_x \\ \mu m_1 v_{\xi_i} + \frac{\mu}{3} m_2 \left(\xi_i\right)_y \\ \mu m_1 w_{\xi_i} + \frac{\mu}{3} m_2 \left(\xi_i\right)_z \\ \mu m_1 m_3 + \frac{\mu}{3} m_2 \left[\left(\xi_i\right)_x u + \left(\xi_i\right)_y v + \left(\xi_i\right)_z w\right] \end{bmatrix} \tag{2.4}$$

where

$$e = \rho\left(C_v T + \frac{1}{2}\left(u^2 + v^2 + w^2\right)\right) \tag{2.5}$$

$$p = (\kappa - 1)\left(e - \frac{1}{2}\rho\left(u^2 + v^2 + w^2\right)\right) \tag{2.6}$$

$$m_1 = \left(\xi_i\right)_x^2 + \left(\xi_i\right)_y^2 + \left(\xi_i\right)_z^2 \tag{2.7}$$

$$m_2 = \left(\xi_i\right)_x u_{\xi_i} + \left(\xi_i\right)_y v_{\xi_i} + \left(\xi_i\right)_z w_{\xi_i} \tag{2.8}$$

$$m_3 = \frac{1}{2}\left(u^2 + v^2 + w^2\right) + \frac{\mu}{\Pr(\kappa - 1)}\frac{\partial a^2}{\partial \xi_i} \tag{2.9}$$

$$U_i = \left(\xi_i\right)_t + \left(\xi_i\right)_x u + \left(\xi_i\right)_y v + \left(\xi_i\right)_z w \tag{2.10}$$

and heat capacity ratio, speed of sound, dynamic viscosity and Prandtl number are defined by the following equations:

$$\kappa = C_P / C_V \tag{2.11}$$

$$a = \sqrt{\kappa p / \rho} \tag{2.12}$$

$$\mu = \mu_{\text{Lam}} + \mu_{\text{Tur}} \tag{2.13}$$

$$\mu / \Pr = \mu_{\text{Lam}} / \Pr_{\text{Lam}} + \mu_{\text{Tur}} / \Pr_{\text{Tur}} \tag{2.14}$$

Substituting $(\xi, \eta, \zeta)$ for $(\xi_1, \xi_2, \xi_3)$, the coordinate transformations is expressed as follows:

$$\begin{bmatrix} \xi_x & \xi_y & \xi_z \\ \eta_x & \eta_y & \eta_z \\ \zeta_x & \zeta_y & \zeta_z \end{bmatrix} = J\begin{bmatrix} y_\eta z_\zeta - z_\eta y_\zeta & z_\eta x_\zeta - x_\eta z_\zeta & x_\eta y_\zeta - y_\eta x_\zeta \\ y_\xi z_\zeta - z_\xi y_\zeta & z_\xi x_\zeta - x_\xi z_\zeta & x_\xi y_\zeta - y_\xi x_\zeta \\ y_\xi z_\eta - z_\xi y_\eta & z_\xi x_\eta - x_\xi z_\eta & x_\xi y_\eta - y_\xi x_\eta \end{bmatrix} \tag{2.15}$$

$$\begin{pmatrix} \xi_t \\ \eta_t \\ \zeta_t \end{pmatrix} = -\begin{bmatrix} \xi_x & \xi_y & \xi_z \\ \eta_x & \eta_y & \eta_z \\ \zeta_x & \zeta_y & \zeta_z \end{bmatrix}\begin{pmatrix} x_t \\ y_t \\ z_t \end{pmatrix} \tag{2.16}$$

where the Jacobian matrix is given as follows:

$$J^{-1} = x_\xi y_\eta z_\zeta + x_\zeta y_\xi z_\eta + x_\eta y_\zeta z_\xi - x_\xi y_\zeta z_\eta - x_\eta y_\xi z_\zeta - x_\zeta y_\eta z_\xi \tag{2.17}$$

## 2.1.2 Discretization and Turbulence Model

Substituting $\left(\hat{E},\hat{F},\hat{G}\right)$ for $\left(\hat{E}_1,\hat{E}_2,\hat{E}_3\right)$ in Eq. (2.1), the partial differential equations can be discretized to

$$\hat{Q}_{j,k,l}^{n+1} = \hat{Q}_{j,k,l}^{n} + \left(\lambda R\left(\hat{Q}_{j,k,l}^{n+1}\right) + (1-\lambda) R\left(\hat{Q}_{j,k,l}^{n}\right)\right) \tag{2.18}$$

where

$$R(\hat{Q}_{j,k,l}^{n}) = -\Delta t \left(\frac{\hat{E}_{j+\frac{1}{2},k,l} - \hat{E}_{j-\frac{1}{2},k,l}}{\Delta\xi} + \frac{\hat{F}_{j+\frac{1}{2},k,l} - \hat{F}_{j-\frac{1}{2},k,l}}{\Delta\xi} + \frac{\hat{G}_{j+\frac{1}{2},k,l} - \hat{G}_{j-\frac{1}{2},k,l}}{\Delta\xi}\right)^{n}$$
$$- \Delta t \left(+\frac{\hat{S}_{j+\frac{1}{2},k,l} - \hat{S}_{j-\frac{1}{2},k,l}}{\Delta\xi}\right)^{n} \tag{2.19}$$

Trapezoidal rule is applied to the calculation of $\hat{Q}$, and central difference method is used for space derivative. Other major information relating to the flow solver is listed in Table 2-1.

Table 2-1 Brief description of computational scheme for flow solver

| | |
|---|---|
| Governing equations | 3-D compressible viscous Navier Stokes |
| Flux splitting | SHUS [70] and 3rd order MUSCL [71] |
| Time stepping | LU-ADI factorization |
| Turbulence modeling | Baldwin-Lomax [72] |

Uni-particle upwind scheme SHUS (Simple High-resolution Upwind Scheme) [70], an AUSM (Advection Upstream Splitting Method) [73] type scheme partially based on Roe's FDS (Flux Difference Splitting) [74], is employed for flux splitting. SHUS is robust in strong expansion, and can capture a moving contact and cure spurious overshoot at a shock front that appeared in original AUSM case [70], [75]. For flow field in wave rotor cell, propagation of pressure waves including shock wave and expansion wave is the most important phenomenon and should be well solved. For this reason, SHUS is appropriate for the present flow solver. In addition, high resolution scheme MUSCL (Monotone Upstream-centered Schemes for Conservation Laws) approach [71] of 3rd order spatial accuracy with van Albada limiter [76] is used for spatial discretization.

Seeing that the number of wave rotor cycles in numerical simulation up till convergence may grow to an unforeseeably large number especially when heat transfer is considered, ADI (Alternating Direction Implicit) method [77] with Lower/Upper decomposition is employed as implicit time-stepping scheme in order to perform numerical analysis with relatively large time step and to accomplish simulation in less computational time.

Baldwin-Lomax model [72], an algebraic zero-equation turbulence model, is used to obtain the eddy viscosity. The robust model is suitable for channel flow that the fluid generally flows parallel along axial

direction with thin attached boundary layers and without large separation, which is the case in wave rotor cell.

### 2.1.3  Inlet and Outlet Boundary Treatments and Leakage Treatment

As has been addressed, during rotation, cell end opens and shuts gradually. The gradual opening and closing behaviors effect the generation of pressure waves and the motions of fluid. The area around the cell end is divided into several zones for illustration in Fig. 2-1. The area in the clearance gap consists of G1 exposed to the port and G2 adjacent to the end wall. Both G1 and G2 are radially connected to the surroundings, and axially connected to the cell fluid. Therefore, G1 and G2 act as inlet or outlet for the fluid domain. Virtual walls are placed at circumferential bounds of gap for the sake of single cell assumption that the domains of the single cell are not affected by neighboring cells.

Grids are generated in the gap and the cell. The volumes in the gap and the cell fluid domain, except for those bordering the port, the end wall, the radial bound or circumferential bound of gap area, or the lateral wall that serve as boundary volumes, are calculated by the computational scheme for fluid domain. Exact Riemann solver [78] is utilized to assess the fluxes illustrated as double headed arrows between zones, including port ↔ G1, end wall ↔ G2, virtual wall ↔ G1, G2 ↔ virtual wall, and G1 & G2 ↔ surroundings. The treatments employed for radial leakage, inflow and outflow are extensions and modifications of Okamoto's [29], [35–37] for the present three-dimensional single cell problem.
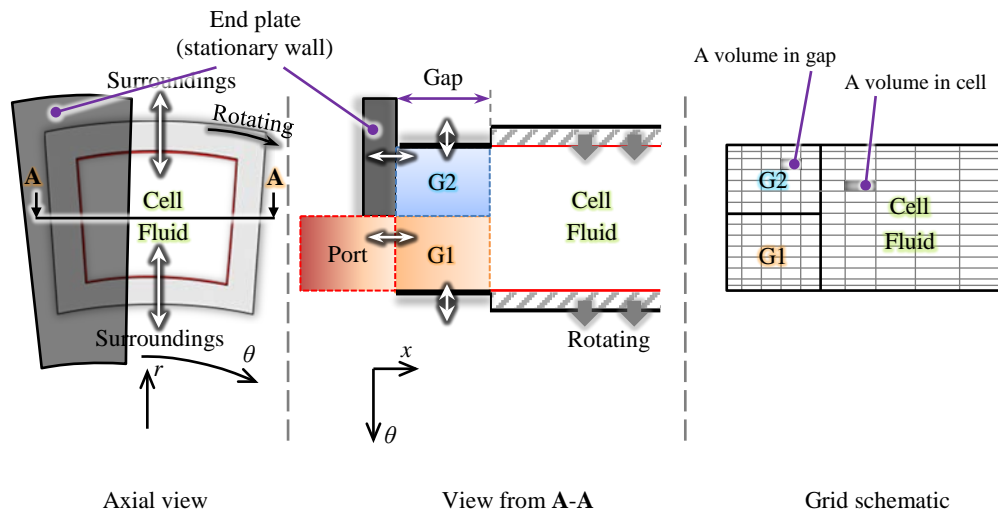


Fig. 2-1 Schematic of a moment when cell end partially opens to port

## 2.2  Computational Model for Solid Domain

To solve the heat transfer equation within lateral solid wall of cell, the heat conduction module is constituted. An example portion of the three-dimensional grid is exhibited in Fig. 2-2. For the grid point $P$, the control volume is denoted by the gray rectangular. Points $E$ (east) and $W$ (west) are neighbors on the $x$ direction, $N$ (north) and $S$ (south) are on the $y$ direction, and $T$ (top) and $B$ (bottom) are on the $z$ direction. The faces of the control volume are marked as $e$, $w$, $n$, $s$, $t$, and $b$, and the distances between neighboring points are $(\delta x)_{nbr}$ ($nbr \in \{e, w, n, s, t, b\}$), accordingly. The governing differential equation can be written as: [79]

$$\rho_s c_{p,s} \frac{\partial T}{\partial t} = \frac{\partial}{\partial x}\left(k_s \frac{\partial T}{\partial x}\right) + \frac{\partial}{\partial y}\left(k_s \frac{\partial T}{\partial y}\right) + \frac{\partial}{\partial z}\left(k_s \frac{\partial T}{\partial z}\right) + S \tag{2.20}$$

where $\rho_s$ is density, $c_{p,s}$ is specific heat capacity, $k_s$ is thermal conductivity, $T$ is temperature, $t$ is time, $x$, $y$ and $z$ are coordinates, and $S$ is rate of volumetric heat generation.

In order to briefly explicate the discretization, the simplified one-dimensional case without internal heat source is introduced (Fig. 2-3), for which the differential equation and the discretization equation are expressed as follows:

$$\rho_s c_{p,s} \frac{\partial T}{\partial t} = \frac{\partial}{\partial x}\left(k_s \frac{\partial T}{\partial x}\right) \tag{2.21}$$

By integrating Eq. (2.21) over time span $t \sim t+\Delta t$ and over the control volume for $P$ in Fig. 2-3, the following equation is obtained:

$$\rho_s c_{p,s} \int_{face\,w}^{face\,e} \int_t^{t+\Delta t} \frac{\partial T}{\partial t} dt\,dx = \int_t^{t+\Delta t} \int_{face\,w}^{face\,e} \frac{\partial}{\partial x}\left(k_s \frac{\partial T}{\partial x}\right) dx\,dt \tag{2.22}$$

By assuming that $T$ at $P$ prevails throughout its control volume, temperature at $t$ denoted by $T_P^0$ and at $t+\Delta t$ denoted by $T_P^1$, it is obtained that

$$\rho_s c_{p,s} \int_{face\,w}^{face\,e} \int_t^{t+\Delta t} \frac{\partial T}{\partial t} dt\,dx = \rho_s c_{p,s} \Delta x \left(T_P^1 - T_P^0\right) \tag{2.23}$$

Further, by evaluating $\dfrac{\partial T}{\partial x}$ from the piecewise-linear profile (Fig. 2-4), Eq. (2.22) is transformed into the following equation:

$$\rho_s c_{p,s} \Delta x \left(T_P^1 - T_P^0\right) = \int_t^{t+\Delta t}\left[\frac{k_{s,e}\left(T_E - T_P\right)}{(\delta x)_e} - \frac{k_{s,w}\left(T_P - T_W\right)}{(\delta x)_w}\right] dt \tag{2.24}$$

Assuming that

$$\int_t^{t+\Delta t} T_P dt = \left[\lambda_{wf} T_P^1 + \left(1 - \lambda_{wf}\right) T_P^0\right]\Delta t \tag{2.25}$$

and that $k_s$ and $\rho_s c_{p,s}$ are constant, given old temperature $T_{nb}^0$ of the previous step, number $nb \in \{(0)\ P,\ (1)\ E,\ (2)\ W\}$, dropping the superscript "1" from new temperature, new temperature of the present step $T_{nb}$ can be derived:

$$\rho_s c_{p,s} \frac{\Delta x}{\Delta t}\left(T_P - T_P^0\right) = \quad \lambda_{wf}\left[\frac{k_{s,e}\left(T_E - T_P\right)}{\left(\delta x\right)_e} - \frac{k_{s,w}\left(T_P - T_W\right)}{\left(\delta x\right)_w}\right]$$
$$+\left(1-\lambda_{wf}\right)\left[\frac{k_{s,e}\left(T_E^0 - T_P^0\right)}{\left(\delta x\right)_e} - \frac{k_{s,w}\left(T_P^0 - T_W^0\right)}{\left(\delta x\right)_w}\right] \tag{2.26}$$

which can be rearranged as

$$a_P T_P = a_E\left[\lambda_{wf}T_E + \left(1-\lambda_{wf}\right)T_E^0\right] + a_W\left[\lambda_{wf}T_W + \left(1-\lambda_{wf}\right)T_W^0\right]$$
$$+\left[a_P^0 - \left(1-\lambda_{wf}\right)\left(a_E + a_W\right)\right]T_P^0 \tag{2.27}$$

where $\Delta t$ time increment for a time step, $\lambda_{wf}$ in the range of [0, 1] is a weighting factor, and

$$a_P = \lambda_{wf}\left(a_E + a_W\right) + a_P^0 \tag{2.28}$$

$$a_E = \frac{k_{s,e}}{\left(\delta x\right)_e} \tag{2.29}$$

$$a_W = \frac{k_{s,w}}{\left(\delta x\right)_w} \tag{2.30}$$

$$a_P^0 = \frac{\rho_s c_{p,s}\Delta x}{\Delta t} \tag{2.31}$$

Owing to the possibly considerable consumption of computation, fully implicit scheme ($\lambda_{wf} = 1$) is adopted to deal with time stepping. The discretization equation Eq. (2.27) is, then, expressed as

$$a_P T_P = a_E T_E + a_W T_W + b \tag{2.32}$$

where Eq. (2.28) is modified as

$$a_P = a_E + a_W + a_P^0 \tag{2.33}$$

and

$$b = a_P^0 T_P^0 \tag{2.34}$$

By adopting the same method, the general discretization equation for three-dimensional diffusion can be written as follows: [79]

$$a_P T_P = \sum_{nb=1}^{6} a_{nb} T_{nb} + b \tag{2.35}$$

for which

$$a_P = \sum_{nb=1}^{6} a_{nb} + a_P^0 - S_P \Delta x \Delta y \Delta z \tag{2.36}$$

$$a_P^0 = \rho_s c_{p,s} \Delta x \Delta y \Delta z / \Delta t \tag{2.37}$$

$$b = S_c \Delta x \Delta y \Delta z + a_P^0 T_P^0 \tag{2.38}$$

where $T_P$ is the new value of temperature, neighbor number $nb \in$ {(1) $E$, (2) $W$, (3) $N$, (4) $S$, (5) $T$, (6) $B$}, $a_{nb}$ is the neighbor coefficient of each face of the control volume, $T_{nb}$ is the neighbor temperature of each face of the control volume, $T_P^0$ is the old value of temperature, and the source terms $S_p$ and $S_c$ are zero for the present problem. The discretization equation is further developed in Section 2.4 for conjugate consideration.

With respect to the boundary conditions for solid domain, at both ends of the cell, wall surfaces are subject to constant temperature of 890 K, an approximate temperature estimated by cell inlet velocity and inlet temperature in the form of $\frac{\int inlet\ velocity \times inlet\ temperature}{\int inlet\ velocity}$, as is illustrated in Fig. 2-5. The radially ($r$ direction) external surfaces subject to adiabatic condition or external convective heat transfer. The circumferentially ($\theta$ direction) external surfaces subject to adiabatic condition or periodic condition. The internal surfaces compose the conjugate interface.
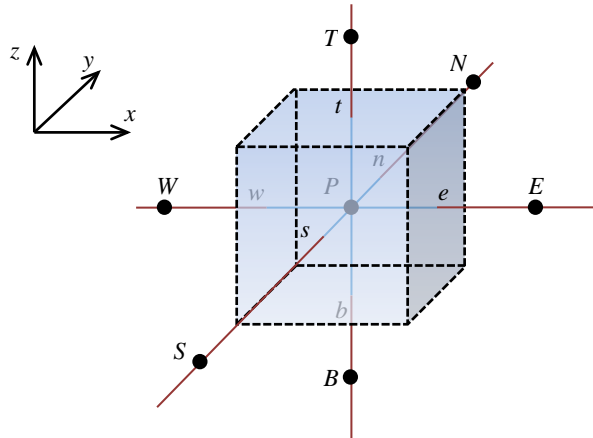


Fig. 2-2 Three-dimensional control volume of solid
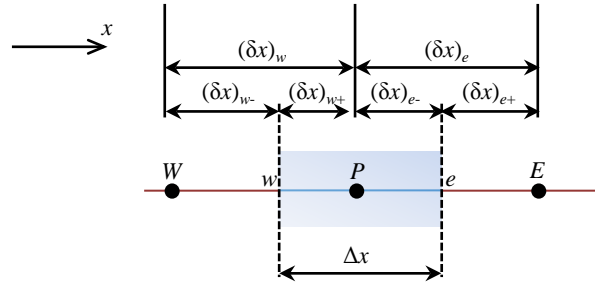
Fig. 2-3 One-dimensional control volume of solid [79]
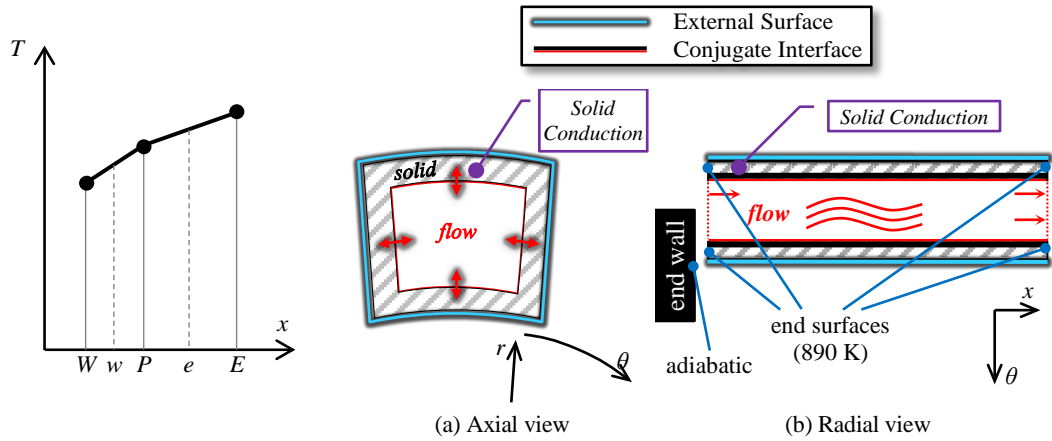


Fig. 2-4 Piecewise linear profile assumption [79]

Fig. 2-5 Locations of end surfaces, external surface and conjugate interface

## 2.3    Approximate Solution of Conjugate Interface Temperature

With regard to boundary conditions at the fluid-solid interface for fluid domain and solid domain, conjugate heat transfer treatment is employed to determine the temperature of the fluid-solid interface. Brief literature study related to conjugate heat transfer is presented in Appendix D. The fluid domain and the solid domain are linked by the conjugate fluid-solid interface (Fig. 2-6) as boundary conditions for both domains. In the conjugate problem, the distribution of temperature along the interface is basically unbeknown. The approximate solution of conjugate interface temperature presented in this section aims to provide both domains with definite temperature boundary conditions at each time step.

The present approximate solution extends the discretization equations in solid domain to the interface with  different material properties, which is inspired by the works of Patankar [79] and Jo et al.[80] Shown in Fig. 2-7 is the temperature of the interface node and its relationship with temperatures of neighboring nodes. The old temperature of the interface node ($T_P^0$) and the temperatures of its neighboring nodes ($T_{nb}$) in fluid domain, solid domain and at the interface contribute to updating the interface node temperature to new value ($T_P$). Like Eq. (2.32), the relationship is described as [79]

$$a_P T_P = a_E T_E + a_W T_W + b \tag{2.39}$$

where

$$a_E = \frac{k_e}{(\delta x)_e} \tag{2.40}$$

$$a_W = \frac{k_w}{(\delta x)_w} \tag{2.41}$$

$$a_P = a_E + a_W + a_P^0 \tag{2.42}$$

$$b = a_P^0 T_P^0 \tag{2.43}$$

$$a_P^0 = \rho_P c_{p,P} \, \Delta x / \Delta t \tag{2.44}$$

The problem of deciding the node temperature is the interface density $\rho_P$ and the interface specific heat capacity $c_{p,P}$ in Eq. (2.44). In literature [79], equivalent conductivity written as

$$k_e = \left( \frac{1 - f_e}{k_P} + \frac{f_e}{k_E} \right)^{-1} \tag{2.45}$$

in which

$$f_e = \frac{(\delta x)_{e+}}{(\delta x)_e} \tag{2.46}$$

is proposed to evaluate the conductivity at *face e* in Fig. 2-3. In the present problem, for Eq. (2.44), as $\rho_{\text{intf}}$ and $c_{p,\text{intf}}$ is associated with *node P*, quick approximate solutions are written as

$$\rho_P = \left( \frac{1 - f_P}{\rho_w} + \frac{f_P}{\rho_e} \right)^{-1} \tag{2.47}$$

$$c_{p,P} = \left( \frac{1 - f_P}{c_{p,w}} + \frac{f_P}{c_{p,e}} \right)^{-1} \tag{2.48}$$

where

$$f_P = \frac{(\delta x)_{e-}}{\Delta x} \tag{2.49}$$

Then, with neighbor nodes in fluid domain and solid domain, the interface temperature is solved every step. Then both the flow solver and the solid conduction solver proceed independently with persistently updated interface temperature distribution as boundary condition.

This approximate solution is simple in formulation and it requires no effort to modify the existing flow solver that has been developed and tested for decades. Nevertheless, since it just provides an approximate of the interface temperature, verifications should be carried out for the present object of research in order to find out if this solution is sufficient for the present research.
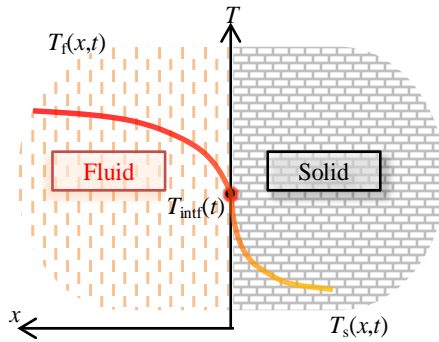


Fig. 2-6 Schematic of temperature distribution around conjugate interface
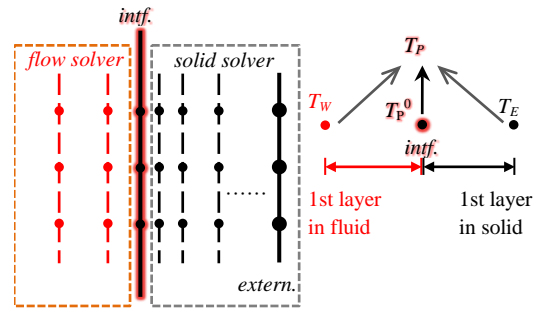
Fig. 2-7 Interface node temperature as function of its old value and neighboring node temperatures

## 2.4 Grids

Three-dimensional orthogonal structured is used for the flow solver. A couple of grid schemes of $121\times41\times41$ (Axial $\times$ Radial $\times$ Circumferential), $181\times81\times81$, and some more schemes have been attempted for conjugate problem of wave rotor cell of relevant scales in the present work. Calculation objects and boundary conditions in grid dependence study are consistent with those of conjugate cases in Appendix E. The results of the first wave rotor cycle are compared, and the greatest differences between neighboring schemes are enumerated in Table 2-2 for one of the sizes (heat flux extreme caused by shock wave is not considered). In fact, from $161\times61\times61$ the greatest differences reduce to below 1%; and the greatest difference changes little from $181\times81\times81$, and the maximum of $y^+$ above lateral surfaces is lower than 1 in most of the time. Ultimately, $201\times101\times101$, a conservative scheme of approximately 2 million nodes, is chosen after studying grid dependency of all sizes of wave rotor cell. Image for the grid of the whole fluid domain is displayed in Fig. 2-8, and two detailed ones are exhibited in Fig. 2-9. With this grid, parallel computation for a wave rotor cycle costs around 6 hours on a 12-thread i7 CPU.

Table 2-2 Comparisons of greatest difference among relevant sizes within the first wave rotor cycle

| Grid scheme | $161\times61\times61$ | $181\times81\times81$ | $201\times101\times101$ | $241\times121\times121$ |
|---|---|---|---|---|
| Grid for comparison | $121\times41\times41$ | $161\times61\times61$ | $181\times81\times81$ | $201\times101\times101$ |
| Greatest difference in conserved quantity | 0.7% | 0.3% | 0.1% | 0.07% |
| Greatest difference in heat flux | 6% | 0.3% | 0.06% | 0.05% |

Difference = 1 - (value in present scheme / corresponding value in scheme for comparison)
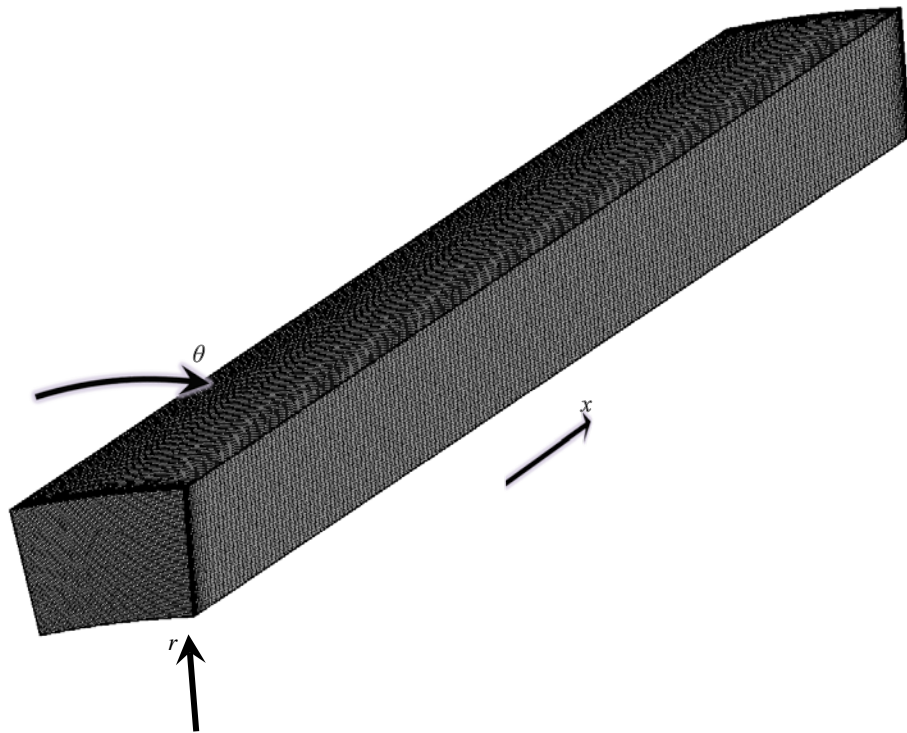
Fig. 2-8 Grid for the fluid domain of wave rotor cell

In the solid wall, from the internal surfaces (conjugate interface) to the external surfaces, the grid spacing in depth grows rapidly for the concern that great momentary heat flux occurs near the conjugate interface while heat flux (or temperature gradient) deep in the wall is much more moderate. The distances between nodes in solid domain and the conjugate interface are shown in Fig. 2-10. On the remaining two dimensions, the nodes are aligned to those in the fluid domain which are exemplified in Fig. 2-11.
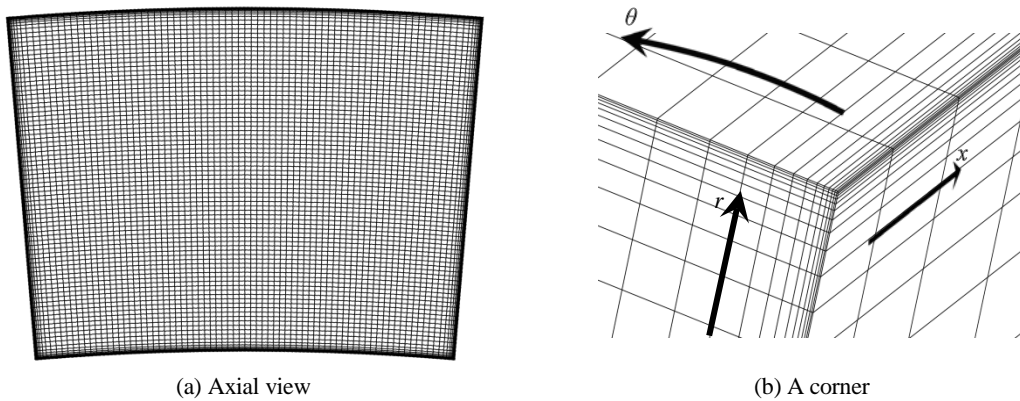


(a) Axial view



(b) A corner

Fig. 2-9 Grid on the end surface and around a corner
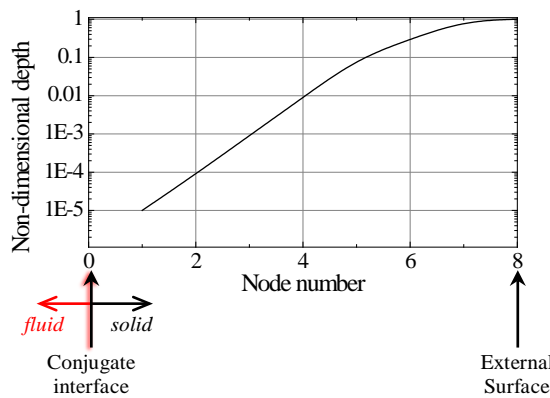
Fig. 2-10 Node distances from conjugate interface in wall (normalized by wall thickness)
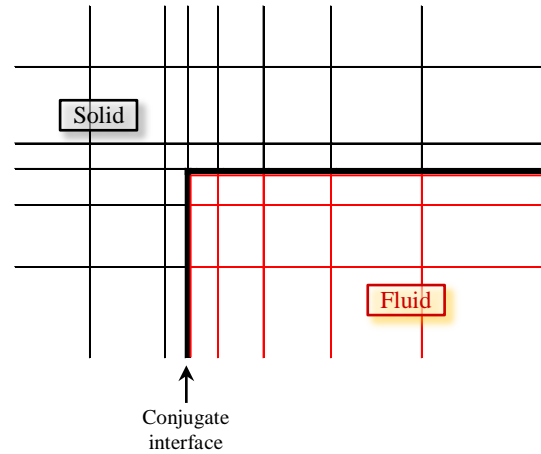


Fig. 2-11 Schematic of grids in fluid domain and solid domain around conjugate interface

## 2.5 Convergence judgment

During the process of calculation, in order to judge whether limit cycle is achieved, comparison in flow field and wall temperature between a present wave rotor cycle and its previous one is implemented at each time step. A wave rotor cycle is regarded as having reached limit cycle when the difference between the previous cycle and the present cycle is small enough: both L2 residual of flow field and maximum residual of normalized wall temperature are less than $1\times10^{-5}$. Normalization criterion for wall temperature is described in Section 4.1. Naturally, convergence judgment is implemented only for the flow side, provided that heat transfer is not taken into account.

## 2.6 Verification for Solid Conduction

In order to examine its primary capability of solving the unsteady heat conduction in wall, the solid conduction solver is verified for an infinite plate with convection on both sides. The physical model of the nonsymmetrical heat transfer problem of infinite plate is illustrated in Fig. 2-12. Both side surfaces 1 and 2 are subject to constant external convective heat transfer conditions. The thickness of the plate is $\delta$, and $x$ is the coordinate along depth direction starts as 0 on side 1. Initially, the temperature of the plate is uniform $T_0$, the same as that of the fluid of side 1. Both sides' external flows are different in temperature $T$ and heat transfer coefficient $h$. Four cases involving combinations of different Biot numbers and final Fourier numbers that are shown in Table 2-3 are performed for different heat transfer intensities and durations. Biot number gives an indication of the relative significance of conduction and convection in unsteady temperature development, and Fig. 2-13 exemplifies the effect of Biot number. Low Biot number (Bi≪1 i.e. Bi→0) represents the situation that internal conduction prevails; Biot number near 1 represents the situation that external convection and internal conduction are comparatively influential; and larger Biot number (Bi≫1) stands for the situation that external convection prevails. Fourier number (Fo $= \alpha t/\delta^2$) indicates the non-dimensional time of the process. The analytical solution can be described as [1]

$$\Theta = \frac{T(x,t) - T_0}{T_f - T_0}$$

$$= \frac{1 + \mathrm{Bi}_1\, x/\delta}{1 + \mathrm{Bi}_1 + \mathrm{Bi}_1/\mathrm{Bi}_2} - \sum_{n=1}^{\infty} A_n \left( \cos\mu_n\, x/\delta + \frac{\mathrm{Bi}_1}{\mu_n} \sin\mu_n\, x/\delta \right) \cdot \exp\left(-\mu_n^2 \mathrm{Fo}\right) \qquad (2.50)$$

$$A_n = \left\{ \left(1 + \frac{\mathrm{Bi}_1}{\mathrm{Bi}_2}\right) \frac{\sin\mu_n \cos\mu_n + \mu_n}{2\sin\mu_n} + \frac{\mathrm{Bi}_1}{\mu_n} \sin\mu_n \right\}^{-1} \qquad (2.51)$$

$$\mathrm{Bi}_1 = h_1 \delta / k\,, \quad \mathrm{Bi}_2 = h_2 \delta / k \qquad (2.52)$$

$$\cot(\mu_n) = \left( \frac{\mu_n}{\mathrm{Bi}_2} - \frac{\mathrm{Bi}_1}{\mu_n} \right) \left( 1 + \frac{\mathrm{Bi}_1}{\mathrm{Bi}_2} \right)^{-1} \qquad (2.53)$$

under the initial condition and the boundary condition that

$$T(x,0) = T_0 = \text{const}, \quad 0 < x < \delta \qquad (2.54)$$

$$\frac{\partial T(0,t)}{\partial x} + \frac{h_1}{k}\left[T_0 - T(0,t)\right] = 0\,, \quad -\frac{\partial T(\delta,t)}{\partial x} + \frac{h_2}{k}\left[T_f - T(\delta,t)\right] = 0 \qquad (2.55)$$

where $k$ is the thermal conductivity in plate.

On the other hand, numerical simulation using solely the solid solver is performed for the same problem. For each case, the temperature evolutions at selected depth locations of the numerical result are compared with those of the analytical solution. The locations $x/\delta = 1 \times 10^{-6}$ denotes a place extremely near the side surface 1; $x/\delta = 0.01$ is near side surface 1 and $x/\delta = 0.2$ is regarded as relatively nearer side surface 2. The comparisons are shown in Fig. 2-14. Since the solid solver merely deals with the unsteady conduction in the plate, it is natural for the solver to achieve the exact outcomes obtained by analytical solution. The capability of simulating the unsteady conduction in the solid wall is sufficient.

Fig. 2-12 Boundary conditions and initial condition of infinite plate with convection on both sides

Table 2-3 Unsteady one-dimensional conduction cases

| Case | $Bi_1$ | $Bi_2$ | $Fo_{fin}$ |
|------|--------|--------|------------|
| a | 0.049 | 0.093 | 0.040 |
| b | 0.049 | 9.3 | 0.040 |
| c | 4.9 | 0.093 | 0.40 |
| d | 4.9 | 9.3 | 0.40 |
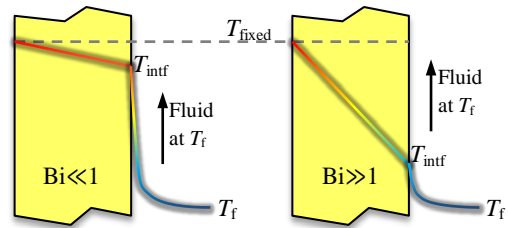


Fig. 2-13 Comparison of solid temperature profiles at different Biot numbers under fully developed flow [81]



Numerical: $x/\delta = 1 \times 10^{-6}$  $x/\delta = 0.01$  $x/\delta = 0.2$
Analytical: $x/\delta = 1 \times 10^{-6}$  $x/\delta = 0.01$  $x/\delta = 0.2$

(a) Case a

(b) Case b

(c) Case c

(d) Case d
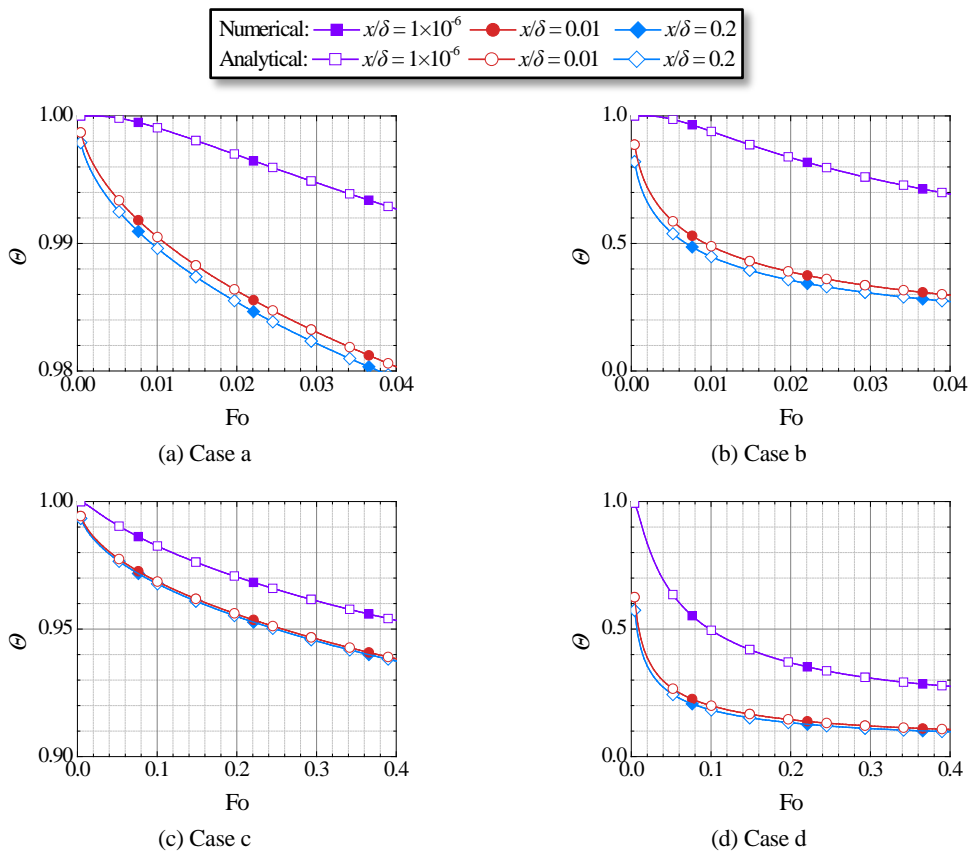
Fig. 2-14 Numerical and analytical results of temperature evolutions at several depth locations in infinite plate

## 2.7    Verification for Shock Tube Convective Heat Transfer

The code's capability of unsteady heat flux prediction, especially for associated heat transfer when shock wave propagates in channel, is verified for a relatively large shock tube test. In this verification, the coupling solver composed by the flow solver and the solid conduction solver with conjugate heat transfer boundary treatment is put into action.

This verification borrows a shock tube test disclosed in by Roediger et al. in literature [82], whose size is large and the shock wave can be regarded to be close to perfect one-dimensional shock wave. The test was performed to study the local heat transfer rate of shock tube wall by using fast-response heat flux gauges. Two different types of heat flux gauges have been employed. The specifications of the thin-film heat flux gauge are listed in Table 2-4. The novel heat flux gauge called Atomic Layer Thermopile (ALTP) that has been calibrated by the same research groups is employed to observe the transition mechanisms from laminar to turbulent in shock-induced flow. The commercial thin-film gauge produced by Shock Wave Laboratory (Stoßwellenlabor, RWTH Aachen, Deutschland) was also employed for their purpose of comparison between sensors.

The experimental conditions of the related test runs are listed in Table 2-5. $W_s$ is the propagation speed of the primary shock wave caused by rupture of MYLAR diaphragm, and $Ma_s$ is the corresponding Mach number. $Ma_2$, $u_2$ and $T_2$ are the Mach number, velocity and temperature in zone "2" (to be addressed later). Run 1 experiences noticeable transition from laminar to turbulent; only the portion before transition (laminar part) is associated with the concerned comparison. Run 3 is for turbulent situation.

The schematic of the shock tube is shown in Fig. 2-15. The driver section is 2 m long and separated by a diaphragm from the driven section. The driven section is 7 m long for run 1 and 6.5 m long for Run 3. Inner diameter of the tube is 70 mm. The heat flux sensors are located far from the MYLAR diaphragm (6 m in distance) to ensure that a nearly perfect shock wave has already formed when it arrives at measuring point. Subscripts "1", "2" and "4" denote the zone before the passage of the primary shock wave (also the initial state to the right of the diaphragm), the zone after the passage of the primary shock wave, and the initial state to the left of the diaphragm. Initially, pressure in zone "1" is lower than in zone "4". Rupture of the diaphragm induces shock wave propagating rightwards. This primary shock wave arrives at the right end and is reflected. The reflected shock wave travels leftwards. Between the arrivals of the primary shock wave and the reflected one, the heat flux history is measured.

The time traces of heat flux at the measuring point during the arrival of the primary shock wave the reflected shock wave are shown in Fig. 2-16. The red line denotes the history measured by ALTP. The first dramatic increase of heat flux is caused by the primary shock wave. Basically, as is shown in Fig. 2-18, after the passage of the primary shock wave, the temperature is lifted over the wall temperature. And owing to the new boundary layer development behind shock wave, the heat transfer coefficient increases drastically to a peak value and then decreases. Therefore, the heat flux jumps and then falls down. The second steep rise is regarded to be caused by the reflected shock wave by Roediger et al. in literature [82]. A sudden rise at about 3800 μs implies transition occurs since then. For the present concern, transition is not considered; therefore, the time span for comparison is restricted between 0 and 3800 μs.

The blue line in Fig. 2-16 reflects the classical analytical solution of Eq. (2.56) for laminar flow over an isothermal plate. The black line is the numerical result for laminar flow. Both numerical result and measured result are not too far away from the analytical one. The discrepancy between the measured result and the analytical one is supposed to be caused by disturbances in the shock front and possible

preceding flow due to a slight asymmetric burst of the MYLAR diaphragm [82]. The numerical heat flux result is close to the measured one in descending rate. Besides, in the history of numerical simulation, the rise rate when the primary shock wave arrives and the decline rate after the passage of the primary shock wave are similar to those of the measured ones.

$$\mathrm{Nu}_x = 0.332 \times \mathrm{Re}_x^{1/2} \times \mathrm{Pr}^{1/3} \tag{2.56}$$

In regard to the turbulent situation, the blue line in Fig. 2-17 stands for measured result. Drastic rises of heat flux caused by the primary shock wave and the reflected shock wave are also observed. After having declined from the great heat flux value caused by the passage of the primary shock wave, before the arrival of the reflected shock wave, the heat flux is relatively stable. Compared with the measured result, the numerical heat flux history fits close to the heat flux trace measured by the thin film gauge in the relatively stable heat flux interval, and in the arrival time of the reflected wave. Besides, the decline after the passage of the primary shock wave noted in the measured result is also observed in the numerical result, and the decline rates in both results conform with each other.

For both test runs concerning laminar or turbulent situations, the numerical heat fluxes agree well with the results measured by the thin film gauge between the primary wave and the reflected wave. It is rational to confirm that the solver is capable of dealing with convective heat transfer in unsteady flow field induced by shock wave propagation.

Admittedly, the flow field and heat transfer in shock tube test are not sufficient to represent the complex flow dynamics and heat transfer phenomena in wave rotor. Therefore, in order to examine its feasibility for complex internal flow dynamics and heat transfer in a wave rotor, the solver is verified for the flow field and heat transfer that are designed to resemble phenomena in wave rotor. The detailed verification is presented in Chapter 3.

Table 2-4 Specifications of heat flux sensors [82]

| Sensor (Serial Number) | Active area (mm$^2$) | Sensitivity (GAIN = 1) | $\sqrt{\rho c k}$ of substrate (J·cm$^{-1}$·K$^{-1}$·s$^{-1/2}$) | Resistance (Ω) |
|---|---|---|---|---|
| ALTP (798) | 0.4×2.0 | 182 μV/(W/cm$^2$) | 0.5246 | 125 |
| Thin Film Gauge (P-657) | 0.3×0.9 | 3852 μV/(Ws$^{1/2}$/cm$^2$) | 0.3223 | 28.57 |

Table 2-5 Experimental conditions of test runs [82]

| Run | Ma$_s$ | $W_s$ m/s | Ma$_2$ | $u_2$ m/s | $T_2$ K |
|---|---|---|---|---|---|
| 1 (Lam→Tur) | 1.78 | 618 | 0.82 | 352 | 443 |
| 3 (Turbulent) | 3.28 | 1156 | 1.43 | 880 | 881 |
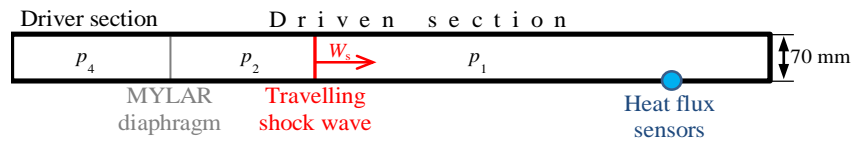
Fig. 2-15 Schematic of the shock tube test and the positioning of sensors [82]
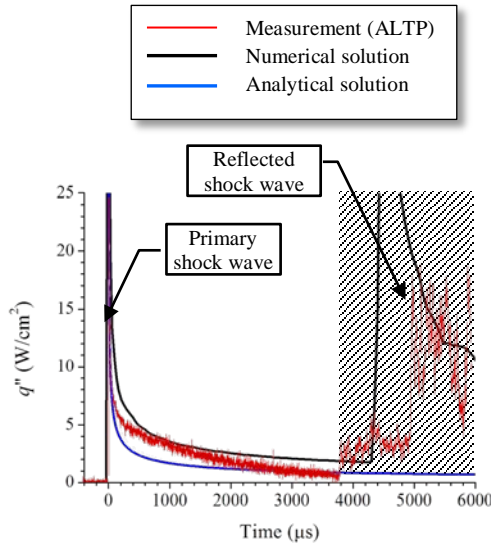


Fig. 2-16 Evolutions of heat flux for Run 1 at the measuring point (measured data acquired from literature [82])
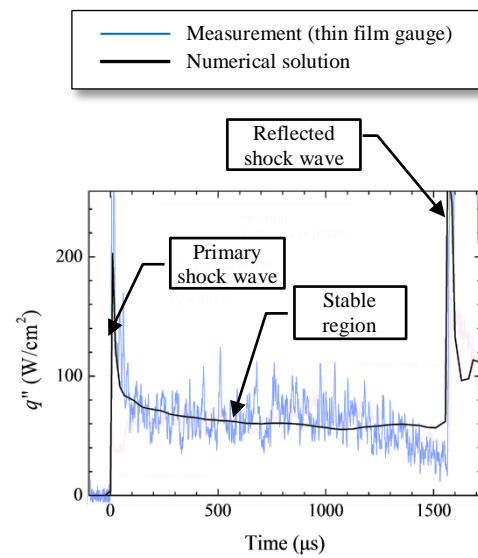
Fig. 2-17 Evolutions of heat flux for Run 3 at the measuring point (measured data acquired from literature [82])



(a) Flow velocity

(b) Fluid temperature

(e) Right-going shock wave and boundary layer development behind it

(c) Boundary layer thickness

(d) Heat flux
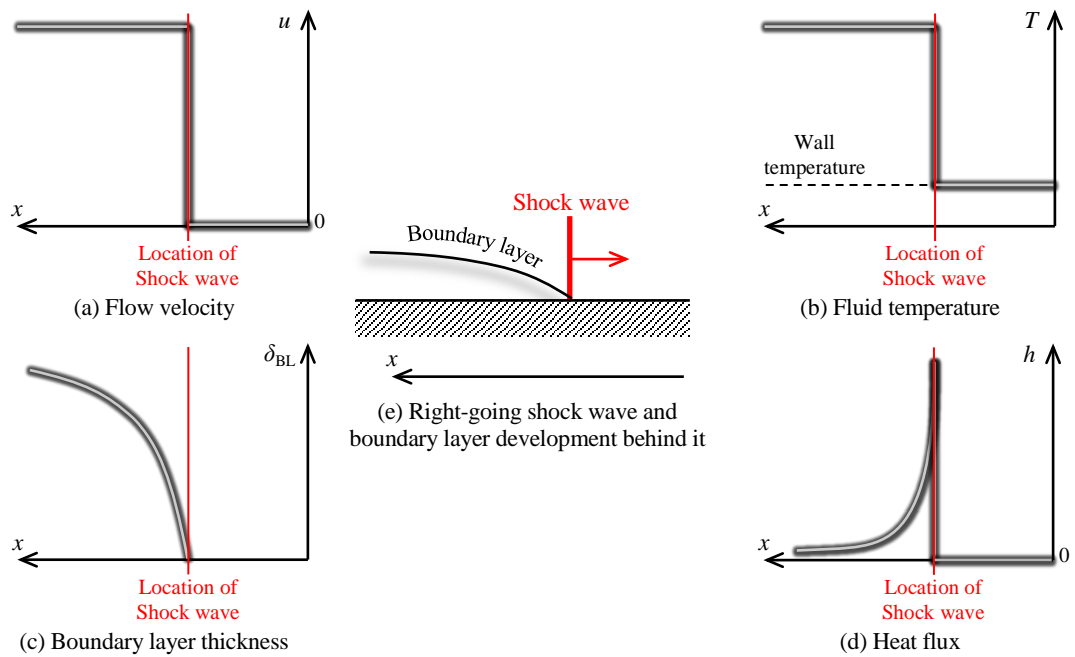
Fig. 2-18 Normal shock wave propagation and relevant variations of flow states

## 2.8    Verification for Conjugate Interface Temperature

Since the interface temperature that plays the role of boundary condition of both fluid and solid domains is obtained by the approximate solution in which the formulation is associated with two sets of different material properties, it is necessary to verify the numerical solution of the interface temperature by comparing with analytical solution.

The schematic shown in Fig. 2-19 describes the problem in the verification. Consider an infinite plate with temperature $T_{0,1}$. The medium temperature is $T_{0,2} < T_{0,1}$. At the initial moment, it is placed into the medium. The plate is cooled by heat conduction. [1]

The material properties of the infinite plate $\rho$, $c_p$ and $k$ are different from corresponding ones of the surrounding medium, and subscript 1 and 2 in Fig. 2-19 refer to the plate and the medium, respectively. Table 2-6 shows the material properties used for 1 and 2 in Fig. 2-19. 1(a) ~ 1 (c) covers the range of the material properties of fluid involved near the wall surface in the present wave rotor cell (introduced in Section 4.1). 1(a) corresponds to the smallest density in the wave rotor cell, 1(b) to a moderate one, and 1(c) to the greatest. 2 denotes the solid wall.

The problem can be described as [1]

$$\frac{\partial T_1(x,t)}{\partial t} = \alpha_1 \frac{\partial^2 T_1(x,t)}{\partial x^2} \quad (t>0; -1<x/\delta<1) \tag{2.57}$$

$$\frac{\partial T_2(x,t)}{\partial t} = \alpha_2 \frac{\partial^2 T_2(x,t)}{\partial x^2} \quad (t>0; 1<|x/\delta|<\infty) \tag{2.58}$$

Initial state    $\qquad T_1(x,0) = T_{0,1} \quad T_2(x,0) = T_{0,2}$ \hfill (2.59)

Interface heat flux    $\qquad \pm K_k \dfrac{\partial T_1(\pm\delta,t)}{\partial x} = \pm \dfrac{\partial T_2(\pm\delta,t)}{\partial x}$ \hfill (2.60)

Interface temperature    $\qquad T_1(\pm\delta,t) = T_2(\pm\delta,t)$ \hfill (2.61)

Center and infinite location    $\qquad \dfrac{\partial T_1(0,t)}{\partial x} = 0, \quad \dfrac{\partial T_2(\infty,t)}{\partial x} = 0$ \hfill (2.62)

where $\alpha_1$ and $\alpha_2$ are thermal diffusivities for 1 and 2, respectively, and $\alpha = \frac{k}{\rho c_p}$; $\delta$ is half thickness of plate; $t$ is time; $K_k = \frac{k_1}{k_2}$ is ratio of thermal conductivity.

The analytical solutions of temperature are [1]

$$\Theta_1 = \frac{T_1(x,t)-T_{0,2}}{T_{0,1}-T_{0,2}} = 1 - \frac{1}{1+K_\varepsilon} \sum_{n=1}^{\infty} (-H)^{n-1} \left[ \mathrm{erfc}\left( \frac{(2n-1)\delta - x}{2(\alpha_1 t)^{1/2}} \right) + \mathrm{erfc}\left( \frac{(2n-1)\delta + x}{2(\alpha_1 t)^{1/2}} \right) \right] \tag{2.63}$$

$$\Theta_2 = \frac{T_2(x,t) - T_{0,2}}{T_{0,1} - T_{0,2}}$$

$$= \frac{K_\varepsilon}{1+K_\varepsilon}\mathrm{erfc}\left(\frac{x-\delta}{2(\alpha_2 t)^{1/2}}\right) - \frac{K_\varepsilon(1+H)}{1+K_\varepsilon}\sum_{n=1}^{\infty}(-H)^{n-1}\mathrm{erfc}\left(\frac{x-\delta+2n\delta(\alpha_2/\alpha_1)^{1/2}}{2(\alpha_2 t)^{1/2}}\right) \tag{2.64}$$

$$\Theta_{\mathrm{intf}} = \frac{T_{\mathrm{intf}}(t) - T_{0,2}}{T_{0,1} - T_{0,2}} = \frac{K_\varepsilon}{1+K_\varepsilon} - \frac{2K_\varepsilon}{1+K_\varepsilon}\sum_{n=1}^{\infty}(-H)^{n-1}\mathrm{erfc}\left(\frac{n\delta}{(\alpha_1 t)^{1/2}}\right) \tag{2.65}$$

where $\Theta$ is dimensionless temperature; subscript intf denotes interface; $K_\varepsilon = \frac{\varepsilon_1}{\varepsilon_2}$ is ratio of thermal effusivity and $\varepsilon = (\rho c_p k)^{1/2}$; $H = \frac{1-K_\varepsilon}{1+K_\varepsilon}$ is a dimensionless number.

Analytical dimensionless temperature distribution as time proceeds ($t$ and Fo increase) for 1(b) & 2 is shown in Fig. 2-20 as an example. The Fourier number $\mathrm{Fo}_1 = a_1 t/\delta^2$. As time proceeds, the temperature falls down gradually.

Short-term

This paragraph explains the verification of the approximate solution for interface temperature response in very short time when the thermal boundary layer is extremely thin. As for material properties 1(b) & 2, with the temperature distribution at $\mathrm{Fo}_1 = 1.0{\times}10^{-8}$ ($t = 1.0{\times}10^{-8}$ s) obtained by analytical approach as initial distribution (Fig. 2-21 and Fig. 2-22), numerical calculation with the present grid spacing for fluid domain and solid domain and the approximate solution of interface temperature described in Subsection 2.3 is fulfilled for $\mathrm{Fo}_1 = 1.0{\times}10^{-8} \sim 2.0{\times}10^{-8}$, and the result is compared with that of the analytical approach in Fig. 2-23. Obviously, the numerical result almost coincides with the analytical one. Similar comparisons for material properties 1(a) & 2 and 1(c) & 2 exhibited in Fig. 2-24 and Fig. 2-25 also shown great agreement between numerical and analytical results.

Long-Term

The verification of the approximate solution is presented in this paragraph for interface temperature in a relatively long period in order to understand the accumulative difference in a long run of numerical simulation of many wave rotor cycles that may be necessary before limit cycle is reached (for example, for 1X size wave rotor to be introduced in Section 4.1 and for material properties 1(b), the time of a wave rotor cycle corresponds to $\mathrm{Fo}_1=4.4{\times}10^{-3}$). For material properties 1(b) & 2, the temperature distribution at $\mathrm{Fo}_1 = 5.8{\times}10^{-2}$ is solved by analytical approach as initial distribution (Fig. 2-26 and Fig. 2-27). Then, numerical calculation similar to that described in the previous paragraph is implemented for $\mathrm{Fo}_1 = 6.0{\times}10^{-2} \sim 1.0{\times}10^{-1}$, and the result is compared with that of the analytical approach. The dimensionless temperature at the interface is compared for material properties 1(b) & 2 in Fig. 2-28. The absolute difference between numerical and analytical results $\Delta_a = |\Theta_{\mathrm{Numerical}} - \Theta_{\mathrm{Analytical}}|$ is around $6{\times}10^{-5}$, and the relative difference $\Delta_r = |1 - \Theta_{\mathrm{Numerical}}/\Theta_{\mathrm{Analytical}}|$ is around 6%. Likely, for material properties 1(a) & 2 and 1(c) & 2, the dimensionless temperature at the interface is compared in Fig. 2-29 and Fig. 2-30, respectively. The absolute differences are about $4{\times}10^{-5}$ and $1{\times}10^{-4}$, and the relative differences are about 2% and 7%, respectively. Considering the possible temperature range (400 K ~ 1300 K) of the mainstream in the present wave rotor cell, the absolute difference $\Delta_a \times (1300\text{ K} - 400\text{ K})$ is up to 0.1 K. In addition, Fig. 2-31 ~ Fig. 2-33 show temperature distributions around interface ($x/\delta=1$) at different long-term Fourier numbers for different material properties 1(b), 1(a) and 1(c). Since the difference in interface

temperature, as well as interface temperature itself, is small, the differences in temperature at other nodes are also limited.

Table 2-6 Material properties for 1 and 2

|  | Density $\rho$ | Specific heat capacity $c_p$ | Thermal conductivity $k$ |
|---|---|---|---|
|  | kg/m$^3$ | J/(kg·K) | W/(m·K) |
| 1(a) | 1.00 | $1.00\times10^3$ | 0.0407 |
| 1(b) | 2.80 | $1.00\times10^3$ | 0.0407 |
| 1(c) | 4.60 | $1.00\times10^3$ | 0.0407 |
| 2 | $8.00\times10^3$ | $5.00\times10^2$ | 25.0 |
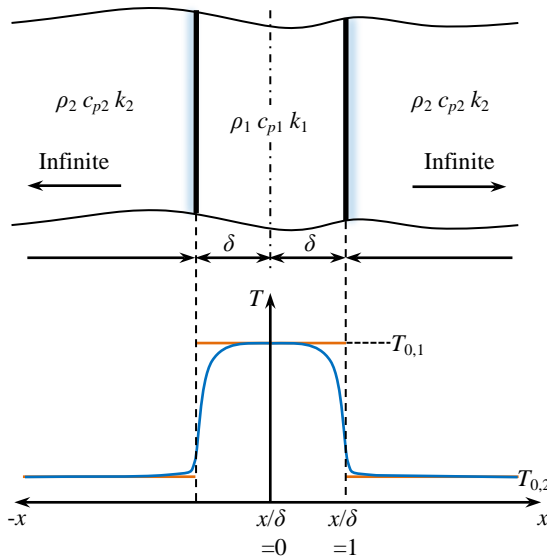
Fig. 2-19 Cooling a plate in an infinite medium [1]
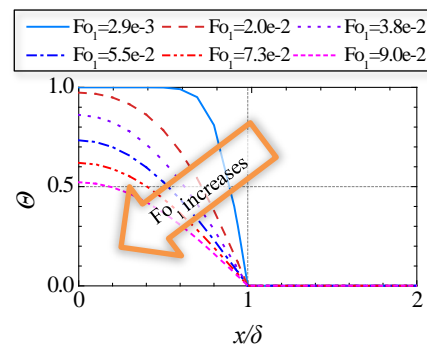
Fig. 2-20 Analytical solution of temperature distribution along $x$ direction for 1(b) and 2
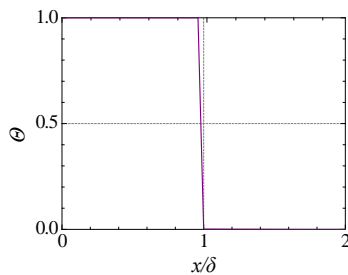
Fig. 2-21 Initial temperature field obtained by analytical approach for short-term verification
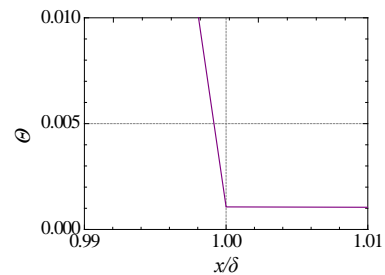
Fig. 2-22 Local temperature distribution around interface (locally enlarged view of Fig. 2-21)
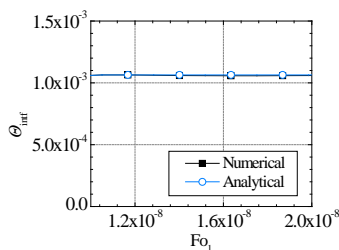
Fig. 2-23 Short-term histories of interface temperature of numerical and analytical results for 1(b) and 2
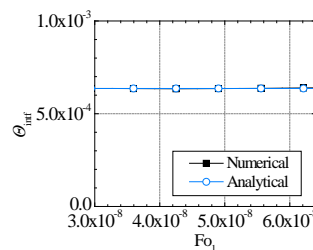
Fig. 2-24 Short-term histories of interface temperature of numerical and analytical results for 1(a) and 2
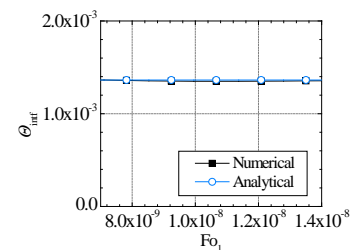
Fig. 2-25 Short-term histories of interface temperature of numerical and analytical results for 1(c) and 2
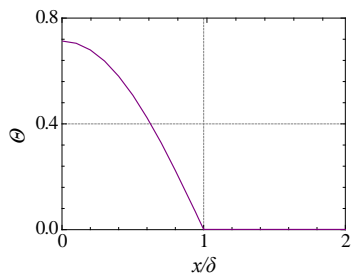
Fig. 2-26 Initial temperature field obtained by analytical approach for long-term verification
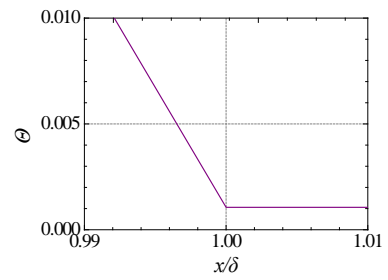


Fig. 2-27 Local temperature distribution around interface (lcocally enlarged view of Fig. 2-26)
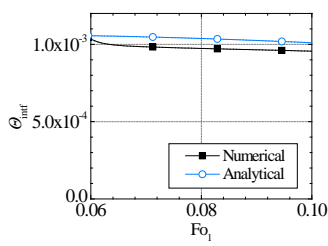


Fig. 2-28 Long-term histories of interface temperature of numerical and analytical results for 1(b) and 2
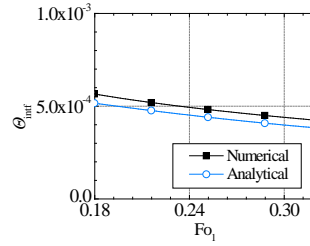


Fig. 2-29 Long-term histories of interface temperature of numerical and analytical results for 1(a) and 2
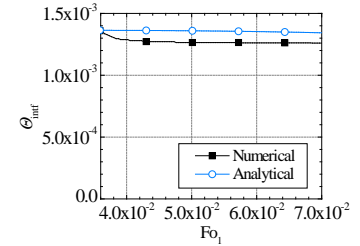


Fig. 2-30 Long-term histories of interface temperature of numerical and analytical results for 1(c) and 2
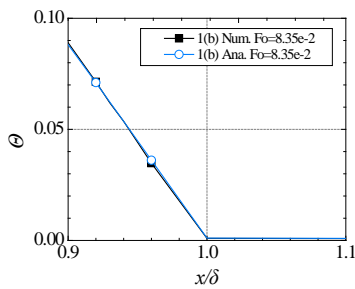


(a) At $Fo_1=8.35\times10^{-2}$
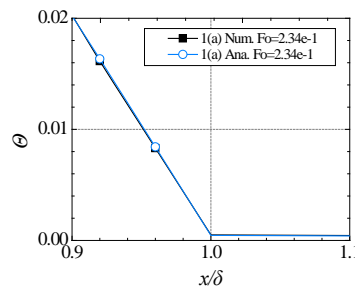


(a) At $Fo_1=2.34\times10^{-1}$
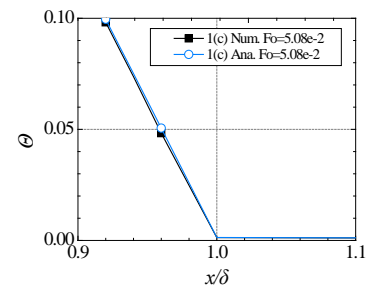


(a) At $Fo_1=5.08\times10^{-2}$
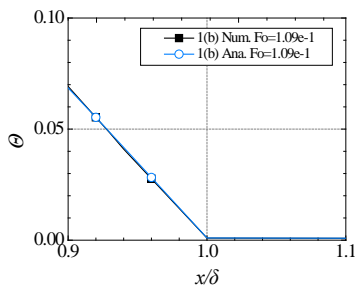


(b) At $Fo_1=1.09\times10^{-1}$
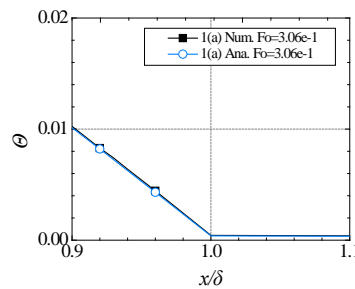


(b) At $Fo_1=3.06\times10^{-1}$
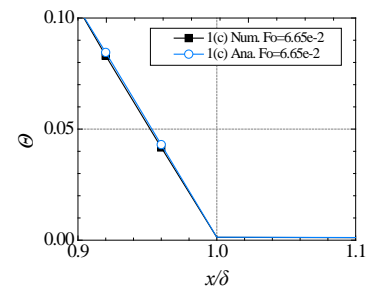


(b) At $Fo_1=6.65\times10^{-2}$

Fig. 2-31 Temperature distributions around the interface of numerical (Num.) and analytical (Ana.) results for 1(b) and 2

Fig. 2-32 Temperature distributions around the interface of numerical (Num.) and analytical (Ana.) results for 1(a) and 2

Fig. 2-33 Temperature distributions around the interface of numerical (Num.) and analytical (Ana.) results for 1(c) and 2

# CHAPTER 3: VERIFICATION FOR WAVE-ROTOR-LIKE FLOW FIELD AND HEAT TRANSFER

## 3.1 Introduction of experiment for Wave-Rotor-Like Flow Field and Heat Transfer

The verification taking on essential characteristics of the complex flow field in a wave rotor cell is performed to confirm the capability of the solver to simulate flow field and heat transfer for wave rotor cell. The wave-rotor-like flow field is produced by experiments, and the verification is performed through comparison between numerical simulation and test run.

### 3.1.1 Brief Introduction of the Previous Experiment

The experimental apparatus is developed on the basis of an existing one that was built to visualize the internal flow dynamics of small tubes, in which fundamental flow dynamics of wave rotor cell was generated [35]. The concept of the previous experiment was to produce pressure wave propagations similar to that in the compression process of wave rotor. Shown in Fig. 3-1 is the existing one used in the previous study [35] before being improved for the present research. Since the ports were openings on the rotating disc, the ports rotated with the rotating disc, and the cell was stationary. This configuration was opposite to wave rotors and the rotation effect was not taken into account. In fact, according to the knowledge of 3-D simulations revealed by Larosiliere [55], the rotation effect does not have large influence on pressure waves [35]. Moreover, only at the left end did the cell open to ports; the other end was closed. This configuration was designed for simplicity and the fundamental flow dynamics in the test cell is not much different from real wave rotor cell. [35] In the test run, high pressure air at room temperature flowed into cell through charging port and shock wave was generated. After that, the high pressure air in cell flowed out through the gap between cell and rotating disc into the surroundings when the cell end no longer opened to charging port. A pair of charging ports was mounted on the rotating disc, implying that one revolution contained two cycles. Two test sections of different lengths (168 mm and 42 mm) made of crystal glass were used for comparison, which are shown in Fig. 3-2. The right end is blocked with an unsteady pressure transducer mounted. Shock wave visualization with Schlieren method, velocity measurement with Laser Doppler Anemometry and stagnation pressure measurement were carried out.
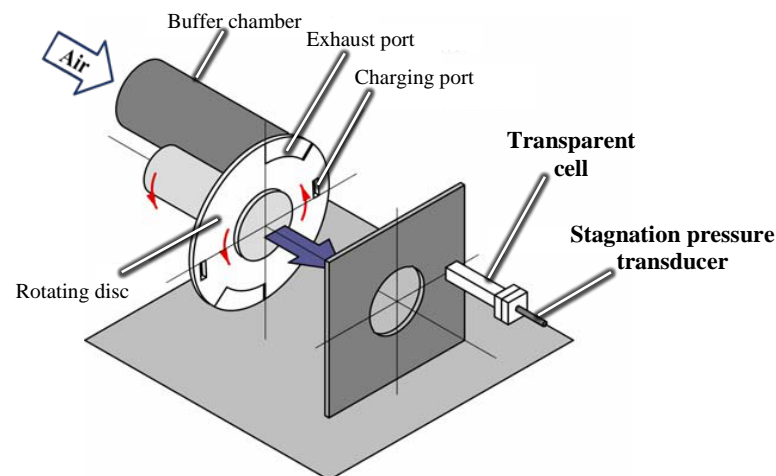


Fig. 3-1 Equipment for investigation of internal flow dynamics [10]
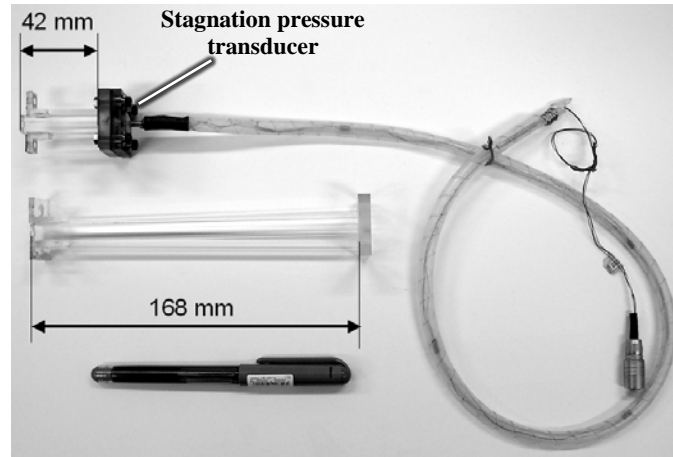
Fig. 3-2 Test cells in the previous study [35]

### 3.1.2 Motivation and Purpose of the Present Experiment

Although in Section 2.7, the code is verified for pressure and heat flux related to propagation and reflection of normal shock wave, it is still not so persuasive when the present study attempts to cope with internal flow field and associated heat transfer phenomena in wave rotor cell. The shock tube test cited in Section 2.7 refers to perfect shock wave that travels in fluid of uniform and constant state, and the dimension of the shock tube is large (diameter of 70 mm). As regards shock waves in a wave rotor cell, the primary shock wave generated by opening cell of low pressure fluid to high pressure port is gradually formed by many compression waves produced by gradually opening cell to port, which is distinguished from the sharp shock wave in the shock tube test; and the shock waves propagates in fluids of varied temperature (or density), differing from the uniform fluid ahead of shock wave in the shock tube test.

Therefore, the present research needs to examine the general performance of predicting the development of flow field and associated heat transfer when performing numerical simulation of wave rotor cell flow and heat transfer caused by complex pressure wave dynamics, and to find out if the code is sufficient for wave rotor cell flow and heat transfer. To satisfy this need, flow field and heat transfer solved by numerical simulation is compared with experimentally produced flow field and heat transfer of the essential characteristics of wave rotor's flow field and heat transfer.

The experiment aims to reproduce flow field similar to that of the compression process in wave rotor: compression waves gradually converge and coalesce to form a finite primary shock wave, the primary shock wave is reflected and travels in fluids of varied temperature that is divided by complex contact front, and shutting the inlet causes expansion waves propagating in the cell. In this progress, heat flux is expected to rise as shock waves cause fluid motion and lift the fluid temperature higher than wall temperature, and to decline as expansion waves cause decrease of fluid temperature. Besides, since the present study focuses on small wave rotor, flow passage of hydraulic diameter closer to small size (Table 1-1) would also leads to better similarity between the experimental flow field and that in small wave rotor.

Then, the pressure of the unsteady flow field and the rates of rise and decline of heat flux (resulting in accumulation of heat flux into wall and accumulation of heat flux out from wall) in the progress of propagation of shock waves and expansion waves are expected to be simulated well by numerical approach.

### 3.1.3    Differences between the Present Experiment and the Previous One

Regarding the present experiment, similar to the previous one, the flow field of the test rig is designed to reproduces travelling shock waves and expansion waves that characterize the unsteady flow field in wave rotor cell. Particularly, the development process of the wave-rotor-like flow field includes gradual opening and closing at cell end, propagation of primary shock wave and reflected shock wave, compression process caused by propagation of shock wave, and expansion process caused by propagation of expansion waves. Different from the previous experiment that used air at room temperature as driver fluid, the present one utilizes high temperature gas to realize temperature difference between supply gas and the surroundings for better observation of heat transfer phenomena. Furthermore, instead of the transparent cell that was used for visualization, stainless steel cell is employed in the present experiment because the rate of heat conduction of stainless steel is similar to that of metal material used in wave rotor. Besides, the side lengths of the square cross-sections of the cells in the previous experiment were 3 mm, but they are 7 mm in the present experiment since the diameter of the heat flux sensor, which will be addressed later, is over 6 mm.

### 3.1.4    Scheme of the Present Experiment

The pressure wave processes and the contact front movement of the proposed test runs are plotted in Fig. 3-3. The default rotation speed corresponds to Fig. 3-3 (a) and the doubled rotation speed corresponds to Fig. 3-3 (b).

First to introduce is the default one in Fig. 3-3 (a). The left end of the cell begins to open to the charging port from 0° and begins to shut from 11°. The right end is blocked. At the default rotation speed, the primary shock wave induced by opening to the port propagates in the cell and the compression process commences from 0°. The reflected shock wave arrives at the left end at 11° as soon as the cell begins to shut. The shut causes expansion waves propagating in the cell and the expansion process commences. The hot gas flows into the cell behind the shock wave, and thus creates a contact front between the hot gas and the compressed air. Then, the right-going contact front is hampered by the reflected shock wave. As the expansion waves move in the cell, the fluid in the cell gradually moves out. Therefore the contact front moves leftwards in the expansion process until the gas is completely scavenged.

However, at the doubled rotation speed in Fig. 3-3 (b), since the port moves faster, the time of opening interval is halved for the same degree 0° ~ 11°, and the arrival degree of reflected shock wave is presumably doubled. Inasmuch as the reflected shock wave arrives much later than the initiation of expansion waves at 11°, the reflected shock wave and the expansion waves intersect in the left half of the cell. Under this faster rotation speed, the arrivals of pressure waves cannot match the shutting degree of 11° any more. This kind of mismatch is possible in numerical simulation for wave rotor cell with heat transfer effects, since the propagation of pressure waves are potentially affected when heat transfer in taken into consideration. To cope with mismatch, the code is additionally verified for flow field and heat transfer at doubled rotation speed.

Generation of shock wave requires pressure difference; therefore, it is necessary to supply with fluid of pressure higher than that initially in cell. Since it is intended to induce heat transfer resembling that in the compression process in wave rotor, the temperature of the charging fluid should be higher than that initially in the cell.

To compare the flow fields of numerical simulation and test run, the pressure of the flow field is used for the consideration that through observing pressure the propagation of the shock waves can be learned. To compare the heat transfer, the heat flux caused by evolution of the flow field is used.

Compared with the verification done in Section 2.8, this verification handles complex flow field that is close to the flow field in wave rotor cell during compression process. Besides, the cells' sizes of the test rig are much closer to the size of the small wave rotor cell in Table 1-1, and the cells are remarkably smaller than the shock tube.



(a) Under default rotation speed
(1800 RPM for 168-mm and 7200 RPM for 42-mm)

(b) Under doubled rotation speed
(3600 RPM for 168-mm)
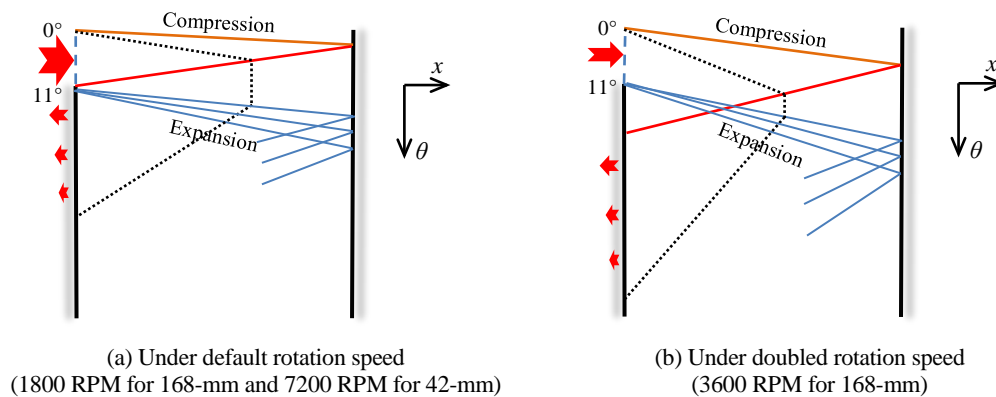
Fig. 3-3 Schematic wave diagrams for different ratation speeds

## 3.2    Experimental Setup

For the purpose of measuring flow field and heat transfer of cell, the cell in the test rig is stationary, periodically opening to rotating port, through which the high-pressure hot gas flows to the cell. The flow path is plotted in Fig. 3-4. The high pressure air from the compressor flows through large air reservoirs and undergoes heating in the electric heater. Then the high-pressure hot gas is stabilized in the buffer chamber. The opening end of the cell is aligned with the outlet of the buffer chamber. When the port opens to them, the hot gas surges into the cell; otherwise, it flows into the surroundings.

The key components realizing the wave diagrams in Fig. 3-3 are the rotating disc handling the opening and closing for the cell, the buffer chamber that supplies high-pressure hot gas, and the cell in which the flow field and the heat transfer is monitored. The assembly of these components is shown in Fig. 3-5, and Fig. 3-6 displays the axially exploded view, in which the separated components and their relative positions are distinct. The red axis line associated with flow aligns the buffer chamber, the shaped exit for the buffer chamber, and the cell. The blue axis line associated with rotation aligns the shaft, the rotating disc, and the plates that fix the rotating disc on the shaft. The cell is mounted in the hole machined in the standing board, and the free end is blocked by metal sealed with adhesive. The standing board divides the assembly into the supply side and the cell side. The photograph for the supply side is shown in Fig. 3-7, and Fig. 3-8 presents the sight on the other side. In particular, Fig. 3-9 and Fig. 3-10 illustrate the charging ports on the rotating disc, and Fig. 3-11 displays the progression of opening and closing actions. Two cells of different lengths are studied for comparison at different sizes. In one-dimensional theory, by adapting rotation speed to length, it is possible to realize the same wave diagram for different length. The lengths are 42 mm and 168 mm, for which the default rotation speeds are 1800 RPM and 7200 RPM, respectively. The cross section is 7 mm square and the stainless steel wall is 1 mm in thickness for either length.

The gas supplied by the buffer chamber is characterized by high temperature and high pressure compared with the air in the cell. Using the initial pressure and the initial temperature in the cell to normalize corresponding parameters throughout this verification, the supply total pressure and the supply total temperature are 2.7 and 1.3, respectively.

In order to realize the planned wave diagram and to provide the numerical simulation with supporting data, pressure, temperature, heat flux and rotation speed are monitored through instrumentation. The pressure and the temperature of the cell's surroundings are acquired by barometer and thermometer; these are used to decide the initial state in the air. The rotation speed is monitored by digital multimeter that counts the frequency of signal transmitted from fiber optic photoelectric sensor, as well as by the inverter (TOSHIBA TOSVERT™ VF-AS1) for the Fuji 3-phase induction motor that drives the rotation of the rotating disc.

The major items in measurement are specified in Fig. 3-12. The total pressure and the total temperature are measured in the buffer chamber and adjusted in accordance with the supply condition $P_0$ = 2.7 and $T_0$ = 1.3 that are regarded as nominal inlet conditions for numerical simulation. The external temperature distribution on one side of the wall is captured by the infrared thermography camera Thermoviewer JTG-5200 developed by JEOL Ltd. The external temperature is virtually stable provided that no change occurs in the rotation speed, the surroundings and the supply gas. The external temperature acquired by Thermoviewer is used as boundary condition in numerical simulation. The unsteady parameters, the static pressure and the heat flux, are measured at one or more axial locations along the cell. They delivers fundamental understandings of propagation of pressure waves and relevant heat flux of test run, and more importantly they provides the data representing internal flow field and heat transfer in the comparison of experimental and numerical results.

The total pressure in the buffer chamber is measured by pre-amplified pressure gauge XFPM-200KPG produced by Fujikura Ltd., which is capable of measuring gauge pressure up to 200 kPaG. The total temperature in the buffer chamber is measure by Type K thermocouple (class 2), tolerance of which is ±2.5 °C. The boundary condition is decided by the thermograph, and an example of the raw thermograph is shown in Fig. 3-13. The raw data of the graph is converted to actual temperature distribution by employing the correction method and the tables of radiant emittance vs. temperature provided by the instructions for Thermoviewer [83]. An example of converted image is shown in Fig. 3-14. The axial distribution of temperature is employed as boundary conditions applied on the external surfaces of the four sides of the cell wall.

The unsteady static pressure at cell wall is measured by Kulite® XCQ-093 miniature pressure transducer, whose active surface is less than 2 mm in diameter, and its response is so fast that the signal can be regarded as realtime ($\ll$ 1μs). To mount the pressure transducer on the cell, a socket shown Fig. 3-15 and Fig. 3-16 in is applied.

The unsteady heat flux is measured by Vatell Heat Flux Microsensor (HFM) HFM-8E/L shown in Fig. 3-17 and Fig. 3-18, and it is mounted on the cell with the socket shown in Fig. 3-15. The heat flux sensor is deposited thin film (< 2μm) composed of differential thermopiles for fast response (Fig. 3-19 and Fig. 3-20). And hundreds of thermopile pairs in active area for output boost. The surface of HFM is about 6 mm in diameter and the active area of the thermopiles is about 15 mm$^2$. The time constant of the fast response sensor is $\tau_{63.2\%}$ = 50 μs, much faster than other heat flux sensors but yet relatively slow if it has to confront heat transfer induced by shock wave. The sensor's response would follow the equation for a first order system:

$$R = I \times \left(1 - e^{-t/\tau}\right) \tag{3.1}$$

where $R$ is the response; $I$ is the input, i. e. actual heat flux or temperature here in the sensor system; $t$ is the time and $\tau$ is the time constant of about 200 μs referring to the total delay of heat flux measurement. The distortion caused by slow response is schematically portrayed in Fig. 3-21. The vessel providing HFM with constant reference temperature is exhibited in Fig. 3-22. The reference junction is immersed in distilled water of a bath of ice and water at atmospheric pressure to maintain constant 0 °C. With this heat flux measurement, the rate of heat flux increase in the progress of shock wave propagation and that of heat flux decrease in the progress of expansion wave propagation can be obtained.

External surface temperature, pressure and heat flux are measured for the cell at the same time, and the layout is shown in axial view (Fig. 3-23) and in side view (Fig. 3-24 and Fig. 3-25). In 42-mm-long cell the measurement of unsteady parameters takes place at the middle of cell, whereas in 168-mm-long cell, axial locations 1/4, 1/2 and 3/4 are measured. The physical 168-mm-long cell with sockets mounted is shown in Fig. 3-26. It is mounted to the standing board on the right side and blocked on the left side in this picture. Two of the axial locations (1/8 and 7/8) installed with sockets in Fig. 3-26 are not put to use in further discussion since the characteristics are similar to their neighbor locations'.

Finally, the essential components are assembled and exhibited in Fig. 3-27, equipped with measurement apparatus.
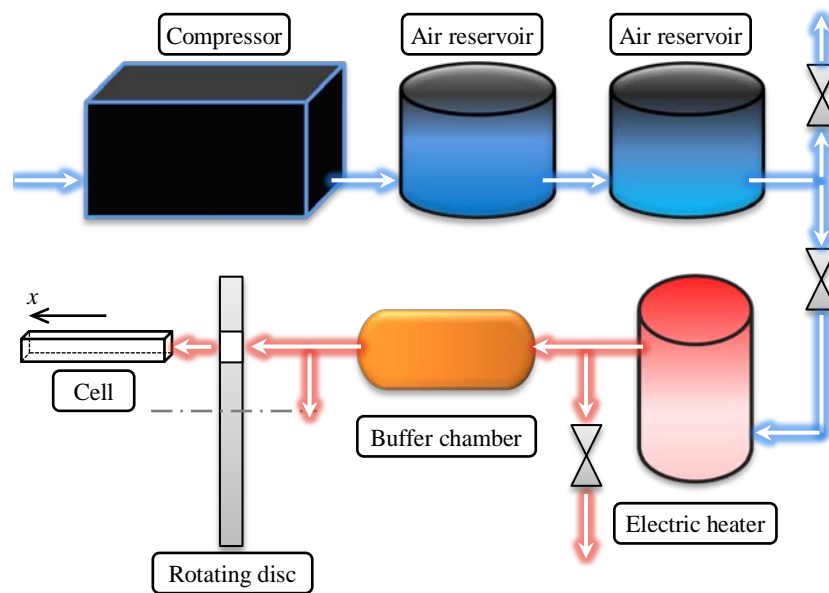


Fig. 3-4 Framework of flow scheme
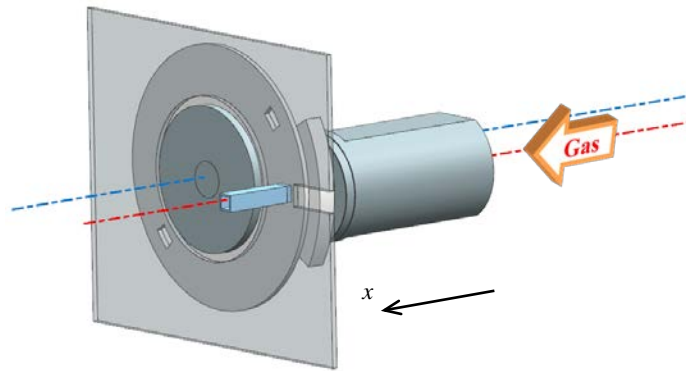
Fig. 3-5 3-D drawing of major assembly of test rig
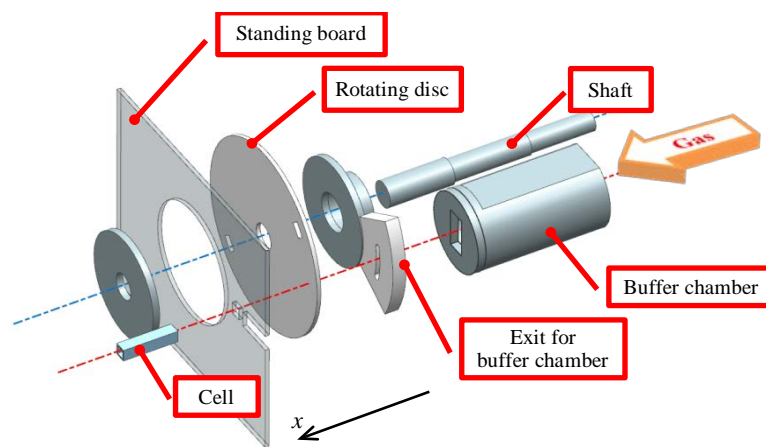


Fig. 3-6 Exploded view drawing of major assembly of test rig
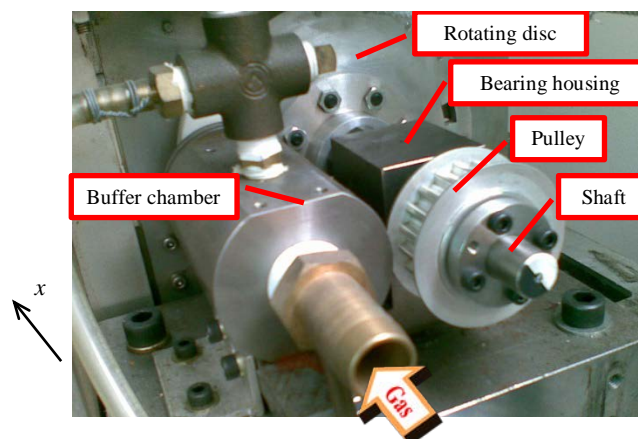


Fig. 3-7 Supply side with rotation components
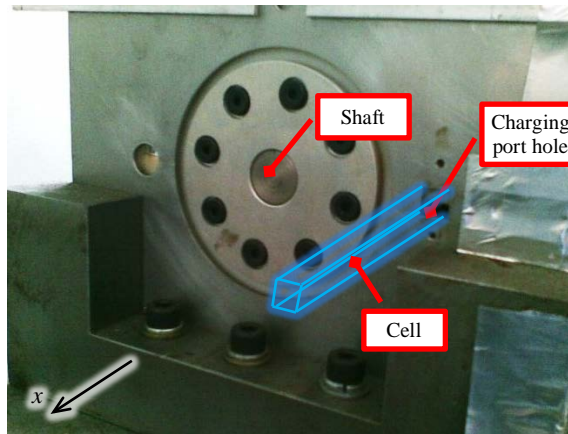
Fig. 3-8 View of cell side
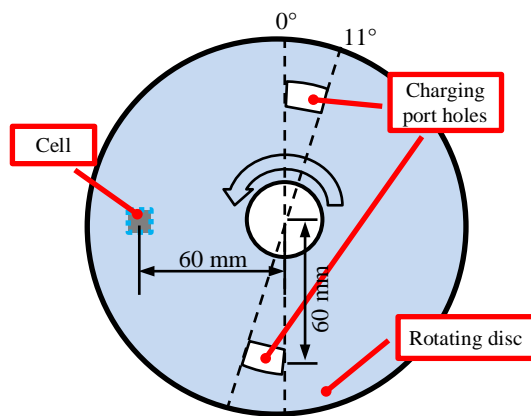


Fig. 3-9 Charging port holes on disc
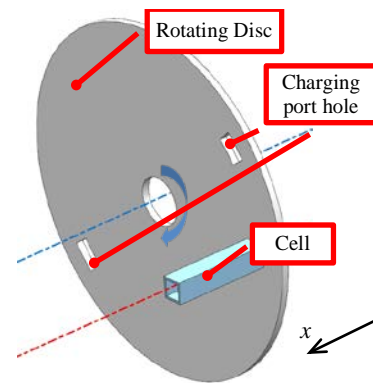


Fig. 3-10 Rotating disc and stationary cell



(a) Prior to opening (closed)

(b) Partial open

(c) Full open

(d) Partial open (partial close)

(e) Closed (after opening)
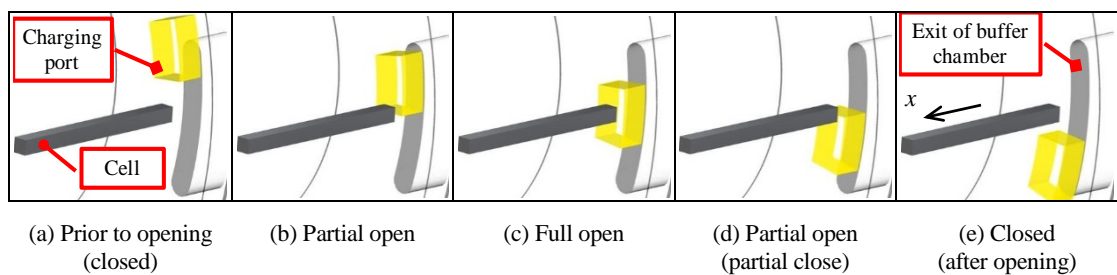
Fig. 3-11 Course of events as port rotates
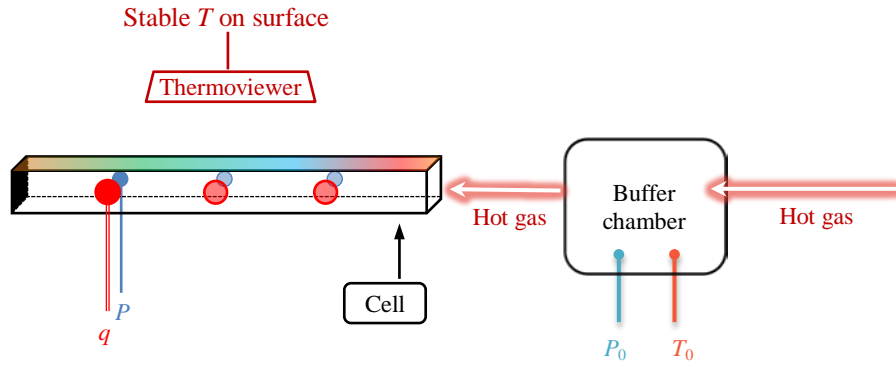
Fig. 3-12 Main measurements
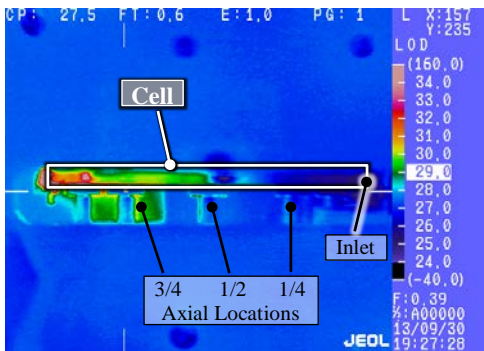


Fig. 3-13 Example thermograph
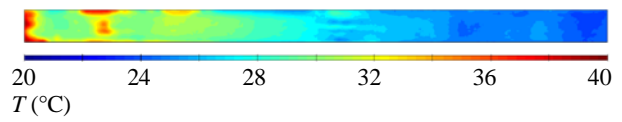


Fig. 3-14 A converted temperature distribution
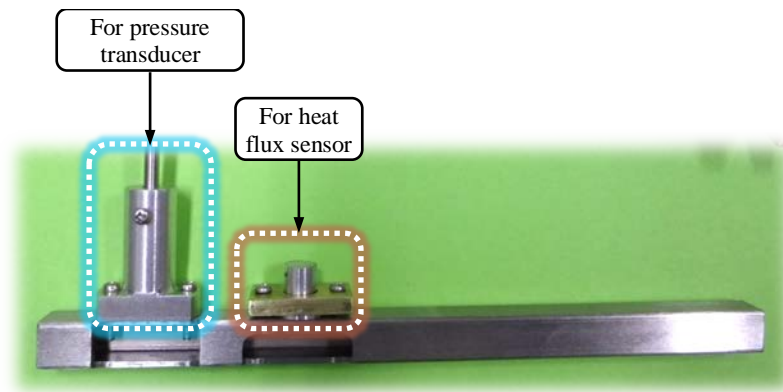


Fig. 3-15 Sockets and dummies for pressure transducer and heat flux sensor (photographed by K. Yamaguchi)
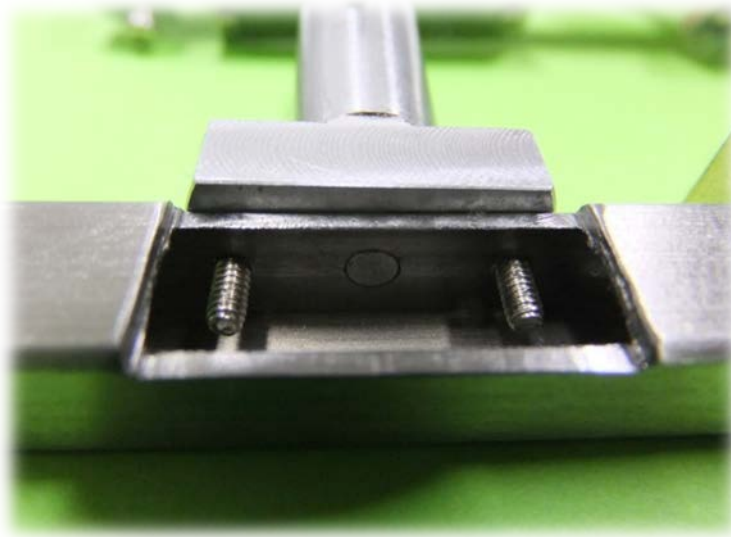
Fig. 3-16 Socket for pressure transducer with dummy sensor (unfitted screw replaced later)
(photographed by K. Yamaguchi)



Fig. 3-17 Official photograph of HFM heat flux sensor [84]
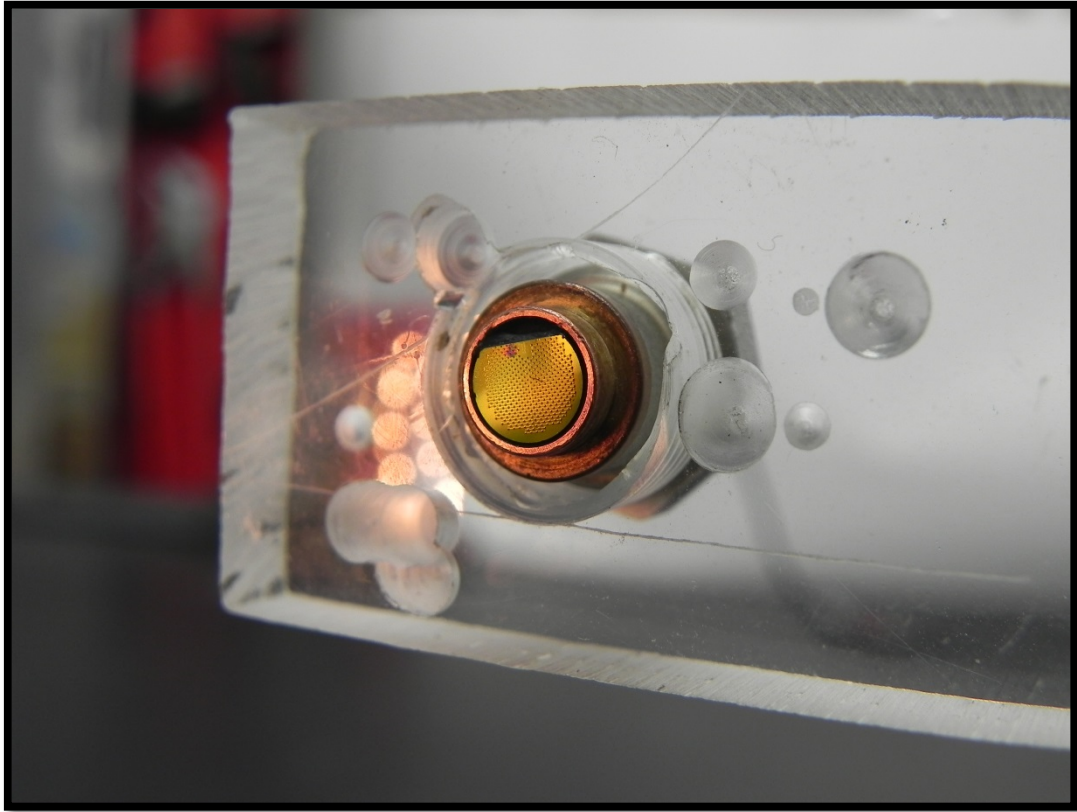
Fig. 3-18 Photograph of HFM-8E/L heat flux sensor (photographed by T. Hisamura)
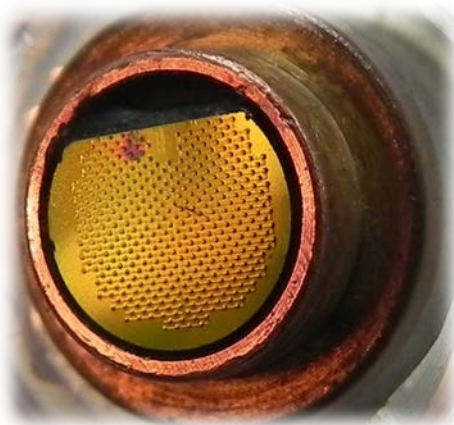


Fig. 3-19 Enlarged view of photograph of
HFM-8E/L heat flux sensor head
(photographed by T. Hisamura)
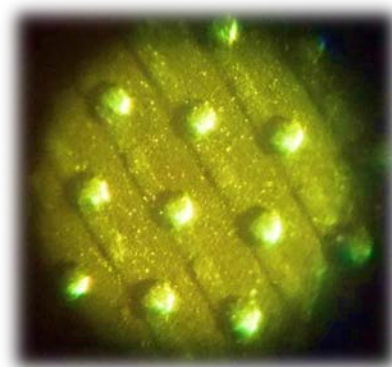


Fig. 3-20 Photomicrograph of thermopile
mounted on surface of HFM-8E/L
(photographed by K. Yamaguchi)
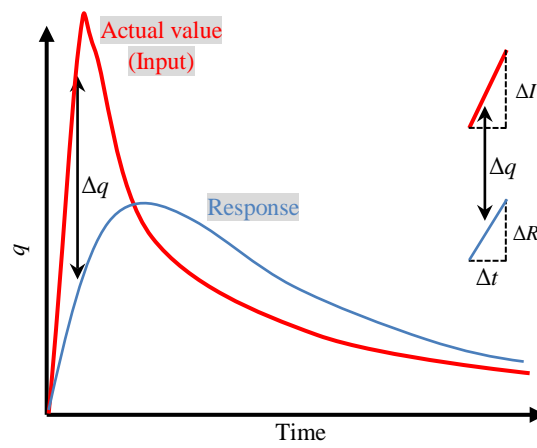
Fig. 3-21 Relation between actual heat flux (or static pressure) and measured heat flux (or static pressure) response



Fig. 3-22 Cold junction apparatus equipped with wiring terminals (photographed by K. Yamaguchi)
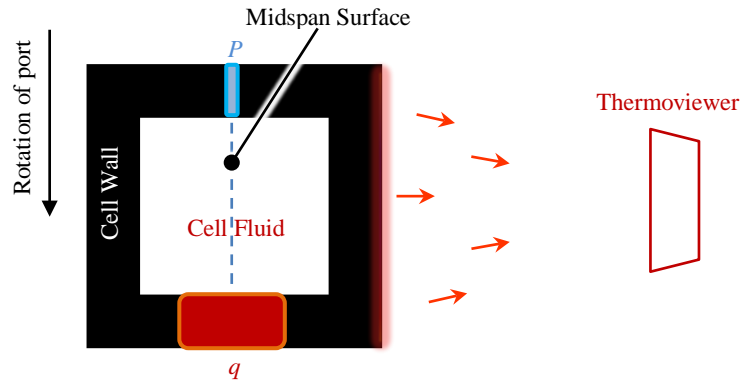
Fig. 3-23 Axial view of layout of measurement for external wall temperature, static pressure ($p$) and heat flux ($q$) for cell
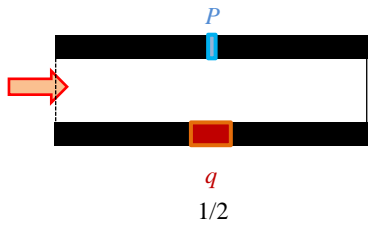


Fig. 3-24 Side view of layout of pressure transducer ($p$) and HFM ($q$) for 42-mm-long cell
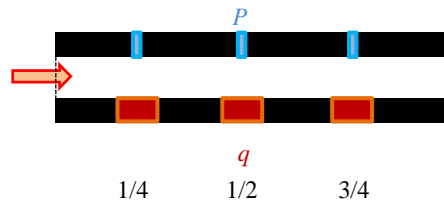


Fig. 3-25 Side view of layout of pressure transducer ($p$) and HFM ($q$) for 168-mm-long cell
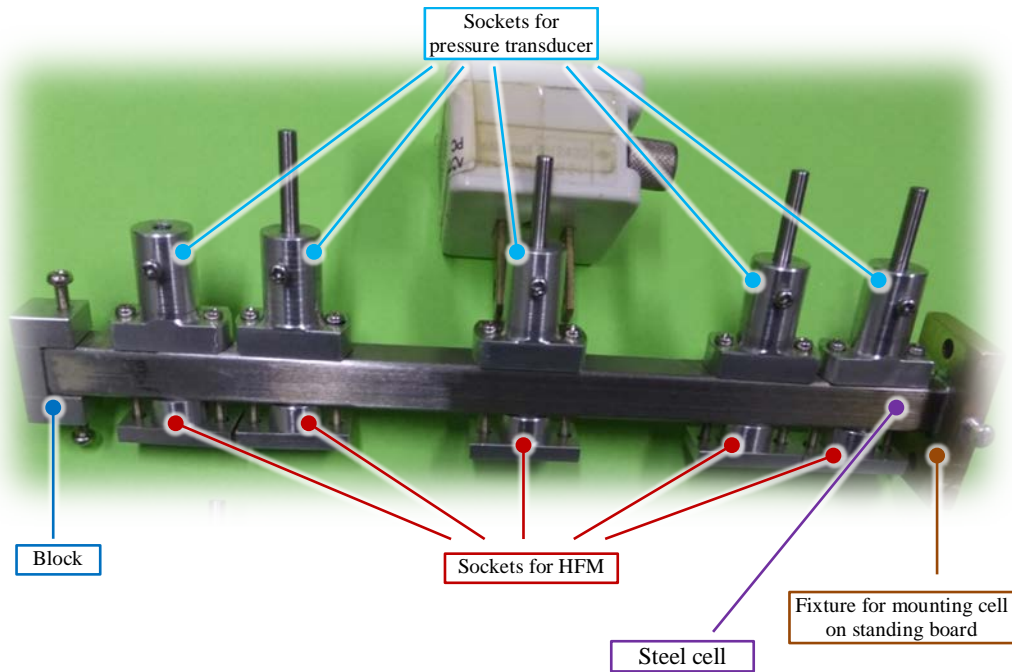
Fig. 3-26 Photograph of 168-mm-long cell with accessories (photographed by K. Yamaguchi)
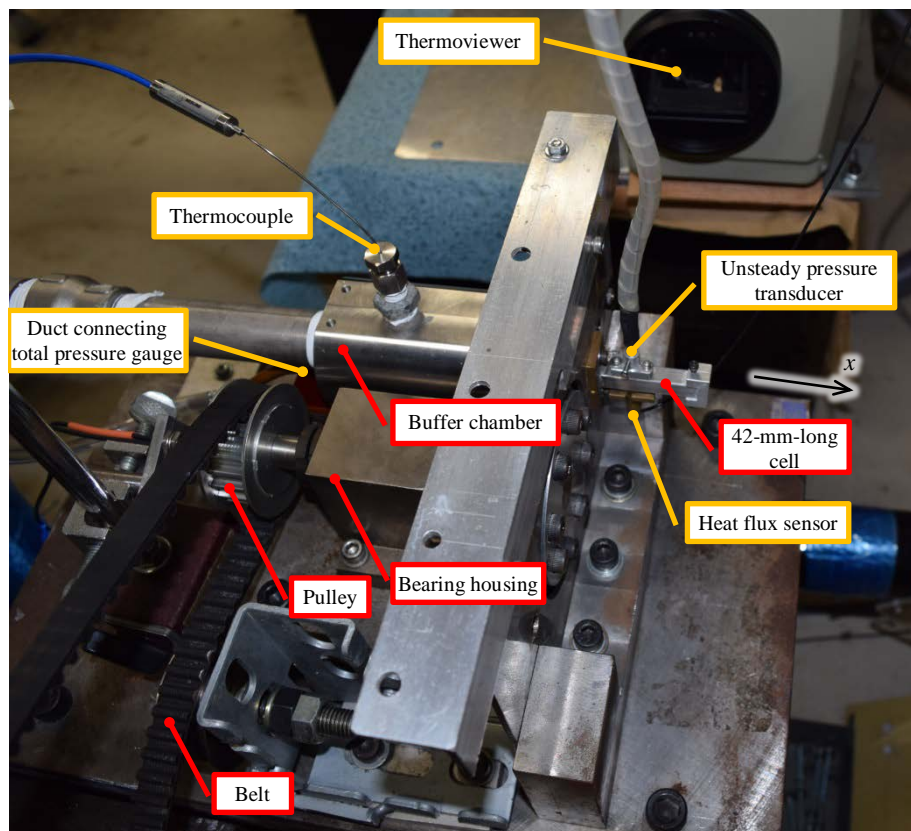


Fig. 3-27 Photograph of major assembly of test rig with connected sensors and Thermoviewer
(photographed by T. Hisamura)

### 3.3    A Preliminary Verification for Unsteady Flow Field

The present test rig is improved to observe heat flux from an original one that was designed to investigate the internal flow dynamics of wave rotor cell with supply gas of **room temperature** in a previous study [35]. The configuration is shown in Fig. 3-1. The propagation of shock wave in the transparent cell was visualized, and the stagnation pressure at the blocked end was measured.

A preliminary verification is carried out for the stagnation pressure of the unsteady flow field without consideration of heat transfer. The measured degree history of stagnation pressure for the 42×3×3 ($L{\times}W{\times}H$, all in mm) cell at default rotation speed 7200 RPM is shown in Fig. 3-28. The arrival of primary shock wave initiates the sharp increase during 5° ~ 6°, and the expansion waves cause declining from peak from about 16°. Because of gradual opening, at the exit of buffer chamber or the inlet of test cell, pressure does not step up to nominal supply total pressure immediately (Fig. 3-29), and therefore the pressure rising at the stagnation end is not consistently sharp. At the end, the stagnation pressure falls back to atmosphere level at about 40°. The numerical result fits close to the experimental curve, which can be observed in Fig. 3-28, indicating that the flow solver is capable of handling the propagation of unsteady pressure waves.
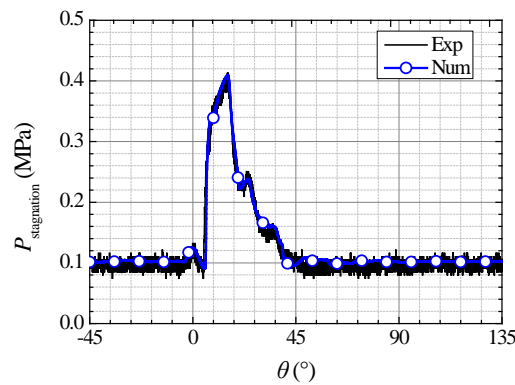


Fig. 3-28 Stagnation pressure histories of experimental result (Exp) [35] and numerical result (Num)
for 42-mm-long cell at 7200 RPM
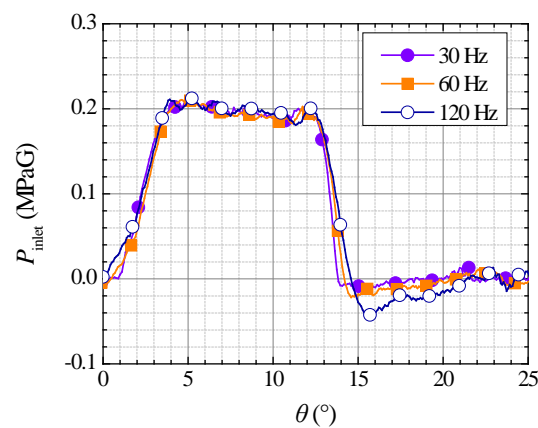


Fig. 3-29 Measured degree traces of cell inlet total pressure at rotation speeds of 30 Hz (1800
RPM), 60 Hz (3600 RPM) and 120 Hz (7200 RPM)

## 3.4    Numerical Study of the Proposed Test Runs

The internal flow dynamics and heat flux are studied by 3-D numerical simulations with the nominal operating conditions used in the experimental test runs, i.e. $P_0 = 1.0$ and $T_0 = 1.0$, and nominal initial state in the cell of $P_0 = 0.37$ (1 atm) and $T_0 = 0.77$ (300 K). With such numerical results, the realization of expected flow field can be confirmed, and the flow field and heat flux can be examined in detail.

### 3.4.1    With Respect to 168-mm-Long Cell

First to show is the numerical predication of the flow field and heat transfer concerning 168-mm-long cell at its default rotation speed 1800 RPM. Shown in Fig. 3-30 is the degree sequence of static temperature distribution on the midspan surface (defined in Fig. 3-23) during the propagation of the primary shock wave. As the left end opens to inlet port gradually, compression waves are generated and propagate rightwards, causing fluid motion (see velocity vectors) and leading to gradual increase of static temperature at each of the axial locations in the cell. As the compression waves moves further, they gradually coalesce into a shock wave (primary shock wave) and the static temperature gradient along axial direction becomes steeper. Far behind the shock wave, complex contact front between fluids of different static temperatures can be observed. Shown in Fig. 3-31 (a) is the degree sequence of static temperature distribution on the midspan surface (defined in Fig. 3-23) up to 30°. The propagation of the right-going primary shock wave elevates the static temperature behind it and brings about flow velocity of the same direction (1st and 2nd cells). It is reflected at the blocked right end (3rd cell). The reflected shock wave travels leftwards, and the air is compressed to even higher static temperature (right side of 3rd ~ 8th cells). Meanwhile, the distorted contact front between the compressed air and inflow gas is perceptible, though dimly. After the compression process, the expansion waves propagate in the cell and cool the fluid in cell to light blue color. By averaging the 3-D flow field on each cross-section, 1-D flow field for each time step is obtained, and the degree sequence of the 1-D static temperature distributions, or the wave diagram colored in static temperature, is shown in Fig. 3-31 (b). The contour line gathers where the gradient is steep. Therefore it is effortless to determine the trace of the primary shock wave by the first dramatic rise of static temperature: it is generated at 0° at the left end, and arrives at the right end at about 5°. Similarly, the second large ascending gradient is caused by the reflected shock wave that travels from the right end at about 5° to the left end at 11°. The characteristic lines of both shock waves are depicted in solid lines in Fig. 3-32 (b). Also in Fig. 3-31 (b), a series of contour lines between the primary shock wave and the reflected shock wave help distinguish the hot gas from the compressed air and locate the contact front between gas and air. The first section of the contact front is depicted as straight dotted line in Fig. 3-32 (b). Behind the reflected shock wave (i.e. to the right of the reflected shock wave), the second section of the characteristic line of contact front is an approximation according to the local axial velocity. The second section of contact front and the expansion waves cannot be easily distinguished, and therefore in Fig. 3-32 (b) the dotted lines denoting the contact front and the dashed line denoting the front position of expansion waves are approximate. This process is similar to the compression process of a wave rotor.

To give an overview on the numerical results for the default rotation speed, the wave diagrams colored in static pressure, static temperature, axial velocity and heat flux are shown in Fig. 3-32. Charging from the inlet port and discharging through the clearance gap between the rotating disc and the stationary cell can be identified in the velocity contour in Fig. 3-32 (c). The degree scale of the wave diagrams is magnified for clear observation of the characteristic lines. Static pressure, static temperature and axial velocity are normalized by nominal inlet total pressure (total pressure measured in the buffer chamber), nominal inlet total temperature and speed of sound at nominal inlet total temperature (total temperature measured in the buffer chamber); and heat flux is normalized by $q_{nominal}$, which is evaluated by the following equations:

$$q_{\text{nominal}} = h \times \left(T_0 - T_{\text{HFM}}\right) \tag{3.2}$$

$$h = \text{Nu}_L \times k / L \tag{3.3}$$

$$\text{Nu}_L = 0.037 \times \text{Re}_L{}^{0.8} \times \text{Pr}^{0.43} \tag{3.4}$$

where $h$ is the nominal heat transfer coefficient, $T_0$ is the nominal inlet total temperature measured in the buffer chamber, $T_{\text{HFM}}$ is the wall temperature measured by heat flux gauge HFM, $\text{Nu}_L$ is the average Nusselt number for turbulent flow over a flat plate [85], and the characteristic length $L$ is the cell length.

The characteristic lines in the wave diagrams for default rotation speed reveal that the internal flow field proceeds in accordance with the designed wave diagram in Fig. 3-3 (a). Regarding heat transfer, in general, heat flux rises behind the primary shock wave and drops when the expansion waves work. The air is compressed and accelerated behind the primary shock wave, causing heat transfer to the wall from the air whose temperature becomes higher than the wall. Then the air is compressed again by the reflected shock wave and the temperature becomes even higher. Therefore, although the velocity falls back to near zero (can be found between the characteristic lines of reflected shock wave and expansion wave in Fig. 3-32 (c)), the heat flux is not attenuated. On the other hand, the hot gas enters the cell with high speed and causes great heat flux; and then it is compressed by the reflected shock wave, and the heat flux is not attenuated, either. When the expansion waves propagate in the cell, the temperature of both fluids becomes lower and closer to that to the wall, and the heat flux descends.

The numerical responses of pressure transducer and heat flux sensor at axial locations (axial locations 1/4, 1/2 and 3/4) for default rotation speed are shown in Fig. 3-33. These numerical responses have already taken into account the response time of the heat flux sensor by the following equation:

$$\Delta R = \Delta q \times (1 - e^{-\Delta t / \tau}) \tag{3.5}$$

for which the parameters are defined in Fig. 3-21. At each step in numerical simulation, the difference $\Delta q$ between the input heat flux (or static pressure) $I$ and the response heat flux (or static pressure) $R$ is calculated, and the increment of response heat flux(or static pressure) $\Delta R$ is obtained by Eq. (3.5); for heat flux $\tau$ is 200 μs and for static pressure it is 2 μs. Both sensors' active areas are also considered (diameter of heat flux sensor: 6.3 mm; diameter of pressure sensor: 1.5 mm) by averaging node heat fluxes or node static pressure in sensor area based on area of each node in numerical simulation. Concerning the static pressures in Fig. 3-33, the rises caused by the primary shock wave and the reflected shock wave are identified at all three axial locations as the rising procedure obviously includes two sections caused by different shock waves. Owing to gradual opening, the first rise is not so steep at axial location 1/4 but becomes more and more drastic at further axial locations, and the second rise induced by the reflected shock wave becomes sharper as the axial coordinate locates closer to the entrance, farther from the right end where the reflected shock wave starts. As for heat flux, generally, the heat flux responses increase and decrease with static pressure. Because the response of heat flux sensor is relatively slower than that of the pressure sensor and the area of the heat flux sensor is larger, drastic increase of heat flux behind shock waves is not observed except for at the axial locations 1/4 and 1/2 when the sharp reflected shock wave passes by.

Secondly, wave diagrams for 3600 RPM, an "off-design" rotation speed faster than the default one, are shown in Fig. 3-34. The meeting point of the expansion waves and the reflected shock wave is located

in the left half and near the midst of the cell, and the intersection of the contact front and the reflected shock wave occurs to the right of the midst. In the velocity contour (Fig. 3-34 (c)), the hot gas is apparently decelerated after 11° because the expansion waves enter the cell before the reflected shock wave arrives in the left half. In this region between the expansion wave and the reflected shock wave, the static temperature of the expanded gas is close to the wall temperature, and consequently the heat flux drops to small value. And then, the gas is compressed by the reflected shock wave; therefore, the static temperature of gas and the heat flux ascend again (Fig. 3-34 (d) and 18° ~ 24° in Fig. 3-35 (a)). Another detail distinguishing the doubled from the default rotation speed is that the static pressure rises caused by shock waves are more drastic, which can be acquired by comparing the increase rates of static pressure between Fig. 3-33 and Fig. 3-35. A reason for more drastic pressure rise is that gradual opening less effective as the cell opens to the port faster and thereby the static pressure gradient induced by shock wave is steeper.

At either rotation speed (Fig. 3-33 or Fig. 3-35), after the expansion process (>40°), the static pressure in cell is close to the atmospheric pressure and the heat flux is almost zero.
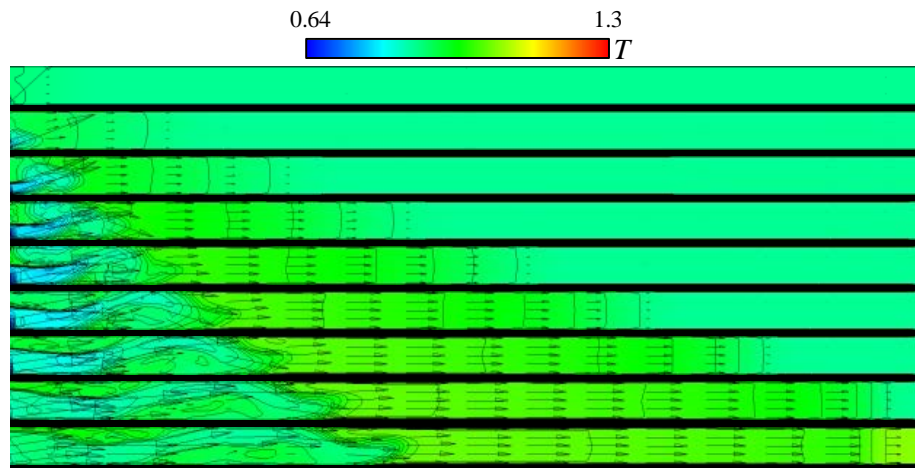


Fig. 3-30 Degree series of midspan static temperature during primary shock wave propagates with flow velocity vectors

(a) Degree series of midspan static temperature

(b) Wave diagram of static temperature
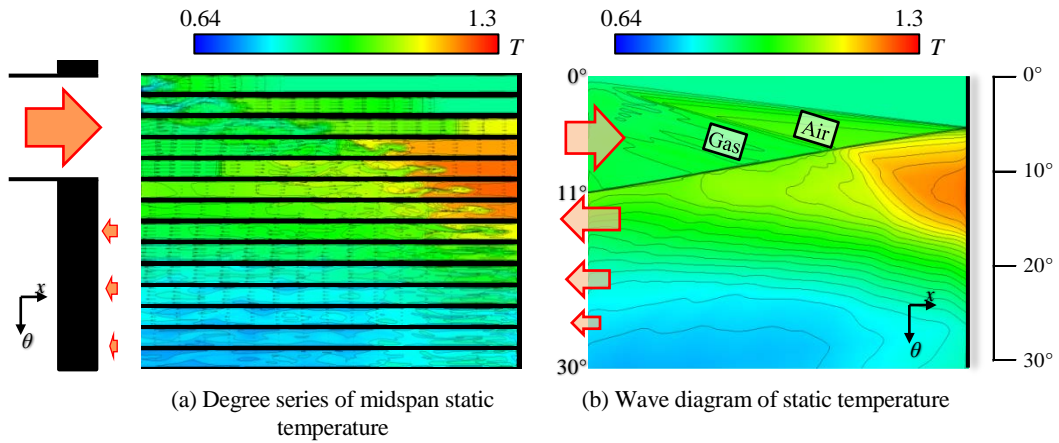
Fig. 3-31 Development of temperature field for 168-mm-long cell at default rotation speed



(a) Static pressure

(b) Static temperature

(c) Axial velocity
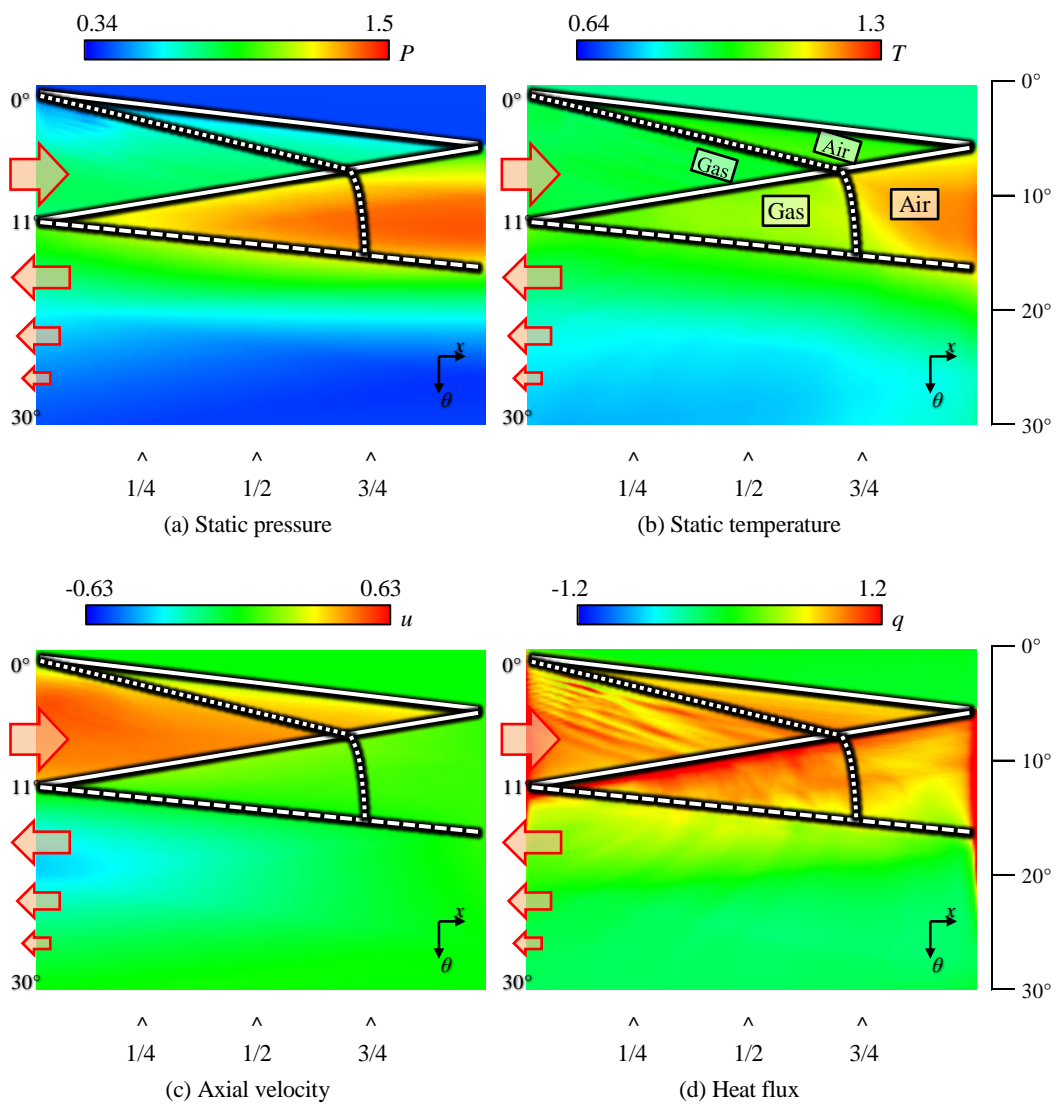
(d) Heat flux

Fig. 3-32 Wave diagrams (0° ~ 30°) of numerical results for 168-mm at default rotation speed (scaled along degree coordinate 5 times for better observation)
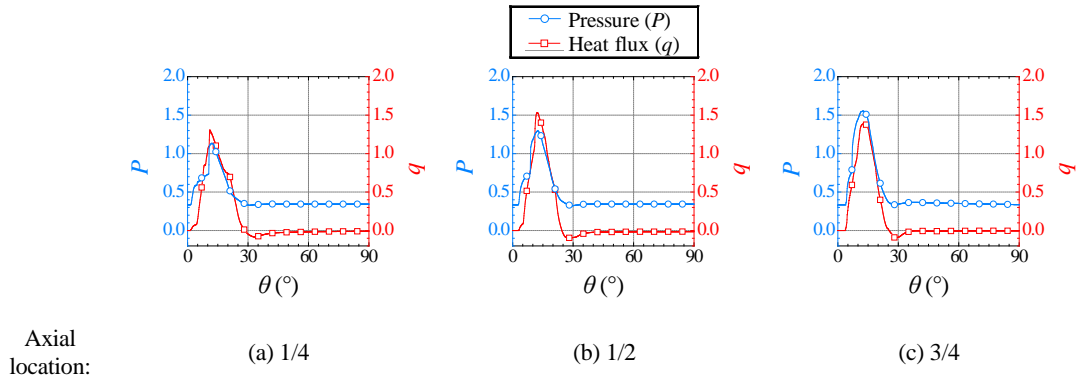
Fig. 3-33 Predicted degree traces of static pressure and heat flux at axial locations 1/4, 1/2 and 3/4
for cell length of 168 mm at default rotation speed



(a) Static pressure

(b) Static temperature

(c) Axial velocity
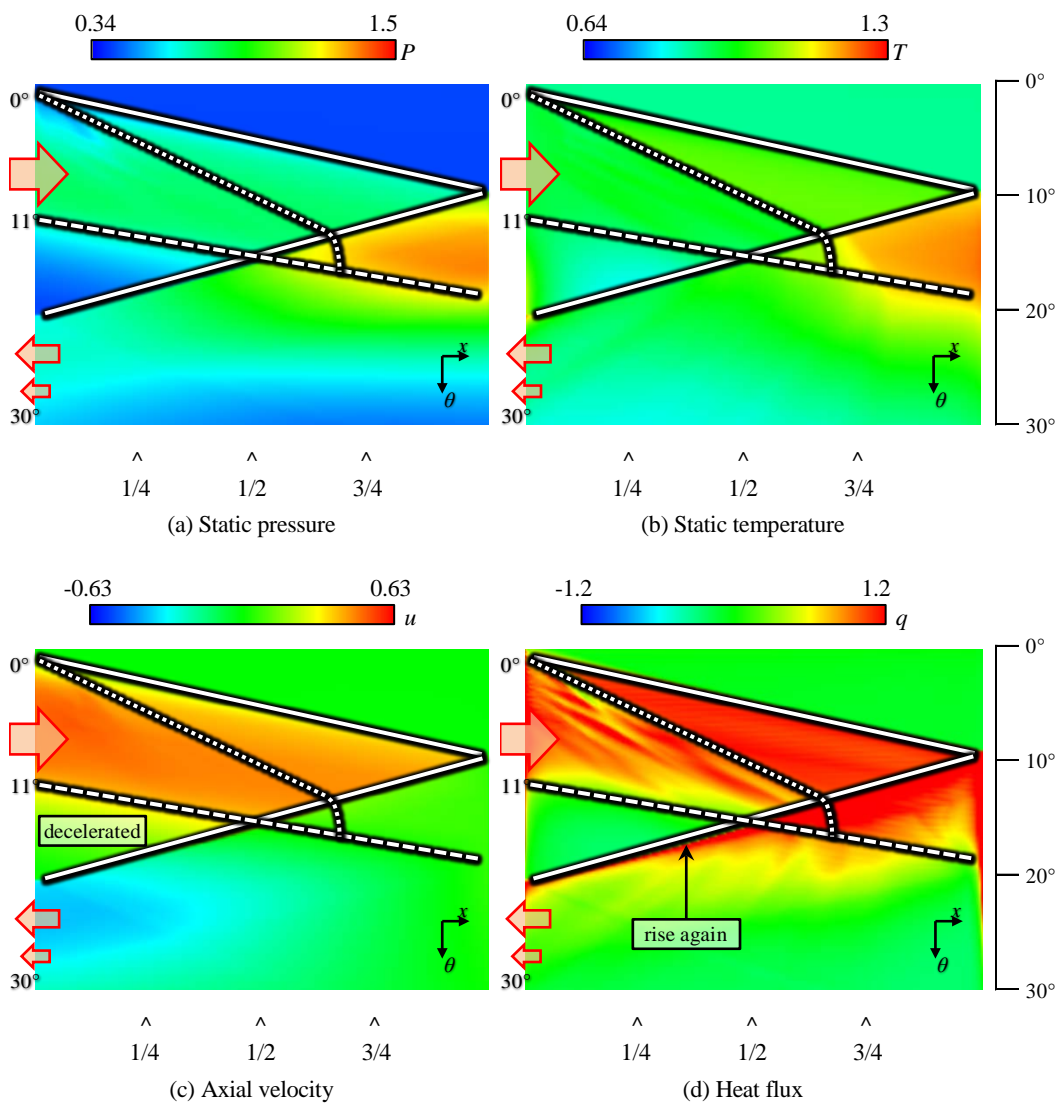
(d) Heat flux

Fig. 3-34 Wave diagrams (0° ~ 30°) of numerical results for 168-mm at doubled rotation speed
(scaled along degree coordinate 5 times for better observation)
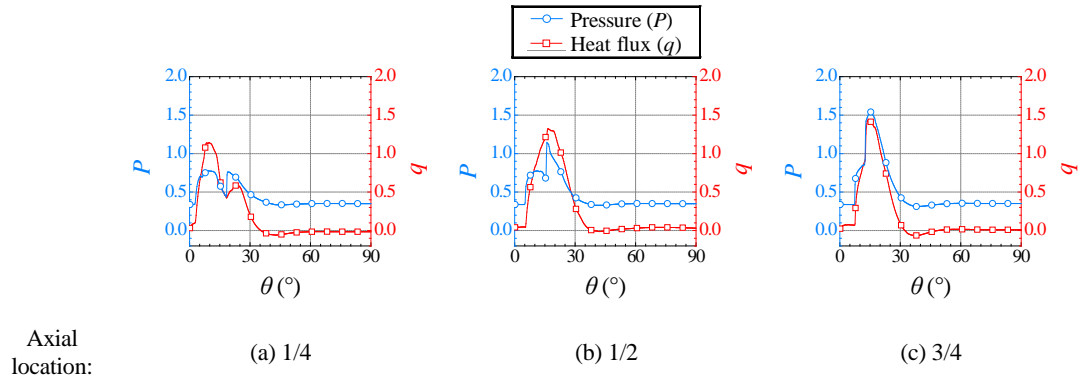
Fig. 3-35 Predicted degree traces of static pressure and heat flux at axial locations 1/4, 1/2 and 3/4
for cell length of <u>168 mm</u> at <u>doubled</u> rotation speed

### 3.4.2 With Respect to 42-mm-Long Cell

As for the shorter cell, the internal flow field is believed to resemble that of the 168-mm-long one at their respective default rotation speeds, and potential differences may correlate with partial opening since in the three dimensions only the axial length is scaled to 1/4. The default rotation speed is 7200 RPM, 4 times that of 168-mm. Therefore, to undergo the same degree, it costs 1/4 of the time required for 168-mm.

Shown in Fig. 3-36 are the wave diagrams for the default rotation speed. The characteristic lines of pressure waves and contact front are drawn in the same manner as in the cases of 168-mm. The characteristic lines are identical to those of 168 mm at default rotation speed, indicating that the propagation speeds of pressure waves and contact fronts do not subject to change across sizes (lengths, exactly). This fact conforms to expectation.

Responses of static pressure and heat flux at the middle of the cell are shown in     Fig. 3-37. Compared with those at axial location 1/2 in 168-mm, it is worth noting that static pressure's increase rate caused by the primary shock wave is greater, conducing to the sharper first rise of static pressure.
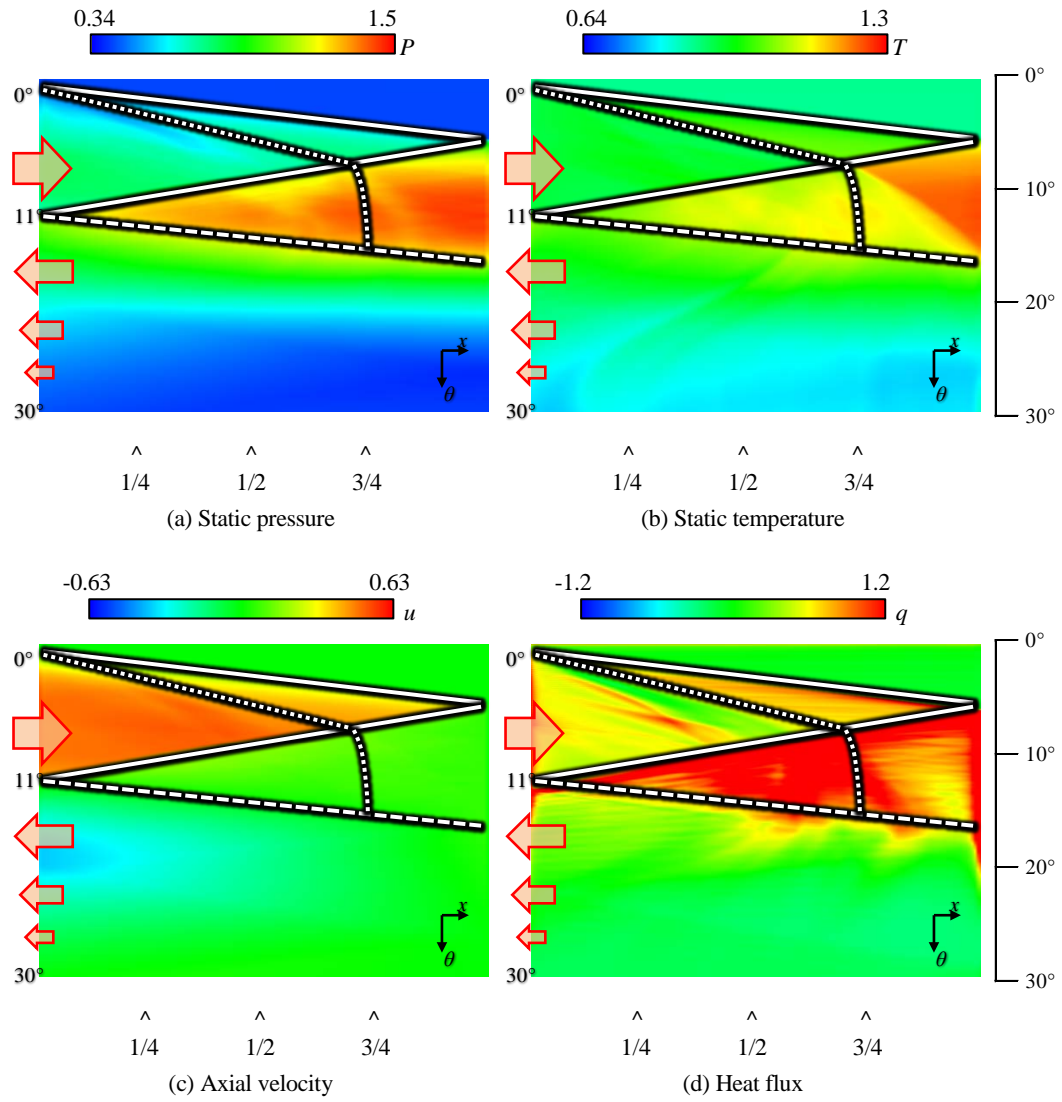
Fig. 3-36 Wave diagrams (0° ~ 30°) of numerical results for <u>42-mm</u> at <u>default</u> rotation speed
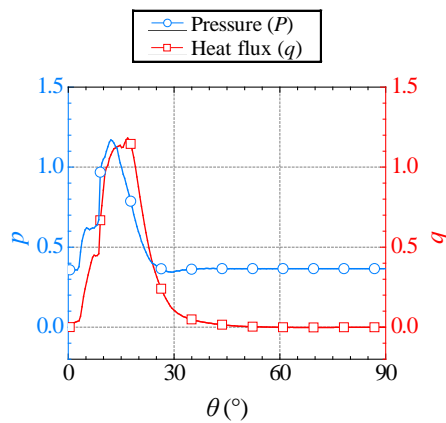


Fig. 3-37 Predicted degree traces of static pressure and heat flux at the middle for cell length of <u>42 mm</u> at <u>default</u> rotation speed

## 3.5    Comparisons between Predicted and Measured Data

The measured histories of static pressure and heat flux are shown in Fig. 3-39 ~ Fig. 3-43 indicated by filled symbols, where the graphical representation of the greatest range of error bar ($\pm 3\sigma$, $\sigma$: standard deviation) is added for experimental results in Fig. 3-39 (a) for static pressure ($3\sigma$ for $P$ is about 0.055) and Fig. 3-40 (a) for heat flux ($3\sigma$ for $q$ is about 0.045). The sampling rate is 2 MHz through the test runs, and such a sampling rate inevitably brings on massive amounts of data. To avoid this inconvenience and for better observation of the trend of measured quantity, the measured data are averaged. Every 100 continuous values of the raw data are averaged into a single value, and the averaged data of several cycles is averaged into one cycle. An example of such a process of averaging is shown in Fig. 3-38. This process maintains the essential features of distinct change in static pressure or heat flux that are intended to be captured and observed in the present experiment, such as the rates of rapid rise and drop of static pressure or heat flux.



(a) An example of raw data of static pressure in 3 cycles        (b) Averaged static pressure history
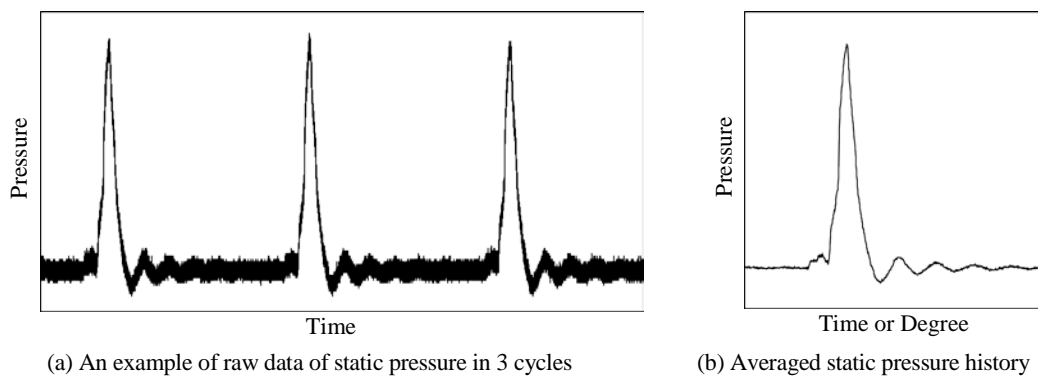
Fig. 3-38 Data reduction

When comparing the numerical results and the experimental results in static pressure (Fig. 3-39, Fig. 3-41, and Fig. 3-43 (a)), it is found that in the rates of rapid rise and decline, as well as in the arrival degrees of shock waves and the starting degree of expansion, the numerical responses and the measured responses of static pressure agree with each other well, suggesting that the flow solver is capable of calculating the internal flow field. Admittedly, it is found that some weak pressure waves travel in the cell after the effective expansion process and cause fluctuation in pressure, and such phenomena are not reflected in the numerical results. Insofar as the present verification focuses on the propagation of shock waves and expansion waves in compression process and expansion process that characterize the unsteady flow field in wave rotor cell, the estimate of flow field is acceptable, as verified by experimental data.

Responses of heat flux sensor in numerical and experimental results are compared in Fig. 3-40, Fig. 3-42 and Fig. 3-43 (b). The gradient of increase during compression caused by shock waves, the rate of decline during expansion caused by expansion waves, and the relatively stable period after expansion process are well simulated. And the numerical results' starting degrees of ascent and descent also closely match corresponding ones in the measured records. The agreement of heat flux demonstrates that the conjugate heat transfer thermal boundary treatment is adequate for the heat transfer related to wave-rotor-like flow field. Theses comparisons at cell lengths of 168 mm and 42 mm show the present code's capability of calculating wave-rotor-like flow field and associated heat transfer at different sizes.

As a conclusion of this chapter of groundwork for heat transfer analysis of wave rotor cell, the proposed numerical method is sufficient for the present investigation on wave-rotor-like internal flow field and heat transfer. Therefore, it is rational to employ this method to study heat transfer effects for wave rotors.
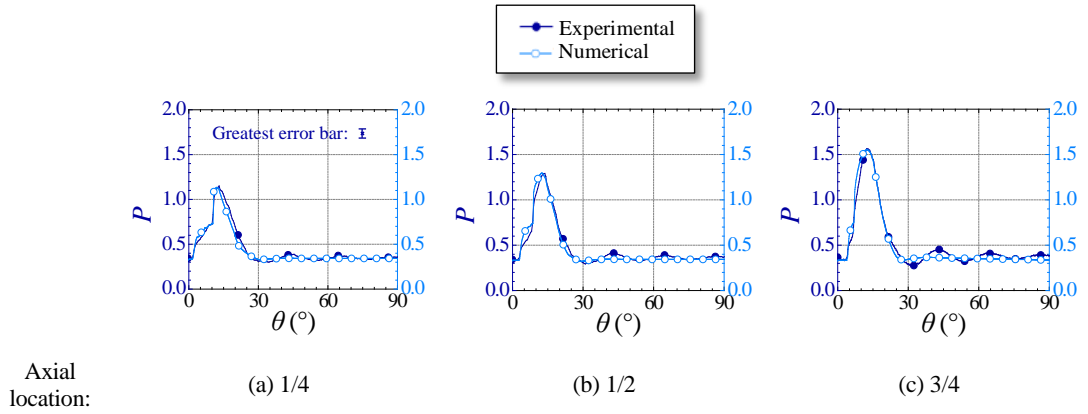
Fig. 3-39 Comparisons of static pressure between numerical and experimental results for cell length of 168 mm at default rotation speed
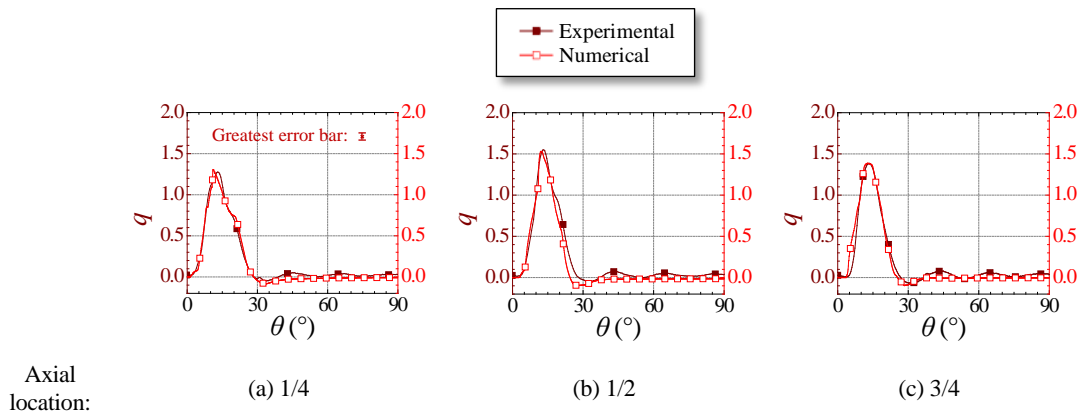


Fig. 3-40 Comparisons of heat flux between numerical and experimental results for cell length of 168 mm at default rotation speed
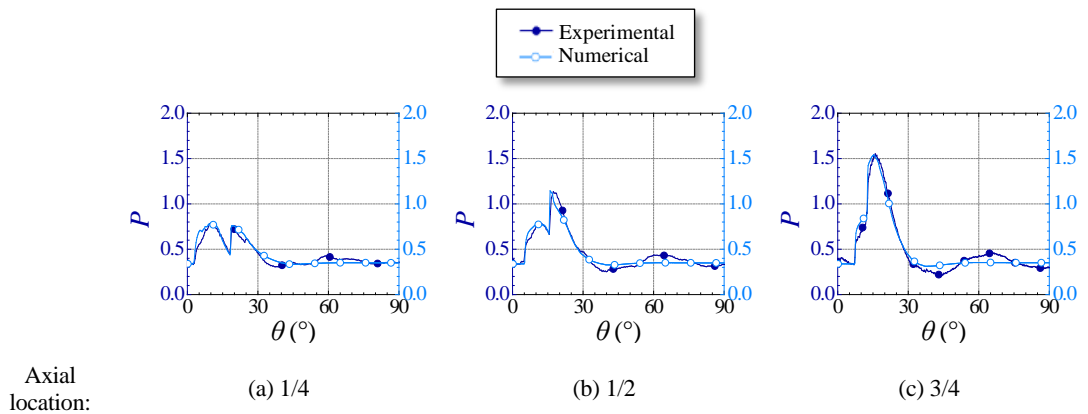


Fig. 3-41 Comparisons of static pressure between numerical and experimental results for cell length of 168 mm at doubled rotation speed
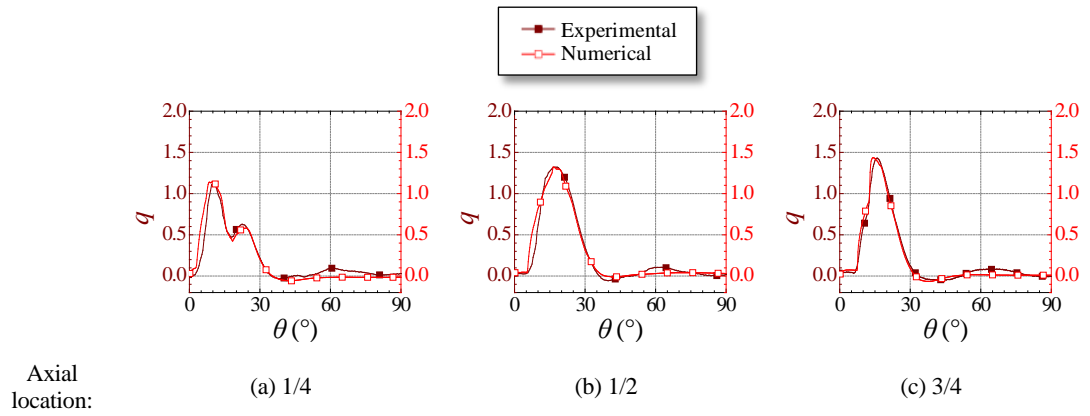
Fig. 3-42 Comparisons of heat flux between numerical and experimental results for cell length of
168 mm at doubled rotation speed



(a) Pressure          (b) Heat flux
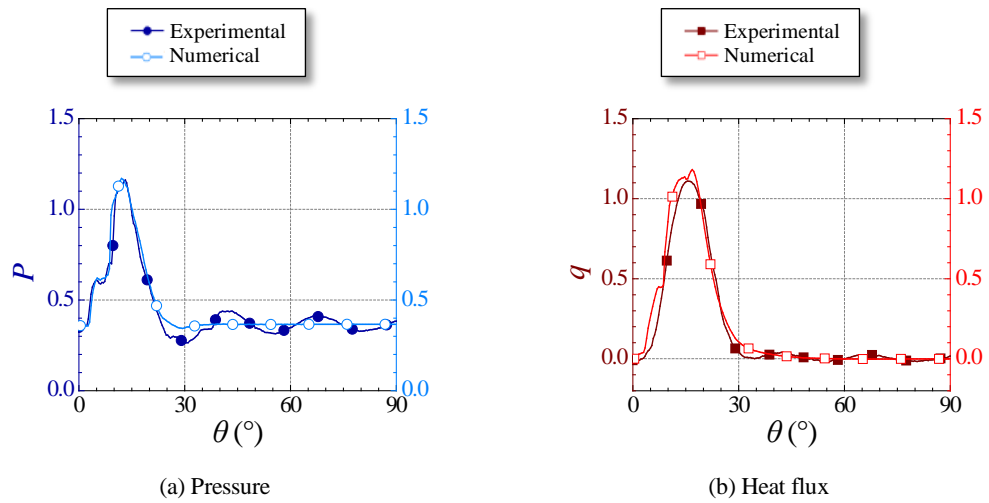
Fig. 3-43 Comparisons of static pressure and heat flux between numerical and experimental results
for cell length of 42 mm at default rotation speed

## CHAPTER 4: RESULTS AND DISCUSSION

### 4.1    Physical Model

#### 4.1.1    Cell

Wave rotor cells of five different sizes are investigates for comparison across size. The 69-mm-long cell of the micro wave rotor [10], [36], [39] is introduced as the 1X size. Designed to be integrated into the micro gas turbine of kilowatt-level output, the constant section straight cell is 69 mm in axial length and the midspan diameter is 47.0 mm. It is assumed that the compression ratio of the baseline gas turbine is 3.0, the total temperature at the compressor exit is 440 K and the mass flow rate from the compressor (through AL port to wave rotor) is about 20 g/s [36]. For dimension simplicity, the wall enveloping the flow passage has a uniform thickness of 1 mm. The remaining four sizes are scaled geometrically. The size information is presented in Table 4-1, and the dimension parameters are defined in Fig. 4-1. To deliver a prompt and efficient overview of the scales of these cells, Table 4-2 enumerates the hydraulic diameter ($D_H$) and surface-area-to-volume ratio ($A/V$) for each of the sizes involved. Apparently, both $D_H$ and $A/V$ are inversely proportional to scale. In the present study, 10X size and 3X size are artificially placed in the category of conventional sizes of wave rotor cell that are enumerated in Table 1-1, in which heat transfer effects may be insignificant. On the other hand, 1X size, 1/3 size and 1/10 size are categorized as small wave rotor cells since they are equal to or smaller than the "small size" cell in Table 1-1. 1/10 size is the smallest size in the present investigation, at which the most profound effects of heat transfer is expected to be observed. Through comparing among the sizes from 10X to 1/10, the trend of heat transfer effects as size reduces can be obtained.

Accordingly, rotation speed rises as size reduces. The rotation speeds for 10X, 3X, 1X, 1/3 and 1/10 are 3100 RPM, 10050 RPM, 30000 RPM, 88000 RPM and 264000 RPM, respectively.

Respecting the wall, the material properties of AISI 304 stainless steel are introduced as wall properties, and the related parameters are listed in Table 4-3. The four sides of wall are named as front, back, shroud and hub, respectively (Fig. 4-1). The boundary conditions for wall are illustrated in Fig. 2-5, in which the external surfaces of shroud and hub subject to adiabatic boundary condition for Section 4.2 or constant convective heat transfer for Section 4.3, and the external surfaces of front and back subject to adiabatic boundary condition for Section 4.2 or periodic condition for Section 4.3.



|                    |                                    |
|--------------------|------------------------------------|
| (a) Array of cells | (b) Constant cross-section of single cell |
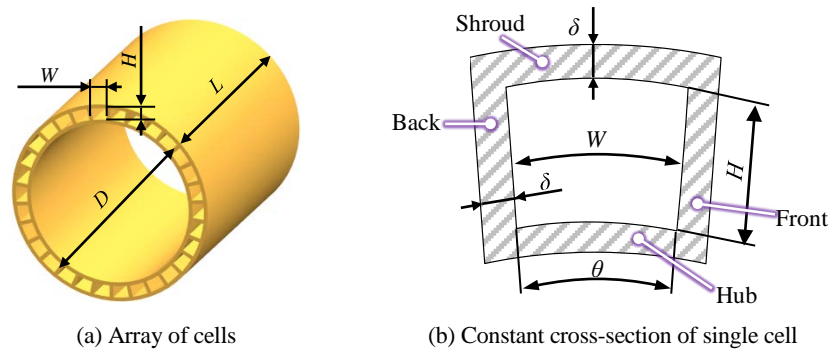
Fig. 4-1 Definitions of dimensions of cell

Table 4-1 Dimensions relating to the cells

| Parameter | | Size | | | | | Unit |
|-----------|---|---|---|---|---|---|------|
| | | Conventional size | | Small size | | | |
| | | 10X | 3X | 1X | 1/3 | 1/10 | |
| Midspan diameter | $D$ | 470 | 157 | 47.0 | 15.7 | 4.70 | mm |
| Cell length | $L$ | 690 | 230 | 69.0 | 23.0 | 6.90 | mm |
| Cell internal midspan width | $W$ | 39.2 | 13.1 | 3.92 | 1.31 | 0.392 | mm |
| Cell internal height | $H$ | 30.0 | 10.0 | 3.00 | 1.00 | 0.300 | mm |
| Cell internal degree | $\theta$ | 9.56 | 9.56 | 9.56 | 9.56 | 9.56 | ° |
| Cell wall thickness | $\delta$ | 10.0 | 3.33 | 1.00 | 0.333 | 0.100 | mm |

Table 4-2 Hydraulic diameters and surface-area-to-volume ratios of cells

| | | Cell hydraulic diameter $D_H$ (mm) | Surface-area-to-volume Ratio $A/V$ (mm$^{-1}$) |
|---|---|---|---|
| Conventional size | 10X | 34.3 | 0.118 |
| | 3X | 11.4 | 0.392 |
| Small size | 1X | 3.43 | 1.18 |
| | 1/3 | 1.14 | 3.53 |
| | 1/10 | 0.343 | 11.8 |

Table 4-3 Material properties of wall solid

| Parameter | | Value | Unit |
|-----------|---|-------|------|
| Thermal conductivity | $k_s$ | 25 | W/(m·K) |
| Density | $\rho_s$ | 8000 | kg/m$^3$ |
| Specific heat | $c_{p,s}$ | 500 | J/(kg·K) |

## 4.1.2 Ports

For the four-port through-flow wave rotor, in which the flow goes through the cell from one end to the other (from left to right in this work), the ports shown in Fig. 4-2 are classified as charging ports on the left side and discharging ports on the right side. As the cell rotates clockwise around the axis, the left end of cell opens to GH and AL ports, and the right end opens to AH and GL ports sequentially. Every 180° finalize a wave rotor cell. That is, the cell goes through two wave rotor cycles for each revolution of the rotor, i.e. 2 cycles per revolution. Slight degree adjustments are applied in 1/3 size and 1/10 size in accordance with flow field difference due to the effect of viscosity in downsized cells. The starting degrees of opening and shutting are listed in Table 4-4.

The conditions in each port enumerated in Table 4-5 are assumed to be constant. The values are normalized by corresponding ones in AL port ($P_{port,tot} = 0.30$ MPa and $T_{port,tot} = 440$ K) since AL port is

the beginning point "1" where the wave rotor starts to function in thermodynamic cycle of wave rotor topping gas turbine (Fig. 1-3).



(a) Left side  (b) Right side
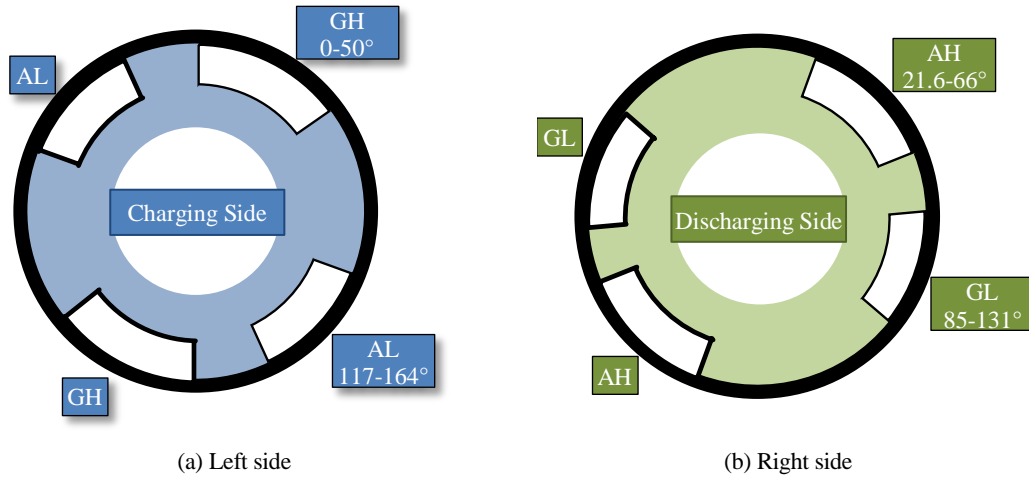
Fig. 4-2 Port positions and degrees of 1X size

Table 4-4 Port degrees (starting opening or shutting)

| | | Size | | |
|---|---|---|---|---|
| | | 10X, 3X & 1X | 1/3 | 1/10 |
| GH | open | 0.00 | 0.00 | 0.00 |
| | shut | 50.0 | 50.0 | 49.0 |
| AL | open | 117 | 117 | 118 |
| | shut | 164 | 166 | 166 |
| AH | open | 21.6 | 22.0 | 21.6 |
| | shut | 66.0 | 66.6 | 66.0 |
| GL | open | 85.0 | 81.0 | 80.0 |
| | shut | 131 | 128 | 128 |

Table 4-5 Normalized port conditions

| | | Charging ports | | Discharging ports | |
|---|---|---|---|---|---|
| | | GH | AL | AH | GL |
| Total pressure [*] | $P_{port,0}$ | 3.1 | 1.0 | 3.4 | 1.2 |
| Total temperature [*] | $T_{port,0}$ | 2.8 | 1.0 | 2.1 | 2.2 |

[*] Normalized by total pressure in AL of 0.30 MPa or total temperature in AL of 440 K

### *4.1.3    Clearance Gap and Surroundings*

The pressure and temperature of surroundings connected with the clearance gap are the same to those in AL port of the lowest pressure among ports. The fluid in the surroundings is assumed to be motionless.

The axial width of clearance gap is constantly 0.1 mm for 1X size, in accordance with the design parameter in a previous study [39]. And definitely, the width for other size is scaled geometrically.

### *4.1.4    Summary of Simplifications and Assumptions for Single Cell*

Firstly, flow in each of the ports is assumed to be constant – steady in time and uniform in space. Circumferential velocity of port flow equals linear velocity of rotating cell. In addition, the effect of inflow blockage is neglected.

Besides, a single cell does not interact with its neighbor cell. The flow is assumed to be turbulent.

In relation to leakage, flow speed in the surroundings is assumed to be zero, and the walls associated with clearance gap – the end wall and the surfaces of cell ends (Fig. 2-5 (b)) – are regarded as adiabatic.

Last but not least, material properties in wall solid are constant, and wall thickness is uniform all around.

## 4.2    Externally Insulated Cases

Five phases comprise this section. First of all, the adiabatic flow field of 1X size is explained, which does not include heat transfer and shows the essential characteristics of the unsteady flow field. Besides, under adiabatic boundary condition, flow fields of scaled sizes are presented to explain the characteristics of flow field excluding heat transfer effects.

Secondly, regarding heat transfer, 1) causes of intense heat transfer are analyzed, 2) heat transfer effects on internal flow field, charging and discharging are explicated, and 3) heat transfer effects across sizes and the trend as size reduces will be summarized.

Finally, the effect of applying an acquired average wall temperature to the lateral boundaries of flow passage is discussed.

### *4.2.1    Adiabatic Cases*

### *4.2.1.1    1X Size*

As a baseline treatment for the wave rotor of 1X size, adiabatic boundary condition is applied on the lateral surfaces of the fluid passage. The midspan surface and the meridional surface are illustrated in Fig. 4-3, and shown in Fig. 4-4 and Fig. 4-5 are the degree sequences of total pressure distributions on midspan surface and on meridional surface, respectively. Pressure parameters in this chapter are normalized by the total pressure in AL port of 0.30 MPa. The locations of primary and reflected shock waves are identified and marked with orange color triangles. After the duration of charging from GH port

comes to an end, right-going expansion waves induced by shutting the left end cause pressure reduction in the cell. Opening to GL port causes expansion waves traveling leftwards in the cell and further reducing the pressure. After discharging to GL port is completed, the observable locations of the compression wave induced by shutting the right end are marked with yellow triangles.

The temperature distributions on midspan surface and meridional surface at selected degrees are shown in Fig. 4-6 and Fig. 4-7, respectively. Temperature parameters in this chapter are normalized by the total temperature in AL port of 440 K. Together with velocity vectors, it is also possible to identify several locations of shock wave, although relatively obscure compared with those on pressure contours. Furthermore, the contact front between gas and air can be observed in these 3-D contours. In Fig. 4-6, owing to gradual opening, the shape of the planar distribution of the hot gas colored in red in the first cell opening to GH port is found to be complex. The twisted contact front is prolonged as it travels rightwards. The axial length relating to the contact front is marked with trapezoid above each contour. The fresh air charged from AL port also creates a twisted contact front propagating in the cell. On the meridional surface in Fig. 4-7, the fresh air is found to gather in the upper side, i.e. the radially further side, because of rotation. Fluid of greater density (lower temperature) tends move to radially further position due to centrifugal force. This phenomenon has been addressed in meteorology [86] and in a previous study about temperature boundary condition for wave rotor cell [50]. It can be inferred from the contact fronts on the midspan surface and the meridional surface that the contact fronts are warped in 3-D space.

The axial velocity distributions on midspan surface and meridional surface are shown Fig. 4-8 in and Fig. 4-9, respectively. In the first cell opening to GH port, the dramatic variation of flow speed indicates clearly where the primary shock wave is located. Then, as the reflected shock wave propagates leftwards, the rightward movement of fluid is prohibited. The propagations of pressure waves can be observed as clearly as in pressure contours.

At each degree, one-dimensional flow field can be obtained by averaging the three-dimensional flow field on each of the cross-sections. By piling up the axial distributions of one-dimensional flow field in order of degree, contours in Fig. 4-10 (a) ~ (c) are generated. The end walls are also drawn as black blocks next to the contours, between each vertical pair are blank area representing opening span for GH, AL and AH, GL ports. Each of the opening spans is adjusted according to the degrees starting opening or closing listed in Table 4-4. In the upper half on each of the contours, convergent contour lines extended from the top-left corner to lower right, and then to lower left are plainly visible. Referring to the designed wave diagram for the 1X size depicted in Fig. 4-10 (d), it is confirmed that the convergent contour lines indicate the propagation of the primary shock wave (PSW) and the reflected shock wave (RSW). In the same manner, the compression wave (CW) can also be located on the total pressure and the axial velocity contours (Fig. 4-10 (a) and (c)), obscure on the total temperature contour (Fig. 4-10 (b)), though. Expansion waves do not form steep gradient, but the head of an expansion fan can be found on the contours that connecting the lower sides of GH and AH ports. The other one extended from the top side of GL port to lower left can be seen on the total pressure and the axial velocity contours. Both correspond to the characteristic lines of expansion waves (EW) in the schematic wave diagram. In regard to contact front, the dotted lines in Fig. 4-10 (d) denote the characteristic lines of contact front. As has been addressed, contact fronts of complex shape develop in the cell, and the non-uniform profiles on cross section of 3-D flow field lead to relatively widely separated contour lines between fluids of different temperatures on the contour for total temperature (Fig. 4-10 (b)).

By depicting the characteristic lines on contours and removing the contour lines for clear observation, wave diagrams shown in Fig. 4-11 are obtained. Since the contact fronts between gas and air are ambiguous, approximate characteristic lines of contact fronts are depicted. The characteristic lines of

contact fronts are located at approximate positions between the region almost occupied by gas and the region almost occupied by air. Besides, each of the characteristic lines of expansion waves indicates locations a little behind the head of expansion fan (about 5%~10% of pressure ratio of expansion fan). With these wave diagrams in a pellucid style, the development of flow field discussed in this sub-section is easier to observe. Admittedly, conversion from 3D flow field to 1D would lead to information loss of 3D distributions, especially for temperature since its 3D distribution is so noticeable that wave diagram cannot reveal the actual contact front between cold air and hot gas but just displays the regions containing contact front like gradual change of temperature. Therefore, as this downside of discussing by one-dimensionalized distributions make it insufficient to explain some of the phenomena involved in the present research, it is necessary, on occasion, to return to the 3D temperature field for some truth.

According to the analyses of 3-D flow field and its 1-D appearances with schematic wave diagram, it can be concluded that the flow field in the numerical simulation develops as designed in adiabatic case.
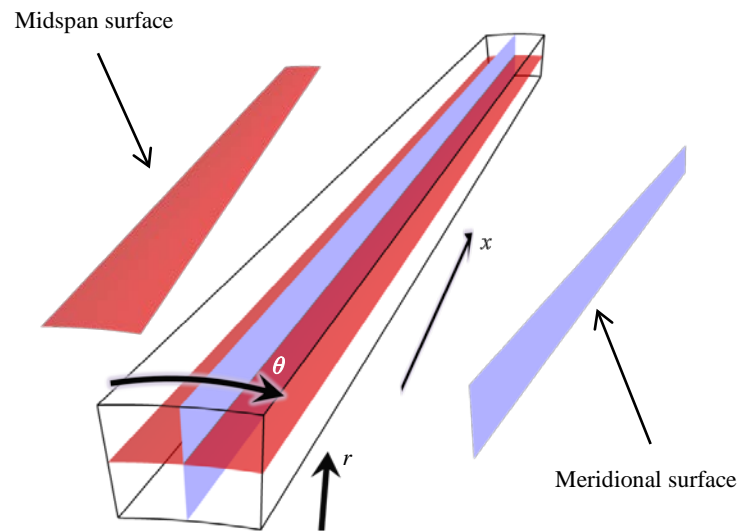


Fig. 4-3 Perspective drawings of midspan and meridional surfaces
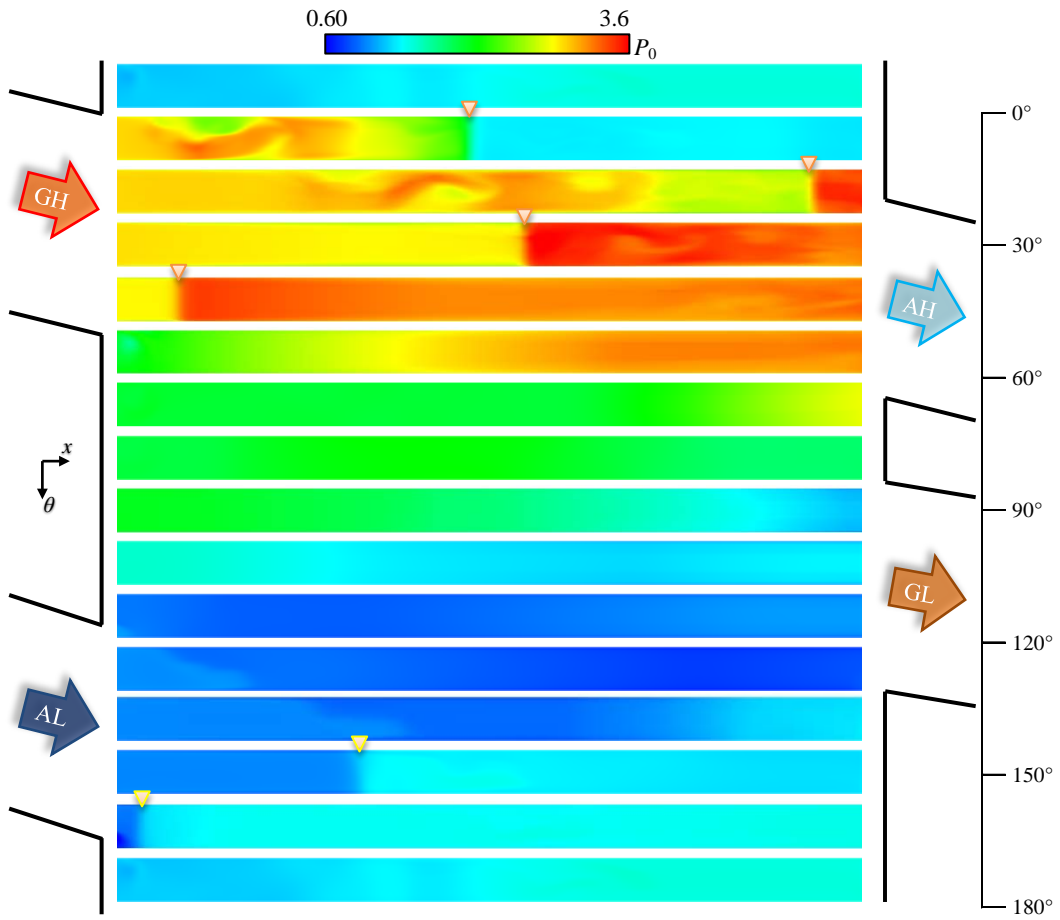
Fig. 4-4 Degree series of <u>midspan</u> total <u>pressure</u> distributions for adiabatic case of 1X size
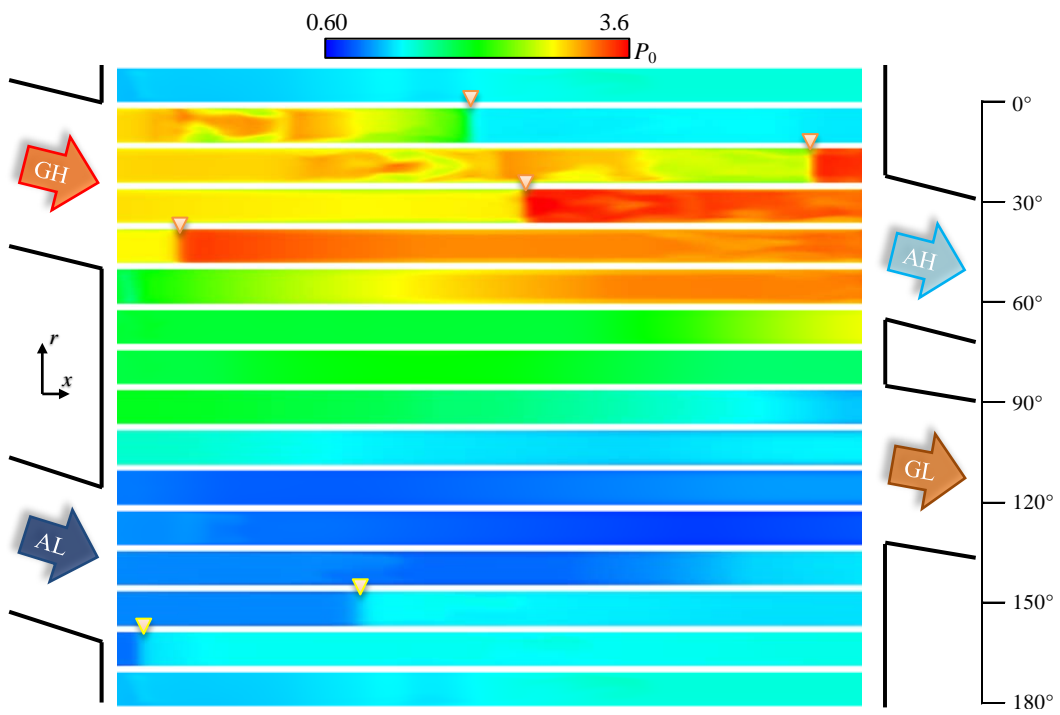


Fig. 4-5 Degree series of <u>meridional</u> total <u>pressure</u> distributions for adiabatic case of 1X size
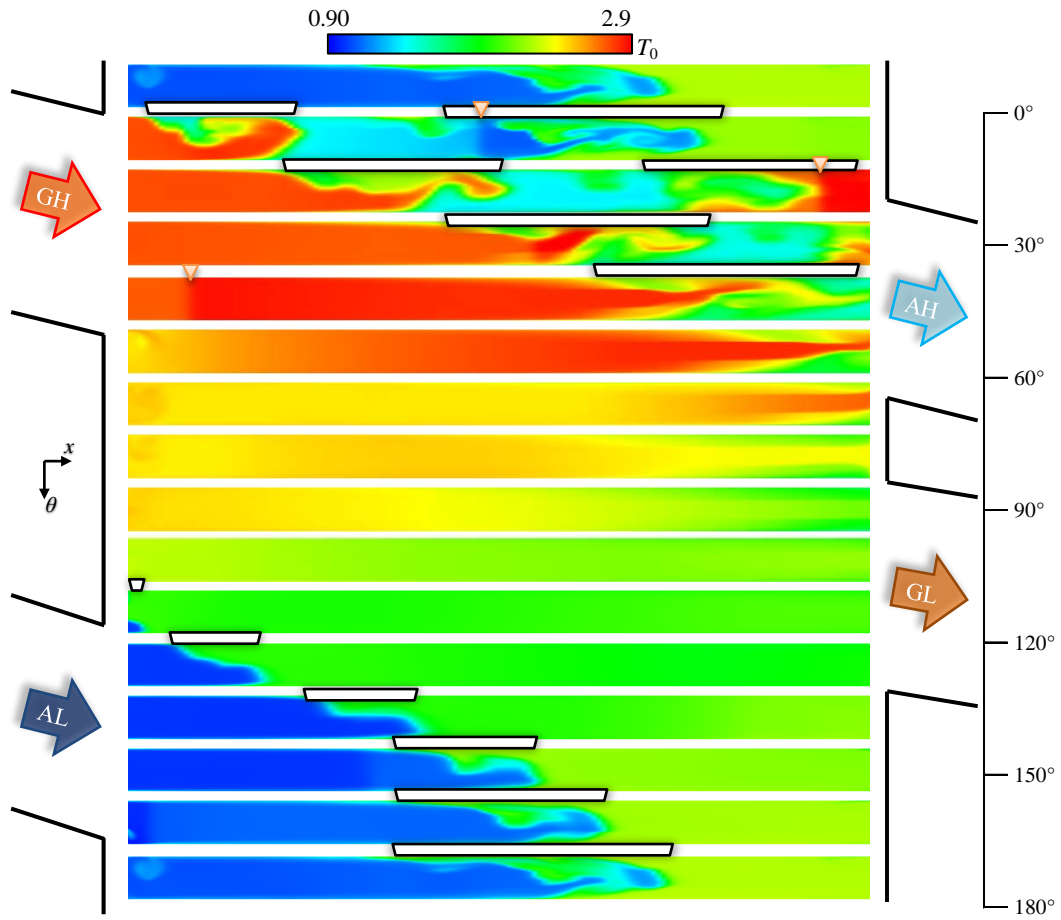
Fig. 4-6 Degree series of <u>midspan</u> total <u>temperature</u> distributions for adiabatic case of 1X size
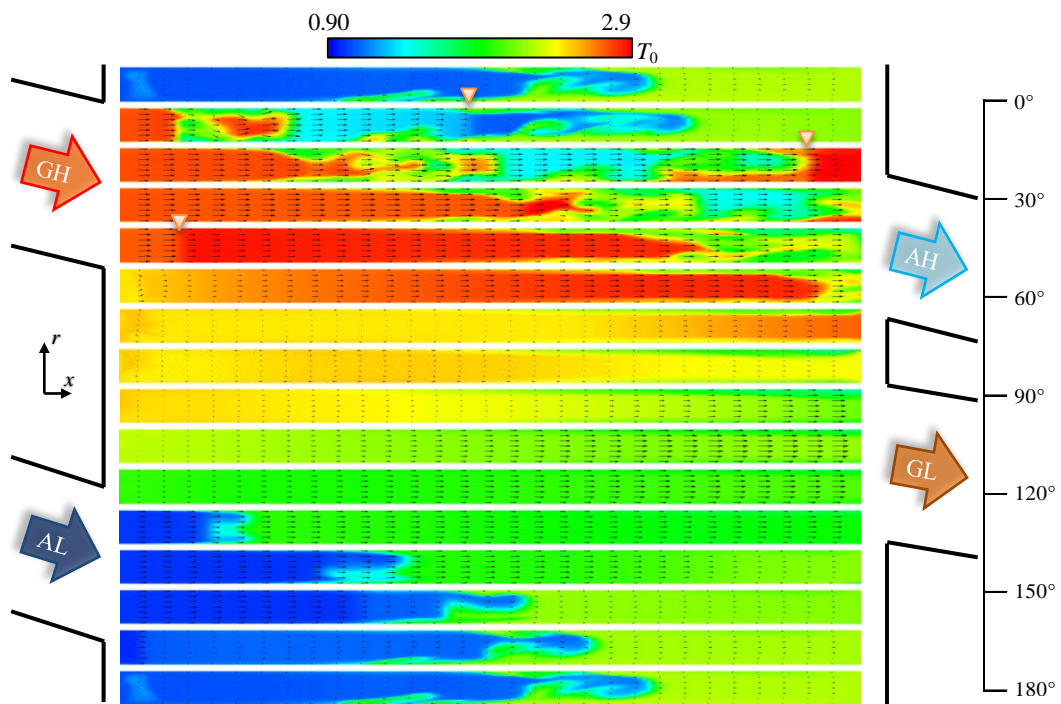


Fig. 4-7 Degree series of <u>meridional</u> total <u>temperature</u> distributions for adiabatic case of 1X size
(with velocity vectors)
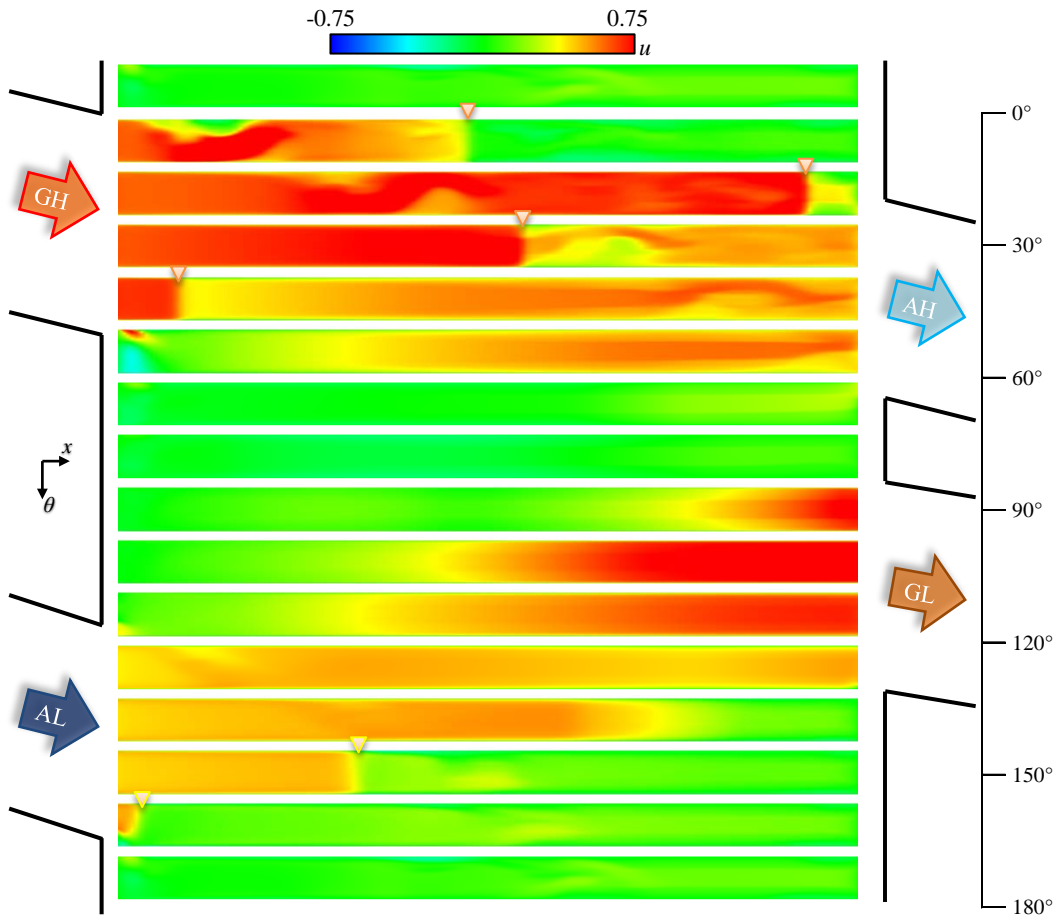
Fig. 4-8 Degree series of <u>midspan</u> axial <u>velocity</u> distributions for adiabatic case of 1X size
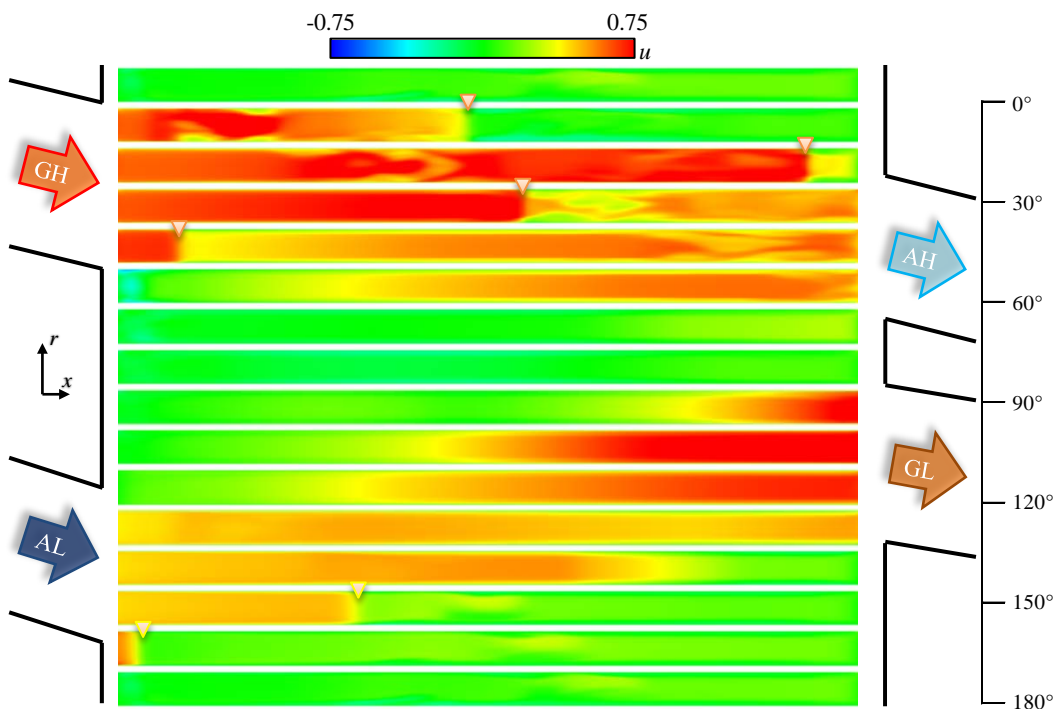


Fig. 4-9 Degree series of <u>meridional</u> axial <u>velocity</u> distributions for adiabatic case of 1X size

0.60        3.6  $P_0$

(a) Total pressure

0.90        2.9  $T_0$

(b) Total temperature

-0.75       0.75  $u$

(c) Axial velocity

(d) Schematic wave diagram
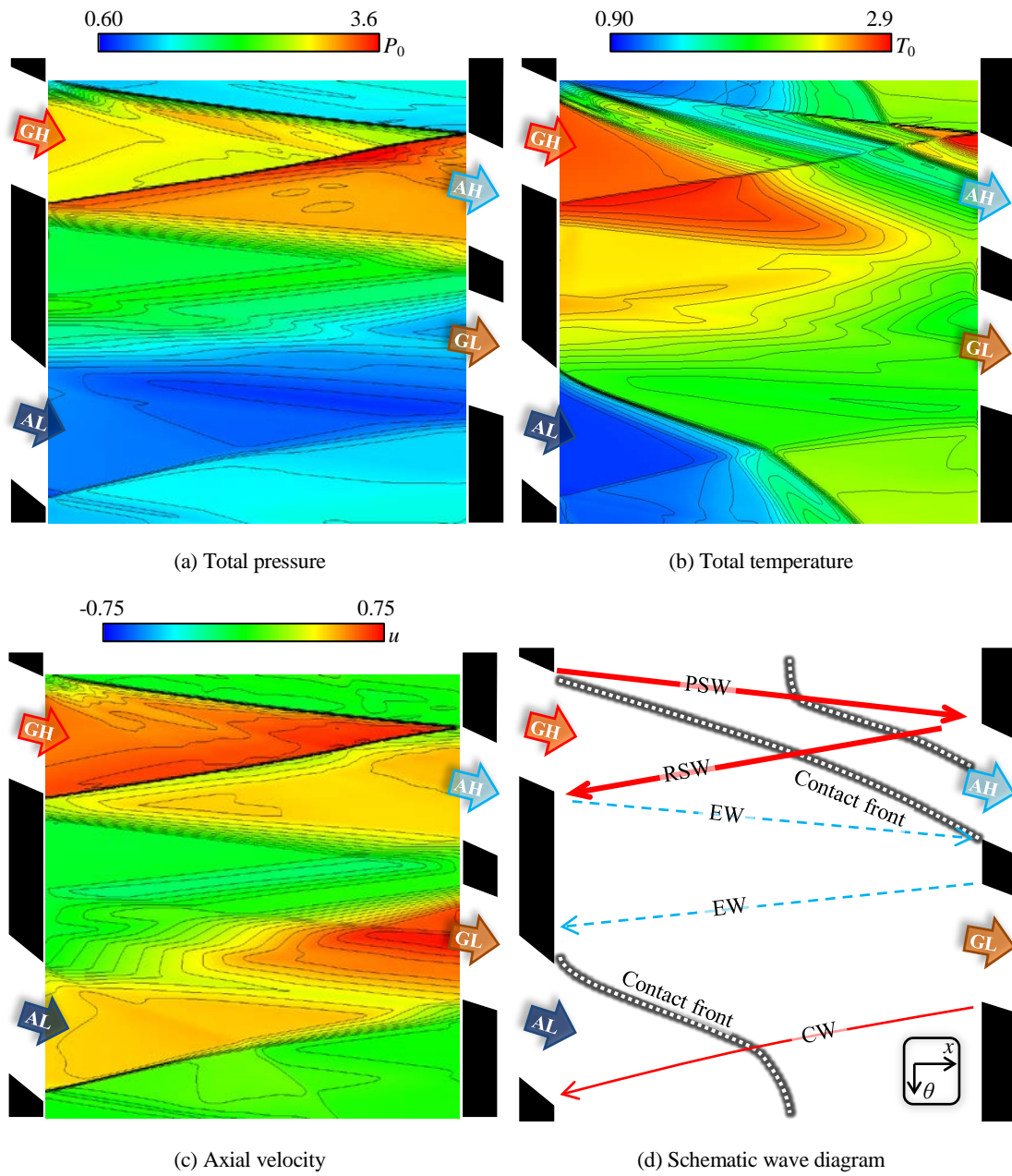
Fig. 4-10 Contours and schematic wave diagram for adiabatic case of 1X size

(PSW: primary shock wave; RSW: reflected shock wave; EW: expansion wave; CW: compression wave)

(a) Total pressure

(b) Total temprature

(c) Axial Velocity
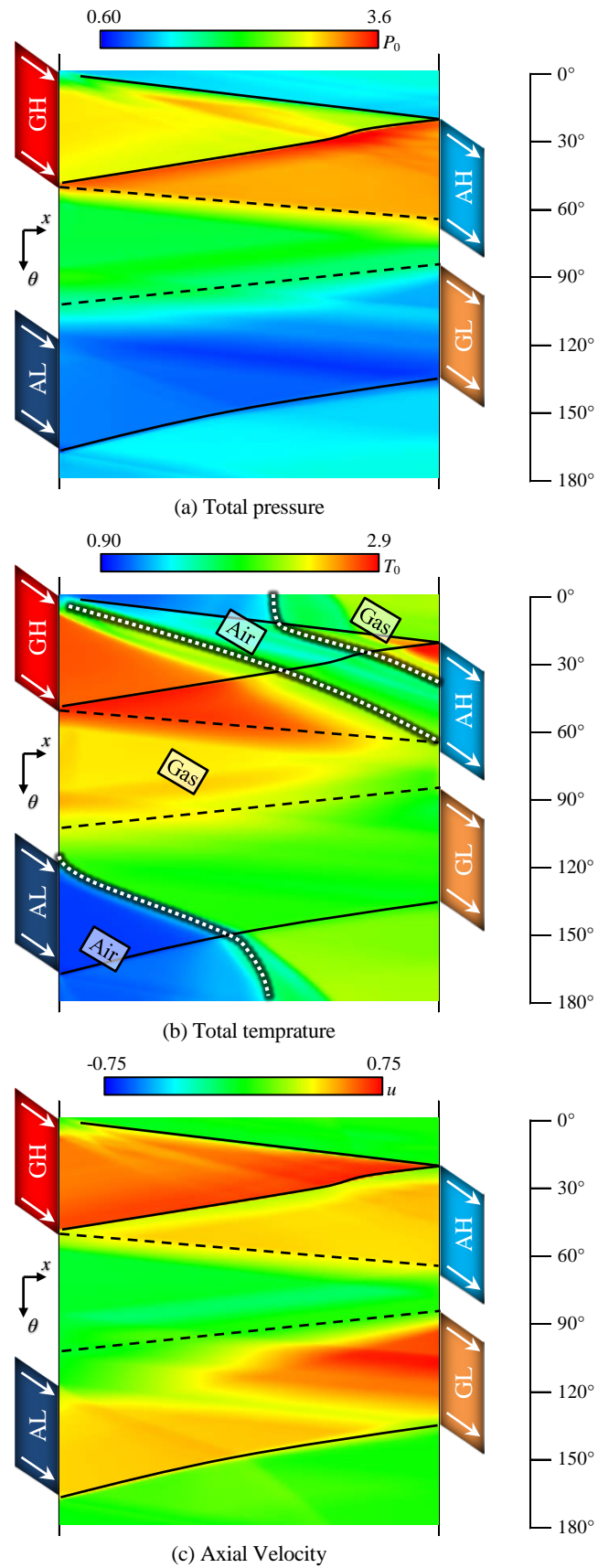
Fig. 4-11 Wave diagrams with depicted characteristic lines for <u>adiabatic</u> case of <u>1X</u> size

*4.2.1.2    Scaling*

In Subsection 4.1.1, rotation speeds at various sizes are mentioned. Obviously, rotation speed is not inversely proportional to size. It was guessed that for 1X wave rotor rotates at 30000 RPM, 1/10 size rotates at 300000 RPM and 10X size rotates at 3000 RPM. In Subsection 4.1.2, it is mentioned that port degrees are adjusted for small sizes. Although heat transfer is not considered when adiabatic boundary condition is applied, rotation speed and port degrees subject to change when cell is geometrically scaled, because some other factors (e.g. viscosity) potentially affects propagation of pressure waves even though cell is proportionally resized and rotation speed is proportionally adjusted. In consistence with the design concept of wave rotor that pressure waves should arrive at cell ends on time, rotation speed and / or port degrees need to be accommodated to pressure wave arrivals, especially to arrival timings of shock waves. Then, with the slightly adjusted designs at different sizes that have taken other factors into account, it is possible to study the sole effects of heat transfer.

For example, the wave diagrams for adiabatic cases related to 10X size and 1/10 size are exhibited in Fig. 4-22 and Fig. 4-33, in which the propagation of pressure waves and contact fronts can be seen. Primary shock wave arrives when the right end starts to open to AH port, and reflected shock wave arrives when the left ends starts to shut. All the characteristic lines behave as designed in Fig. 4-10 (d).

*4.2.2    Causes of Intense Heat Transfer*

After several calculation cycles, limit cycle (explanation of limit cycle is presented in Section 2.5) is reached that the flow field and the wall temperature virtually varies cyclically, and the results will be discussed. When heat transfer is considered for wave rotor cell, a first necessity is to delve into heat flux across the fluid-solid interface. In order to explore the characteristics of heat flux common in all scales, regions and causes intense heat transfer of 10X size are explained firstly. Secondly, concerning the characteristics only considerable in small sizes, the characteristics of intense heat flux in 1/10 size are presented.

*4.2.2.1    10X Size*

The temperature distribution on the interface surfaces (internal surfaces of wall) at $\theta = 0°$ is shown in Fig. 4-12, the temperature in which is normalized by total temperature in AL port of 440 K (and the same below for wall temperature). In addition, the temperature distribution on the external surfaces of wall at $\theta = 0°$ is shown in Fig. 4-13. From either temperature distribution it is easy to obtain an overview where the relatively hot zones are located: hub side and left side (left near inlet ports GH and AL while right near outlet port AH and GL). Temperature distributions on selected cross-section surfaces are shown in Fig. 4-14. Consistent with those relatively hot zones in temperature distributions on internal and external surfaces of wall, axial 15% position is relatively hot and hub side on each of the cross-section surfaces is hotter than corresponding shroud side. At several degrees, temperature distributions on meridional surface and midspan surface are shown in Fig. 4-15 with temperature distributions on the cross-section surfaces, where different legend ranges for fluid and wall should be noticed. For these moments, contact front between fluids of different temperatures is twisted, and it can be found that colder fluid inclines to occupy the shroud side (upper side) on meridional surface and on cross-section surface. To find out the relationship between fluid and wall temperatures, on the selected cross-section surfaces, two points in flow domain are picked to represent fluid close to hub side (lower side) or shroud side (upper side), denoted by "Fluid pt1" and "Fluid pt2" in Fig. 4-17 (b). Meanwhile, the wall temperature on shroud side internal surface is averaged into shroud wall temperature $T_{\text{shroud}}$ on each cross-section, as is illustrated in Fig. 4-17 (a). Similarly, hub wall temperature $T_{\text{hub}}$ is obtained for each cross-section, and $T_{\text{shroud}}$, $T_{\text{hub}}$, $T_{0,\text{Fluid pt1}}$ and $T_{0,\text{Fluid pt2}}$ in a wave rotor cycle are shown in Fig. 4-18 for the selected cross-sections. In

general, total temperature at Fluid pt1 is higher than that at Fluid pt2. This explains higher temperature in hub than in shroud.

Furthermore, for each of the four sides of the wall (defined in Fig. 4-1 (b)), the temperature on the internal surface of wall (conjugate interface in Fig. 2-11, also "intf." in Fig. 2-7) is averaged at each of the axial locations, and the axial distributions of wall internal surface temperature in four wall sides are shown in Fig. 4-19 (b). Temperature related to wall is always normalized by total temperature in AL port ($T_{port,tot}$ = 440 K). The wall internal surface temperature in four wall sides is further averaged into $T_w$ (Fig. 4-17 (b)) and the axial distribution of $T_w$ is shown in Fig. 4-19 (a). To simplify, "wall temperature" denotes this average wall inner surface temperature $T_w$ in the remaining discussions. The oscillation of wall temperature in a wave rotor cycle is very limited (< 10 K or < 0.022 in dimensionless value, Fig. 4-20), therefore, it is reasonable to select wall temperature at any degree to stand for the wall temperature of numerical result. It is confirmed in Fig. 4-19 (a) that relatively higher temperature is located in the left half, and in Fig. 4-19 (b) that hub temperature is higher than shroud temperature. As has been explained in Subsection 4.2.1, under rotation, centrifugal force helps fluid of greater density (or lower temperature under the same pressure) gather in radially further region, and this causes lower temperature in shroud side.

A quick calculation is performed to check the development of thermal boundary layer by using the following equations for turbulent boundary layer over a flat plate [87]

velocity boundary layer thickness $\qquad \delta = \dfrac{0.37x}{\mathrm{Re}_x^{1/5}}$ $\hfill$ (4.1)

thermal boundary layer thickness $\qquad \delta_T = \delta$ $\hfill$ (4.2)

For the moment when the inflow in the left half has developed adequately, the midspan temperature is shown in Fig. 4-16 (a), and the temperature distribution along circumferential direction (y) at axial 30% position on the midspan is exhibited in Fig. 4-16 (b), where the relative thermal boundary layer thickness $\delta_T/Width$ is measured as 0.09~0.1. $\delta_T/Width$ estimated by Eq. (4.1) & (4.2) is 0.096. The thermal boundary thickness is regarded as reasonable in numerical simulation.

The heat transfer processes, which consist of heating and cooling, are shown in the wave diagram for heat flux (Fig. 4-21). Cold color or negative heat flux means that fluid is heated by wall, whereas warm color or positive heat flux means fluid loses heat and wall is heated. The wave diagrams colored in total pressure, total temperature and axial velocity for adiabatic case and for heat transfer case are shown in Fig. 4-22 and Fig. 4-23, respectively. For detailed examination of the wave diagrams, the axial distributions at selected degrees are shown in Fig. 4-24 ~ Fig. 4-26, accompanied with supplementary descriptions of the degrees listed in Table 4-6.

In the wave diagram colored in heat flux (Fig. 4-21), the characteristic lines are depicted in the same manner as in the wave diagram colored in total temperature (Fig. 4-23 (b)). The contact fronts divide the area into gas division and air division. In general, most warm color regions exist in gas division and most cold color regions in air division. Some regions characterized by intense heat flux, positive or negative are addressed in the following paragraphs, including 1) the inlets vicinity marked as "1)" in Fig. 4-21, which relates to inflows of hot gas and cold air, 2) the compressed fluid marked as "2.1)", "2.2)", "2.3)" and "2.4)" in Fig. 4-21, and 3) shock wave downstream vicinity.

1) High-speed inflows of hot gas and cold air

The high-speed inflows of hot gas from GH port and cold air from AL port result in great heat flux near the inlets. In the wave diagram colored in total temperature for the heat transfer case Fig. 4-23 (b), the values of port temperature for AL and GH are indicated on the color bar; as reference, the approximate range of wall temperature ($T_w$) from Fig. 4-19 (a) is indicated by trapezoid on the color bar. Obviously, the port temperatures are at both extremes while the wall temperature nears the midpoint. The regions of hot gas flow and cold air flow are highlighted with triangles numbered with "1)" on the wave diagram. Besides, from Fig. 4-23 (c), the exact regions of hot gas flow and cold air flow highlighted in the same manner are found to subject to fast flow speed. The resultant intense heat transfer is observed in Fig. 4-21 indicated by "1)".

2) Compressed fluid

The intense heat fluxes related to compressed fluid (both air and gas) are marked in Fig. 4-21 as "2.1)" ~ "2.4)". They include: 2.1 & 2.2) the gas existing in the cell at 0° compressed by the primary shock wave and the reflected shock wave, 2.3) the air existing in the cell at 0° compressed by the primary shock wave, and 2.4) the hot gas from GH port compressed by the reflected shock wave. The following paragraphs expand the four items.

The temperature of the gas exists in the right half at 0° is close to wall temperature, which can be inferred from Fig. 4-23 (b). As can be seen in the top right of Fig. 4-23 (b), it is compressed twice to higher temperature and discharged to AH port. The compressions for this gas lead to large temperature difference between fluid and wall. In Fig. 4-21, it is found to cause notable heat flux indicated by "2.1)" and "2.2)".

Also in Fig. 4-21, the compressed gas leads to intense heat flux marked as "2.3)". The hot gas from GH port is compressed by the reflected shock wave and then resumes moving rightwards because the process of discharging to AH is in progress. The temperature and the velocity of this region can be seen in Fig. 4-23 (b) and (c). The flowing hot gas accounts for the intense heat flux in this region.

About the heat flux region marked as "2-4)" in Fig. 4-21, axial distributions in cell at 14.4° is used for more tangible explanation. The air exists in the left half at 0° in wave diagram in Fig. 4-23 (b) undergoes compression by the primary shock wave, and moves right wards behind the primary shock wave. Before being compressed at 0°, the air is located in the "air" section in Fig. 4-24 (b-1), and great temperature difference between the air and the wall is obvious. After being compressed, at the moment when the primary shock wave is located about $x = 0.6$, the right-going primary shock wave is located in Fig. 4-24 (a-2) ~ (d-2) and marked by vertical dashed lines. The air has moved right and can be located in $x = 0.3$~0.6 marked as "Air" in Fig. 4-24 (b-2). Although the air is compressed and the temperature of air is increased, the temperature difference between the air and the wall is still large. The temperature difference, together with the great flow speed induced by the primary shock wave ("air" section in Fig. 4-24 (c-2)), explains the relatively considerable heat transfer caused by compressed air, which are marked as "2-4)" in Fig. 4-21.

3) Shock waves (except for propagation in air)

Generally, behind a compression wave or a shock wave, new boundary layer develops (already illustrated in Fig. 2-18), and heat transfer coefficient dramatically hikes and gradually falls down. As long as temperature difference is apparent, great heat flux would appear.

Right behind both shock waves the heat fluxes are great. The axial distributions for a moment when the primary shock wave travels in the cell are displayed in Fig. 4-24 (a-2) ~ (d-2). It is apparent that notable positive heat flux appears in the downstream vicinity of right-going the primary shock wave in Fig. 4-24 (d-2). However, the one-dimensional temperature appears to be lower than wall temperature. In fact, as has been explicated, between the gas and the air, the contact front is warped. The temperature averaged on cross-section, though helpful for analysis of flow field development, conceals some information that may be necessary for analysis in some cases. Therefore, by switching back to three-dimensional flow field, the true colors can be exposed. Shown in Fig. 4-27 are the meridional temperature distributions associated with the propagation of the primary shock wave (PSW). It is clear that the temperature near wall is quite different from that in the center. A location right after the passage of primary shock wave is singled out in Fig. 4-27 (b) and the radial temperature distribution for it is exhibited in Fig. 4-28 (b). Compared with top and bottom where fluid temperature near wall becomes higher than wall temperature after the passage of the primary shock wave, $r = 0.2{\sim}0.8$ is characterized by lower temperature that influences the average temperature level. The higher fluid temperature near wall leads to heat transfer from fluid to wall, i.e. positive heat flux. This profile originates from a precedent one shown in Fig. 4-28 (a), which is caused by the process that the wall keeps heating the fresh air of low temperature ever since it flows into the cell before the primary shock wave is generated (great negative heat flux located bottom left in Fig. 4-21).

A moment when the reflected shock wave travels in the cell is chosen for demonstration in Fig. 4-24 (a-3) ~ (d-3). The reflected shock wave moves left and causes significant pressure rise at around the middle of the cell, and at the same position a local maximum of heat flux is observed.
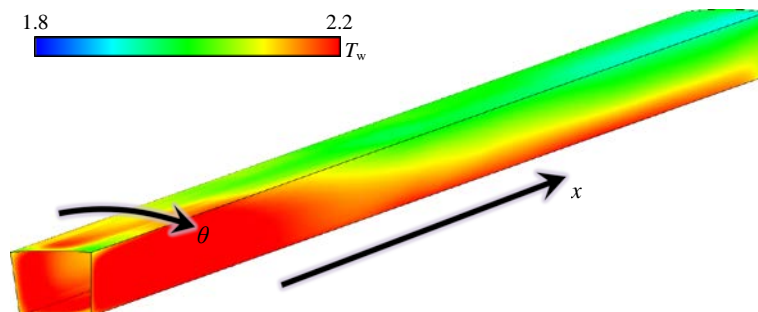


Fig. 4-12 Temperature distribution on internal surfaces of wall (interface) at $\theta=0°$ for 10X size (normalized by $T_{0,AL}=440$K, the same below for wall temperature)
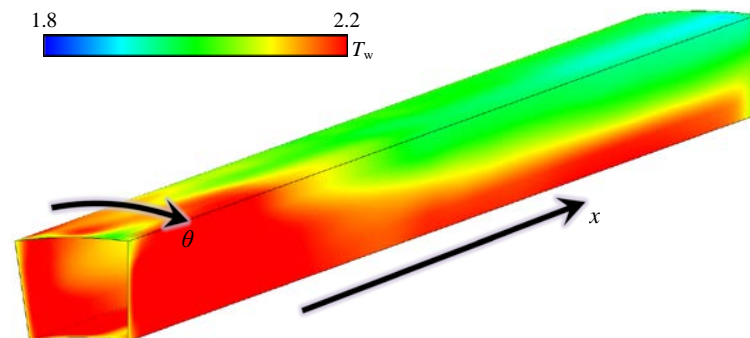


Fig. 4-13 Temperature distribution on external surfaces of wall at $\theta=0°$ for 10X size
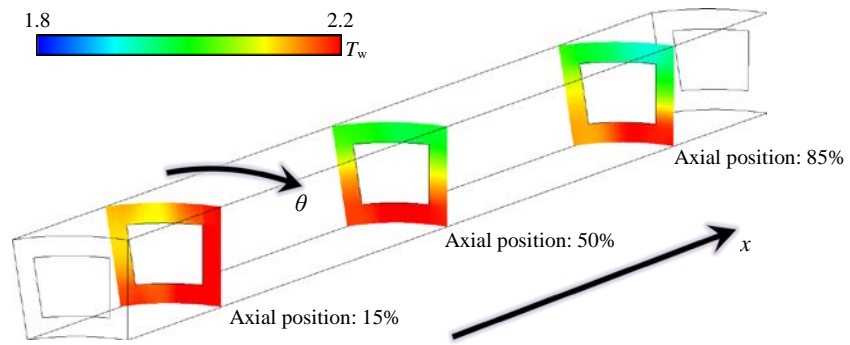
Fig. 4-14 Temperature distributions on cross-section surfaces of wall at $\theta=0°$ for 10X size
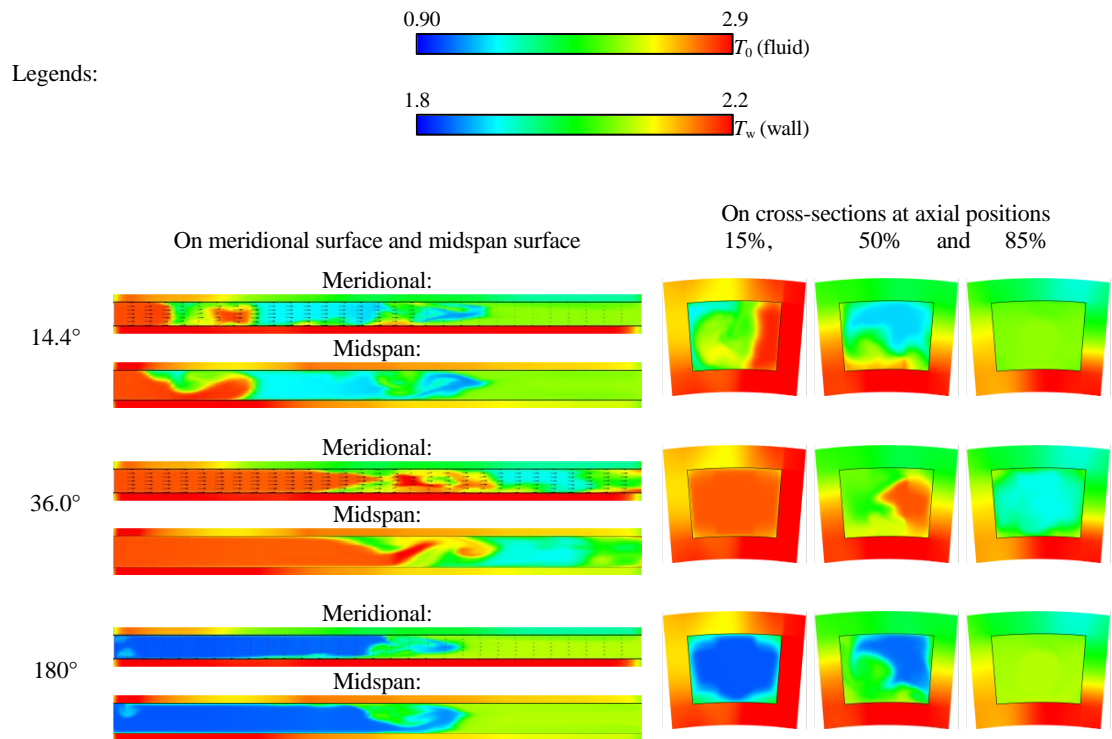


Fig. 4-15 Wall temperature and fluid temperature at 14.4°, 36.0° and 180° for 10X size
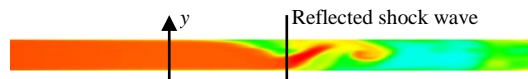
(a) Midspan temperature at 36.0°
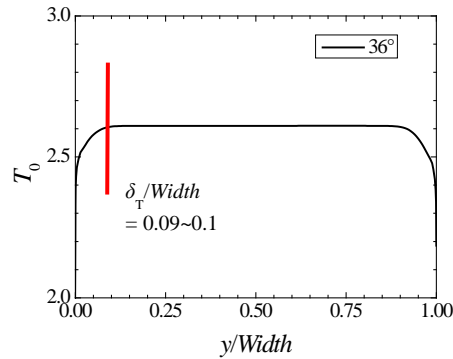


(b) Thermal boundary layer thickness at axial position
30% at 36.0°

Fig. 4-16 Example of temperature distribution when reflected shock wave propagates (10X size)
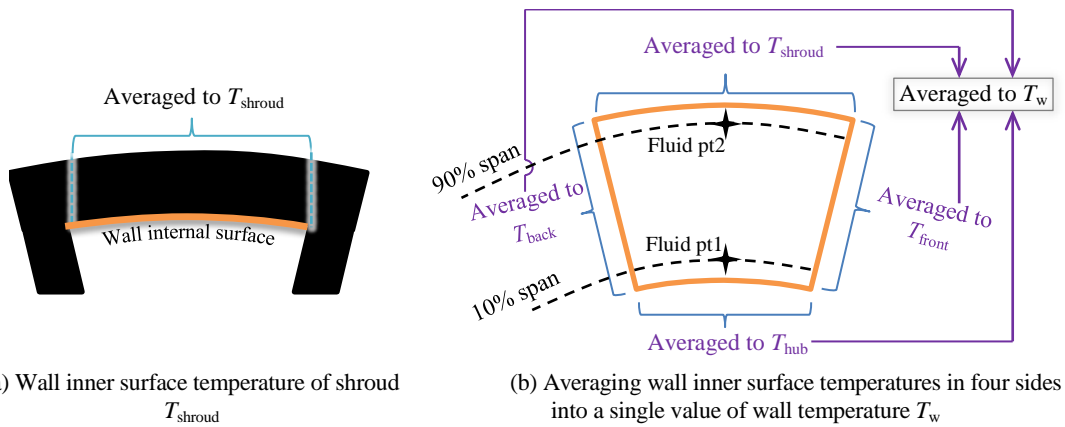


(a) Wall inner surface temperature of shroud
$T_{shroud}$



(b) Averaging wall inner surface temperatures in four sides
into a single value of wall temperature $T_w$

Fig. 4-17 Definition of wall inner surface, wall temperature and point "Fluid pt1", "Fluid pt2" on
each cross-section
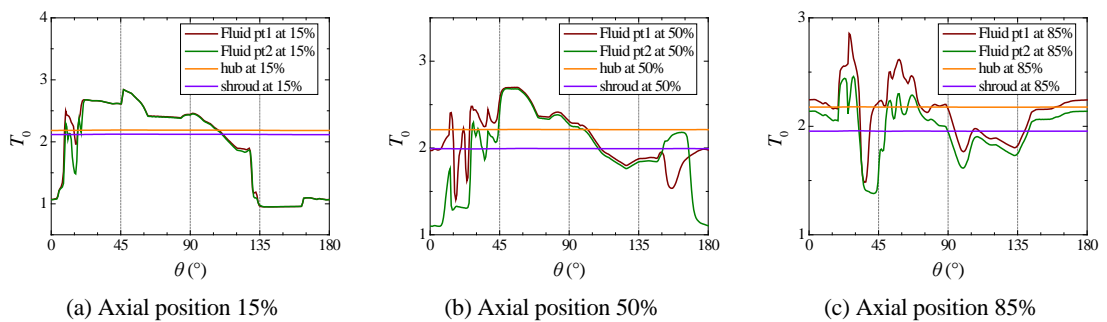


(a) Axial position 15%



(b) Axial position 50%



(c) Axial position 85%

Fig. 4-18 Comparisons between hub-side and shroud-side fluid and interface temperatures

(a) Interface temperature averaged on cross-sections   (b) Interface temperature in four wall sides
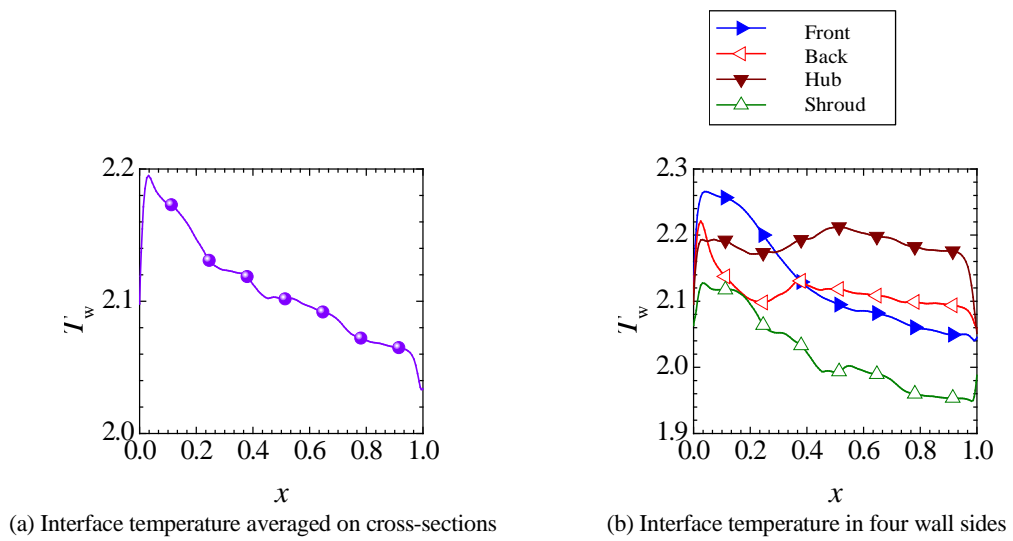
Fig. 4-19 Axial distributions of <u>interface temperature</u> at initial degree for heat transfer case of <u>10X</u> size (also normalized by total temperature in AL port)
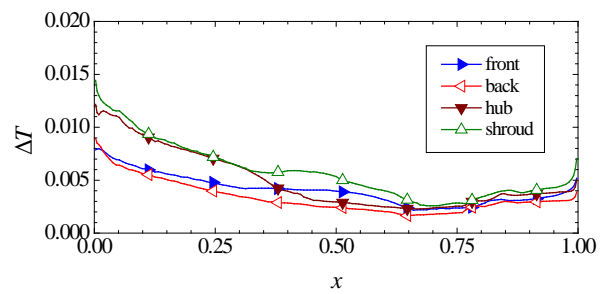


Fig. 4-20 Cyclic fluctuation amplitude of interface temperatures of four sides for 10X size
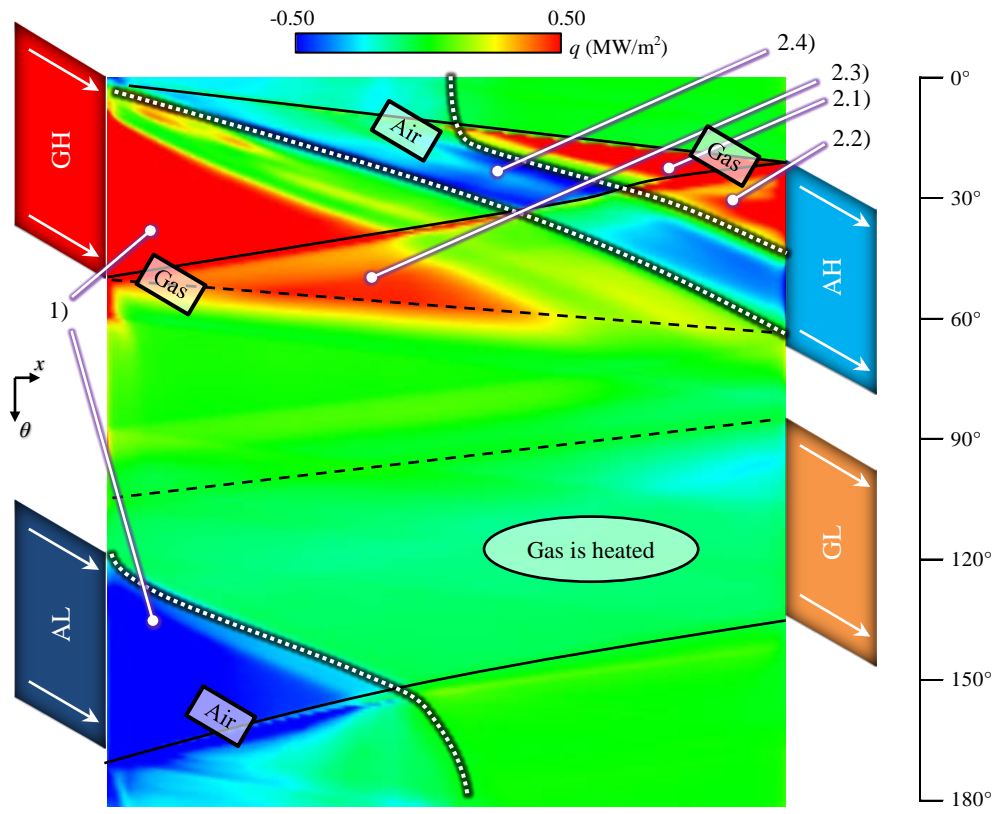
Fig. 4-21 Wave diagram colored in <u>heat flux</u> for heat transfer case of <u>10X</u> size

(a) Total pressure

(b) Total Temperature

(c) Axial Velocity
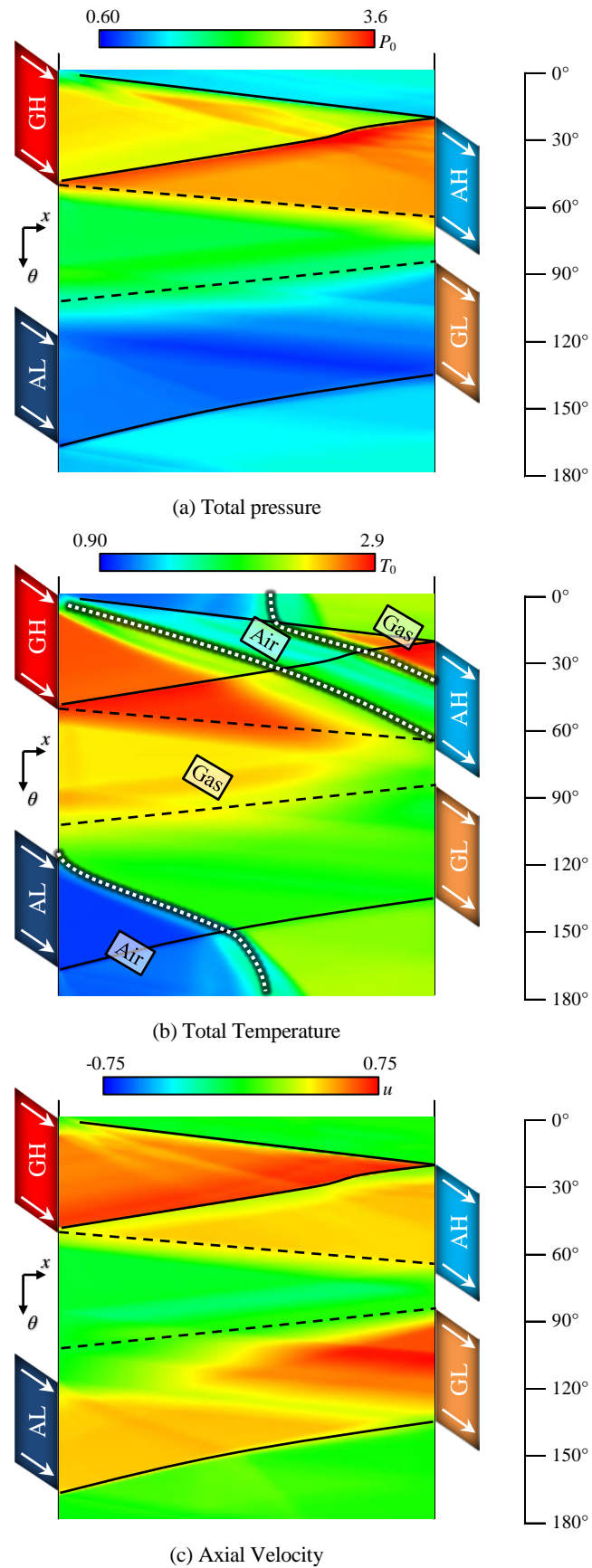
Fig. 4-22 Wave diagrams with depicted characteristic lines for <u>adiabatic</u> case of <u>10X</u> size

(a) Total pressure

(b) Total Temperature

(c) Axial Velocity
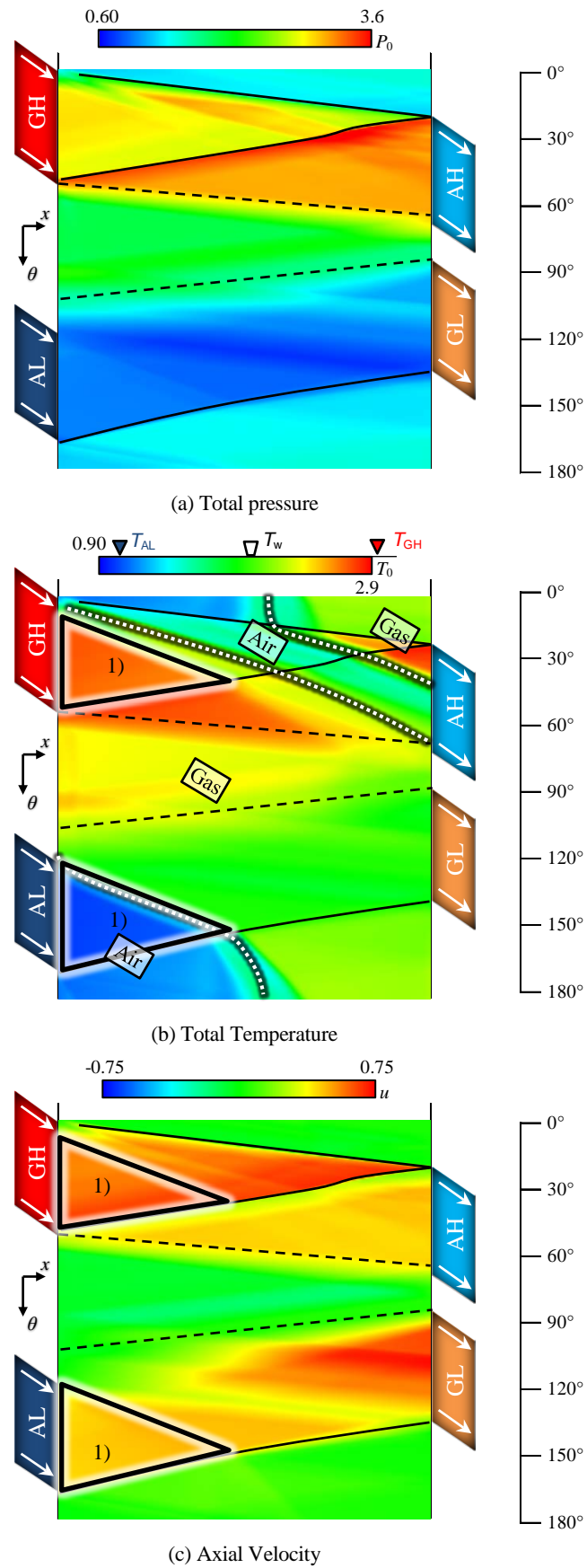
Fig. 4-23 Wave diagrams with depicted characteristic lines for <u>heat transfer</u> case of <u>10X</u> size
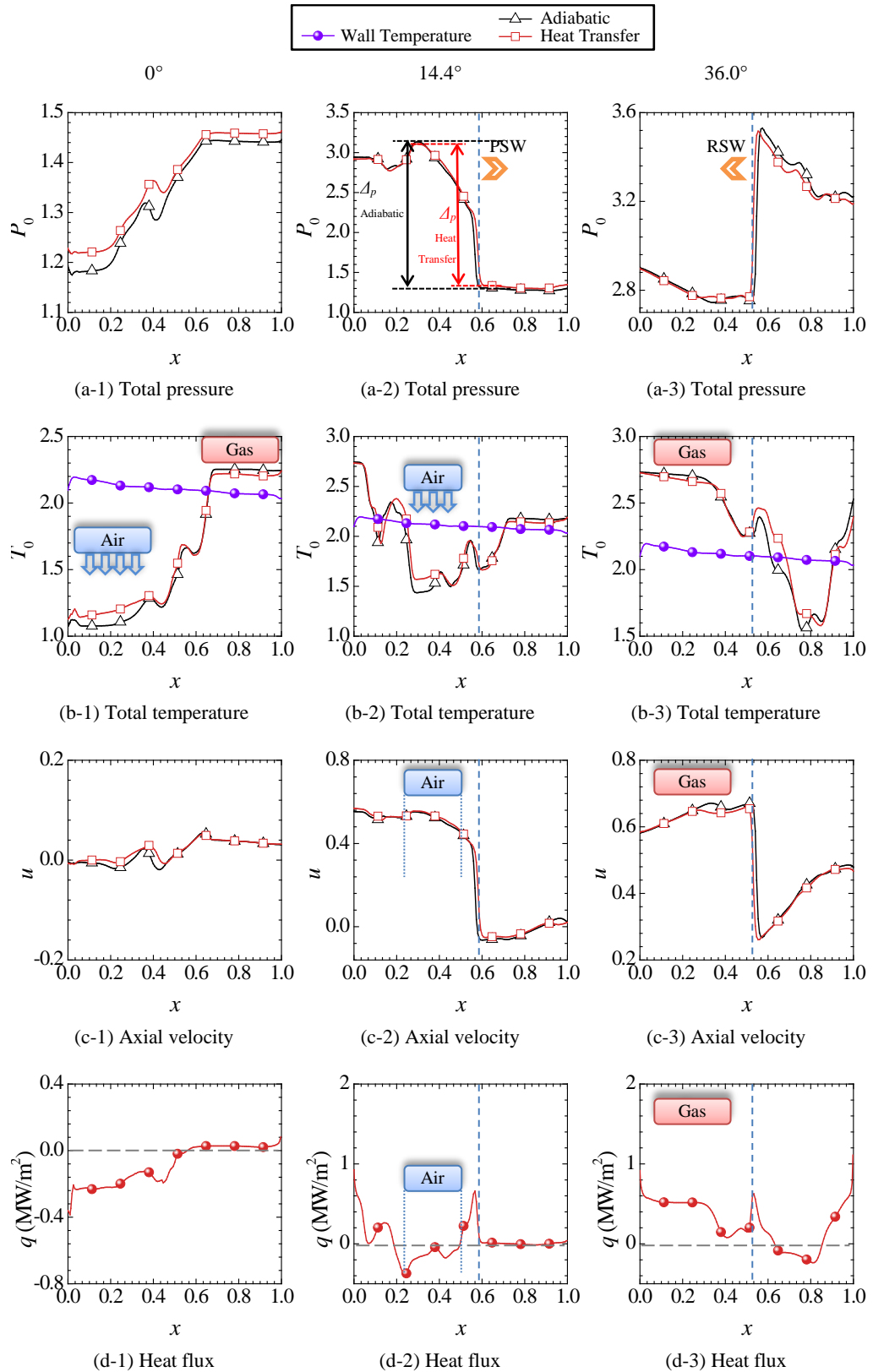
Fig. 4-24 Axial distributions at 0°, 14.4° and 36.0° for both adiabatic case and heat transfer case of 10X size (PSW: primary shock wave; RSW: reflected shock wave)
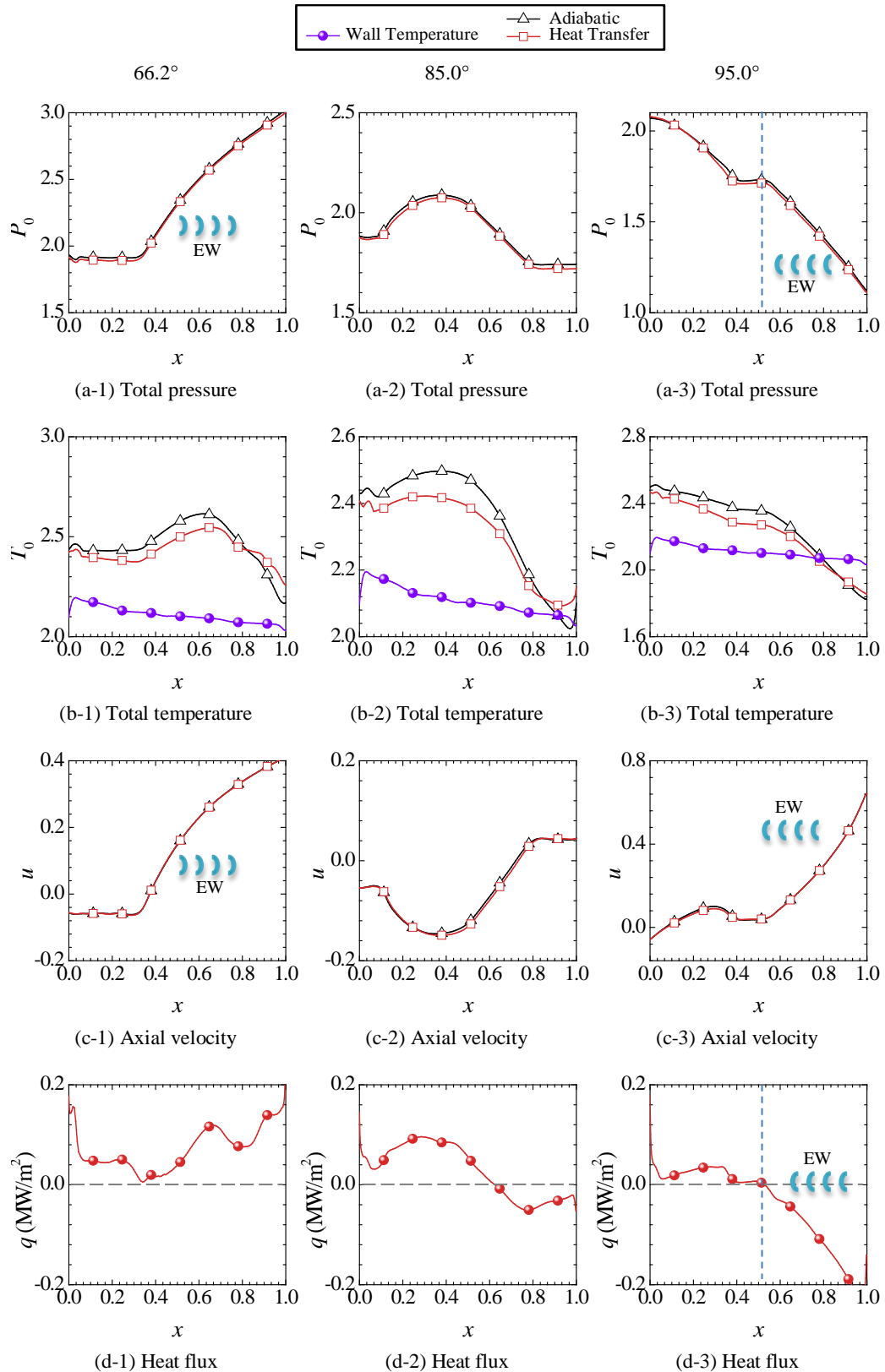
Fig. 4-25 Axial distributions at 66.2°, 85.0° and 95.0° for adiabatic case and heat transfer case of 10X size (EW: expansion waves)
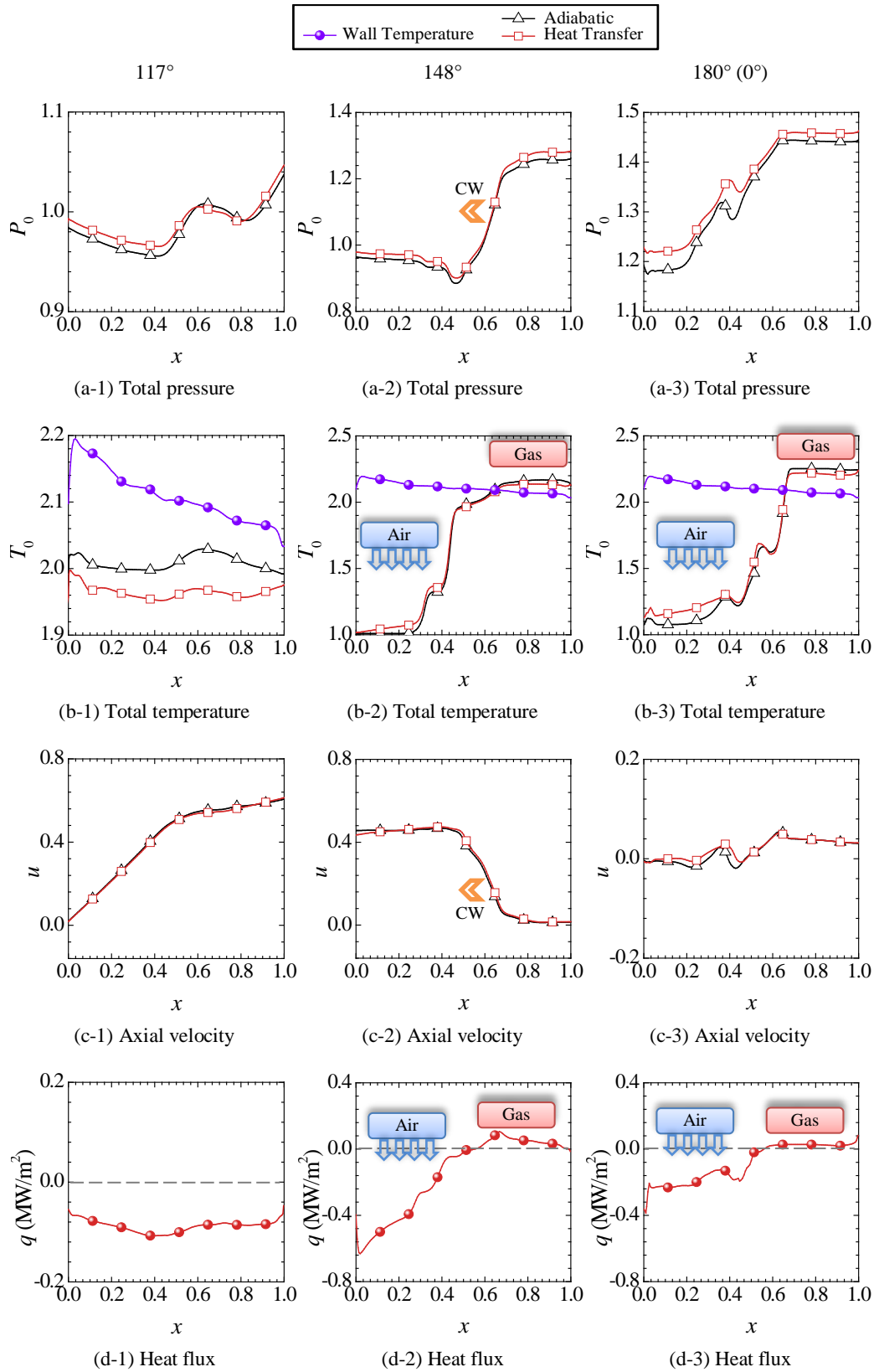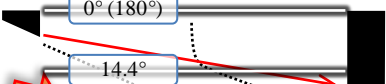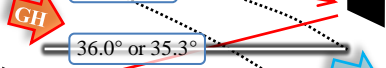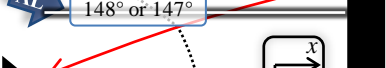
Fig. 4-26 Axial distributions at 117°, 148° and 180° (0°) for adiabatic case and heat transfer case of 10X size (CW: compression wave)

Table 4-6 Attributes of selected degrees

| Schematic wave diagram | Degree for 10X | Degree for 1/10 | Description |
|---|---|---|---|
| | 0 (180) | 0 (180) | Initial state; before opening to GH port; before compression process |
| | 14.4 | 14.4 | Primary shock wave propagating |
| | 36.0 | 35.3 | Reflected shock wave propagating |
| | 66.2 | 66.2 | Expansion waves propagating to end compression process |
| | 85.0 | 79.9 | Right before opening to GL port |
| | 95.0 | 90.0 | Expansion waves propagating to discharge fluid to GL port |
| | 117 | 117 | Right before opening to AL port |
| | 148 | 147 | During opening to AL port |

0.9      2.9   $T_0$

(a) 13.7°

(b) 14.4°

(c) 15.1°
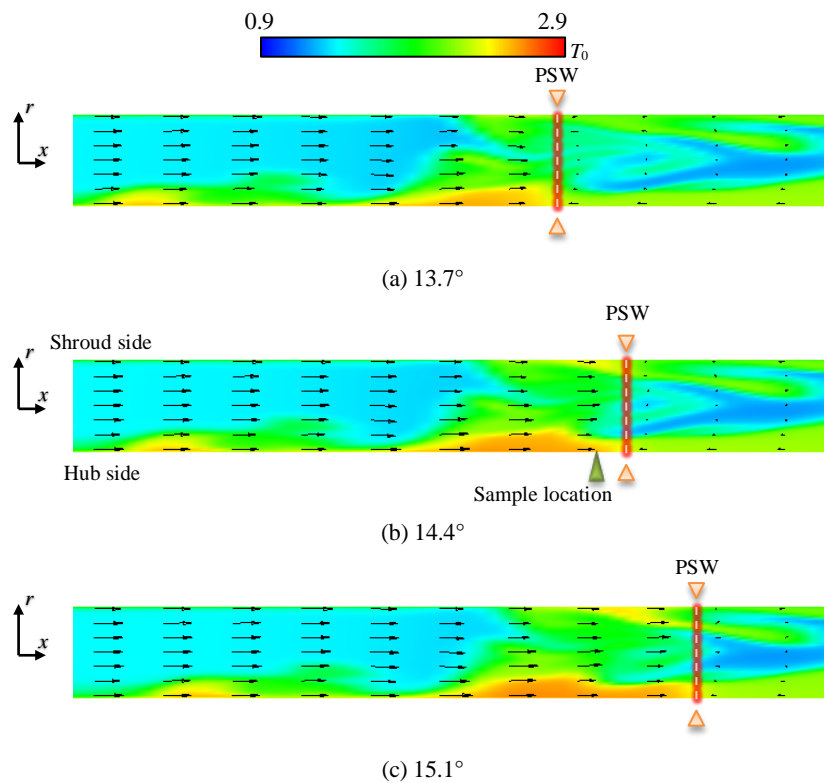
Fig. 4-27 Meridional total temperature distributions with velocity vectors near primary shock wave for heat transfer case of 10X size ($x$: 0.32~0.68)
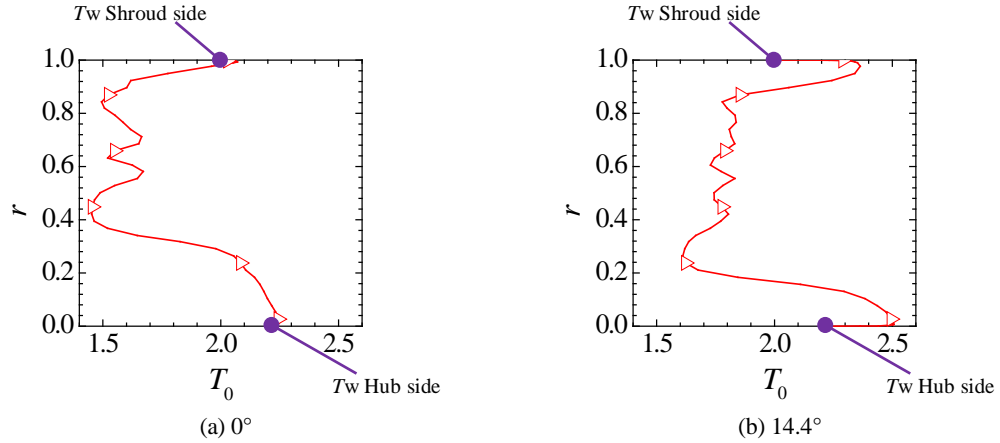
Fig. 4-28 Radial total temperature profiles at the sample location in Fig. 4-27 at 0° and 14.4° for heat transfer case of 10X size

### 4.2.2.2    1/10 Size

As size reduces, thermal boundary layer becomes thicker. For example, for a moment when the inflow has developed enough in the left half, the midspan temperature distribution is shown in Fig. 4-29 (a). The temperature distribution along circumferential direction ($y$) at axial 30% position on the midspan is shown in Fig. 4-29 (b), in which the relative thermal boundary layer thickness $\delta_T/Width$ is 0.21. $\delta_T/Width$ estimated by Eq. (4.1) & (4.2) is 0.24. Obviously, compared with that in 10X size, the thermal boundary layer in 1/10 size is much thicker at the same location for inflow.

Naturally, intense heat transfer occurs in 10X size becomes even greater at smaller 1/10 size. The wave diagram of heat flux for 1/10 size is shown in Fig. 4-31. To better observe the regions of relatively intense heat flux within a specific size (but not to compare between sizes), heat flux can be normalized by heat transfer coefficient under assumption of steady flow condition ($h_{L,avg}$) listed in Table A-5 in Appendix B and temperature difference estimated by half difference between highest port temperature ($T_{0,GH}$) and lowest port temperature ($T_{0,AL}$):

$$q_{Norm} = h_{L,avg} \left( \frac{T_{0,GH} - T_{0,AL}}{2} \right) \tag{4.3}$$

dimensionless heat flux $\qquad\qquad q" = q/q_{Norm}$ $\qquad\qquad\qquad$ (4.4)

where $h_{L,avg}$ is estimated by average Nusselt number $Nu_{L,avg}$ in Eq. (A.4) for turbulent flow over an isothermal plate. Thereby, the dimensionless heat flux is compared between 10X size and 1/10 size in Fig. 4-30 to find out the differences in regions where relatively intense heat flux occur. Those regions of intense heat transfer found in 10X size in Fig. 4-21 or Fig. 4-30 (a) are also observed in 1/10 size shown in Fig. 4-31 or Fig. 4-30 (b). Apart from those, in 1/10 size, intense heat transfer appears in several regions where no remarkable heat flux is found in 10X size. Different from Fig. 4-21 or Fig. 4-30 (a), in Fig. 4-31 or Fig. 4-30 (b): 1) the primary shock wave causes great heat flux in the downstream vicinity also in air, 2) the expansion waves generated by shutting the left end cause noticeable negative heat flux, and 3) the compression wave causes noteworthy heat flux in downstream vicinity.

The axial distributions of average wall inner surface temperature (wall temperature) and wall inner surface temperature in four wall sides are shown in Fig. 4-32. The wave diagrams for adiabatic case and for heat transfer case are shown in Fig. 4-33 and Fig. 4-34, respectively. Also, the approximate range of wall temperature is marked on the color bar in Fig. 4-34. The axial distributions at selected degrees are shown in Fig. 4-35 ~ Fig. 4-37, and the descriptions of the degrees are listed in Table 4-6.

## 1) Primary shock wave in air

The primary shock wave causes great heat flux in the downstream vicinity also in air, because the local fluid temperature is higher than wall temperature, but the root cause is greater immediate heat transfer for the fresh air.

Charged from AL port, the fresh air is continuously heated, and the result is a higher temperature in air at 0° when compared with adiabatic case in Fig. 4-35 (b-1). In 10X size, this difference is smaller, as can be inferred by comparing temperature differences between adiabatic case and heat transfer case in air part in Fig. 4-24 (b-1) and Fig. 4-35 (b-1). Part of the meridional total temperature distributions are for heat transfer cases of both 10X size and 1/10 size are shown in Fig. 4-38 (a) and (c), respectively, for more detailed information. Compared with 10X size, the local fluid temperature in 1/10 size has been heated more. After being compressed by the primary shock wave, in Fig. 4-38 (b), the upper side near shroud is still lower, whereas in Fig. 4-38 (d) both upper and lower sides have similar temperature. The heat fluxes across shroud and hub for Fig. 4-38 (b) and (d) are shown in Fig. 4-39. Evident heat flux difference is found between shroud side and hub side in 10X size, but in 1/10 both sides show similar heat flux. As a result, in 10X size, the average heat flux (avg) is close to zero. After several degrees, when the primary shock wave propagates farther, negative heat flux for hub and positive heat flux for shroud, as well as resultant near-zero average heat flux is more clearly observed in 10X size shown in Fig. 4-40 (c), while in 1/10 size the positive heat fluxes persists, as is shown in Fig. 4-40 (d).

## 2) Expansion waves

As is shown in Fig. 4-36 (d-1), the expansion waves generated by shutting the left end induce notable negative heat flux in and behind the expansion waves. The absolute value increases where the expansion waves propagate, and the region is specified in Fig. 4-36 (a-1) ~ (d-1) in the right half. The tail of the expansion waves is marked by vertical dashed lines. Again, the average temperature is higher than wall temperature, but the local fluid temperature near wall is lower. To exemplify the local fluid temperature, Fig. 4-41 (e) shows the temperature distribution above wall in the flow right after expansion at 66.2°. Obviously, in 1/10 size, the local temperature falls below wall temperature. Before being expanded, the local fluid temperature near wall is lower than mainstream temperature and near wall temperature because of persistent heat transfer between fluid and wall. When the expansion waves pass by, the local fluid temperature near wall becomes lower than wall temperature since the fluid is expanded. The direct cause is lower local temperature as expansion proceeds and after expansion, and the ultimate reason is, again, more significant heat transfer in small size. In fact, the flow field is affected by heat transfer more profoundly. Not only the direct heat transfer from the hot gas to wall, but the state before compression has certain influence, which is to be explained in Subsection 4.2.3.

## 3) Compression wave

The compression wave causes relatively great heat flux in downstream vicinity. Especially, in the air part, in 10X size the heat flux caused by compression shock wave is negative (Fig. 4-21), but in 1/10 size it turns out to be positive (marked as "3)" in Fig. 4-31).

This dramatic change is linked with the heating process for fresh air from AL port. A region highlighted as "3A" in Fig. 4-31 indicates the location to be discussed. In the exact region, before and after passage of the compression wave, the near-wall portion of the air shown in Fig. 4-42 (b) and (d) has been heated much and a vast green area is close to wall temperature in 1/10 size, compared with Fig. 4-42 (a) and (c) for 10X size. This comparison demonstrates the difference in effect of heating between 10X size and 1/10 size. Since a considerable portion near wall is heated to approximately wall temperature before being compressed (green area in Fig. 4-42 (b)), the local temperature in a certain distance from wall naturally goes above wall temperature after compression (area extremely near wall, obscure in Fig. Fig. 4-42 (d)), and the heat flux becomes positive as the local fluid loses heat to wall.
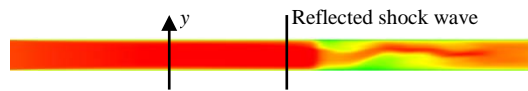


(a) Midspan temperature at 35.3°
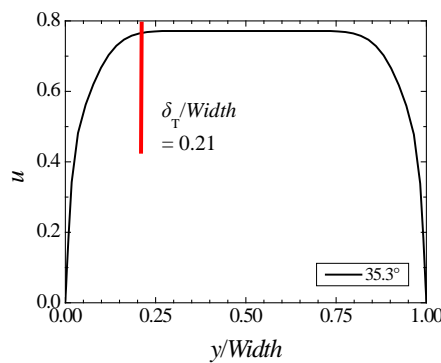


(b) Thermal boundary layer thickness at axial position
30% at 35.3°

Fig. 4-29 Example of temperature distribution when reflected shock wave propagates (1/10 size)
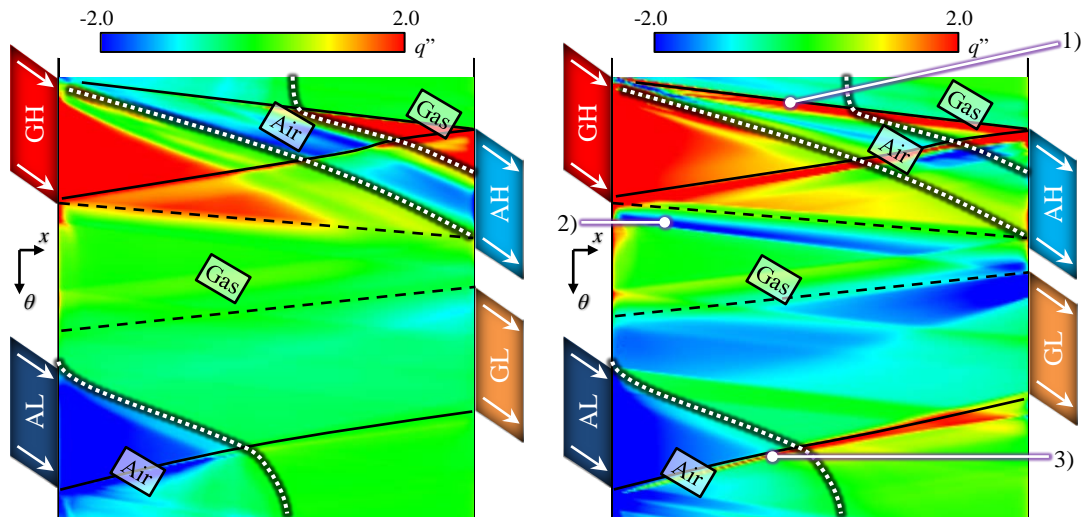


(a) 10X size (normalized by $q_{Norm} = 0.26$ MW/m$^2$)      (b) 1/10 size (normalized by $q_{Norm} = 0.64$ MW/m$^2$)

Fig. 4-30 Wave diagram colored in dimensionless heat flux for heat transfer case of 10X size and
1/10X size
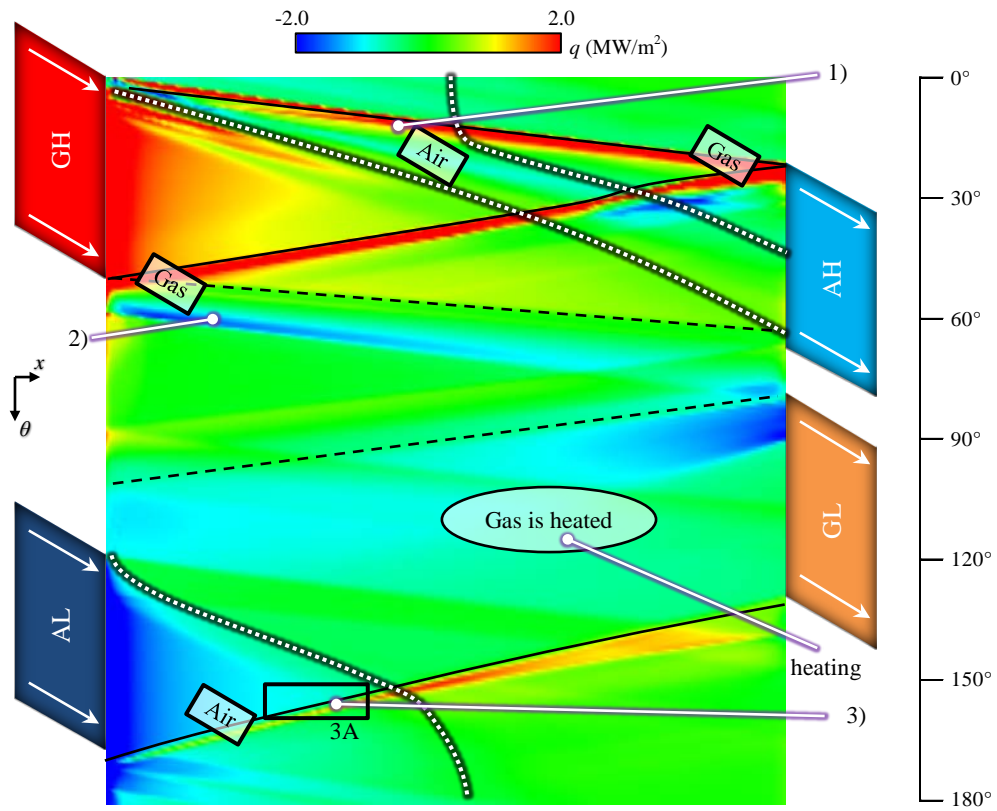
Fig. 4-31 Wave diagram colored in <u>heat flux</u> for heat transfer case of <u>1/10X</u> size
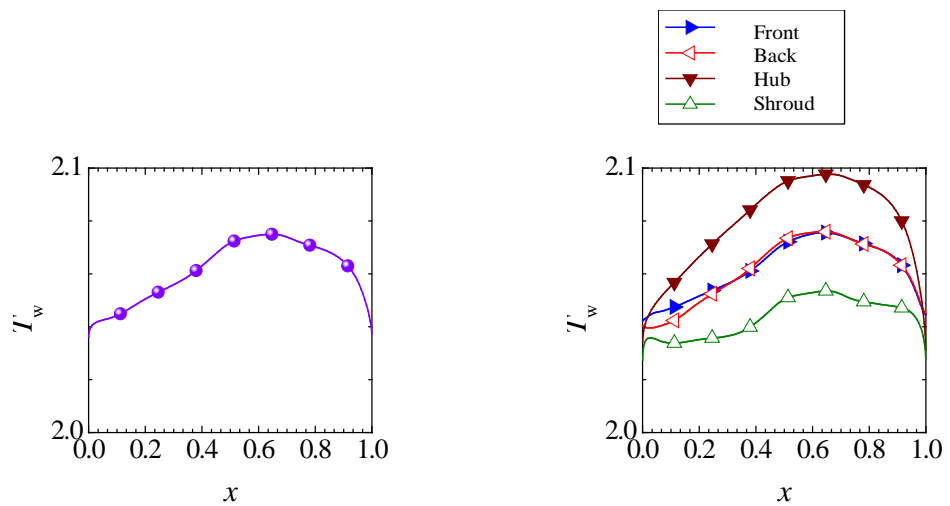


(a) Interface temperature averaged on cross-sections

(b) Interface temperature in four wall sides

Fig. 4-32 Axial distributions of <u>interface temperature</u> at initial degree for heat transfer case of <u>1/10</u> size (also normalized by total temperature in AL port)
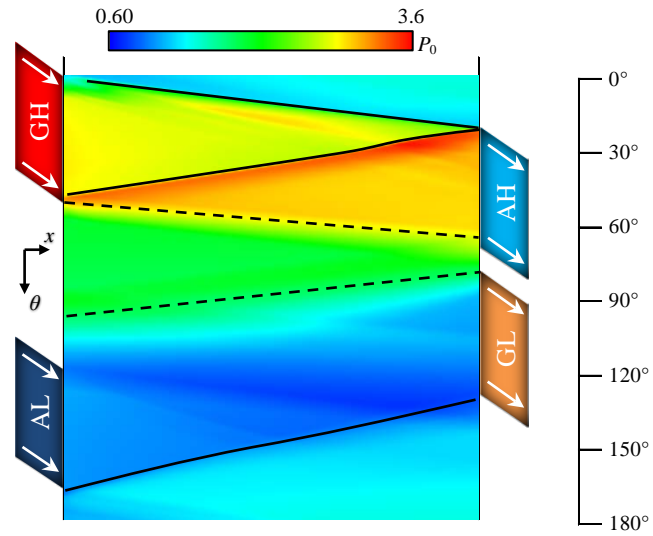
(a) Total pressure
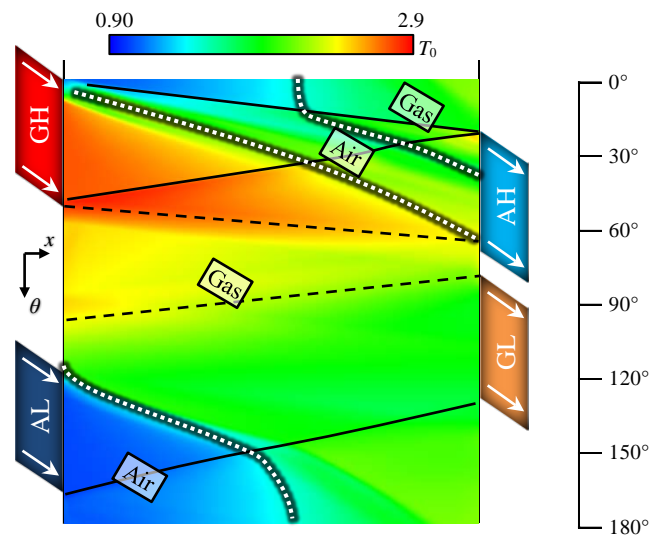
(b) Total Temperature
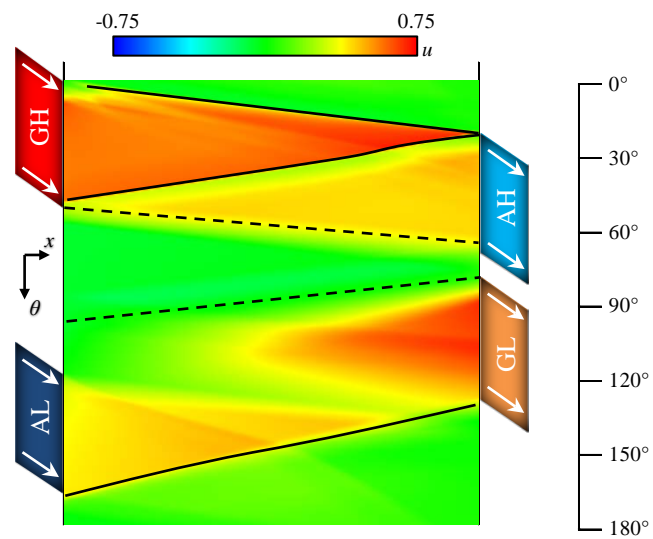
(c) Axial Velocity

Fig. 4-33 Wave diagrams with depicted characteristic lines for adiabatic case of 1/10 size
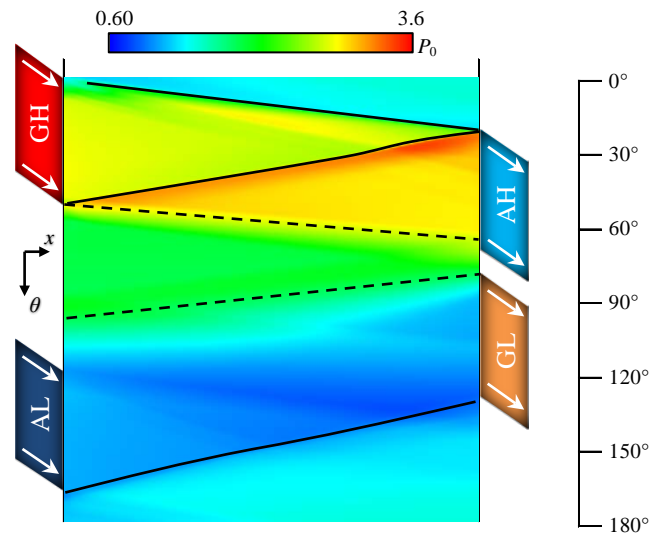
(a) Total pressure
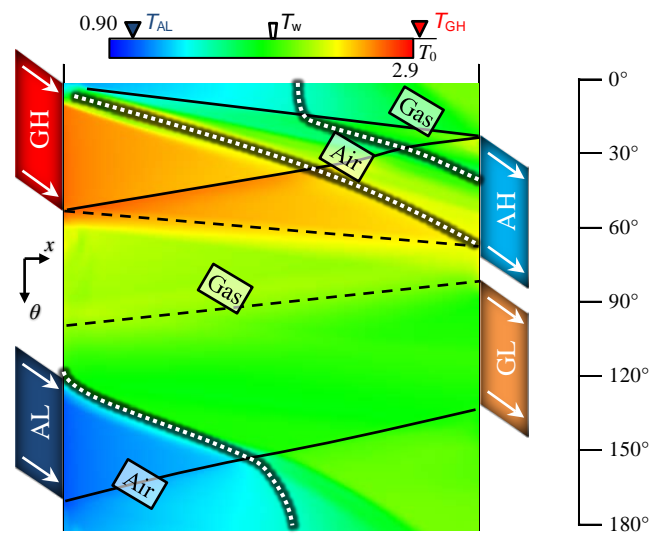
(b) Total Temperature
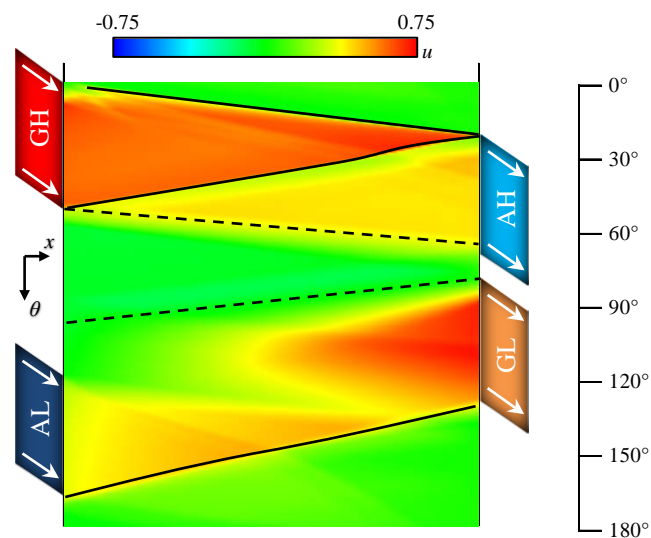
(c) Axial Velocity

Fig. 4-34 Wave diagrams with depicted characteristic lines for <u>heat transfer</u> case of <u>1/10</u> size
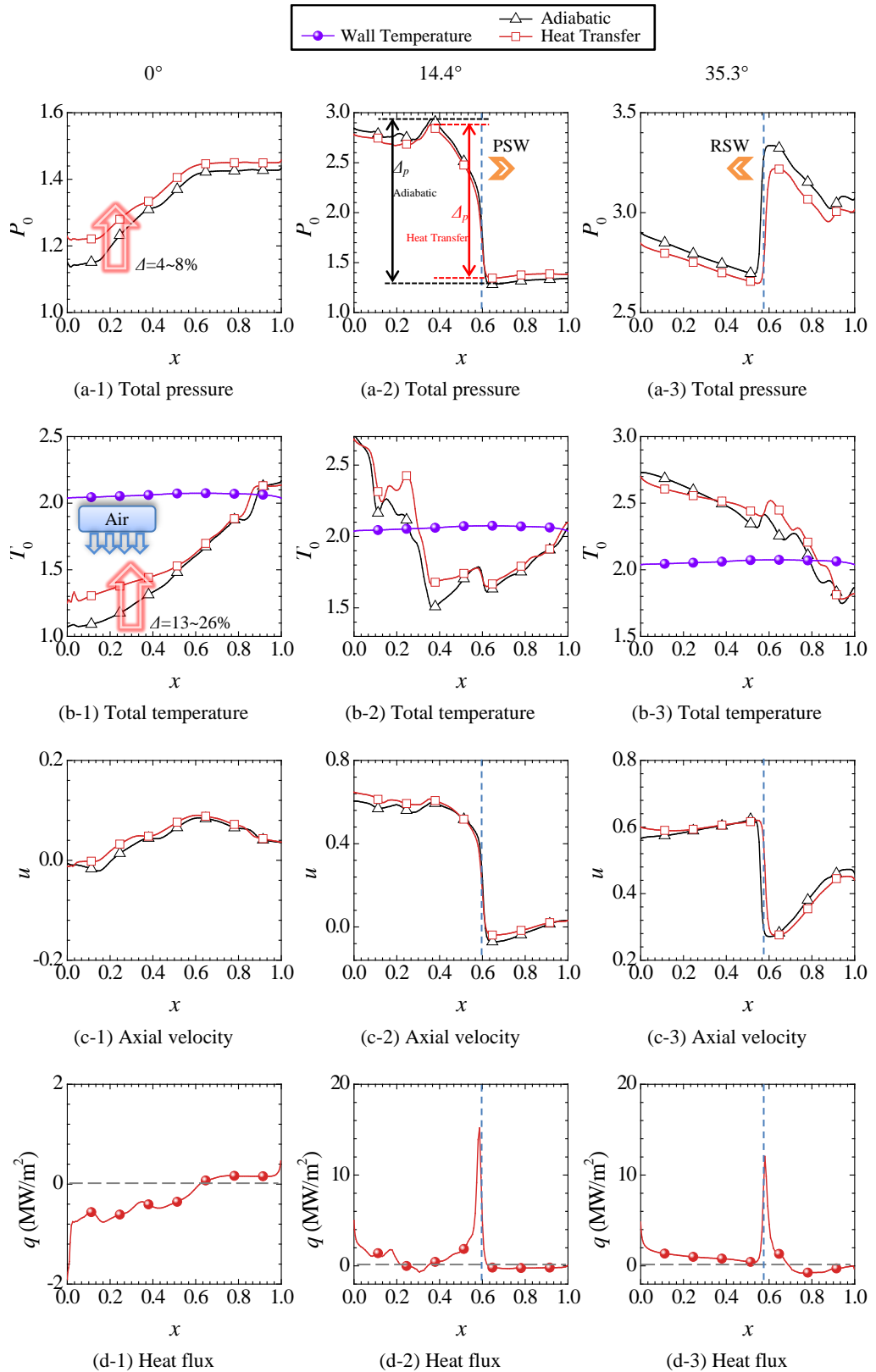
Fig. 4-35 Axial distributions at 0°, 14.4° and 35.3° for adiabatic case and heat transfer case of 1/10 size (PSW: primary shock wave; RSW: reflected shock wave)
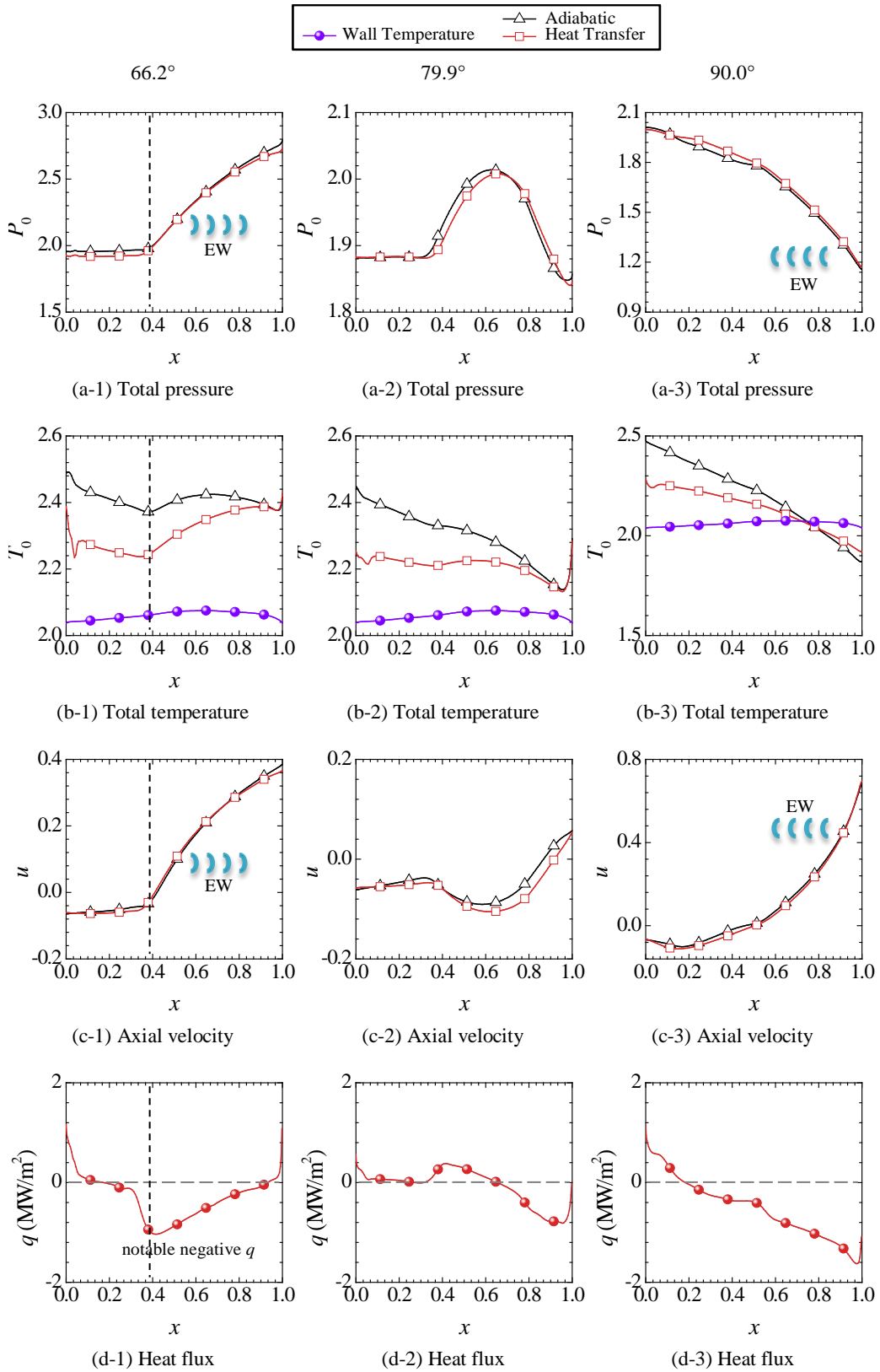
Fig. 4-36 Axial distributions at 66.2°, 79.9° and 90.0° for adiabatic case and heat transfer case of 1/10 size (EW: expansion waves)

Wall Temperature —●—     Adiabatic —△—
Heat Transfer —□—

117°           147°           180° (0°)

(a-1) Total pressure      (a-2) Total pressure      (a-3) Total pressure

(b-1) Total temperature      (b-2) Total temperature      (b-3) Total temperature

(c-1) Axial velocity      (c-2) Axial velocity      (c-3) Axial velocity

(d-1) Heat flux      (d-2) Heat flux      (d-3) Heat flux
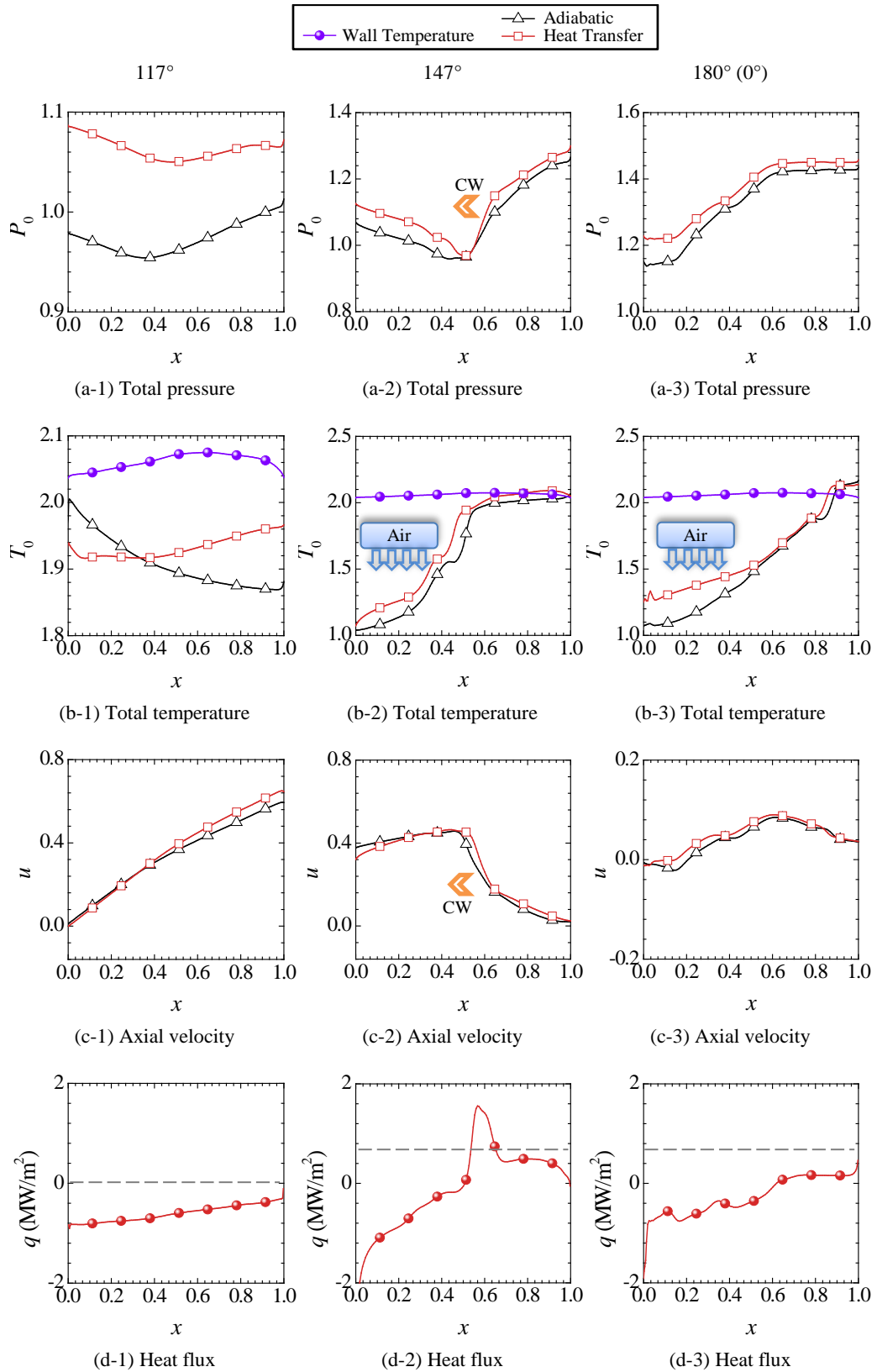
Fig. 4-37 Axial distributions at 117°, 147° and 180° (0°) for adiabatic case and heat transfer case of 1/10 size (CW: compression wave)

(a) 0° for 10X size        (b) 7.2° for 10X size

(c) 0° for 1/10 size        (d) 7.2° for 1/10 size
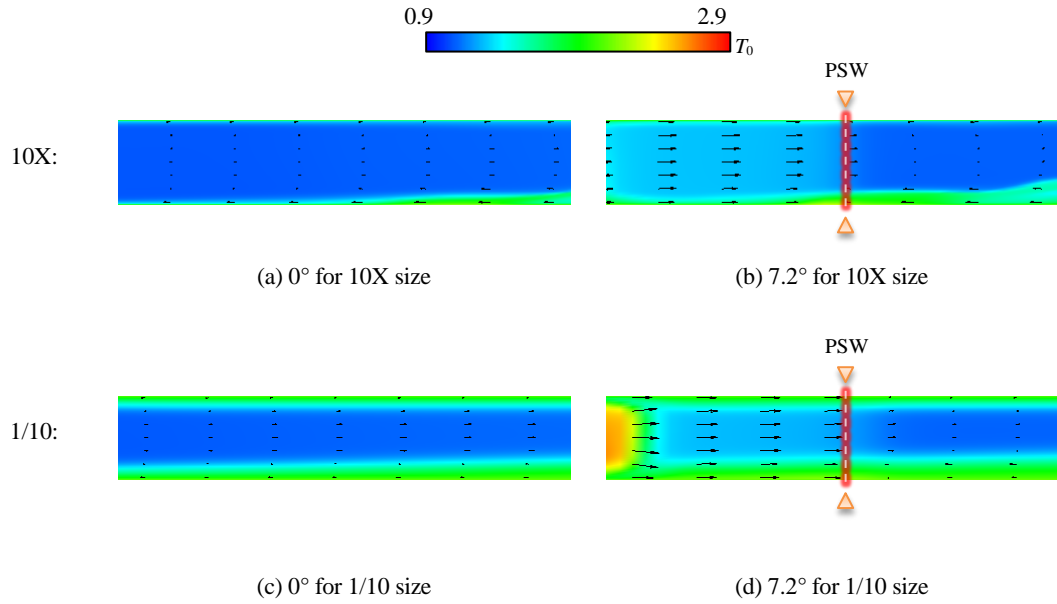
Fig. 4-38 Meridional total temperature distributions with velocity vectors at both 0° and 7.2° for heat transfer cases of 10X size and 1/10 size ($x$: 0.13~0.37)



(a) 10X        (b) 1/10
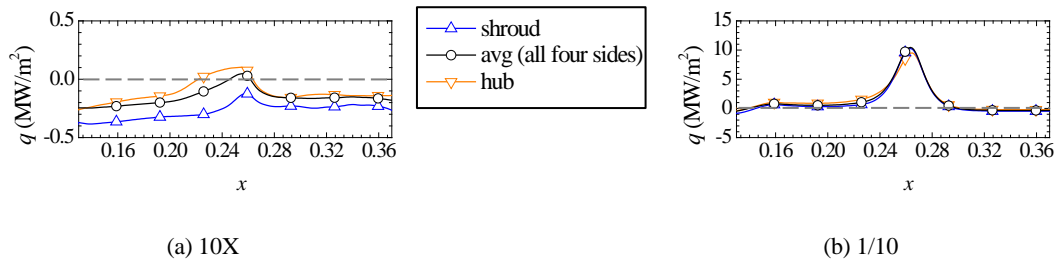
Fig. 4-39 Heat flux distributions of the exhibited sections in Fig. 4-38 (b) and (d)



(a) Meridional distribution for 10X        (b) Meridional distribution for 1/10

(c) Heat flux distributions for 10X        (d) Heat flux distributions for 1/10
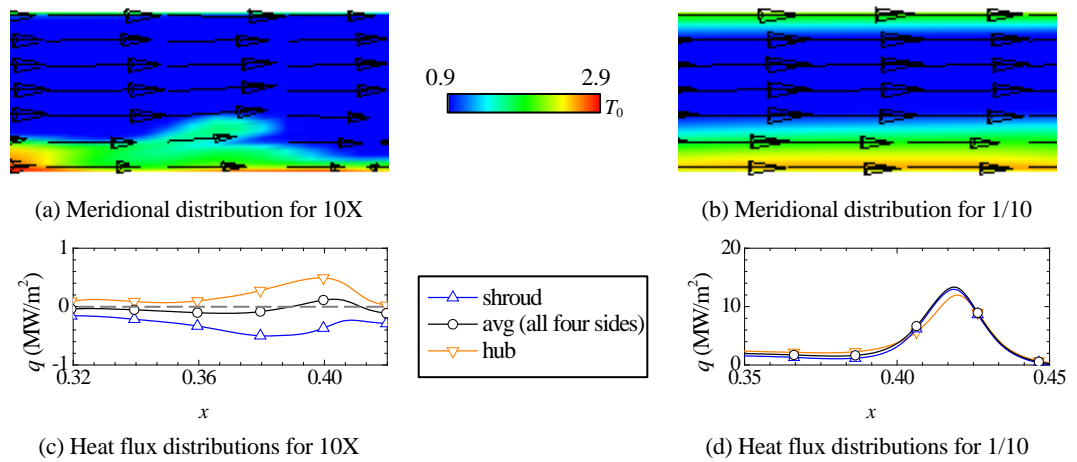
Fig. 4-40 Meridional distributions of total temperature and axial distributions of heat flux at 10.8° for heat transfer cases of 10X size and 1/10 size ($x$ in (a): 0.32~0.42; $x$ in (b): 0.35~0.45)

(a) 10X

(b) 1/10



(c) Enlarged highlighted region in (a)

(d) Enlarged highlighted region in (b)



(e) Temperature profile above wall
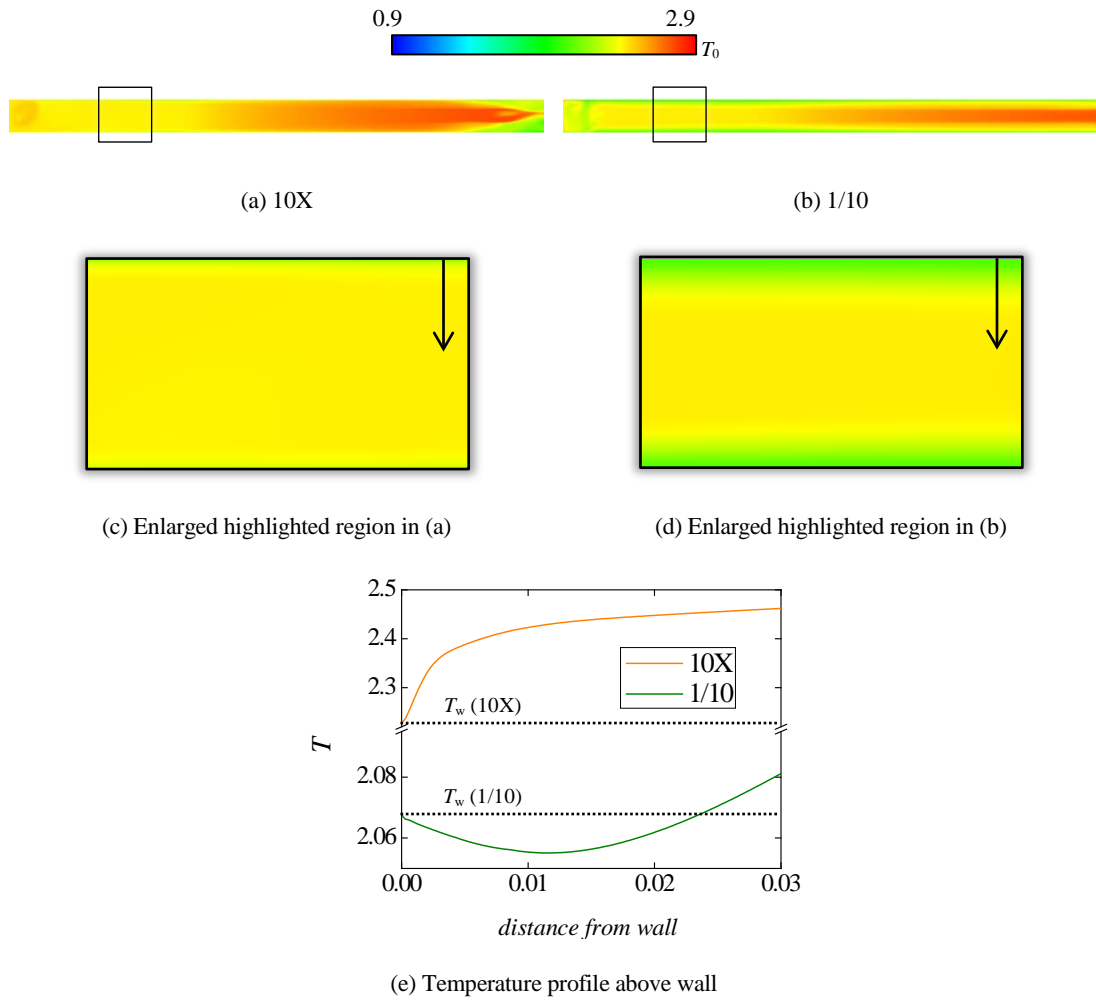
Fig. 4-41 Midspan distributions of total temperature and temperature above wall in fluid at 66.2°
for heat transfer cases of 10X size and 1/10 size



(a) Prior to passage of compression wave in 10X size

(b) Prior to passage of compression wave in 1/10 size

(c) After passage of compression wave in 10X size

(d) After passage of compression wave in 1/10 size
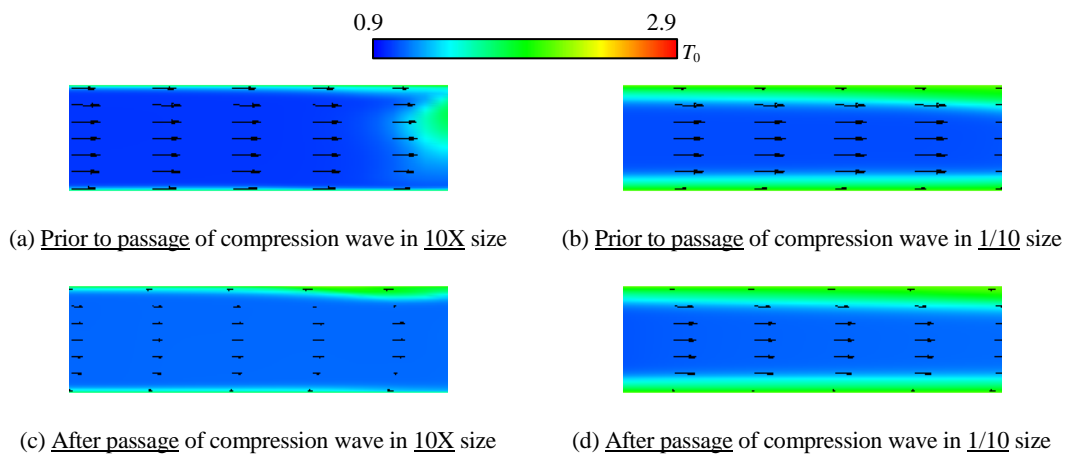
Fig. 4-42 Meridional total temperature distributions for "3A" region (relating to heat transfer case)
in Fig. 4-31

*4.2.3    Heat Transfer Effects on Flow*

As is supposed, generally, heat transfer effects become greater as size gets smaller. The trends of heat transfer effects as size reduces are discussed in Subsection 4.2.4. The present subsection presents heat transfer effects in 1/10 size, the smallest size investigated, at first, since greatest heat transfer effects can be observed at this size. Then, heat transfer effects in 10X size, a conventional size and the largest one in the present study, are addressed to discover whether different sizes share the same features on heat transfer effects.

\*\*\*\*\*\*\*\*\*\*\*\*\*\*\*\*\*\*\*\*\*\*\*\*\*\*\*\*\*\*\*\*\*\*\*\*\*\*\*\*\*\*\*\*\*\*\*\*\*\*\*\*\*\*\*\*\*\*\*\*\*\*\*\*\*\*\*\*\*\*\*\*\*\*\*\*\*\*\*\*\*\*\*\*\*\*\*\*\*
*Note*
*Because the oscillation of wall temperature is trivial, the effects of heat transfer seem to be immediate responses to temperature boundary. However, the wall temperature itself is the outcome of heat transfer between flow and wall for a number of wave rotor cycles in which flow field and wall temperature interact and finally reach limit cycle. Therefore, the resultant changes are inherently affected by heat transfer boundary instead of temperature boundary.*
\*\*\*\*\*\*\*\*\*\*\*\*\*\*\*\*\*\*\*\*\*\*\*\*\*\*\*\*\*\*\*\*\*\*\*\*\*\*\*\*\*\*\*\*\*\*\*\*\*\*\*\*\*\*\*\*\*\*\*\*\*\*\*\*\*\*\*\*\*\*\*\*\*\*\*\*\*\*\*\*\*\*\*\*\*\*\*\*\*

*4.2.3.1    1/10 Size*

The effects on internal flow field, charging and discharging occur in 1/10 size, in an arresting manner. In order to clarify the differences between the adiabatic flow field and the flow field subject to heat transfer, axial distributions at several degrees are exhibited for detailed explanation in Fig. 4-35 ~ Fig. 4-37. The comparison of parameters at cell ends during charging and discharging are presented in Fig. 4-43.

Change in evolution of internal flow field

{Compression process}

During compression process, pressure and temperature in the cell at four selected degrees are shown in Fig. 4-35 and Fig. 4-36 (a-1) ~ (b-1). Right before compression process at 0° (Fig. 4-35 (b-1)), temperature in air part is higher in the heat transfer case for the mentioned reason that the air has been heated by the wall for a while after being discharged into cell from AL port. Compared with the temperature difference, the pressure difference in air part is small for the sake of leakage (Fig. 4-35 (a-1)), about 20% ~ 30% that of the temperature difference. Consequently, in the air, density is lower when heat transfer is considered. When the cell opens to the port of constant high pressure, the pressure ratio of the primary shock wave is lowered in heat transfer case as the pressure increase caused by the primary shock wave is smaller and the pressure before being compressed by the primary shock wave is higher ($\theta = 14.4°$, see pressure differences $\varDelta_p$ in Fig. 4-35 (a-2)), and thus the primary shock wave is weaker. Moreover, the pressure behind the primary shock wave (located to the left of PSW in Fig. 4-35 (a-2)) is lower, too. An analytical argument in Appendix F expounds the cause of the lower post-shock pressure.

The weaker shock wave is reflected and propagates leftwards in the cell ($\theta = 35.3°$, see Fig. 4-35 (a-3)), and the pressure of the twice-compressed fluid behind the weaker reflected shock wave is, without doubt, lower. The expansion waves propagate in the cell to halt the compression process ($\theta = 66.2°$, see Fig. 4-36 (a-1)), and the pressure in the cell is lower after compression process. Thereby, the compression ratio of the compression process is lower when heat transfer works. Besides, temperature after compression process is also lower in heat transfer case (Fig. 4-36 (b-1)) owing to weaker shock waves.

{Expansion process}

Likewise, for the discussion of expansion process, pressure and temperature at selected degrees are shown in Fig. 4-36 (a-2) ~ (b-2), (a-3) ~ (b-3), and Fig. 4-37 (a-1) ~ (b-1), (a-2) ~ (b-2). When affected by heat transfer, as has been addressed, pressure is lower after compression process, which is also true right before expansion process but the difference is very small ($\theta = 79.9°$, see Fig. 4-36 (a-2); notice that the vertical scale is much smaller than in (a-1)). Therefore, when the cell opens to GL port of constant low pressure for discharging, it can be deduced that the expansion effect is a little weaker in heat transfer case, and that the pressure difference between heat transfer case and adiabatic case tends to be even smaller. In addition, in Fig. 4-31 it is apparent that the expanded gas is persistently heated during opening to GL port (indicated by "heating" label). This negative heat flux implying that the fluid receives heat is also observable in the region affected by expansion waves in the axial distribution of heat flux shown in Fig. 4-36 (d-3) and in the whole range in Fig. 4-37 (d-1) when the gas is adequately expanded. For both reasons, at the moment right before opening to AL port ($\theta = 117°$, see Fig. 4-37 (a-1)), the pressure in the heat transfer case is higher, and this difference lasts throughout expansion process, which can be inferred from pressure difference in Fig. 4-37 (a-2) for $\theta = 147°$ when the compression wave propagates to finalize expansion process. After expansion process, air continues being heated and gas is slightly cooled by wall (Fig. 4-37 (d-3)).

Change in charging and discharging

To take a panoramic view, the heat transfer effects on charging and discharging total pressure and total temperature in 1/10 size are most noteworthy when linked with low pressure ports AL or GL, and mass flow rates related to all ports are affected much. Shown in Fig. 4-43 are the properties averaged over cross-section of cell end (left end or right end) during charging and discharging, where series (*letter*-1), (*letter*-2) and (*letter*-3) denote total pressure, total temperature and axial momentum, respectively. Each graph denotes the trace in a whole degree interval opening to a specified port. The axial coordinate in each of the graphs corresponds to the circumferential angular degree of the lower bound of the cell shown in Fig. 4-4 to Fig. 4-9 (not to be confused with the circumferential center of the cell), meaning that the moment when the cell starts to open to GH port the degree is 0°. Between each pair of vertical dashed lines colored in blue is the degree range of full open (F. O.), while in the remaining two sides are partial open (P. O.).

{Total pressure and mass flow rate}

When opening to high pressure ports GH or AH, the pressure is lower in the heat transfer case (Fig. 4-43 (a-1) & (b-1)). When opening to low pressure ports AL and GL, the pressure is higher in the heat transfer case (Fig. 4-43 (c-1) & (d-1)).

The discussions on change in internal flow field reveal that when heat transfer works, pressure in the cell is lower after twice-compression and higher during charging from AL port. As a consequence, compared with the adiabatic case, in the heat transfer case,

1) when opening to GH port, the inflow pressure is lower (Fig. 4-43 (b-1)) and the mass flow rate is enhanced by 5% (can be inferred from Fig. 4-43 (b-3)) as the inflow is faster; the greater inflow speed is explained in Appendix F describing an analytical calculation of ideal shock tube;

2) when opening to AH port, the exhaust pressure is lower (Fig. 4-43 (b-1)) and the mass flow rate is reduced by 5% (can be inferred from Fig. 4-43 (b-3));

3) the inflow from AL port is impeded by higher pressure on the left end during opening to AL port (Fig. 4-43 (c-1)), and thus the mass flow rate is reduced by 12% (can be inferred from Fig. 4-43 (c-3));

4) the pressure of the exhausted gas flowing to GL port is higher (Fig. 4-43 (d-1)), and the mass flow rate is enhanced by 5% (can be inferred from Fig. 4-43 (d-3)).

{Total temperature}

Respecting the fluid temperature discharged towards AH port, although the profile is changed, the change in overall temperature caused by heat transfer is small, since the gas is colder and the air is hotter in heat transfer case.

The discharged gas is colder when heat transfer works because of lower compression ratio of compression process. Although the compression ratio is reduced, the temperature of the exhausted air is a little bit higher (Fig. 4-43 (b-2)) owing to the heating after the fresh air flows into the cell, which can be seen in the air path in Fig. 4-31. The position and length of the air part are approximately confirmed by examining the opening span for AH port on the right side of wave diagram in Fig. 4-33 (b) or Fig. 4-34 (b), as well as by scrutinizing the three-dimensional flow field data.

Delay of arrival of reflected shock wave

Moreover, a more striking effect is noticed in 1/10 size.

Degree traces of total pressure during charging from GH port and discharging to AH port in compression process are shown in Fig. 4-43 (a-1) and (b-1), and the enlarged ones around shock waves' arrivals are shown in Fig. 4-44 (a) and (b), respectively. The vertical dashed lines, as are consistent with those in Fig. 4-43, indicate the degree switching between partial open and full open. In Fig. 4-44 (a) it denotes the beginning of shut of left end, and in Fig. 4-44 (b) it shows the degree that the cell is fully opened to AH port. The vertical solid line indicates complete closure at the left end in Fig. 4-44 (a) and the beginning of opening to AH port in Fig. 4-44 (b). The primary shock wave arrives at the right end as soon as it starts to open to AH port in both adiabatic case and heat transfer case, the arrival of which can be identified by rapid rise of pressure. In Fig. 4-44 (a), the reflected shock wave in adiabatic case arrives at the left end as soon as the end begins shutting, whereas that in heat transfer case arrives late (delayed for 2° ~ 3°). Such a delay of arrival of shock wave calls for degree adjustment in design, and further modifications are necessary in response to degree adjustment. This delay is not observed in 10X size. The reason for the delay is explained in the following paragraphs.

The primary cause of this delay is the higher inflow speed during opening to GH port in heat transfer case. Comparing axial velocities of inflow during opening to GH port in Fig. 4-45, it is found that the velocity difference between adiabatic case and heat transfer case is trivial in 10X size, but in 1/10 size it is distinct and the average velocity in heat transfer case is about 7% greater than that in adiabatic case. Since the reflected shock wave travels left against the rightward moving flow, a higher flow speed in front slows the shock wave.

The higher axial velocity is also caused by heat transfer. As has been demonstrated, compared with the adiabatic case, in the heat transfer case the pressure at 0° is higher (Fig. 4-35 (a-1)) and the temperature is much higher (Fig. 4-35 (b-1)), and hence the density is smaller. Seeing that in Fig. 4-35 (c-1) the axial velocities in both cases are near zero, and given these initial states before opening to GH port, the velocity caused by primary shock wave is greater in heat transfer case (also analyzed in Appendix F).

Fig. 4-43 Total pressure, total temperature and axial momentum at cell ends during opening to ports for adiabatic case and heat transfer case of 1/10 size (P. O.: partial open; F. O.: full open)

(a) Around arrival of reflected shock wave

(b) Around arrival of primary shock wave
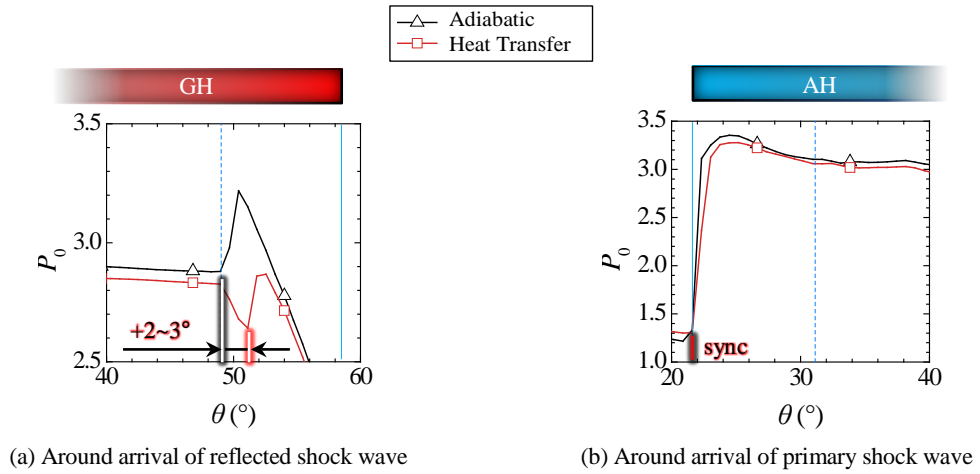
Fig. 4-44 Pressure history on left end and right end during charging and discharging in compression process for 1/10 size
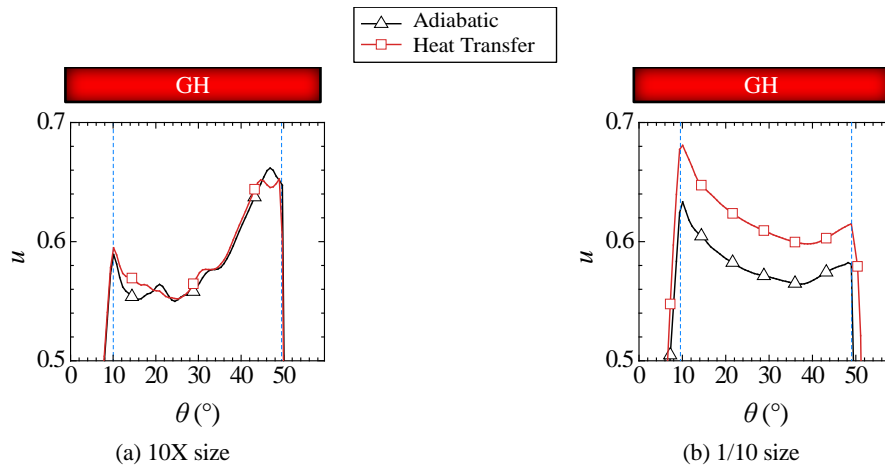


(a) 10X size

(b) 1/10 size

Fig. 4-45 Axial velocity history on left end during opening to GH port for 10X size and 1/10 size

*4.2.3.2    10X Size in Comparison with 1/10 Size*

In 10X size, the effects of heat transfer on flow field are the least among the sizes investigated, and the effects are supposed to be common in conventional size. Axial distributions at selected degrees are shown in Fig. 4-24 ~ Fig. 4-26, and the comparison of cell end parameters during charging and discharging are presented in Fig. 4-46.

The changes in the internal flow field are slight in 10X, but most of the heat transfer effects are consistent with those discussed in 1/10 size. An exception that is worth keeping an eye on is that the "air" temperature discharged towards AH port shows greater difference in 10X size (Fig. 4-46 (b-2)). In fact, the effects on the pressure ratio of primary shock wave is less in 10X size (Fig. 4-24 (a-2)) than in 1/10 size (Fig. 4-35 (a-2)); that is, in 10X size, the strength of primary shock wave is affected less profoundly by heat transfer, and the compression ratio of both shock waves are abated more. Furthermore, it is observable that the difference in charging temperature of air from AL port is about 0.05 in 1/10 size (Fig. 4-43 (c-2)), obviously much greater than that in 10X size (Fig. 4-46 (c-2)). In heat transfer case, this air is heated, compressed, and discharged to AH port. The discharged air temperature exceeds that in adiabatic case by about 0.05 in 1/10 size. With this knowledge, it is inferred that in the competition between weaker compression effect and greater heating effect, the weaker compression becomes as effective as greater heating in 1/10 size. Thereby, it can be further inferred that heat transfer effects on pressure requires more attention in smaller size.
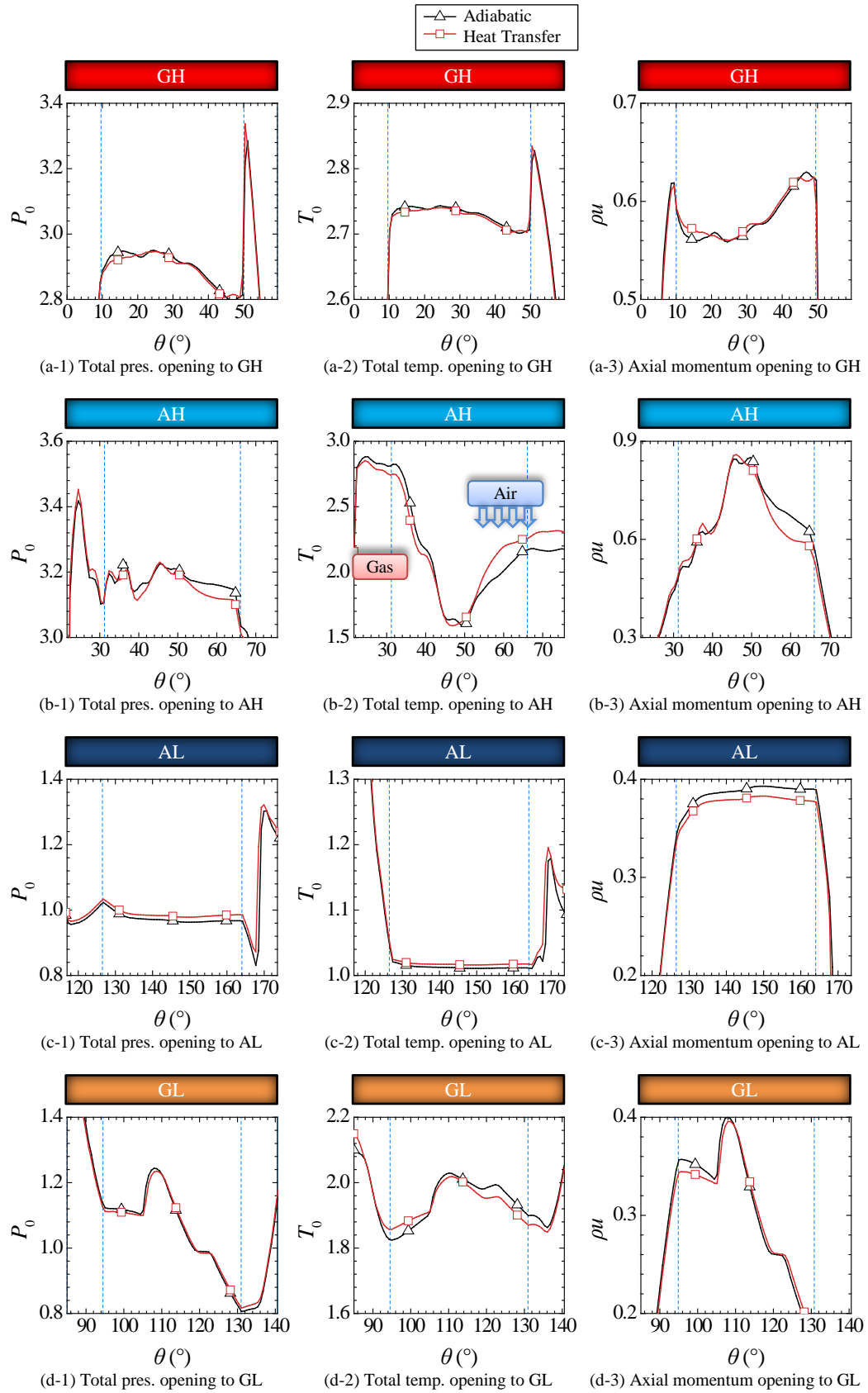
Fig. 4-46 Total pressure, total temperature and axial momentum at cell ends during opening to ports for adiabatic case and heat transfer case of 10X size

### 4.2.4    Heat Transfer Effects across Sizes

The axial momentums at cell ends during opening to ports are shown in Fig. 4-43 (a-3) ~ (d-3) for 1/10 size. Remarkable differences in axial momentum are observed in all ports. As a result, the mass flow rates when opening to ports change for 5~11%, as are summarized in Fig. 4-51. Difference between adiabatic case and heat transfer case is obtained by the following equation:

$$Difference = \frac{Average\ value\ in\ heat\ transfer\ case}{Average\ value\ in\ adiabatic\ case} - 1 \tag{4.5}$$

In comparison, the mass flow rate when opening to port relating to air (AH or AL) changes no more than 3% in 10X size (discussed in absolute value of difference, the same below), and for GH and GL negligible (below 0.2%). Admittedly, it is untenable to take for granted that small sizes share these significant effects or conventional sizes share those insignificant. For instance, 1X size, one of the small sizes, exhibits heat transfer effects on charging and discharging (Fig. 4-47) more like a transition stage when reducing size from 10X (Fig. 4-46) to 1/10 (Fig. 4-43). Therefore, the effects of heat transfer on charging and discharging are studied among 10X, 3X, 1X, 1/3 and 1/10 sizes. 10X and 3X sizes stand for conventional size and 1X, 1/3 and 1/10 sizes stand for small size.

However, it is complicated and arduous to compare the profile differences across sizes. To give a clear image of the trend as size reduces, the differences of pressure, temperature and mass flow rate at cell ends during opening to ports are summarized in Fig. 4-48 ~ Fig. 4-50. Shown in Fig. 4-48 are the differences in mass flow rate. The vertical bars in the graph are divided into four groups standing for four ports. In each group, the differences are displayed in descending order by size. Hereby, the differences of 5%~11% in 1/10 size mentioned earlier are placed fifth for each port. It is apparent that when opening to low pressure ports (AL and GL) the differences caused by heat transfer rise drastically when switching from 1X to 1/3 size. Also for low pressure ports, in small sizes 1/3 and 1/10, the differences are considerable (5%~12%).

Besides, the differences in total pressure and total temperature are enumerated in Fig. 4-49 and Fig. 4-50, respectively. Again, for low pressure ports, the following points are discovered: i) noticeable differences (3% ~ 6%) for 1/3 size and 1/10 size, and ii) drastic increase when reducing size from 1X to 1/3.

With regards common phenomena of the temperature on wall inner surfaces, through comparison among Fig. 4-19 (a) (10X), Fig. 4-52 (a) (1X) and Fig. 4-32 (a) (1/10), it is discovered that wall temperature is generally distributed around 2.1 and varies little along axial direction. As the wall is externally insulated from outside, wall temperature reflects a thermal balance between the flow of hot gas and that of cold air, and the resultant wall temperature is close to 2.14, the value of average temperature of ports defined by Eq. (4.6) in Section 4.3. Moreover, because wall temperature does not change too much across sizes, it can be presumed that even though given the same temperature boundary condition, heat transfer across fluid-solid interface would induce much greater effects on charging and discharging in small sizes in the trend shown in this subsection. By comparing Fig. 4-19 (b) (10X), Fig. 4-52 (b) (1X) and Fig. 4-32 (b) (1/10), it is observed that the shroud side is always colder than the hub side, because the colder fluid inclines to occupy the radially further side (shroud side) in cell under rotation, as has been explained in Subsection 4.2.1.

Fig. 4-47 Total pressure, total temperature and axial momentum at cell ends during opening to ports for adiabatic case and heat transfer case of 1X size
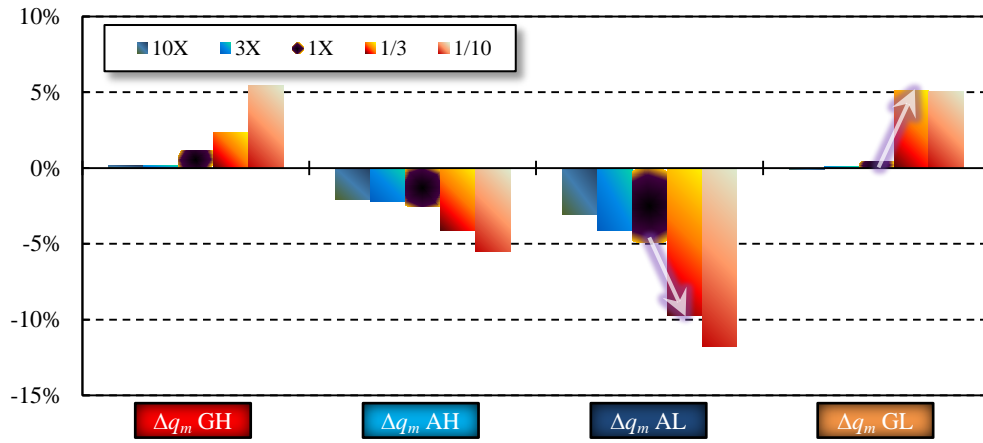
Fig. 4-48 Differences in <u>mass flow rate</u> when opening to ports for various sizes
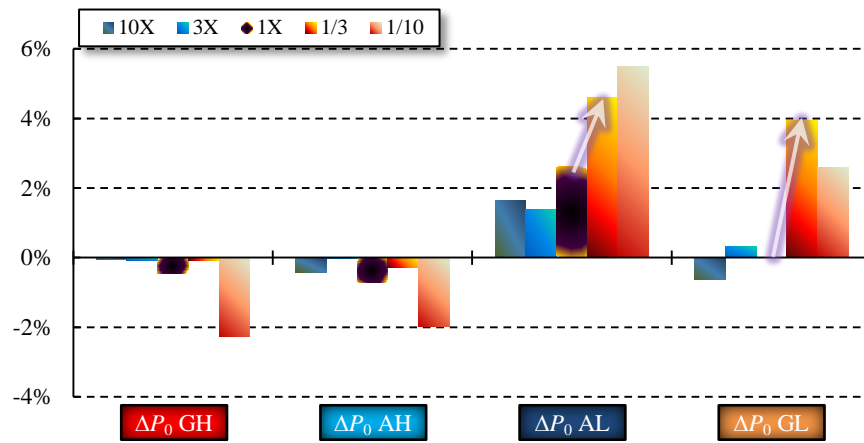


Fig. 4-49 Differences in average total pressure when opening to ports for various sizes
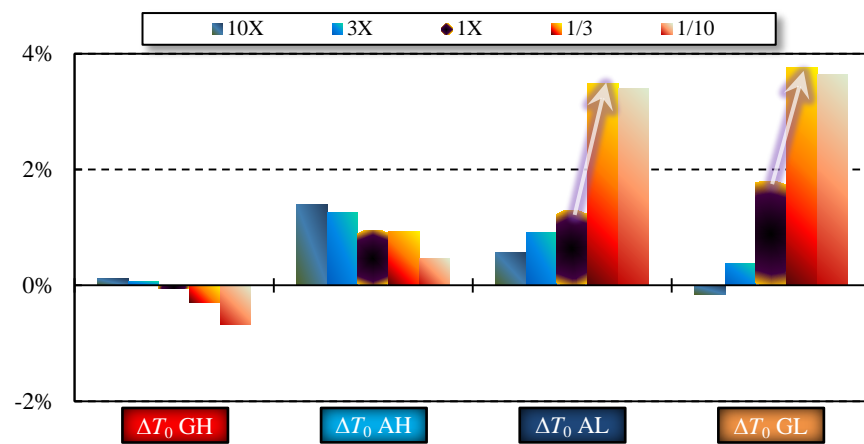


Fig. 4-50 Differences in average total temperature when opening to ports for various sizes
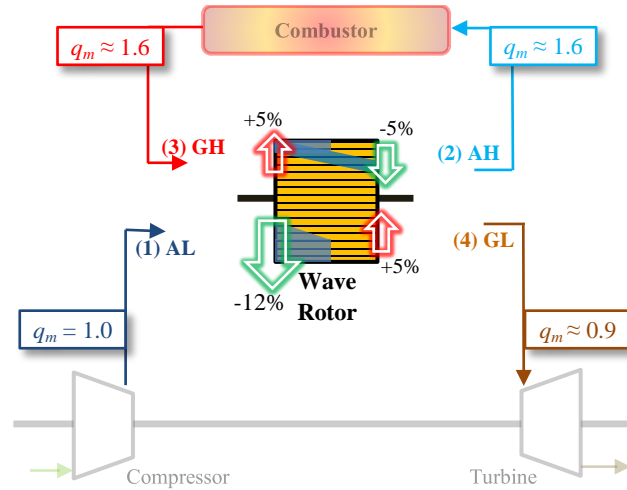
Fig. 4-51 Mass flow rate **through each port** in design ($q_m$) and changes in mass flow rate **through cell ends** caused by heat transfer in 1/10 size
($q_m$ of GH, AH and GL ports normalized by that of AL port)



(a) Interface temperature averaged on cross-sections

(b) Interface temperature in four wall sides
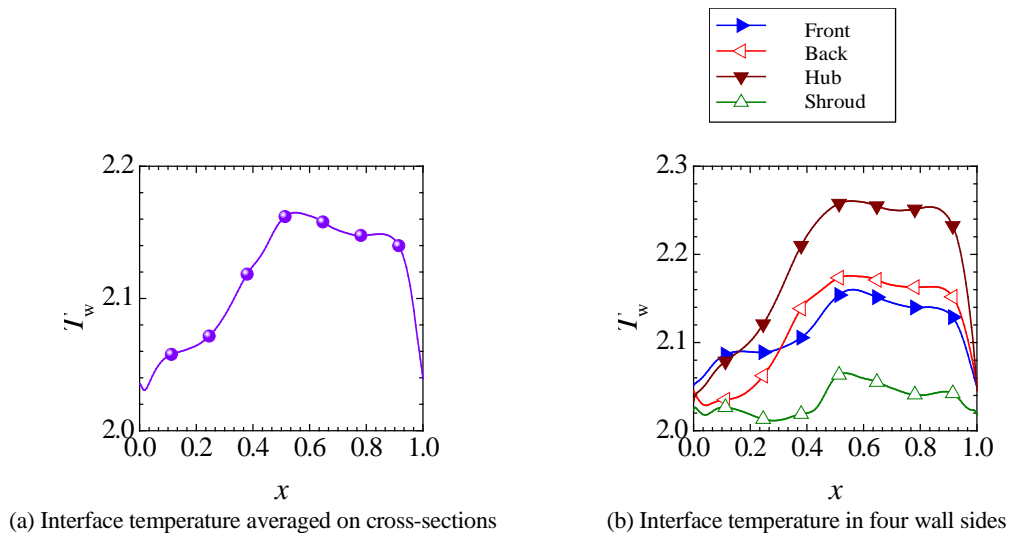
Fig. 4-52 Axial distributions of interface temperature at initial degree for heat transfer case of 1X size

## 4.2.5   Under Averaged Wall Temperature

Axial variation in wall temperature profile and difference among wall sides are noticed in Fig. 4-19 and Fig. 4-32. The range of temperature on wall inner surface without normalization is 80 K (10X size) or 30 K (1/10 size). Compared with the port temperature difference of maximum 800 K, this range is fairly small. For a through-flow wave rotor that taking advantage of cooling effect as hot gas and cold air alternately flow through the cell, it is sound that the wall temperature is well-distributed. Eyeing this fact, it is natural to consider whether an appropriate temperature can be applied as uniform temperature boundary condition when studying heat transfer effects.

Here, as an attempt, a temperature obtained by averaging wall temperature in heat transfer case is applied as the uniform wall temperature. To observe the greatest possible effects, 1/10 size is put into numerical experiment. The normalized wall temperature is 2.07 (≈ 910 K). Shown in Fig. 4-53 are the axial distributions at 0° right before compression process. The conjugate heat transfer case is the heat transfer case appears in previous discussions. For each of the parameters, both cases almost coincide with each other. With regard to charging and discharging, the comparison is presented in Fig. 4-54. Likewise, it is difficult to distinguish the uniform wall temperature case from the conjugate one. Since the uniform wall temperature case resembles the conjugate one in every respect, the heat transfer effects based on comparison with adiabatic case do not change even if the conjugate heat transfer case is substituted by the uniform wall temperature case. More numerical comparisons are conducted for 1X size and 10X size, and each shows resemblance between uniform wall temperature case and conjugate one.

The likeness implies that with an appropriate, or properly estimated, wall temperature, isothermal wall condition may be helpful in analysis of heat transfer effects for through-flow wave rotor, and could be an economical alternative since conjugate heat transfer requires a significant amount of computing resource.
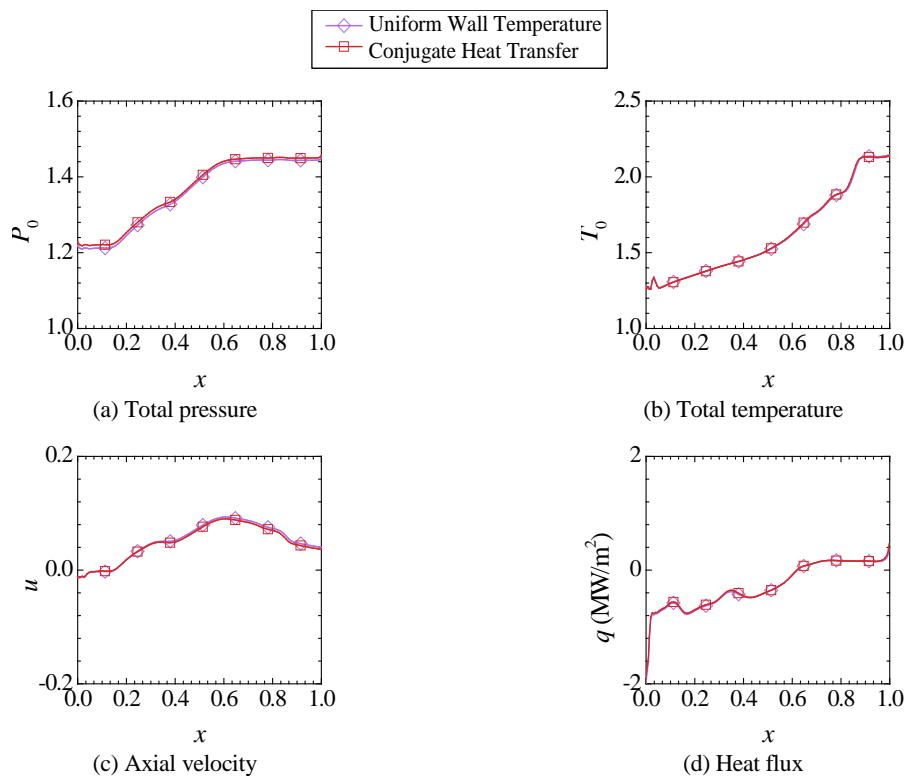


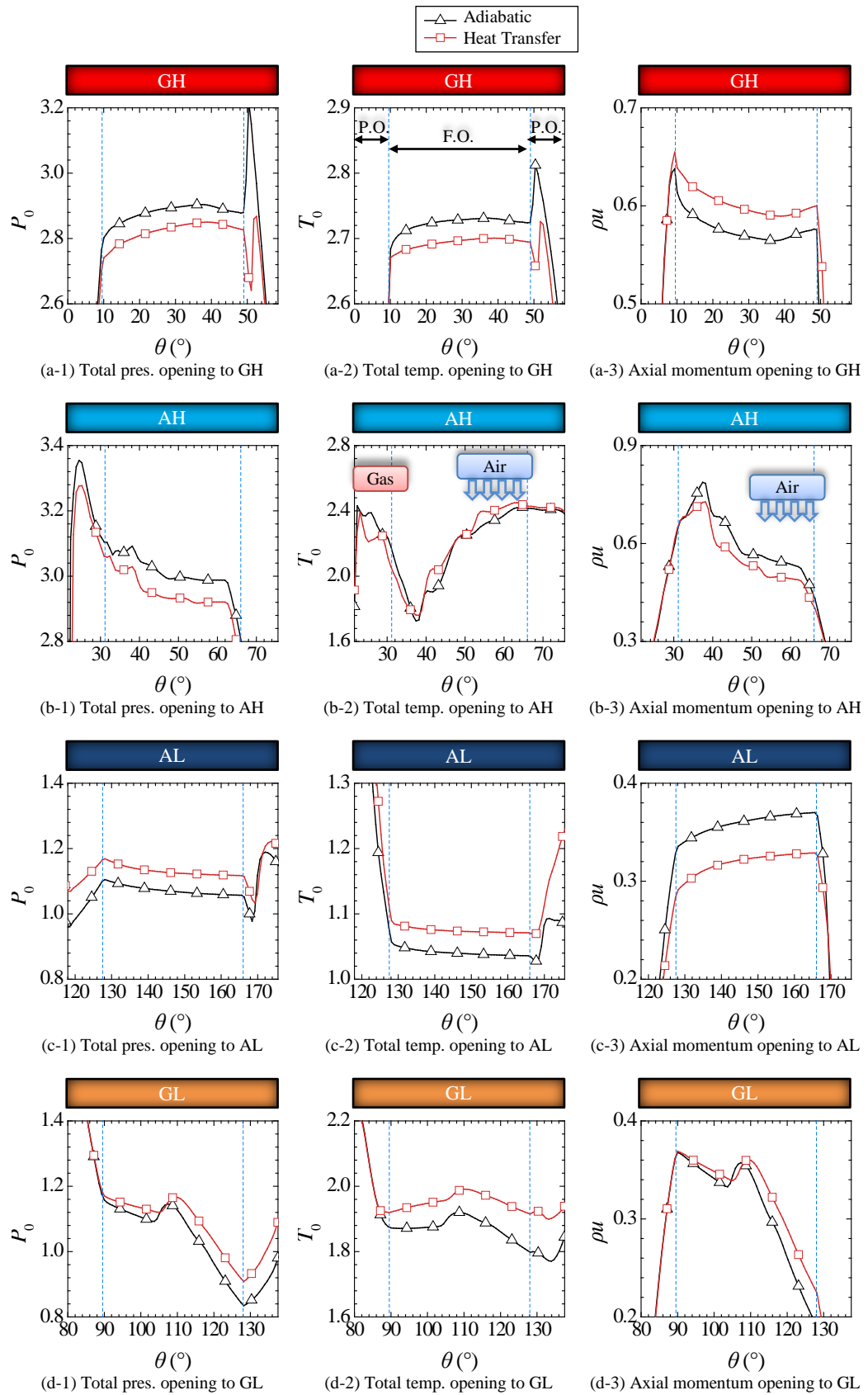Fig. 4-53 Axial distributions at 0° for conjugate heat transfer case and uniform wall temperature case of 1/10 size
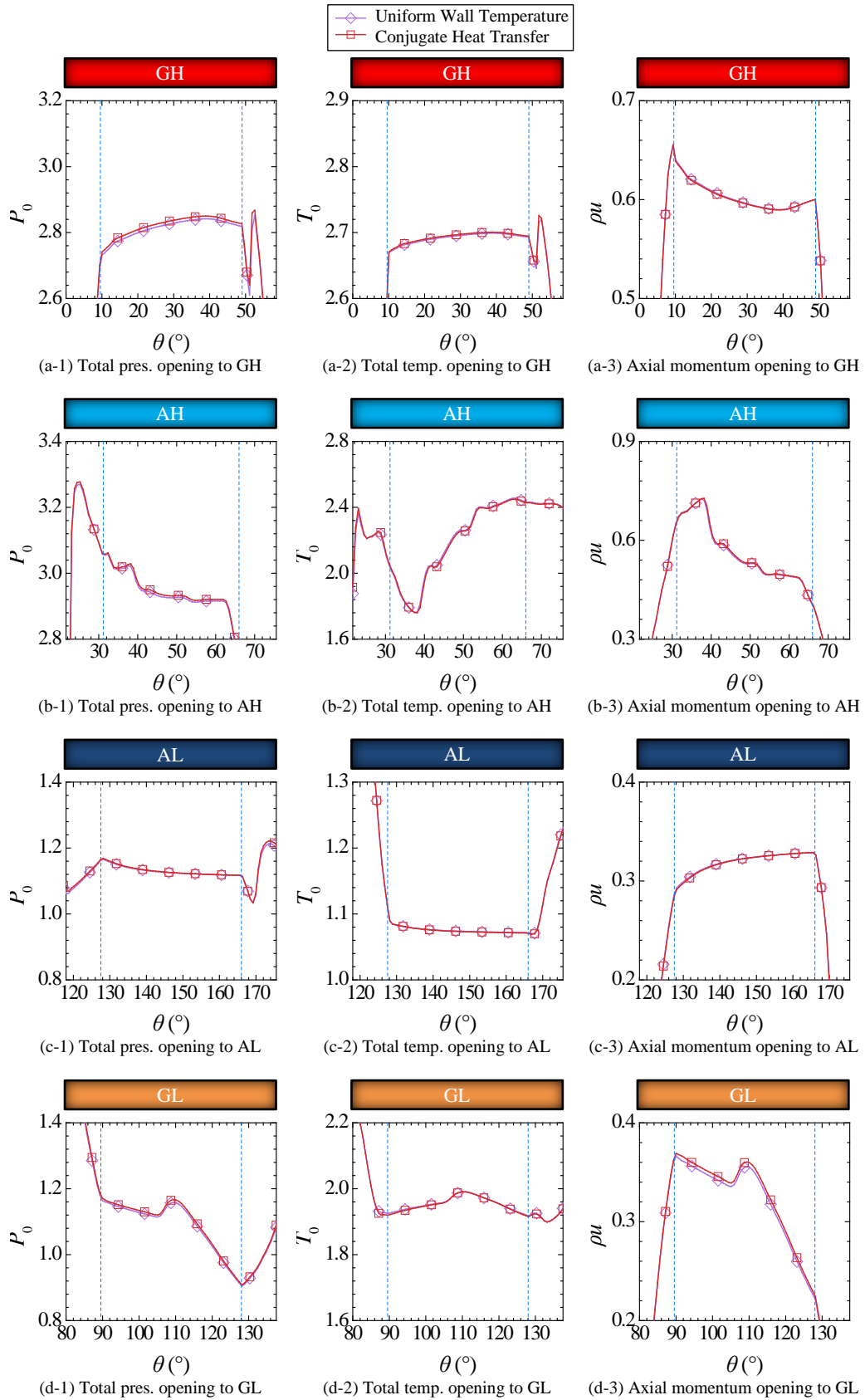
Fig. 4-54 Total pressure, total temperature and axial momentum at cell ends during opening to ports for conjugate heat transfer case and uniform wall temperature case of 1/10 size

## 4.3   Cases Subject to External Heat Transfer

In the previous section, the external boundary of wall is thermally insulated. Since the solid wall is assumed to undergo no heat transfer with the surroundings. Hence, energy only flows into or out from the investigated system with fluid through cell ends. It stands for a condition that the external surface of wall is well insulated. In practice, it may be a necessity to consider heat exchange with surroundings of cell. This section introduces a situation when simple external heat transfer is taken into account.

As has been described in Subsection 4.1.1, for this situation, the external surfaces of shroud and hub are subject to constant convective heat transfer, and those of front and back are subject to periodic condition. For simplification, the external pressure is assumed to be consistent with total pressure in AL port of the lowest pressure, and the external surroundings are assumed to be quiescent and infinite. The external temperature is consistent with an average temperature determined by total temperatures and mass flow rates in all ports:

$$T_{\text{ext}} = \frac{\sum q_{\text{m}} T_{\text{port,tot}}}{\sum q_{\text{m}}} \tag{4.6}$$

where $q_{\text{m}}$ is mass flow rate of port, $T_0$ is total temperature of port, and $T_{\text{ext}}$ is the resultant external flow temperature. A classical solution is employed to determine the convective heat transfer coefficient related to rotating horizontal cylinder in quiescent fluid [88], which can be written as

$$\text{heat transfer coefficient: } h_{\text{ext}} = \frac{\text{Nu}_{\text{avg}} k_{\text{ext}}}{D_{\text{o}}} \tag{4.7}$$

$$\text{average Nusselt number: } \text{Nu}_{\text{avg}} = 0.1 \text{Re}_{\text{r}}^{2/3} \tag{4.8}$$

$$\text{rotating Reynolds number: } \text{Re}_{\text{r}} = \frac{\rho_{\text{ext}} \omega D_{\text{o}}^{2}}{2 \mu_{\text{ext}}} \tag{4.9}$$

where $k_{\text{ext}}$ is thermal conductivity of external fluid, $D_{\text{o}}$ is hub diameter of wave rotor (diameter of cylinder), $\rho_{\text{ext}}$ is density of external fluid, $\omega$ is angular velocity of wave rotor, and $\mu_{\text{ext}}$ is dynamic viscosity of external fluid.

For 1/10 size, the heat transfer coefficient is 612 W/(m²·K), and the normalized external temperature is 2.14 (940 K). This external temperature is greater than but very close to wall temperature in Fig. 4-32. As a result, the wall temperature is a little higher when external heat transfer is considered, as is shown in Fig. 4-55, where the externally insulated case stands for the heat transfer case in the previous section.

Essentially consistent with the previous results and acquisition in Subsection 4.2.5, as long as the change in wall temperature is not so significant, the effects of heat transfer on flow field are almost qualitatively unaffected, which can be known by examine effects of heat transfer on internal flow field at 0° for externally insulated case and external heat transfer case. For 0° in 1/10 size, the comparison between the externally insulated case and the adiabatic case is shown in Fig. 4-35 (a-1), (b-1) and (c-1), and the comparison between the external heat transfer case and the adiabatic case is shown in Fig. 4-56 (a), (b) and (c). It is observable that the changes in distributions of total pressure, total temperature and axial caused by heat transfer are almost the same.

With approximately identical wall temperature and flow field at 0°, the changes in charging and discharging parameters are also very similar. By comparing between Fig. 4-43 and Fig. 4-57, heat transfer effects are found to be changeless when switching from externally insulated case to external heat transfer case.

Stated thus, those discussions in the previous section for 1/10 size can also explain the effects of heat transfer when external heat transfer with the assumptions mentioned above.

Nevertheless, it is imaginable that when the convection condition applied to external surfaces of wall is different, the response of flow field could be changed more or less. The exploration for external heat transfer beyond the bounds of the present study may provide some valuable information. Because the surroundings of the rotating component of wave rotor vary case by case and have much less in common than internal flow field of cell, research approach related to external heat transfer may require great effort.
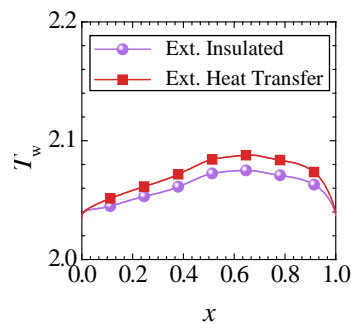


Fig. 4-55 Comparison of axial distributions of wall temperature between <u>externally insulated</u> case and <u>external heat transfer</u> case



(a) Total pressure    (b) Total temperature    (c) Axial velocity
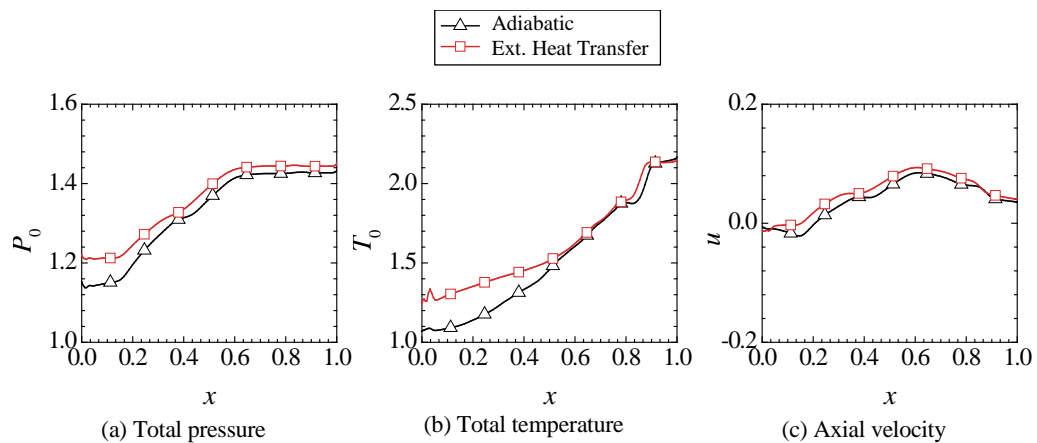
Fig. 4-56 Axial distributions at 0° for <u>adiabatic</u> case and <u>external heat transfer</u> case of <u>1/10</u> size
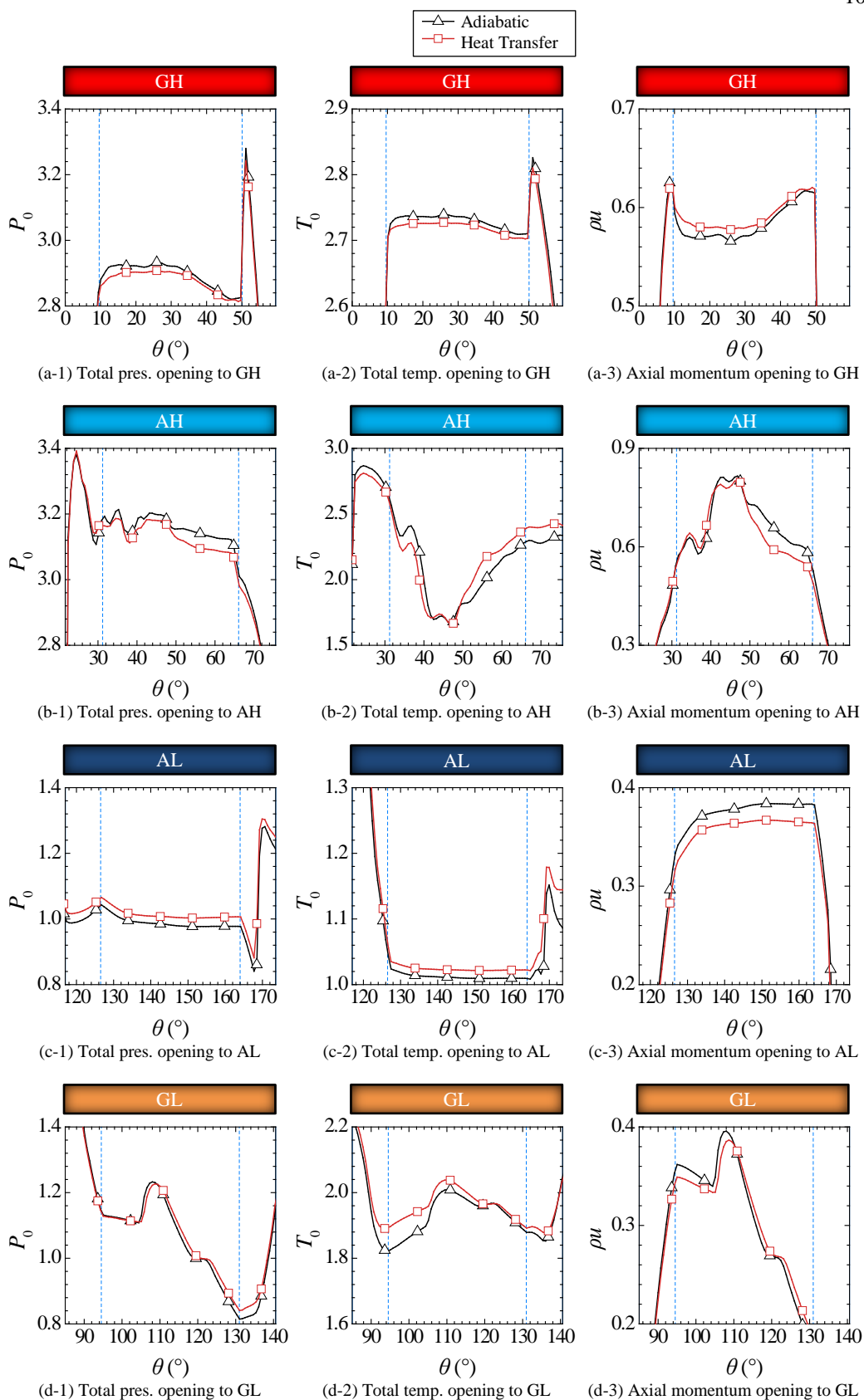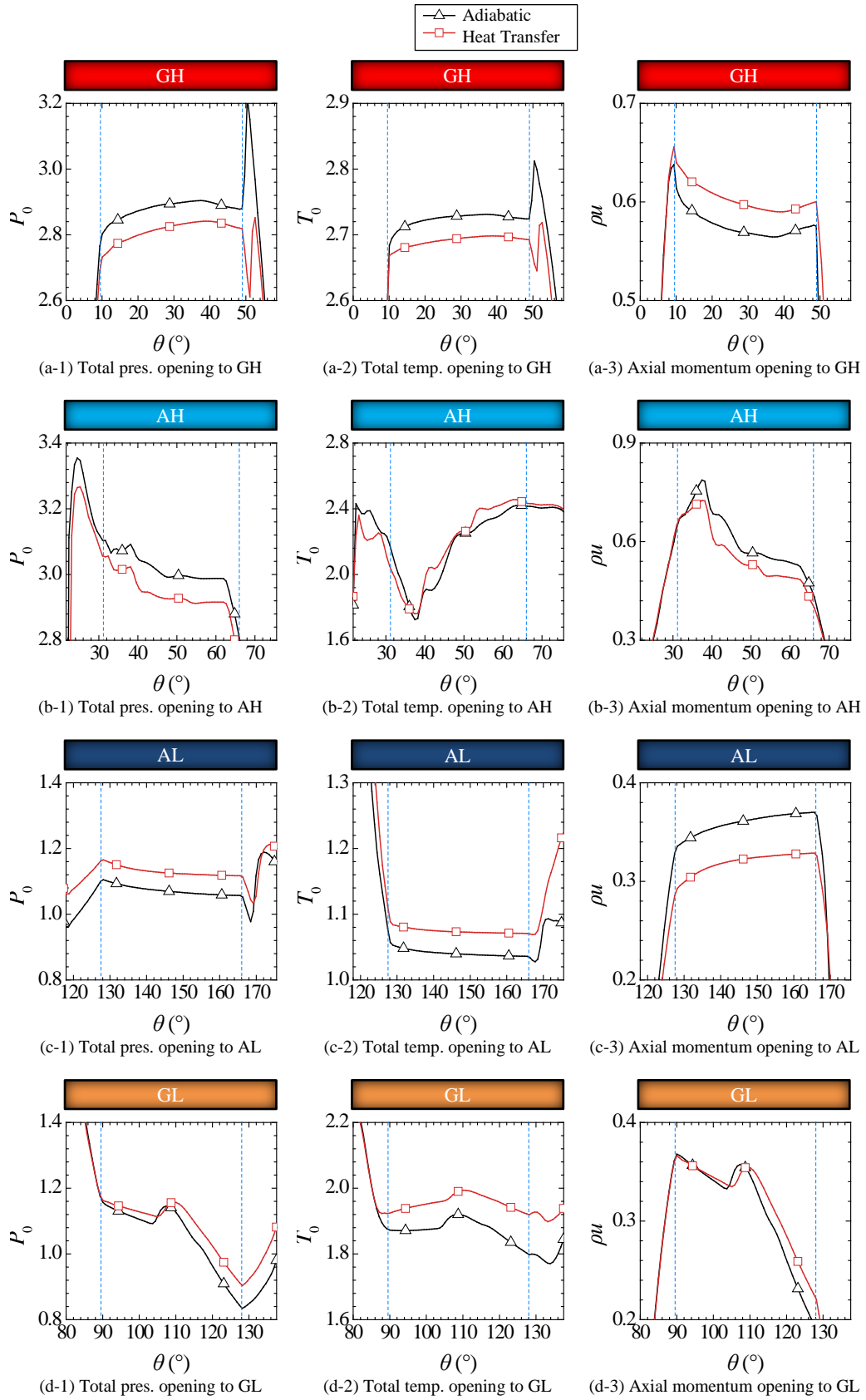
Fig. 4-57 Total pressure, total temperature and axial momentum at cell ends during opening to
ports for <u>adiabatic</u> case and <u>external heat transfer</u> case of <u>1/10</u> size

# CHAPTER 5: SUMMARY AND CONCLUSIONS

The effects of heat transfer across the interface between internal flow passage and cell wall in small wave rotor are investigated. The important conclusions drawn from the investigations of this hitherto barely researched subject are now summarized. The following three principal subjects are addressed: causes of intense heat transfer, the effects of heat transfer in wave rotors of conventional size and small size and their causal phenomena, heat transfer effects on flow across sizes. Two additional cases are studied and corresponding acquisition is gained. Possible extensions of this work which might form the basis of future work are also proposed.

## 5.1 Principal Findings

1) Causes of intense heat transfer

In all sizes investigated, high-speed inflows of hot gas and cold air, as well as gas and air compressed by either primary shock wave or reflected shock wave are found to cause intense heat transfer. Shock waves propagating in gas are found to cause considerable heat flux in corresponding downstream vicinities.

In small size, heat transfer caused by expansion waves and compression wave becomes noticeable, and compression wave induces heat transfer from air to wall, which is different from conventional size. Heat transfer from air to wall caused by primary shock wave is also discovered in primary shock wave downstream vicinity.

2) Effects of heat transfer on flow

Fresh air from low pressure inlet (AL) of lowest temperature is inevitably heated by the wall. Since increase of pressure under heating is hindered by leakage, density becomes lower when heat transfer is considered. As a result, pressure is a little higher than in adiabatic case while temperature is much higher. These differences in states before compression process result in weaker shock waves and many other chain effects in flow field in cell, and consequently affect charging and discharging.

Heat transfer effects on charging and discharging related to air (AL port and air part in AH port) in conventional size are relatively significant among the effects on charging and discharging parameters. In small size, naturally, heat transfer effects on charging and discharging related to all ports are noticeable, and an important change that the arrival of reflected shock wave is delayed is observed (at the size that hydraulic diameter is 0.392 mm or surface-area-to-volume ratio is $1.18 \times 10^4$), which indicates that modification of port degree, as well as corresponding design change on other elements, should be implemented.

3) Effects across sizes

In small size category, heat transfer effects on charging and discharging grow rapidly when reduced from 1X size, i.e. surface-area-to-volume ratio greater than 1.18 mm$^{-1}$. In small sizes 1/3 and 1/10 (surface-area-to-volume ratio greater than 3.53 mm$^{-1}$), low pressure ports are most affected and their related changes caused by heat transfer are considerable, implying that much more attention to heat transfer effects is required in such small wave rotors.

## 5.2 Additional Findings

1) As long as conjugate heat transfer requires a significant amount of computing resource, if an appropriate temperature can be assigned to the lateral wall as uniform wall temperature, isothermal boundary condition could be an economical alternative for investigation of heat transfer for through-flow wave rotor whose wall temperature is distributed relatively evenly.

2) Seeing that external flow temperature is close to wall temperature estimated in externally insulated case, the effects of heat transfer on flow field are qualitatively unaffected by external convective heat transfer.

## 5.3 Suggestions for Future Work

1) Arrival delay of pressure wave requires design modification, and design considers such heat transfer effect is worth attempting.

2) To develop an approach for estimating appropriate isothermal wall temperature is meaningful and challenging.

3) The present work studies flow field and heat transfer related to through-flow type wave rotor, wall temperature range of whose cell is relatively narrow. The other one, reverse-flow type, has wall temperature higher on the gas side and lower on the air side, and the difference can be comparable with flow temperature difference. The effects of heat transfer for reverse-flow type is still unbeknown although the research on through-flow type may provide some knowledge.

# BIBLIOGRAPHY

[1]     A. V. Luikov, *Analytical heat diffusion theory*. Academic Press, New York, USA, 1968, pp. 238–240, 422–426.

[2]     A. Calabria, R. Capata, M. Di Veroli, and G. Pepe, "Testing of the Ultra-Micro Gas Turbine Devices (1-10 kW) for Portable Power Generation at University of Roma 1: First Tests Results," *Engineering*, vol. 5, pp. 481–489, 2013.

[3]     O. Dessornes, S. Landais, R. Valle, A. Fourmaux, S. Burguburu, C. Zwyssig, and Z. Kozanecki, "Advances in the Development of a Microturbine Engine," *Journal of Engineering for Gas Turbines and Power*, vol. 136, pp. 71201–1, 2014.

[4]     A. H. Epstein, "Millimeter-scale, MEMS gas turbine engines," *in ASME Turbo Expo 2003, collocated with the 2003 International Joint Power Generation Conference*, 2003, pp. 669–696.

[5]     K. Isomura, M. Murayama, S. Teramoto, K. Hikichi, Y. Endo, S. Togo, and S. Tanaka, "Experimental verification of the feasibility of a 100 W class micro-scale gas turbine at an impeller diameter of 10 mm," *Journal of micromechanics and microengineering*, vol. 16, no. 9, p. S254, 2006.

[6]     JQR, "A promising technology for powering humanoid robots? - Development of an ultra-compact gas turbine capable of generating large amounts of power anywhere," *Japan Quality Review*, vol. 22, pp. 24–27, Jun. 2012.

[7]     J. Li, S. K. Chou, Z. Li, and W. Yang, "Development of 1D model for the analysis of heat transport in cylindrical micro combustors," *Applied Thermal Engineering*, vol. 29, no. 8, pp. 1854–1863, 2009.

[8]     N. Müller, F. V. Iancu, and P. Akbari, "Ultra-micro gas turbine," US Patent 7,934,368, May.,2011.

[9]     T. Nagashima, "Lessons learnt from the ultra-micro gas turbine development at University of Tokyo," *Micro Gas Turbines*, vol. 131, 2005.

[10]    T. Nagashima, K. Okamoto, and Y. Ribaud, "Cycles and thermal system integration issues of ultra-micro gas turbines," *RTO-AVT-VKI Lecture Series 2005 "Micro Gas Turbines" Educational Notes RTO-EN-AVT-131 Paper 4*, pp. 1–66, 2005.

[11]    A. Robinson, H.-W. Funke, P. Hendrick, E. Recker, and J. Peirs, "Development of a hydrogen fuelled 1 kW ultra micro gas turbine with special respect to designing, testing and mapping of the μ-scale combustor," *in Sustainable Energy Technologies, 2008. ICSET 2008. IEEE International Conference on*, 2008, pp. 656–660.

[12]    T. Stevens and M. Baelmans, "Optimal pressure drop ratio for micro recuperators in small sized gas turbines," *Applied Thermal Engineering*, vol. 28, no. 17, pp. 2353–2359, 2008.

[13]    N. Müller and L. G. Fréchette, "Performance analysis of brayton and rankine cycle microsystems for portable power generation," *in ASME 2002 International Mechanical Engineering Congress and Exposition*, 2002, pp. 513–522.

[14]    C. Seippel, "Gas turbine installation," US Patent 2,461,186, 1949.

[15]    P. K. Doerfler, "Comprex Supercharging of Vehicle Diesel Engines," SAE Technical Paper 750335, 1975.

[16]    G. Gyarmathy, "How does the Comprex® Pressure-Wave Supercharger Work?," SAE Technical Paper 830234, 1983.

[17]    P. Akbari and N. Müller, "Performance investigation of small gas turbine engines topped with wave rotors," *39th AIAA/ASME/SAE/ASEE Joint Propulsion Conference and Exhibit*, AIAA 2003-4414, 2003.

[18]    R. B. Greendyke, D. E. Paxson, and M. Schobeiri, "Dynamic Simulation of a Wave Rotor Topped Turboshaft Engine," *Journal of Propulsion and Power*, vol. 16, no. 5, pp. 792–796, Jul. 2000.

[19]    D. E. Paxson, "A numerical model for dynamic wave rotor analysis," *31st AIAA/ASME/SAE/ASEE Joint Propulsion Conference and Exhibit*, San Diego, California, USA, Jul. 10-12, NASA TM-106997, AIAA-95-2800, 1995.

[20]    D. E. Paxson, J. Wilson, and G. E. Welch, "Comparison between simulated and experimentally measured performance of a four port wave rotor," AIAA 2007-5049, NASA TM-2007-214985, 2007.

[21]    D. W. Paxson, "A General Numerical Model for Wave Rotor Analysis," NASA TM-105740, Jul. 1992.

[22]    P. H. Snyder, "Wave rotor demonstrator engine assessment," NASA CR-198496, Jun.,1996.

[23]    G. E. Welch, "Overview of Wave-Rotor Technology for Gas Turbine Engine Topping Cycles," *Novel Aero Propulsion Systems International Symposium*, The Institution of Mechanical Engineers, pp. 2–17, 2000.

[24]    G. E. Welch, D. E. Paxson, J. Wilson, and P. H. Snyder, "Wave-Rotor-Enhanced Gas Turbine Engine Demonstrator," DTIC Document, NASA TM-1999-209459, ARL-TR-2113, Oct. 1999.

[25]    J. Wilson and D. E. Paxson, "Jet engine performance enhancement through use of a wave-rotor topping cycle," NASA TM-4486, 1993.

[26] J. Wilson, G. E. Welch, and D. E. Paxson, "Experimental results of performance tests on a four-port wave rotor," AIAA 2007-1250, NASA TM-2007-214488, 2007.

[27] A. Fatsis, A. Lafond, and Y. Ribaud, "Preliminary analysis of a three-inlet wave-rotor with the aid of a numerical model," *in Colloque d'Aerodynamique Appliquee, 32 nd, Lyon, France, Mar. 25-27, 1996, ONERA, TP*, 1996, no. 1996–73.

[28] A. Fatsis and Y. Ribaud, "Thermodynamic analysis of gas turbines topped with wave rotors," *Aerospace Science and Technology*, vol. 3, no. 5, pp. 293–299, 1999.

[29] K. Okamoto, "Wave Rotor Gasdynamics for an Aeropropulsion System," *in ICAS PROCEEDINGS*, 2000, no. 734, p. 4.

[30] K. Okamoto, T. Nagashima, and K. Yamaguchi, "Rotor-wall clearance effects upon wave rotor passage flow," *in ISOABE, ISABE- International Symposium on Air Breathing Engines, 15 th, Bangalore, India*, 2001.

[31] Y. Ribaud and V. Quintilla, "The Wave-Rotor for turbine engines and turbojets: description, operation and use," *Nouvelle Revue d'Aéronautique et d'Astronautique*, vol. 6, no. 5, pp. 42–49, 1998.

[32] F. Iancu, P. Akbari, and N. Müller, "Feasibility Study of Integrating Four-Port Wave Rotors into Ultra-Micro Gas Turbines (UμGT)," *Proceedings of 40th AIAA/ASME/SEA/ASEE Joint Propulsion Conference and Exhibit*, Fort Lauderdale, Florida, USA, AIAA2004-3581, 2004.

[33] M. Araki, T. Ishima, T. Obokata, M. Arai, and K. Okamoto, "LDA Measurement of an Intermittent High-Speed Flow inside a Micro Wave Rotor Cell," SAE Technical Paper 2007-01-0010, 2007.

[34] K. Okamoto, "Port condition effects on wave rotor internal flow dynamics," *in 13th International Symposium on Unsteady Aerodynamics, Aeroacoustics and Aeroelasticity of Turbomachines 2012 (ISUAAAT 13)*, Sep., 2012.

[35] K. Okamoto and M. Araki, "Shock wave observation in narrow tubes for a parametric study on micro wave rotor design," *Journal of thermal science*, vol. 17, no. 2, pp. 134–140, Jul. 2008.

[36] K. Okamoto and T. Nagashima, "Simple numerical modeling for gasdynamic design of wave rotors," *Journal of propulsion and power*, vol. 23, no. 1, pp. 99–107, 2007.

[37] K. Okamoto and T. Nagashima, "Visualization of wave rotor inner flow dynamics," *Journal of propulsion and power*, vol. 23, no. 2, pp. 292–300, 2007.

[38] K. Okamoto and T. Nagashima, "A simple numerical approach of micro wave rotor gasdynamic design," *16th International Symposium on Airbreathing Engines*, ISABE-2003-1213, 2003.

[39] K. Okamoto and K. Yamaguchi, "Clearance Variation Effects on Micro Wave Rotor Operation," *in Asian Joint Conference on Propulsion and Power 2008*, 2008, pp. 845–851.

[40] A. Fatsis, A. Lafond, and Y. Ribaud, "Preliminary analysis of the flow inside a three-port wave rotor by means of a numerical model," *Aerospace Science and Technology*, vol. 2, no. 5, pp. 289–300, 1998.

[41] A. A. Kharazi, P. Akbari, and N. Müller, "Preliminary Study of a Novel R718 Turbo-Compression Cycle Using a 3-Port Condensing Wave Rotor," *in ASME Turbo Expo 2004: Power for Land, Sea, and Air*, 2004, pp. 381–388.

[42] J. Wilson, "An experiment on losses in a three-port wave rotor," NYMA Inc., NASA CR-198508, Aug. 1997.

[43] P. Akbari and N. Müller, "Gas Dynamic Design Analyses of Charging Zone for Reverse-Flow Pressure Wave Superchargers," *in ASME 2003 Internal Combustion Engine Division Spring Technical Conference*, 2003, pp. 487–497.

[44] J. Piechna, P. Akbari, F. Iancu, and N. Müller, "Radial-flow wave rotor concepts, unconventional designs and applications," *Proceedings of IMECE04 2004 ASME International Mechanical Engineering Congress*, November 13–19, 2004, Anaheim, California, USA, IMECE2004-59022, 2004.

[45] P. Akbari, A. A. Kharazi, and N. Müller, "Utilizing wave rotor technology to enhance the turbo compression in power and refrigeration cycles," *Proceedings of IMECE'03 2003 ASME International Mechanical Engineering Congress and Exposition*, Washington, D.C., USA, November 16-21, 2003, IMECE2003-44222, pp. 75–83, 2003.

[46] Y. Dai, J. Zou, C. Zhu, P. Liu, J. Zhao, L. Zhang, and D. Hu, "Thermodynamic Analysis of Wave Rotor Refrigerators," *Journal of Thermal Science and Engineering Applications*, vol. 2, no. 2, p. 021011, 2010.

[47] P. Akbari, R. Nalim, and N. Mueller, "A review of wave rotor technology and its applications," *Journal of engineering for gas turbines and power*, vol. 128, no. 4, pp. 717–735, 2006.

[48] F. Iancu, J. Piechna, and N. Müller, "Basic design scheme for wave rotors," *Shock Waves*, vol. 18, no. 5, pp. 365–378, 2008.

[49] G. E. Welch, S. M. Jones, and D. E. Paxson, "Wave-rotor-enhanced gas turbine engines," *Journal of Engineering for Gas Turbines and Power*, vol. 119, no. 2, pp. 469–477, 1997.

[50] K. J. Elloye and J. Piechna, "Influence of the heat transfer on the operation of the pressure wave supercharger," *Archive of Mechanical Engineering*, vol. XLVI, no. 4, pp. 297–309, 1999.

[51] D. E. Paxson and J. Wilson, "Recent improvements to and validation of the one dimensional NASA wave rotor model," NASA TM-106913, May 1995.

[52] L. Pohořelský, P. Sané, T. Rozsas, and N. Müller, "Wave Rotor Design Procedure for Gas Turbine Enhancement," *in ASME Turbo Expo 2008: Power for Land, Sea, and Air*, 2008, pp. 847–860.

[53] H. E. Weber, *Shock Wave Engine Design*. John Wiley & Sons, New York, USA, 1995, pp. 121–126.

[54] G. E. Welch, "Macroscopic balance model for wave rotors," *Journal of Propulsion and Power*, vol. 13, no. 4, pp. 508–516, 1997.

[55] L. M. Larosiliere, "Wave rotor charging process - Effects of gradual opening and rotation," *Journal of Propulsion and Power*, vol. 11, no. 1, pp. 178–184, 1995.

[56] D. E. Paxson, "An incidence loss model for wave rotors with axially aligned passages," TM-1998-207923, Jun. 1998.

[57] D. E. Paxson, "A comparison between numerically modelled and experimentally measured loss mechanisms in wave rotors," AIAA-93-2522, NASA TM-106279, 1993.

[58] G. E. Welch and R. V. Chima, "Two-Dimensional Computational Model for Wave Rotor Flow Dynamics," ARL-TR-924, NASA TM-107192, 1996.

[59] G. E. Welch and R. V. Chima, "Two-dimensional CFD modeling of wave rotor flow dynamics," NASA-TM-106261, 1993.

[60] G. Woschni, "A Universally Applicable Equation for the Instantaneous Heat Transfer Coefficient in the Internal Combustion Engine," 1967.

[61] H. Li, M. R. Nalim, and C. L. Merkle, "Transient thermal response of turbulent compressible boundary layers," *Journal of Heat Transfer*, vol. 133, no. 8, p. 081701, 2011.

[62] I. Zal'Tsman, A. Sokol'Skii, V. Shikov, and E. Eigenson, "Shock tube modeling of heat transfer in flow of a high-temperature gas past cavities," *Teplofizika Vysokikh Temperatur*, vol. 29, pp. 515–520, 1991.

[63] C. Frazier, M. Lamnaouer, E. Divo, A. Kassab, and E. Petersen, "Effect of wall heat transfer on shock-tube test temperature at long times," *Shock Waves*, vol. 21, no. 1, pp. 1–17, 2011.

[64] D. Ngomo, A. Chaudhuri, A. Chinnayya, and A. Hadjadj, "Numerical study of shock propagation and attenuation in narrow tubes including friction and heat losses," *Computers & Fluids*, vol. 39, no. 9, pp. 1711–1721, 2010.

[65] J. Yao, Y. Yao, M. Patel, and P. J. Mason, "On Reynolds number and scaling effects in microchannel flows," *The European Physical Journal - Applied Physics*, vol. 37, no. 02, pp. 229–235, 2007.

[66] K. Fujii and S. Obayashi, "High-resolution upwind scheme for vortical-flow simulations," *Journal of Aircraft*, vol. 26, no. 12, pp. 1123–1129, 1989.

[67] K. Fujii and S. Obayashi, "Navier-Stokes simulations of transonic flows over a practical wing configuration," *AIAA journal*, vol. 25, no. 3, pp. 369–370, 1987.

[68] T. Ogawa and K. Fujii, "Numerical investigation of three-dimensional compressible flows induced by a train moving into a tunnel," *Computers & Fluids*, vol. 26, no. 6, pp. 565–585, 1997.

[69] S. Teramoto, K. Hiraki, and K. Fujii, "Numerical analysis of dynamic stability of a reentry capsule at transonic speeds," *AIAA journal*, vol. 39, no. 4, pp. 646–653, 2001.

[70] E. Shima and T. Jounouchi, "Role of CFD in Aeronautical Engineering (No.14) -AUSM Type Upwind Schemes-," *in Proceedings of the 14th NAL Symposium on Aircraft Computational Aerodynamics, 1997*, 1997, pp. 7–12.

[71] B. van Leer, "Towards the ultimate conservative difference scheme. V. A second-order sequel to Godunov's method," *Journal of Computational Physics*, vol. 32, no. 1, pp. 101–136, Jul. 1979.

[72] Barrett Stone Baldwin and H. Lomax, "Thin layer approximation and algebraic model for separated turbulent flows," *35th AIAA Fluid Dynamics Conference and Exhibit*, Huntsville, Alabama, USA, Jan. 16-18, AIAA 78-257, 1978.

[73] M.-S. Liou and C. J. Steffen Jr, "A new flux splitting scheme," *Journal of Computational physics*, vol. 107, no. 1, pp. 23–39, 1993.

[74] P. L. Roe, "Approximate Riemann solvers, parameter vectors, and difference schemes," *Journal of computational physics*, vol. 43, no. 2, pp. 357–372, 1981.

[75] E. Shima and K. Kitamura, "On new simple low-dissipation scheme of AUSM-family for all speeds," *47th AIAA Aerospace Sciences Meeting including The New Horizons Forum and Aerospace Exposition*, Orlando, Florida, USA, Jan. 5-8, AIAA 2009-136, 2009.

[76] G. van Albada, B. van Leer, and W. Roberts Jr, "A comparative study of computational methods in cosmic gas dynamics," *Astronomy and Astrophysics*, vol. 108, pp. 76–84, 1982.

[77] D. W. Peaceman and H. H. Jr Rachford, "The numerical solution of parabolic and elliptic differential equations," *Journal of the Society for Industrial & Applied Mathematics*, vol. 3, no. 1, pp. 28–41, 1955.

[78] E. F. Toro, *Riemann Solvers and Numerical Methods for Fluid Dynamics*. Springer, New York, USA, 1997.

[79] S. V. Patankar, *Numerical heat transfer and fluid flow*. McGraw-Hill, New York, USA, 1980, pp. 60–102.

[80] J. C. Jo, Y. H. Choi, and S. K. Choi, "Numerical analysis of unsteady conjugate heat transfer and thermal stress for a curved piping system subjected to thermal stratification," *Journal of Pressure Vessel Technology*, vol. 125, no. 4, pp. 467–474, 2003.

[81] T. W. Davies, "Biot number," Thermopedia (TM), http://www.thermopedia.com/ content/585/, 2011.

[82]    T. Roediger, H. Knauss, J. Srulijes, F. Seiler, and E. Kraemer, "A novel fast-response heat-flux sensor for measuring transition to turbulence in the boundary layer behind a moving shock wave," in *Shock Waves*, Springer Berlin Heidelberg, 2009, pp. 415–420.

[83]    JEOL Ltd., "Instructions JTG-5200/5600/5700 Thermoviewer," 1990.

[84]    Vatell Corporation, "Heat Flux Microsensors (HFM)," http://www.vatell.com/ node/5.

[85]    J. H. Lienhard IV and J. H. Lienhard V., *A Heat Transfer Textbook, 3rd Edition*. Cambridge: Phlogiston Press, 2006.

[86]    B. Cushman-Roisin and J.-M. Beckers, *Introduction to geophysical fluid dynamics: physical and numerical aspects*, 2nd ed., vol. 101. Academic Press, 2011, pp. 348–361.

[87]    F. P. Incropera and D. P. DeWitt, *Fundamentals of Heat and Mass Transfer, 4th Edition*. New York: John Wiley & Sons, 1996.

[88]    J. Anderson and O. Saunders, "Convection from an isolated heated horizontal cylinder rotating about its axis," *Proceedings of the Royal Society of London. Series A. Mathematical and Physical Sciences*, vol. 217, no. 1131, pp. 555–562, 1953.

[89]    J. Wilson, "Design of the NASA Lewis 4-Port Wave Rotor Experiment," NYMA, Inc., AIAA-97-3139, NASA CR-202351, Jun. 1997.

[90]    K. Okamoto, K. Yamaguchi, and T. Nagashima, "Development of Micro Wave Rotor Test Model," 45th Asian Joint Conference on Propulsion and Power, the Kitakyushu International Conference Center, Kitakyushu, Japan, Jan., 2005, AJCPP2005-21021.

[91]    A. S. Dorfman, *Conjugate problems in convective heat transfer*. CRC Press, 2010.

[92]    A. Dorfman and Z. Renner, "Conjugate Problems in Convective Heat Transfer: Review," *Mathematical Problems in Engineering*, vol. 2009, no. 927350, p. 27, 2009.

[93]    W. Zhang, Z. Huang, C. Zhang, and G. Xi, "Conjugate wall conduction-fluid natural convection in a three-dimensional inclined enclosure," *Numerical Heat Transfer, Part A: Applications*, vol. 61, no. 2, pp. 122–141, 2012.

[94]    M. Sheremet, "Three-dimensional conjugate natural convection in a vertical cylinder under heat transfer to the surroundings," *Fluid Dynamics*, vol. 46, no. 4, pp. 647–657, 2011.

[95]    F. Montomoli, P. Adami, and F. Martelli, "A finite-volume method for the conjugate heat transfer in film cooling devices," *Proceedings of the Institution of Mechanical Engineers, Part A: Journal of Power and Energy*, vol. 223, no. 2, pp. 191–200, 2009.

[96]    F. Duchaine, S. Mendez, F. Nicoud, A. Corpron, V. Moureau, and T. Poinsot, "Conjugate heat transfer with Large Eddy Simulation for gas turbine components," *Comptes Rendus Mécanique*, vol. 337, no. 6, pp. 550–561, 2009.

[97]    A. R. Crowell, B. A. Miller, and J. J. McNamara, "Computational Modeling for Conjugate Heat Transfer of Shock-Surface Interactions on Compliant Skin Panels," 4-7 April 2011, Denver, Colorado, USA, 52nd AIAA/ASME/ASCE/AHS/ASC Structures, Structural Dynamics and Materials Conference, 2011.

[98]    L. He and M. Oldfield, "Unsteady conjugate heat transfer modeling," *Journal of Turbomachinery*, vol. 133, no. 3, p. 031022, 2011.

[99]    S. Deng, K. Okamoto, and T. Susumu, "Numerical Investigation of Heat Transfer Effects in Small Wave Rotor," Asian Joint Conference on Propulsion and Power 2014, Jeju Island, Korea Mar 5-8, 2014, AJCPP-2014-70, 2014.

# APPENDICES

## Appendix A. Description of the Micro Wave Rotor and Characteristics of the Wave Rotor of the Present Study

The original model of the 1X wave rotor investigated in this work is the micro wave rotor designed for kW scale ultra-micro gas turbines [10], [37]. Key geometry information of the wave rotor cell is shown in Fig. A-1. 30 cells are arranged around the revolution axis, and the rotation speed is 32000 RPM. For this 4-port through-flow wave rotor, the port degrees are shown in Fig. A-2. Port conditions are listed in Table 4-1, and those after normalization based on corresponding AL states are listed in Table 4-5.

Some characteristics of the design of this wave rotor are presented in this paragraph. The first can be exemplified by the total temperature contour calculated by 1-D numerical model for this wave rotor shown in Fig. A-3. Obviously, a portion of gas is not exhausted to GL port in expansion process. It occupies about half of cell length after expansion process and is recirculated in compression process. The second is that the cell undergoes no port opening after expansion process. The idle interval equals to more than half of the wave rotor cycle. This configuration is determined with an eye to related experimental test rig, but is designed to be ready for improvement by simply switching it from "1 cycle per revolution" to "2 cycles per revolution" since the degree span from the beginning of compression process to the end of expansion process only makes use of 160.3°.

In order to find out heat transfer effects for more typical wave rotor in which active span prevails, the present work employs "2 cycles per revolution" configuration improved from this original one as 1X size model. The active span that either end of the cell opens to port composes about 80% of the degree of a wave rotor cycle. Certainly, the 1X size wave rotor has similar recirculation of gas. And the scaled ones (10X, 3X, 1/3, 1/10) share those particulars characterizing the 1X size model except of those related to scaling. To sum up, the wave rotors appear as object of study in the present work is characterized by 1) four-port, 2) axial through-flow, 3) straight cell, 4) with recirculation of gas, and 5) active span prevails.

By taking states in AL port as reference, Reynolds number can be assessed for simplified flow if the flow in cell was steady and its inlet condition was kept identical to states in AL port, although flow in wave rotor cell is indeed highly unsteady. The assessed Reynolds numbers may describe the flow in wave rotor with a cursory sense. The mass flow rate of AL port is about 20 g/s [36]. The inlet flow speed can be written as

$$u_{\mathrm{AL}} = \frac{q_{m,\mathrm{AL}}}{\rho_{\mathrm{AL}} A_{\mathrm{AL\text{-}to\text{-}cells}}} \tag{A.1}$$

where $A_{\mathrm{AL\text{-}to\text{-}cells}}$ denotes the flow area of charging flow from AL port to cells, $\rho_{\mathrm{AL}}$ is density in AL port, and $q_{m,\mathrm{AL}}$ is the mass flow rate of AL port; and Reynolds numbers for flow over a flat plate and channel flow are

$$\mathrm{Re}_x = \frac{\rho_{\mathrm{AL}} u_{\mathrm{AL}} x}{\mu_{\mathrm{AL}}} \tag{A.2}$$

$$\mathrm{Re}_D = \frac{\rho_{\mathrm{AL}} u_{\mathrm{AL}} D_{\mathrm{H}}}{\mu_{\mathrm{AL}}} \tag{A.3}$$

respectively, where $x$ ranging from 0 to cell length $L$, $D_{\mathrm{H}}$ is the hydraulic diameter. The values are listed in Table A-2.

For reference to typical 4-port through-flow wave rotor, Reynolds numbers related to a NASA 4-port wave rotor are also listed in Table A-2. The wave rotor cell is 267×16.5×33.0 (*Length×Width×Height*, in mm), and its blade thickness is 0.762 mm; the outer diameter is 203 mm and the midspan diameter is 170 mm; cell number is 30; and the mass flow rate of AL port varies from 249 g/s to 317 g/s. [26], [89] The opening span of AL port is 81.4° (inferred from literature [20]). Numerical simulations were implemented with the 1-D code for comparison with measured data, and one of the results is shown in Fig. A-4.
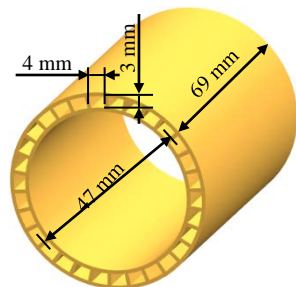


Fig. A-1 Cell size and midspan diameter
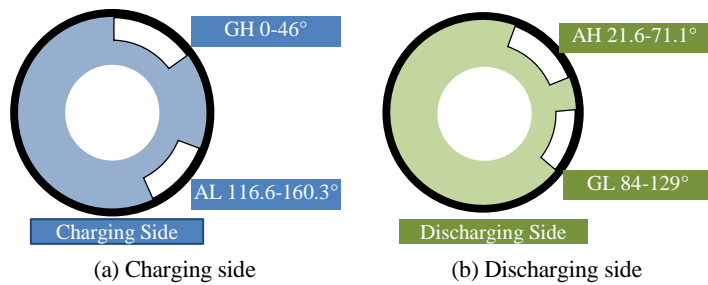
Fig. A-2 Port positions and degrees of original micro wave rotor

(a) Charging side    (b) Discharging side
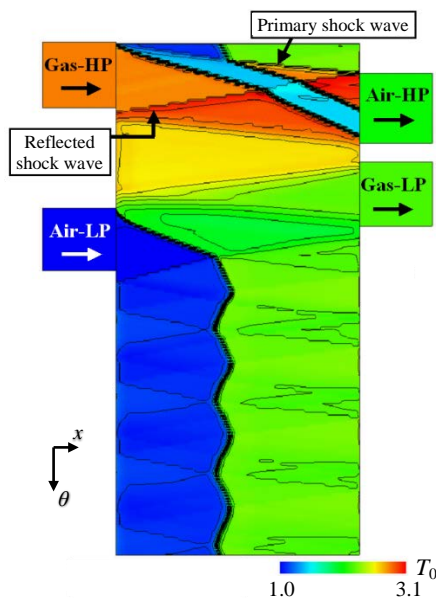


Fig. A-3 Total temperature distribution for micro wave rotor [90]
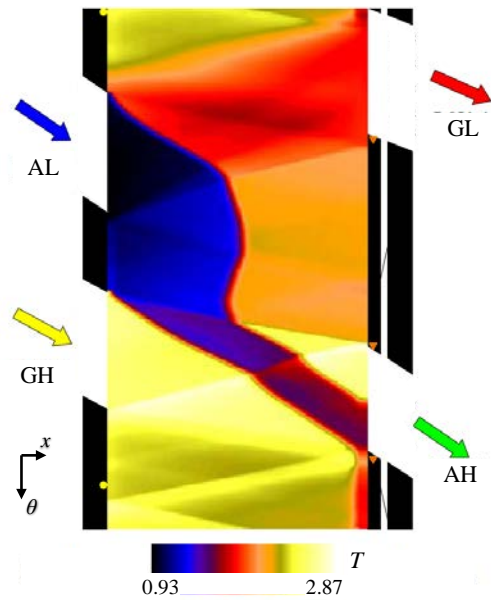
Fig. A-4 Temperature distribution for design point of the NASA 4-port wave rotor (normalized by total temperature in AL of 222 K) [20]

Table A-1 Port conditions of original micro wave rotor

|  | Charging ports | | Discharging ports | |
| --- | --- | --- | --- | --- |
|  | GH (Gas-HP) | AL (Air-LP) | AH (Air-HP) | GL (Gas-LP) |
| Total Pressure (MPa) | 0.93 | 0.30 | 1.02 | 0.37 |
| Total Temperature (K) | 1248 | 440 | 907 | 973 |

Table A-2 Assessment of Reynolds number

| Model | $Re_x$ ($x=L$) | $Re_D$ |
| --- | --- | --- |
| 10X (conventional size) | $9.53 \times 10^6$ | $5.42 \times 10^5$ |
| 3X (conventional size) | $2.86 \times 10^6$ | $1.62 \times 10^5$ |
| 1X (small size) | $9.53 \times 10^5$ | $5.42 \times 10^4$ |
| 1/3 (small size) | $3.18 \times 10^5$ | $1.81 \times 10^4$ |
| 1/10 (small size) | $9.53 \times 10^4$ | $5.42 \times 10^3$ |
| NASA 4-port [20] (conventional size) | $1.09 \times 10^6$ | $1.20 \times 10^5$ |

## Appendix B. Order Estimation for Influence of Heat Transfer on Cell Fluid

In order to make a preliminary survey of possible degree of heat transfer effect on cell fluid, simple estimations assuming cell flow to be steady are presented in this section. A wave rotor cycle consists of idle period that fluid is almost motionless and active period that includes compression process and expansion process. Table A-3 shows duration of a wave rotor cycle and durations of active period (opening to a port) and idle periods for three sizes. Obviously, each of the periods is equivalent to 1/4 of a wave rotor cycle in duration. Assuming that convective heat transfer prevails in active period and conduction prevails in idle period, corresponding influences on cell fluid are assessed in this section.

Table A-3 Characteristic time of wave rotor (3 significant figures)

| Model | Duration of a wave rotor cycle (µs) | Average duration of opening to each port (µs) | Average duration of high-pressure idle period (µs) | Average duration of low-pressure idle period (µs) |
| --- | --- | --- | --- | --- |
| 10X (conventional size) | 9680 | 2520 | 2310 | 2330 |
| 1X (small size) | 1000 | 260 | 239 | 241 |
| 1/10 (small size) | 115 | 29.9 | 26.2 | 27.7 |

### B1. Convection

To ensure consistency in all sizes, the flow is assumed to be turbulent. Average Nusselt numbers for turbulent flow over an isothermal plate and for fully developed turbulent pipe flow are written as [85]

$$Nu_{L,avg} = 0.037 \, Re_L^{0.8} \, Pr^{0.43} \tag{A.4}$$

$$Nu_{D,avg} = \frac{(f/8)Re_D Pr}{1+12.8(Pr^{0.68}-1)\sqrt{f/8}}$$  (A.5)

where $f$ is friction factor, Pr is Prandtl number. The material properties are listed in Table A-4. The velocity boundary layer thickness is estimated by [85]

$$\delta = 0.37 Re_x^{-0.2} x$$  (A.6)

and the ratio of its maximum to half of hydraulic diameter is

$$\frac{\delta_{max}}{D_H/2} = \frac{0.37 Re_L^{-0.2} L}{D_H/2}$$  (A.7)

The assessed Nusselt numbers and heat transfer coefficients are enumerated in Table A-5. As size reduces from 10X to 1X or from 1X to 1/10, the rate of increase of heat transfer coefficient is about 50%. Besides, it is found that $h_{L,avg}$ is close to $h_{D,avg}$ at every size. The remaining estimations in this chapter are then based on $h_{L,avg}$.

Table A-4 Material properties of air based on AL states (3 significant figures)

| Parameter | | Value | Unit |
|---|---|---|---|
| Thermal conductivity | $k_f$ | 0.0359 | W/(m·K) |
| Density | $\rho_f$ | 2.61 | kg/m$^3$ |
| Specific heat | $c_{p,f}$ | 1020 | J/(kg·K) |
| Thermal diffusivity | $\alpha_f$ | $4.40\times10^{-5}$ | m$^2$/s |
| Dynamic Viscosity | $\mu_s$ | $2.48\times10^{-5}$ | kg/(m·s) |
| Prandtl number | Pr | 0.703 | 1 |

Table A-5 Assessment of parameters for fluid

| Model | $Nu_{L,avg}$ | $h_{L,avg}$ (W/(m$^2$·K)) | $Nu_{D,avg}$ | $h_{D,avg}$ (W/(m$^2$·K)) | $\delta_{max}/(D_H/2)$ |
|---|---|---|---|---|---|
| 10X (conventional size) | $1.22\times10^4$ | $6.34\times10^2$ | $6.28\times10^2$ | $6.57\times10^3$ | 0.598 |
| 1X (small size) | $1.93\times10^3$ | $1.00\times10^3$ | $9.98\times10^1$ | $1.04\times10^3$ | 0.948 |
| 1/10 (small size) | $3.06\times10^2$ | $1.59\times10^3$ | $1.59\times10^1$ | $1.66\times10^3$ | 1.50 |
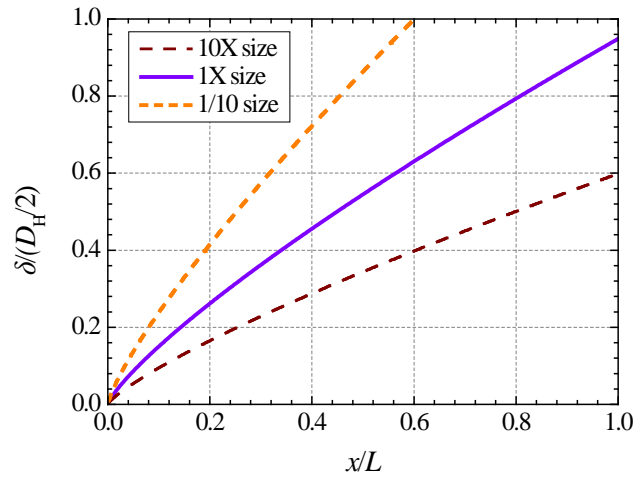
Fig. A-5 Thickness of velocity boundary layer along axial direction

The axial distributions of boundary thickness are shown in Fig. A-5. Within cell length, the maximum thickness of boundary layer normalized by half of hydraulic diameter of each size is listed in Table A-5. Since the thickness of thermal boundary layer equals that of velocity boundary layer, it is known that the fluid is obviously affected. Although the assessment of boundary layer thickness is based on equation for flow over plate, it does provide some references before commencing the present study.

### B2. Conduction

Assuming that only heat conduction works in idle period, the following equation is employed for assessing the extent of boundary temperature's influence:

$$\delta_{99} = 3.64\sqrt{\alpha_\mathrm{f} t} \tag{A.8}$$

where $\delta_{99}$ is the depth location where the normalized temperature $\Theta = \dfrac{T - T_{\mathrm{boundary}}}{T_{\mathrm{initial}} - T_{\mathrm{boundary}}}$ becomes 99%. The relationship between depth $\delta_{99}$ normalized by half of hydraulic diameter and time $t$ normalized by duration of idle period ($t_{\mathrm{idle}}$) is shown in Fig. A-6. It is seen that conduction can only influence a depth less than 10% of half of hydraulic diameter in 10X size, but in 1X and 1/10 sizes the affected temperatures extend to 20% and 70% of half of hydraulic diameter. As an example, the non-dimensional bulk temperature for 1X size may follow the history shown in Fig. A-7, and the resultant Mach number normalized by initial Mach number, if it decreases, may follow the history shown in Fig. A-8. For the maximum Ma reduction of 5%, the primary shock wave, if merely affected by this, may arrive 1° later, and the reflected shock wave may be delayed for 2.5° in 1X size.
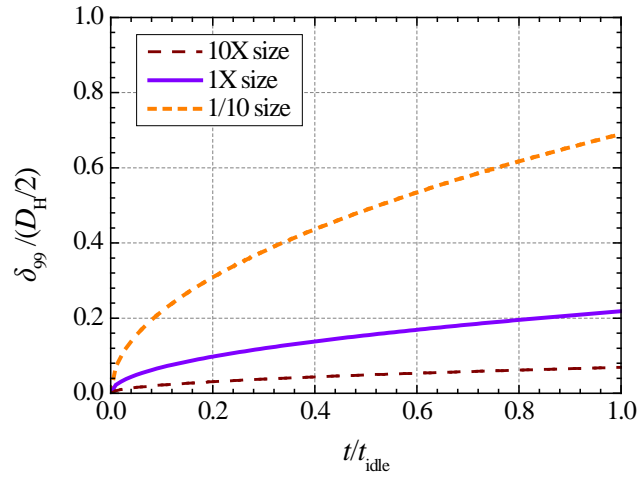
Fig. A-6 Depth of temperature influence (99%) in idle period in conduction
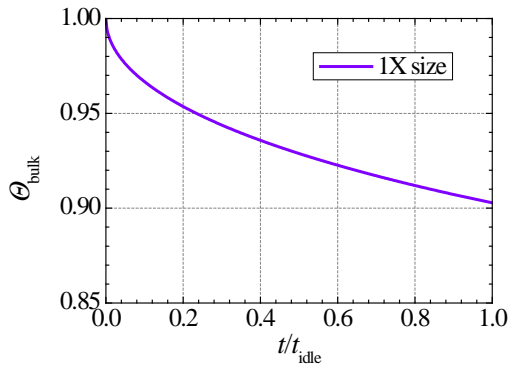


Fig. A-7 Non-dimensional fluid bulk temperature variation under conduction
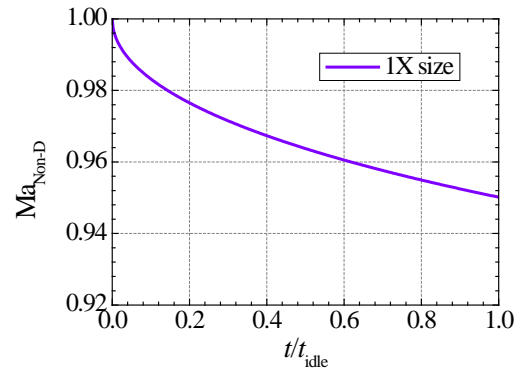


Fig. A-8 Normalized Mach number as bulk temperature varies under conduction

## Appendix C. Order Estimation for Influence of Convective Heat Transfer on Wall

With the convective heat transfer coefficient under steady state flow assessed in the previous section, this section discusses possible temperature distribution along depth direction in solid wall subjecting to steady flow in Appendix B. The material properties of solid are listed in Table A-6.

Regarding the fluid as body subjecting to external heat transfer, the Biot number evaluating the effect of convective heat transfer on wall solid and the Fourier number are expressed as

$$\text{Bi}_s = \frac{h\delta_{\text{wall}}}{k_s} \tag{A.8}$$

$$\text{Fo}_s = \frac{\alpha_s t}{\delta_{\text{wall}}^2} \tag{A.9}$$

where $h$ is convective heat transfer coefficient, and $\delta_{\text{wall}}$ is wall thickness, $t$ uses the time of a wave rotor cycle. From the assessed results listed in Table A-7, it is known that both of the dimensionless numbers are small. Therefore, the temperature distribution along depth is almost uniform, and the temperature variation in a cycle is not significant. For these reasons, sparse nodes are distributed in depth direction in wall solid (Fig. 2-10), and oscillation of wall temperature can be ignored in discussions (4.2.2.1 10X Size). Admittedly, near the surface, temperature gradient should be captured for the good of calculation of unsteady conjugate interface temperature, especially under highly unsteady flow in wave rotor cell.

Table A-6 Material properties of solid (3 significant figures)

| Parameter | | Value | Unit |
|---|---|---|---|
| Thermal conductivity | $k_{\text{s}}$ | 25 | W/(m·K) |
| Density | $\rho_{\text{s}}$ | 8000 | kg/m$^3$ |
| Specific heat | $c_{p,\text{s}}$ | 500 | J/(kg·K) |
| Thermal diffusivity | $\alpha_{\text{s}}$ | $4\times10^{-6}$ | m$^2$/s |

Table A-7 Assessed Biot number and Fourier number for solid

| | $\delta_{\text{wall}}$ (mm) | Bi | Fo |
|---|---|---|---|
| 10X | 10.0 | $2.54\times10^{-1}$ | $3.87\times10^{-4}$ |
| 1X | 1.00 | $4.00\times10^{-2}$ | $4.00\times10^{-3}$ |
| 1/10 | 0.100 | $6.36\times10^{-3}$ | $4.60\times10^{-2}$ |

## Appendix D. Conjugate Heat Transfer

*"The conjugate nature is an inherent feature of any heat transfer problem, because the intention of any heat transfer process is an interaction of at least two mediums or subjects."* [91]

Conjugate heat transfer relates generally to heat transfer process caused by thermal interaction between solid and fluid mediums. A variety of approximate solutions based on analytical methods have been developed for diverse conjugate problems in numerous applications [92]. Usually, for conjugate convective heat transfer problems, analytical methods are studied with known or relatively simple flow field. The flow field is steady or subjects to definite and regular variation pattern. The convective heat transfer coefficient could be acquired through analytical approach, too.

With regard to wave rotor cell, the unsteady flow field is complex and contingent on indeterminate heat transfer to some extent. For this concern, numerical approach for the conjugate problem concerning interaction of internal flow and cell wall is employed.

On the subject of numerical approaches for conjugate problem of natural convection and solid conduction, multi-domain pseudo-spectral method was developed for interactive heat transfer between solid and fluid of 3-D enclosed vessel [93], and unsteady conjugate thermo-gravitational model was established for 3-D enclosed vertical cylinder with the presence of local heat source [94].

As for conjugate problems in gas turbine components, CFD solver coupled to solid domain's Fourier equation solver was developed to process conjugate heat transfer relating to film cooling [95]. For unsteady interaction of wall and flame in combustor and steady state film-cooled turbine vane, the parallel coupling strategy that the flow solver provides heat flux to the solid solver while the solid solver sends interface temperature back to the flow solver was explored (Fig. A-9) [96] (the sequential one is analogous to "improved serial staggered coupling scheme" of a CFD-FEM solver for numerical study of shock-surface interaction [97]). A hybrid approach was adopted to deal with the great mismatch in time scales between fluid domain and solid domain for turbine cascades subjecting to periodic unsteady flow field, and a novel semi-analytical harmonic interface condition was introduced, so that the unsteady conjugate solution is available without simultaneous solution of both fluid and solid [98].

Jo et al. [80] developed a simple and convenient method that treats the unsteady conjugate heat transfer on a non-orthogonal coordinate system with the purpose of solving energy equations in fluid and solid at the same time, which is an extension of the equivalent conductivity concept explained by Patankar [79].



(a) Sequential coupling strategy      (b) Parallel coupling strategy
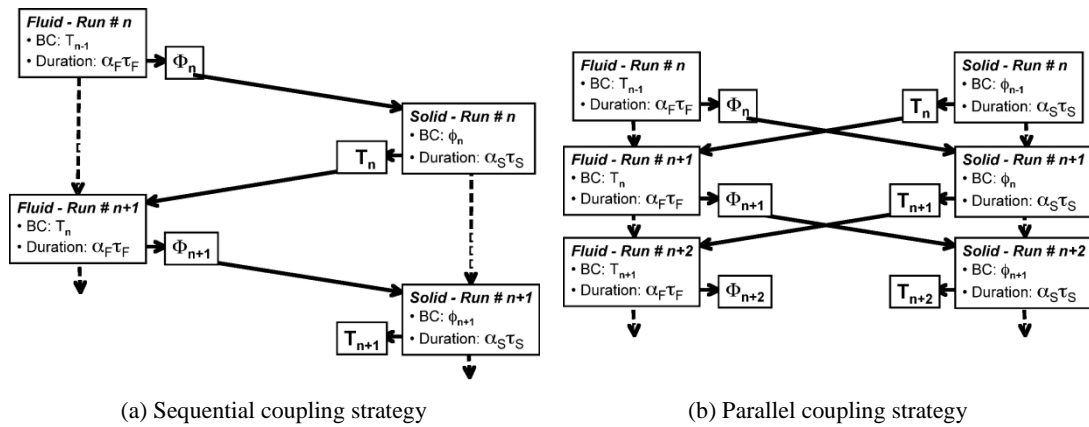
Fig. A-9 Schematic diagrams for coupling strategies [96]

## Appendix E. Comparisons between Conjugate and Steady-State-Based Boundary Treatments

Two approaches other than conjugate heat transfer boundary treatment are available of assessing heat transfer across fluid-solid interface between internal flow and wall of wave rotor cell. Either approach obtains convective heat transfer coefficient in a steady flow manner. By comparing with conjugate heat transfer boundary treatment that is regarded as reliable, the reliability of these approaches is examined for various sizes.

### E1. Adiabatic Case (ADB) at 1X Size

The objects of study in this section are the 1X size single cell of the '1 cycle per revolution' wave rotor introduced in Appendix A and its scaled ones including 3X, 1/3 and 1/10 sizes. Similar to the categorization in Section 4.1, 1X, 1/3 and 1/10 sizes are small sizes and 3X is classified as conventional size. Leakage is NOT considered. Similar to those in Subsection 4.1.2, at smaller sizes the degrees of ports are adjusted according to pressure wave arrivals that are supposed to be affected primarily by augmented viscosity effect. The port degrees are shown in Table A-8, and the conditions in ports are identical to those specified in Table 4-5.

As an example, the wave diagrams for pressure, temperature and axial velocity of adiabatic case in 1X size are shown in Fig. A-10. The wave rotor cycle includes compression process, expansion process and two idle periods, and there is no much difference from the wave rotor cycle shown in the Fig. 4-11 except for the duration of idle period after expansion process. In the '1 cycle per revolution' wave rotor, this idle period composes about half of a wave rotor cycle in degree.

Table A-8 Port degrees for '1 cycle per rev.' wave rotors (starting opening or shutting)

| | | Size | | |
|---|---|---|---|---|
| | | 3X & 1X | 1/3 | 1/10 |
| GH | open | 0 | 0 | 0 |
| | shut | 46 | 49 | 52 |
| AL | open | 117 | 123 | 134 |
| | shut | 160 | 168 | 183 |
| AH | open | 22 | 22 | 24 |
| | shut | 71 | 75 | 79 |
| GL | open | 84 | 88 | 92 |
| | shut | 129 | 135 | 143 |



(a) pressure (b) temperature (c) axial velocity
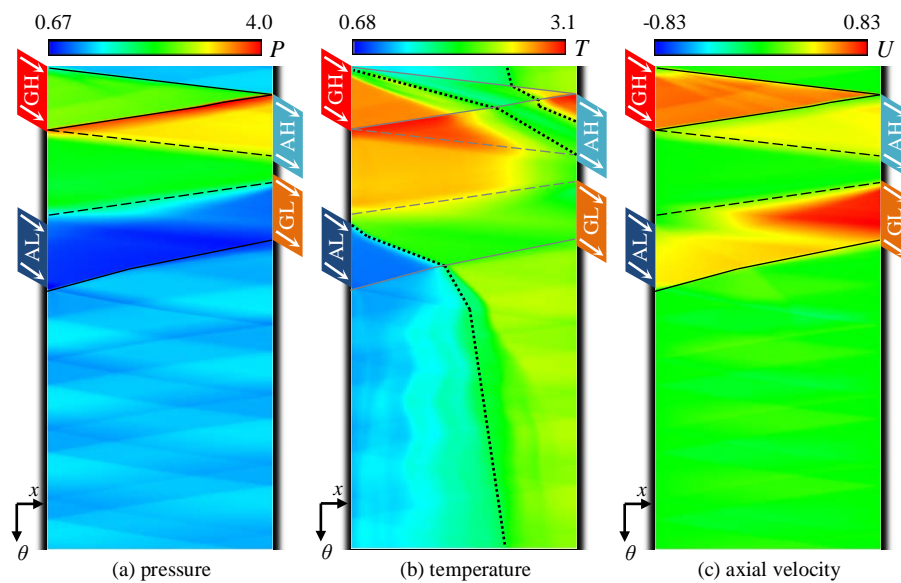
Fig. A-10 Wave diagrams for adiabatic case in 1X size of '1 cycle per rev.' wave rotor

*E2. Conjugate Heat Transfer Case (CHT)*

This subsection briefly describes the heat transfer effects predicted by conjugate heat transfer boundary treatment, and the next two subsections compare results of each steady-state-based boundary treatment to those of conjugate one to study the deviations at various sizes.

The wave diagrams for pressure and temperature of conjugate heat transfer case in 1X size are shown in Fig. A-11. Gas in compression process seems to be less hot than in adiabatic case. During the idle period after expansion process, the temperature of cold air keeps increasing. However, it is difficult to

compare with adiabatic ones by these contours for further and accurate information. Therefore, the following paragraphs explain the differences between adiabatic case (ADB) and conjugate case (CHT) with averaged data, axial distributions and degree histories of local parameters.

Total pressure in cell is averaged (based on mass) at every degree and the evolution of the overall average total pressure is shown in Fig. A-12 (a). Similarly, total temperature is averaged and its evolution is shown in Fig. A-12 (b). The temperature increase after expansion process (>170°) is confirmed. In the heat flux contour shown in Fig. A-13, negative heat flux in the left half after expansion process (>170°) is clear, meaning that the fluid is heated by the wall, which corresponds to the increase of temperature in Fig. A-11 (b) and Fig. A-12 (b). Because leakage is not considered in the numerical simulation, the cell is a sealed vessel in this period, and the fluid in the cell undergoes constant volume heating process. Hence, after expansion process, rate of pressure increase in Fig. A-12 (a) is proportional to rate of temperature increase in Fig. A-12 (b), resulting in higher pressure and temperature at 360° (or 0°) before the compression process of the next wave rotor cycle. Then, similar to the change in evolution of internal flow field explained in 0, in conjugate case, the pressure ratio of shock waves is smaller (Fig. A-14 (a)), the pressure after compression process is lower, and the pressure when charging from AL port is higher (Fig. A-14 (b)).

In charging and discharging, differences in average parameters in each port between adiabatic case and conjugate case are obscure. The degree histories of discharging temperature for AH port and GL port are shown in Fig. A-15. Profile changes are observed; however, average temperature is changeless. In Fig. A-16, changes in charging and discharging pressures related to GH, AH and AL ports are relatively noticeable owing to the pressure changes in cell mentioned above. The arrival of the primary shock wave can be identified by locating the first rapid rise of pressure right on the opening to AH port in Fig. A-16 (c). Although location difference is found when the primary shock wave propagates on its way at the same degree (Fig. A-14 (a)), its arrival is barely affected by heat transfer because of simultaneous increase in overall pressure and overall temperature after expansion process.[99]
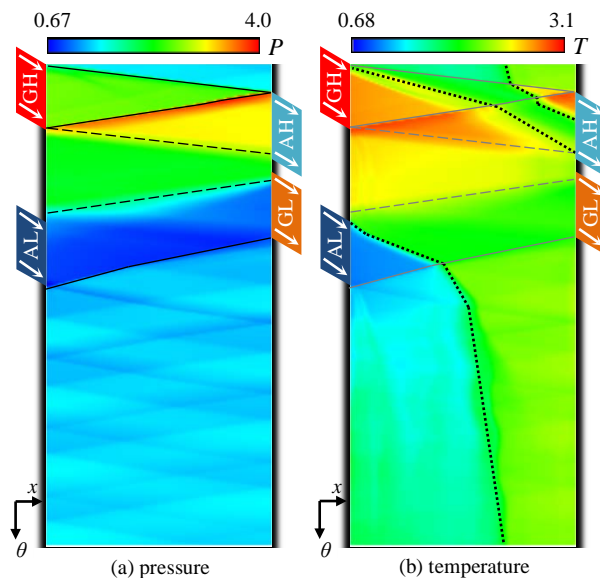


Fig. A-11 Wave diagrams for conjugate case in 1X size of '1 cycle per rev.' wave rotor
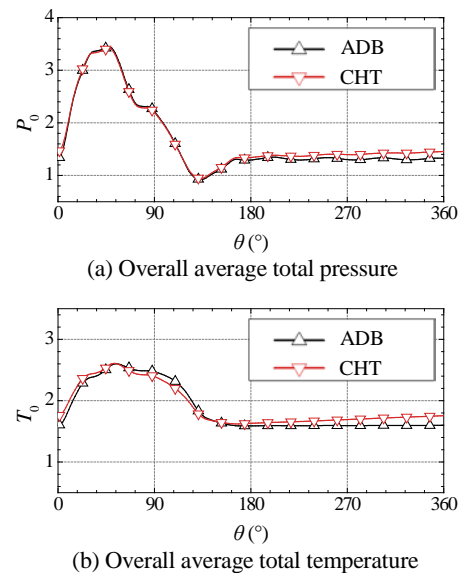
Fig. A-12 Overall average parameters in cell fluid in a wave rotor cycle for adiabatic case and conjugate case of 1X size

Heat flux

Positive: wall is heated and fluid is cooled;
Negative: wall is cooled and fluid is heated
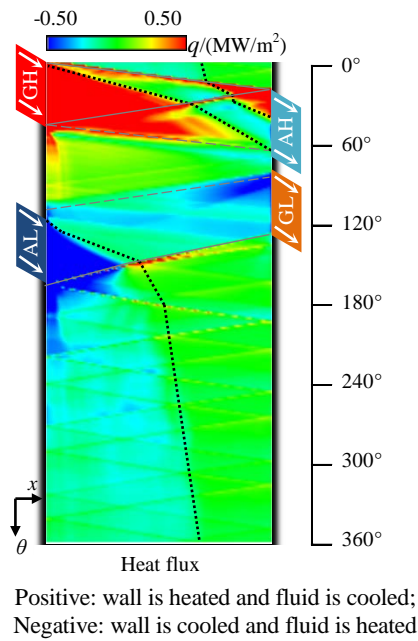
Fig. A-13 Wave diagrams of heat flux for conjugate case in 1X size of '1 cycle per rev.' wave rotor
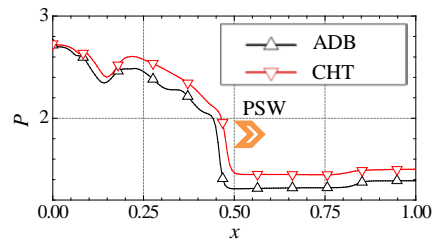


(a) 11.5°
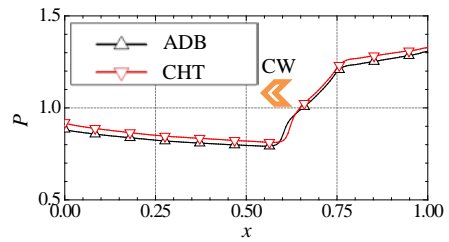


(b) 144°

Fig. A-14 Axial distributions of pressure at 11.5° and 144° for both adiabatic case and conjugate case of 1X size (PSW: primary shock wave; CW: compression wave)



Fig. A-15 Degree traces of temperature at discharging side for adiabatic case and conjugate case of 1X size
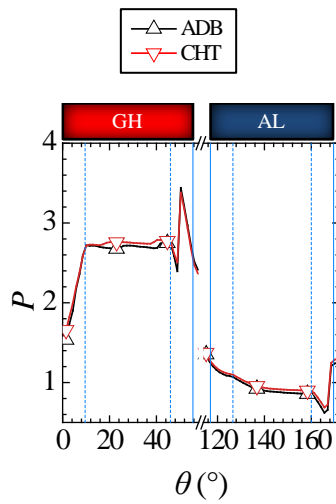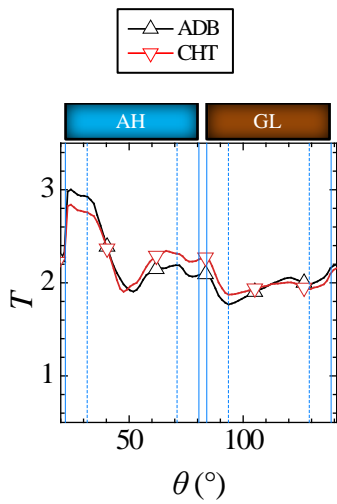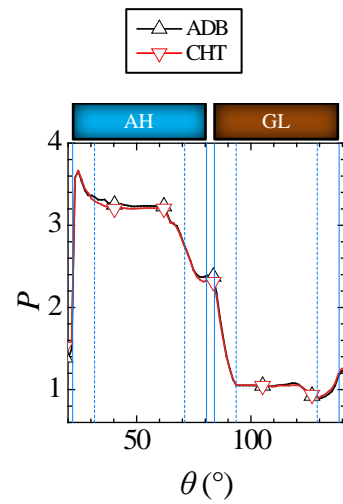
(a) Charging side

(b) Discharging side

Fig. A-16 Degree traces of pressure at cell ends for adiabatic case and conjugate case of 1X size

Fig. A-17 <u>Pressure</u> and <u>axial momentum</u> at cell ends during opening to ports for <u>adiabatic</u> case and <u>conjugate</u> case of <u>1/10</u> size

Certainly, in small sizes, heat transfer is more influential on some parameters and the effects can be exemplified by graphs shown in Fig. A-17, including pressure during opening to AL port (Fig. A-17 (a)) and AH port (Fig. A-17 (c)), and mass flow rate during opening to GH port (Fig. A-17 (b)) and AH port (Fig. A-17 (d)). Besides, in Fig. A-17 (a), during opening to GH port, the arrival of the reflected sho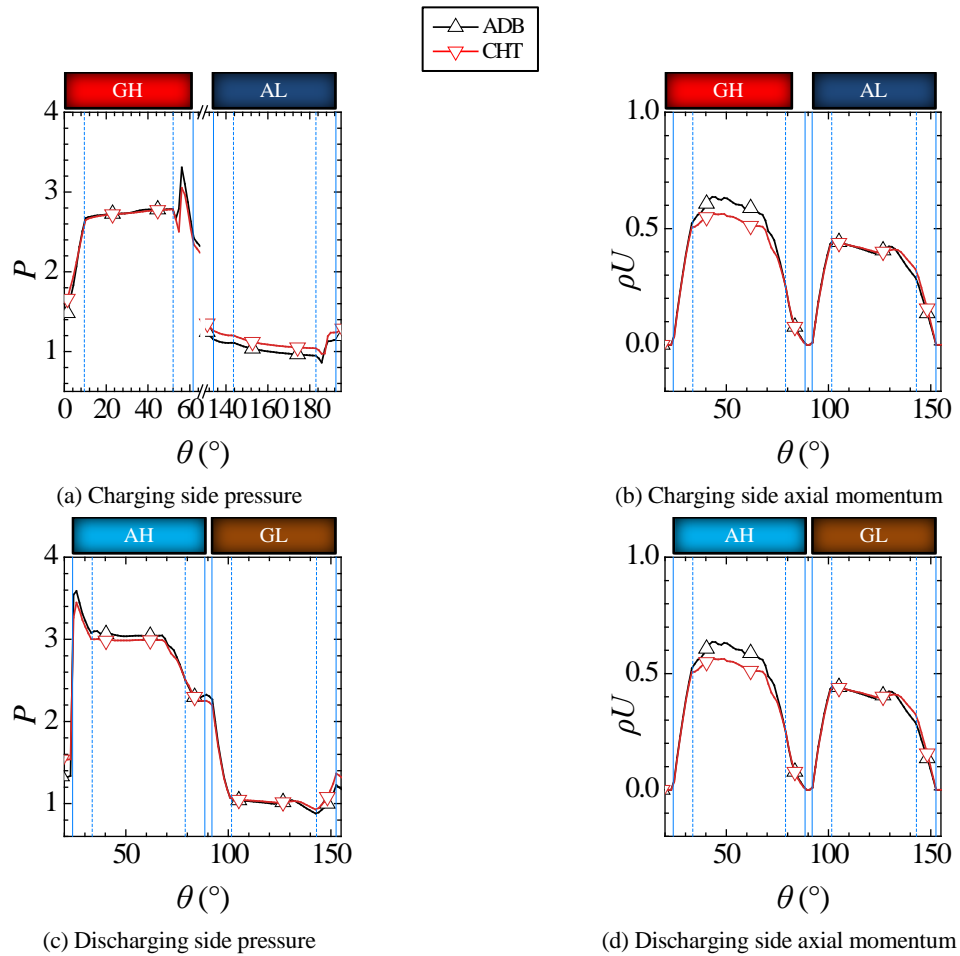ck wave characterized by the second dramatic rise of pressure is found to be a little later in conjugate case than in adiabatic case.

## E3. Comparison between CHT and ISO

Distinguished from the conjugate heat transfer boundary treatment (CH) that requires so much computational resource, the isothermal boundary treatment (ISO) is another candidate for through-flow wave rotor for the sake of its low consumption of computational resource. The key issue in applying ISO is how to estimate isothermal wall temperature that is not known in advance.

In order to estimate isothermal wall temperature, a method developed by Weber [53] is employed, which assumes that after the passage of pressure wave the development of boundary layer is analogous to that of an impulsive start over a flat plate. It is also assumed that a new thermal boundary layer is initiated behind the contact front between hot gas and cold air. Therefore, the wave diagram can be divided into many regions by characteristic lines of pressure waves and contact front. In each region, an average

temperature and an average heat transfer coefficient are assessed, and hereby with temperatures and heat transfer coefficients in all regions a definite isothermal wall temperature can be obtained. This wall temperature is updated at the end of each wave rotor cycle in flow field calculation using the wave diagram of the present cycle, and limit cycle of flow field can be reached after several cycles. Of course, for a flow field in limit cycle, the wall temperature is also changeless as:

$$\left| 1 - \frac{Wall\ temperature\ of\ present\ cycle}{Wall\ temperature\ of\ previous\ cycle} \right| < 1.0 \times 10^{-5} \qquad (A.10)$$

The results of the isothermal wall temperatures are depicted in Fig. A-18 as horizontal straight lines labeled by ISO. The wall temperatures of conjugate cases (CHT) are also shown in Fig. A-18 for comparison. Apparently, difference between conjugate wall temperature and isothermal wall temperature exists in every size involved, and in the right half the difference is more noticeable. As an example, the wave diagrams colored in heat flux for both CHT and ISO cases in 1/10 size are shown in Fig. A-19. Because of the distinctly lower isothermal wall temperature in the right half, the heat flux in the highlighted areas in the right half shows apparent difference that heat transfer from fluid to wall is more and from wall to fluid is less in ISO.

Respecting the effects on internal flow, pressure difference is relatively great in the high-pressure stage. The axial distribution of pressure at a moment when the primary shock wave is propagating is shown in Fig. A-20 (a). The pressure distribution of ISO falls between those of CHT and ADB (adiabatic case). A moment when the compression wave is propagating is shown in Fig. A-20 (b). ISO curve is close to CHT curve. As a result, pressure difference during opening to ports is noticeable only when related to high pressure ports, especially GH port, which is shown in Fig. A-21. Naturally, change of wall temperature has influence on flow temperature. The mostly affected charging and discharging temperatures are shown in Fig. A-22. To collate the effect of using ISO instead of CHT, the following equation is used to evaluate the relative difference in average parameter during opening to ports between ISO and CHT:

$$\Delta_1 = \left| \frac{A_{\mathrm{ISO}} - A_{\mathrm{CHT}}}{A_{\mathrm{ADB}} - A_{\mathrm{CHT}}} \right|, \quad A = \overline{P}_{\mathrm{port}}\ or\ \overline{T}_{\mathrm{port}} \qquad (A.11)$$

meaning the ratio of difference between ISO and CHT to that between ADB and CHT, since difference between ADB and CHT is considered as reliable heat transfer effect. And the deviation from CHT is expressed as:

$$\Delta_2 = \left| \frac{A_{\mathrm{ISO}} - A_{\mathrm{CHT}}}{A_{\mathrm{CHT}}} \right|, \quad A = \overline{P}_{\mathrm{port}}\ or\ \overline{T}_{\mathrm{port}} \qquad (A.12)$$

$\Delta_1$ and $\Delta_2$ are calculated and listed in Table A-9 for various sizes. $\Delta_1$ seems to be inconsistent as size changes. For example, AH in 3X size and GL in 1X size are very large. The cause is small difference between adiabatic case and conjugate case that bring about small denominator and consequently great $\Delta_1$. Therefore, it is better to analyze differences using $\Delta_2$. As for the average pressure or the average temperature in GH, the difference increases drastically from 3X to 1X, and among small sizes 1X, 1/3 and 1/10 the increase is relatively moderate. The difference in GL temperature also increases rapidly from 3X to 1X, while in AH the greatest increasing degree is found between 1/3 and 1/10. From these evidences, isothermal boundary treatment with isothermal wall temperature estimated by Weber's method [53]

potentially brings relatively noticeable inaccuracy in small sizes. Therefore, for small wave rotor cell, employing isothermal boundary treatment should be cautious.



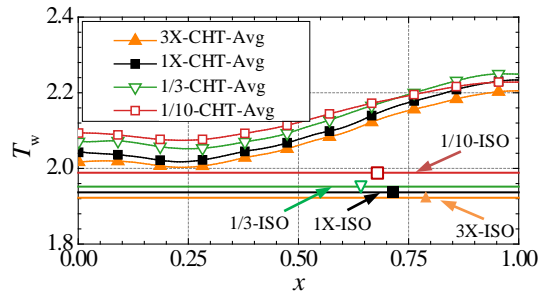Fig. A-18 Axial distributions of wall temperature for both conjugate and isothermal cases of various sizes
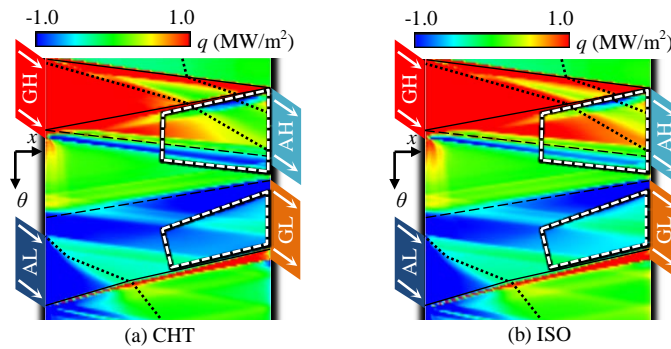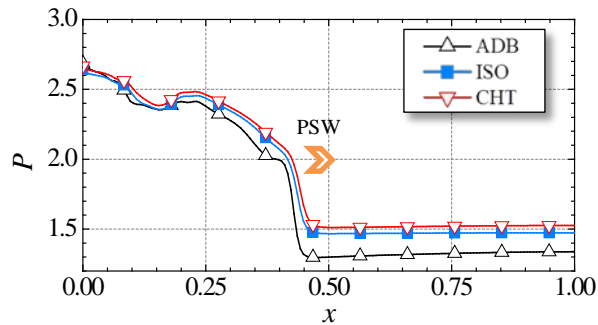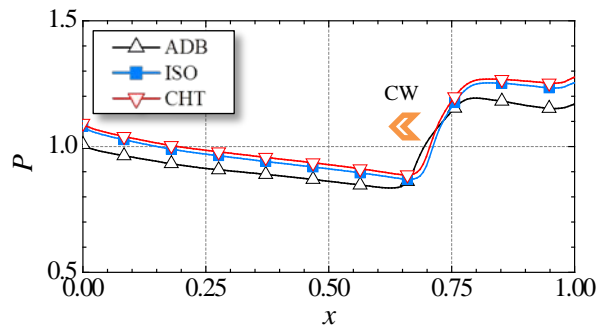


(a) CHT  (b) ISO

Fig. A-19 Wave diagrams colored in heat flux for both conjugate and isothermal cases of 1/10 size



(a) 11.5°



(b) 158°

Fig. A-20 Axial distributions of pressure at 11.5° and 144° for both adiabatic case and conjugate case of 1/10 size (PSW: primary shock wave; CW: compression wave)

(a) Charging side　　(b) Discharging side
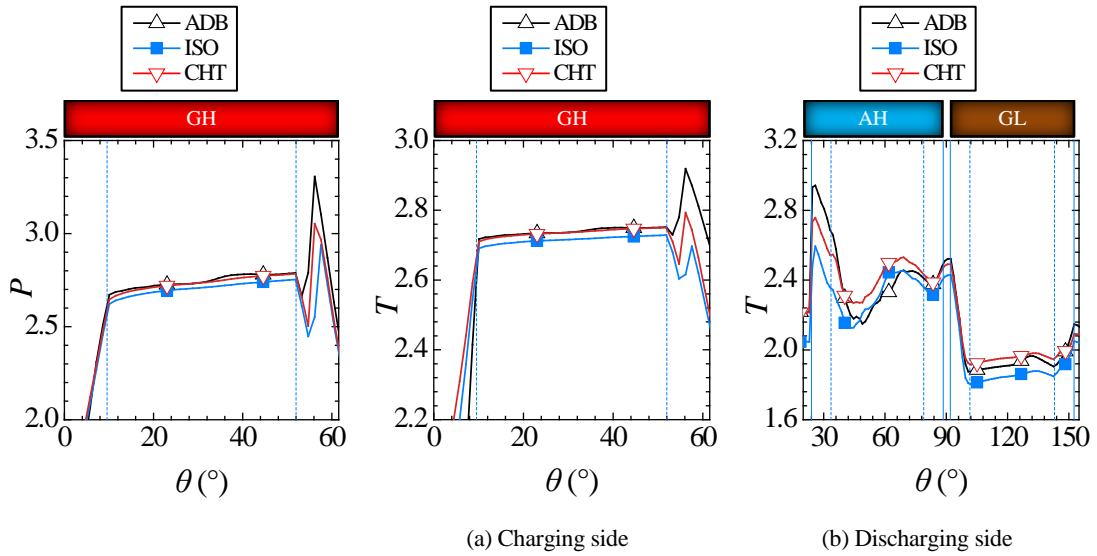
Fig. A-21 Degree traces of <u>pressure</u> at discharging side for <u>adiabatic</u> case, <u>isothermal</u> case and <u>conjugate</u> case of <u>1/10</u> size

Fig. A-22 Degree traces of <u>temperature</u> at cell ends for <u>adiabatic</u> case, <u>isothermal</u> case and <u>conjugate</u> case of <u>1/10</u> size

Table A-9 Noticeable relative differences in average pressure and average temperature during opening to ports between <u>isothermal</u> case and <u>conjugate</u> case

| Size | Pressure | | Temperature | | | | | |
| | GH | | GH | | AH | | GL | |
| | $\Delta_1$ | $\Delta_2$ | $\Delta_1$ | $\Delta_2$ | $\Delta_1$ | $\Delta_2$ | $\Delta_1$ | $\Delta_2$ |
|---|---|---|---|---|---|---|---|---|
| 3X | 49.0% | 0.327% | 0.359% | 0.00401% | 228% | 1.61% | 109% | 1.32% |
| 1X | 90.9% | 0.778% | 31.4% | 0.361% | 146% | 2.07% | 219% | 3.46% |
| 1/3 | 98.8% | 0.826% | 66.4% | 0.517% | 183% | 2.65% | 184% | 3.70% |
| 1/10 | 504% | 0.873% | 93.5% | 0.749% | 313% | 4.91% | 230% | 5.62% |

*E4. Comparison between CHT and STB*

In Paxson's 1-D numerical model [19], [57], on estimating wall temperature, heat transfer coefficient and average skin friction coefficient are calculated based on the Reynolds-Colburn analogy. Heat transfer coefficient is expressed as

$$h_L = 0.664 \frac{k}{L} \text{Re}_L^{1/2} \text{Pr}_L^{1/3} \tag{A.13}$$

where $k$ is thermal conductivity, $L$ is cell length. With the flow field calculated by the present flow solver, $h_L$ and corresponding wall temperature can be calculated, too. Like in ISO, the wall temperature is

updated at the end of each wave rotor cycle in numerical simulation, and the results after limit cycle and convergence of wall temperature are reached are presented and compared with CHT in this subsection.

The wall temperature assessed by the method introduced above, naming it as STB, is shown in Fig. A-23 (a) for 3X size, together with conjugate wall temperature (CHT-Avg). Apparent difference is observed between the wall temperatures. For small sizes 1X ~ 1/10, wall temperatures of STB and CHT are shown in Fig. A-23 (b) ~ (d). Difference in wall temperature is relatively small in 1/3 size and 1/10 size.

Similar to the previous subsection, noticeable $\Delta_2$ differences are listed in Table A-10. Despite greater difference in wall temperature in 3X and 1X sizes and smaller ones in 1/3 and 1/10 sizes, the difference in discharging temperature (AH and GL) increases as size reduces. Besides, rapid increase is found between 1X and 1/3. Therefore, it is worth noting that because increasing heat transfer effects in small size, it is right to be cautious on wall temperature estimation based on steady state assumptions.



(a) 3X size

(b) 1X size
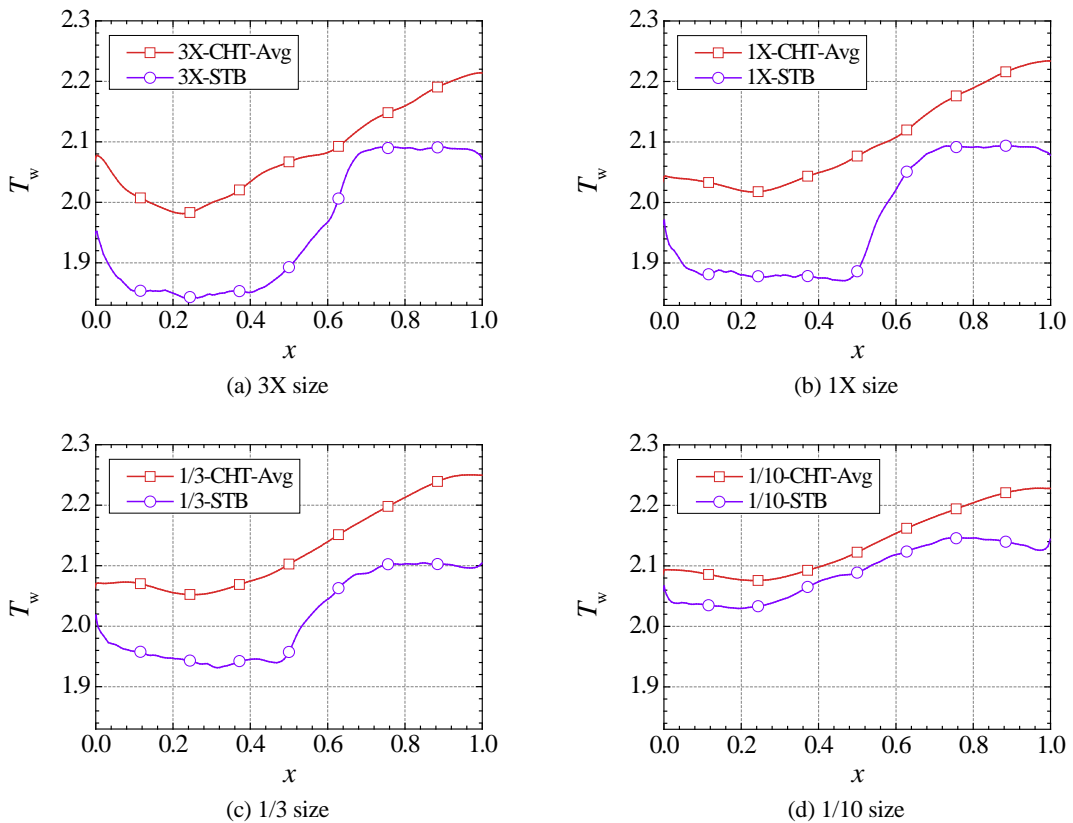
(c) 1/3 size

(d) 1/10 size

Fig. A-23 Axial distributions of wall temperature for both conjugate and steady-temperature-boundary cases of various sizes

Table A-10 Noticeable relative differences in average temperature during opening to ports between steady-temperature-boundary case and conjugate case

| Size | Temperature | |
| --- | --- | --- |
| | AH | GL |
| 3X | 0.851% | 0.417% |
| 1X | 0.946% | 0.615% |
| 1/3 | 1.67% | 1.81% |
| 1/10 | 2.58% | 2.15% |

## Appendix F. Analytical Argument for Post-Shock Properties Related to Primary Shock Wave

This section analytically explains the parameters of flow field behind the primary shock wave. To understand the flow field caused by primary shock wave generated by opening cell to GH port, it is meaningful to refer to simple one-dimensional shock tube problem as the pressure wave propagations shown in Fig. A-24.

In Fig. A-24, the typical isentropic flow in a shock tube is schematically depicted. At initial time, the shock tube is divided by diaphragm into low-pressure air region of state 1 and high-pressure gas region of state 4. Sudden rupture of the diaphragm causes a right-going compression wave and a series of left-going expansion waves. As time proceeds, the regions not affected by pressure waves are still in state 1 or 4, while a part of the air formerly at state 1 is compressed to state 2 as the compression wave propagates rightwards. Meanwhile, the contact front between gas and air moves rightwards behind the compression wave since the flow velocity behind the compression wave is right and lower than the propagation speed of the compression wave. The state between the contact front and the expansion waves is labeled 3.

For this shock problem, with the given initial pressure ratio $P_{14}=P_1/P4$ and initial temperature ratio $T_{14}=T_1/T_4$, the pressure ratio $P_{21}=P_2/P_1$ can be derived by the following equation:

$$P_{14} = \frac{1}{P_{21}} \left\{ 1 - \left(P_{21}-1\right) \left[ \frac{\beta_4 E_{14}}{\alpha_1 P_{21}+1} \right]^{\frac{1}{2}} \right\}^{1/\beta_4} \tag{A.14}$$

where $E_{14} = \frac{(c_v T)_1}{(c_v T)_4} = T_{14}$, $\alpha = \frac{\gamma+1}{\gamma-1} = \frac{1.4+1}{1.4-1} = 6$, and $\beta = \frac{\gamma-1}{2\gamma} = \frac{1.4-1}{2\times1.4} = \frac{1}{7}$. Across the contact front, velocities and pressures are the same. Therefore, pressure and velocity behind the compression wave satisfy $P_3=P_2$ and $u_3=u_2$.

Regarding the problem in wave rotor, the schematic of cell opening to GH port is shown in Fig. A-25. Before opening to GH port, the left half of cell plays the role of air part and GH port acts like gas part at the initial time in Fig. A-24. Then, when it opens to GH port, the contact front and the shock wave propagates in cell. State in GH corresponds to 4 and initial state in left half of cell corresponds to 1. According to Eq. (A.14), with given port state as 4 and air state in cell as 1, pressure ratio $P_2$ and $u_2$

related to pressure and velocity behind the primary shock wave can be calculated. Table A-11 lists the calculated parameters concerning adiabatic case (ADB) and heat transfer case (CHT) for 1/10 size (discussed in Section 4.2). $T_1$ is higher in CHT than in ADB because the air is heated by wall. $P_1$ is also higher owing to heating, but leakage leads to less rate of increase of pressure. Consequently, from ADB to CHT, $P_{14}$ increases less than $T_{14}$. As a result, $P_{21}$ is 2.87 for ADB and 2.64 for CHT (Table A-11). With constant pressure $P_4$ as reference, $P_{24}=P_2/P_4$ is 0.471 for ADB and 0.462 for CHT. Apparently, lower pressure occurs behind the primary shock wave in CHT. The velocity behind the primary shock wave ($u_2$) is also obtained for ADB and CHT and shown in Table A-11, where $u_2$ corresponding to inflow speed when cell opens to GH port is found to be higher in CHT.
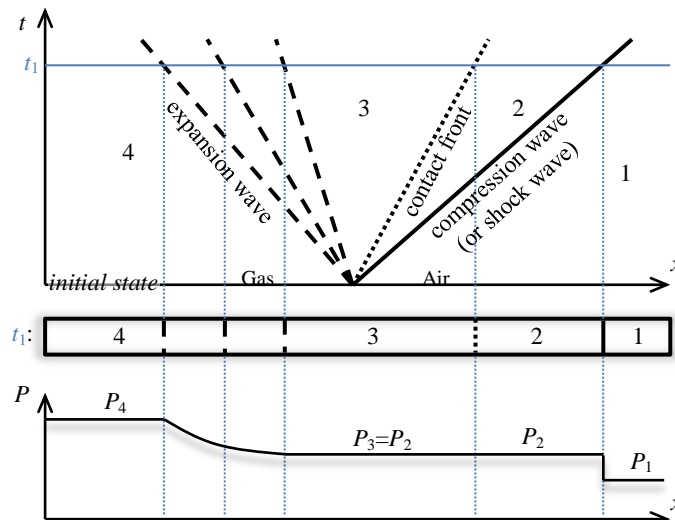


Fig. A-24 Wave systems following sudden rupture of diaphragm in shock tube
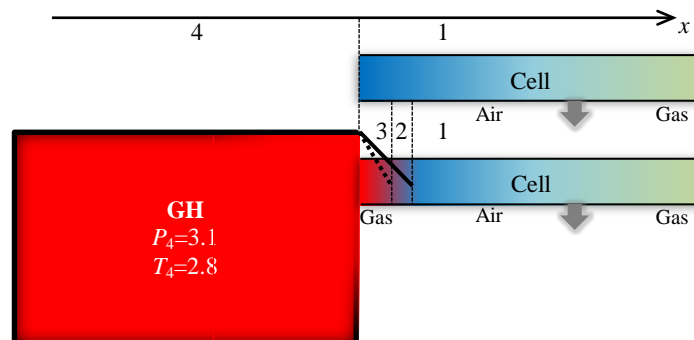


Fig. A-25 Schematic of opening a cell to GH port

Table A-11 Calculation of state parameters

|  | $P_{14}$ $P_1/P_4$ | $T_{14}$ $T_1/T_4$ | $P_{21}$ $P_2/P_1$ | $u_2$ (m/s) |
|---|---|---|---|---|
| ADB | 0.164 | 0.378 | 2.87 | 360 |
| CHT | 0.175 | 0.476 | 2.64 | 369 |

## Appendix G. Substituting Laminar for Turbulent

The present study implements numerical simulations at various sizes with a consistent assumption that the flow in cell is fully turbulent at all sizes involved for the purpose of ensuring consistent numerical model across sizes. However, according to Table A-2, in some scales the flow in cell may fall into laminar regime. Although it can be generally regarded as working under turbulent state for the present configuration and for a wave rotor in a gas turbine system, sometimes a researcher may have to deal with cell flow under laminar state. This subsection presents the evidence that the characteristics and conclusions addressed under turbulent assumption can be similarly obtained under laminar assumption. To keep the subsection brief and descriptive, the demonstration focuses on comparison between laminar adiabatic case and laminar heat transfer case of 1/10 size since most striking heat transfer effects occurs in 1/10 size among the sizes studied.

Firstly, in the heat-flux-colored wave diagram shown in Fig. A-26 for laminar case, those intense heat flux also observed in conventional sizes in the regions of 1) inflow of hot gas and cold air, 2) compressed fluid, and 3.1) downstream vicinity of shock wave in gas are also located and marked. Those regions of intense heat flux only observable in small size including 3.2) downstream vicinity of shock wave in air, 4) expansion waves, and 5) downstream vicinity of compression wave are also found in Fig. A-26. During expansion process, gas is heated by wall, which is the same as in turbulent case, too.

Secondly, major effects of heat transfer on charging and discharging are illustrated in Fig. A-27. When opening to charging ports GH and AL, the changes of average values caused by heat transfer can be easily observed and they are consistent with those related to GH and AL in Fig. 4-43. As for the discharging port AL in Fig. A-27, the differences in total pressure, total temperature in air part, and axial momentums in air part between ADB and CHT also resembles corresponding ones in Fig. 4-43. In regard to the noticeable difference related to the discharging port GL, higher temperature in turbulent heat transfer case (Fig. 4-43 (d-2)) also occurs in laminar heat transfer case (Fig. A-27 (d-2)). Since the changes in port parameters are outcomes of heat transfer effects on internal flow field, it is possible to infer from the similarities of differences in port parameters that the changes of flow field caused by heat transfer are also similar to those in turbulent case.

Last but not least, the delay of arrival of reflected shock wave for about 3° in heat transfer case is also identified in Fig. 4-43 (a-1) where the pressure drastically rises again (around 50°).

To sum up, all the causes of intense heat transfer and heat transfer effects on flow addressed under turbulent assumption can also be achieved with laminar assumption.
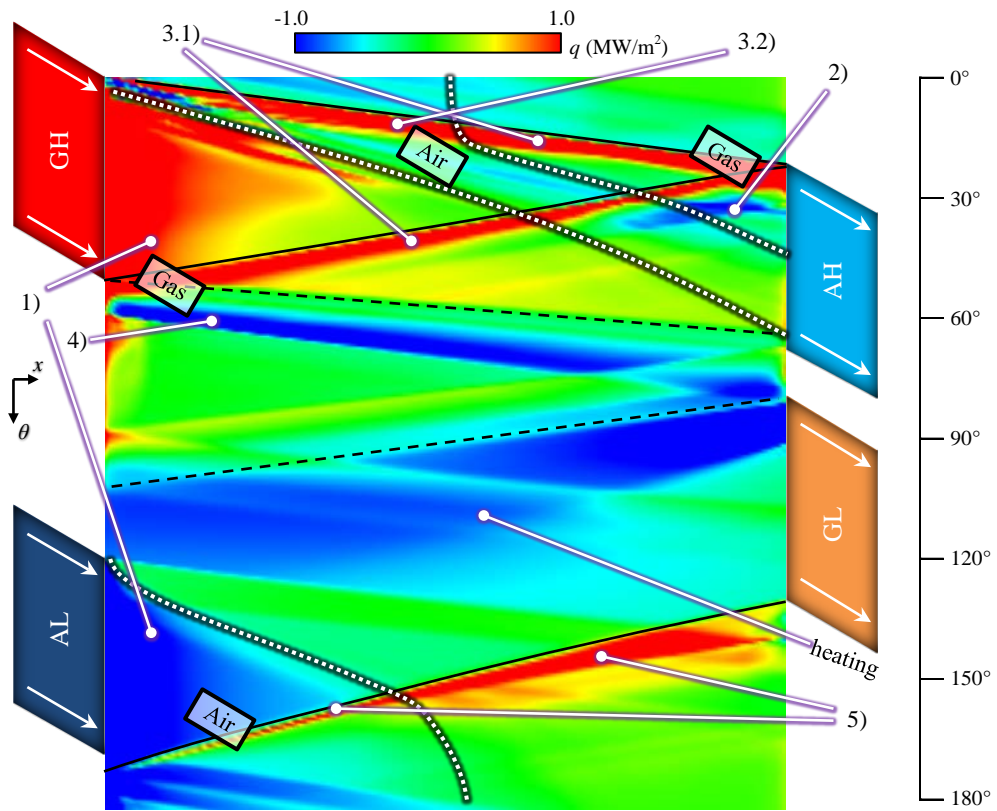
Fig. A-26 Wave diagram colored in heat flux for heat transfer case of 1/10X size (laminar)
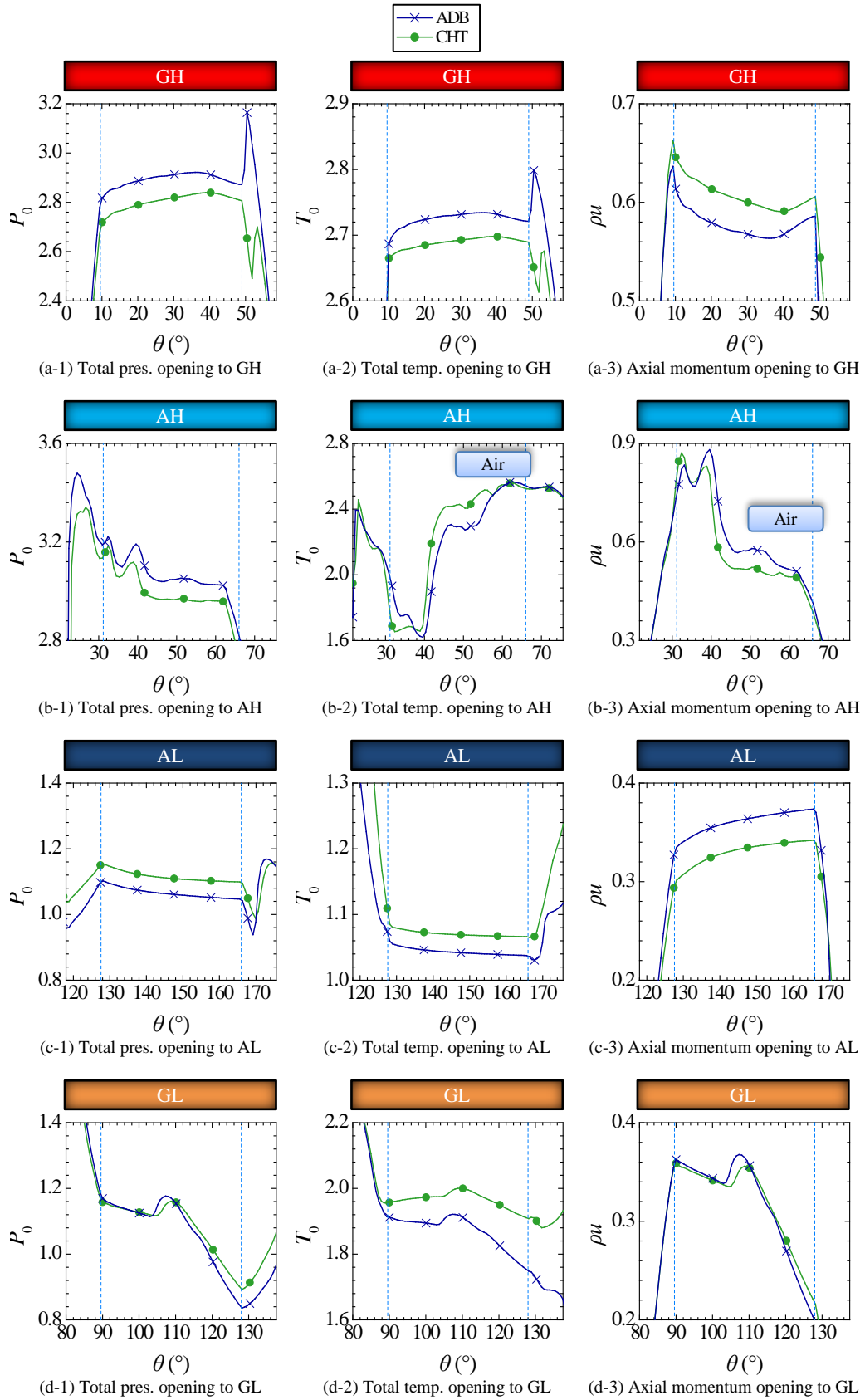
Fig. A-27 Total pressure, total temperature and axial momentum at cell ends during opening to ports for adiabatic case (ADB) and heat transfer case (CHT) of 1/10 size

# Publication List

## Conference Paper

[1] Shi Deng, Koji Okamoto and Susumu Teramoto, "Numerical investigation of heat transfer effects in small wave rotor", AJCPP2014-070, *Asian Joint Conference on Propulsion and Power (AJCPP) 2014*, March 5-8, 2014, Jeju Island, Korea.

[2] Shi Deng, Koji Okamoto, Kazuo Yamaguchi and Susumu Teramoto, Numerical Investigation of Heat Transfer Effects on Internal Flow Dynamics of Micro Wave Rotor, *The 22nd International Symposium on Airbreathing Engines*, October 25 - 30, 2015, Phoenix, Arizona, USA. (To be presented)

## Journal Paper

[1] Shi Deng, Koji Okamoto and Susumu Teramoto, (2015), "Numerical investigation of heat transfer effects in small wave rotor", *Journal of Mechanical Science and Technology*. (Accepted)